ADVANCES IN SOFT X-RAY PERFORMANCE OF MICROCHANNEL PLATE DETECTORS

by

JAMES FINDLAY PEARSON

Thesis submitted to the University of Leicester for the degree of Doctor of Philosophy

April 1984

X-ray Astronomy Group
Department of Physics
University of Leicester

Abstract

This thesis discusses the design and improvement of microchannel plate (MCP) chevron detectors for imaging soft X-ray astronomy. Particular attention is focused on the MCP quantum detection efficiency and output pulse height distribution.

Graded density electrodes are shown to be a suitable two dimensional image encoding system for MCP's. Details are given of a specially constructed vacuum system for testing chevron MCP detectors.

Significant reductions in output pulse height distribution FWHM are demonstrated by applying an accelerating potential between the two MCP's of a chevron. Preliminary work on the development of a curved surface MCP detector, for use with grazing incidence optics, is reported and recommendations given for future development.

The rational behind using CsI reflection photocathodes to improve the MCP's quantum detection efficiency is examined. Existing CsI photocathode techniques are reviewed and extended to allow the deposition of 14,000 Å thick layers. A detailed set of efficiency measurements is presented.

Increased high angle efficiencies are obtained by using a repeller grid with a CsI coated MCP. The results of attempting to produce an MCP with an input electrode that does not penetrate into the channels are also described. The overall usefulness of a repeller grid is discussed.

Significant intrinsic energy resolution is achieved, for the first time, from a CsI coated MCP chevron. The resolution is sufficient to allow two colour photometry, separating energies above and below 1 keV. One attempt to improve the energy resolution is documented together with suggestions for further ways in which this might be achieved.

Declaration

I hereby declare that no part of this thesis has been previously submitted to this or any other University as part of the requirements for a higher degree. The work described here was conducted by the undersigned except for the contribution of colleagues indicated in the text.

James F Pearson

James F. Pearson

April 1984

Dedication

To my Mother, Father and Friends.

In appreciation of the support and encouragement which I was fortunate to receive.

Acknowledgements

It gives me great pleasure to acknowledge the help and encouragement given to me by various members of the Department of Physics during the work described in this thesis. In particular I would like to express my sincere thanks to my two supervisors, Dr. G.C. Smith and Dr. G.W. Fraser, for the excellent supervision which I received. Dr. G.C. Smith provided me with a solid grounding in, and enthusiasm for, experimental work. Dr. G.W. Fraser has guided my subsequent work, supplied the theoretical models for interpreting the results and made many valuable comments on the initial drafts of this thesis. I gratefully acknowledge the many stimulating and enlightening discussions held with them both. I would also like to thank Dr. E. Mathieson for his help during the development of the graded density electrodes and for very kindly agreeing to read the final draft of my thesis.

My thanks also go to Professor K.A. Pounds for the opportunity to study at Leicester University, to Mr. H. Chapman for his excellent work on the construction of the test equipment described in Chapter 3, and to Mrs. H. Townsend for typing this thesis. I would also like to express my thanks to Mr. J. Dowson and everyone else in the Department of Physics who assisted me in any way during my work.

I gratefully acknowledge financial support from the Science and Engineering Research Council through a research studentship.

List of Publications

Some of the experimental results reported in this thesis have been incorporated in the following papers. The chapters to which these papers refer are given in brackets.

1. "Microchannel plate read-out using graded density electrodes" ; G.C. Smith, J.F. Pearson and E. Mathieson, Nuclear Instruments and Methods 192 (1982) 383-386. (Chapter 2)

2. "The gain characteristics of microchannel plates for X-ray photon counting" ; G.W. Fraser, J.F. Pearson, G.C. Smith, M. Lewis and M.A. Barstow, IEEE Transactions on Nuclear Science NS-30 (1983) 455. (Chapter 4)

3. "The stability of CsI-coated microchannel plate X-ray detectors" ; M.J. Whiteley, J.F. Pearson, G.W. Fraser and M.A. Barstow, Nuclear Instruments and Methods in Physics Research (in press). (Chapter 5)

4. "Soft X-ray energy resolution with microchannel plate detectors of high quantum detection efficiency" ; G.W. Fraser and J.F. Pearson, Nuclear Instruments and Methods in Physics Research 219 (1984) 199-212. (Chapters 5,7)

5. "The soft X-ray detection efficiency of coated microchannel plates" ; G.W. Fraser, M.A. Barstow, J.F. Pearson, M.J. Whiteley and M. Lewis, Nuclear Instruments and Methods in Physics Research (in press). (Chapter 6)

CONTENTS

Page

CHAPTER 1

MICROCHANNEL PLATES (MCP's) AND THEIR APPLICATIONS

1.1 Microchannel Plates

Microchannel Plates (MCP's) are glass disks, 25-60 mm in diameter and 0.5-1.5 mm thick, which contain 10^6-10^7 miniature channel electron multipliers (CEM's) fused together in a hexagonal packing structure [1,2,3] (fig.1.1). These devices are intrinsically sensitive to electrons, protons, high energy pions, ions, γ rays, X-rays and UV radiation, and when combined with a suitable photocathode can be used to detect visible light. Each individual channel, 8-100 μm in diameter, acts as an independent continuous dynode photomultiplier. Gains of 10^3-10^4 can be obtained with single straight channel MCP's (Section 2.1.3), while curved channel MCP's produce gains of $\sim 10^6$ and "chevron" pairs of plates gains of 10^7-10^8 (Section 2.1.4).

The importance of MCP's stem from their ability to produce very high gains, within a very small volume, uniformly over an area of many square centimetres. The high gain and small channel pitch allows the production of high resolution imaging, photon counting detectors and high gain image intensifiers.

1.2. MCP Applications

MCP's were originally developed for use in high resolution image intensifiers [4,5]. Here the MCP is placed immediately behind a photocathode (e.g. S 25 multi-alkali) and used as an electron amplifier in both proximity focused (Fig.1.2(a)), and electron lens (Fig.1.2(b)), type tubes. The output from the MCP is then accelerated onto a phosphor screen to produce a visible image. When operated with a low bias voltage the MCP is a linear device and produces good contrast images. When the

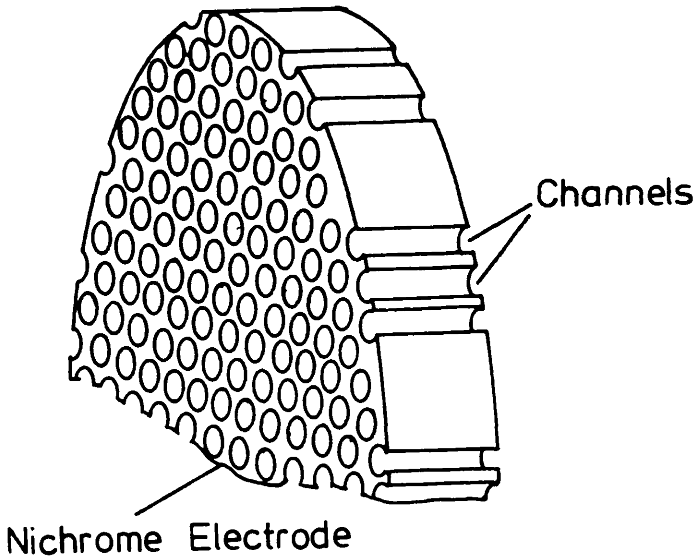

1.1. Schematic drawing of part of an MCP. The microchannels are normally arranged in a regular hexagonal pattern. Electrical contact is made via a Nichrome electrode, applied to front and rear surfaces, that penetrates one channel diameter into the channel (adapted from ref.[6]).

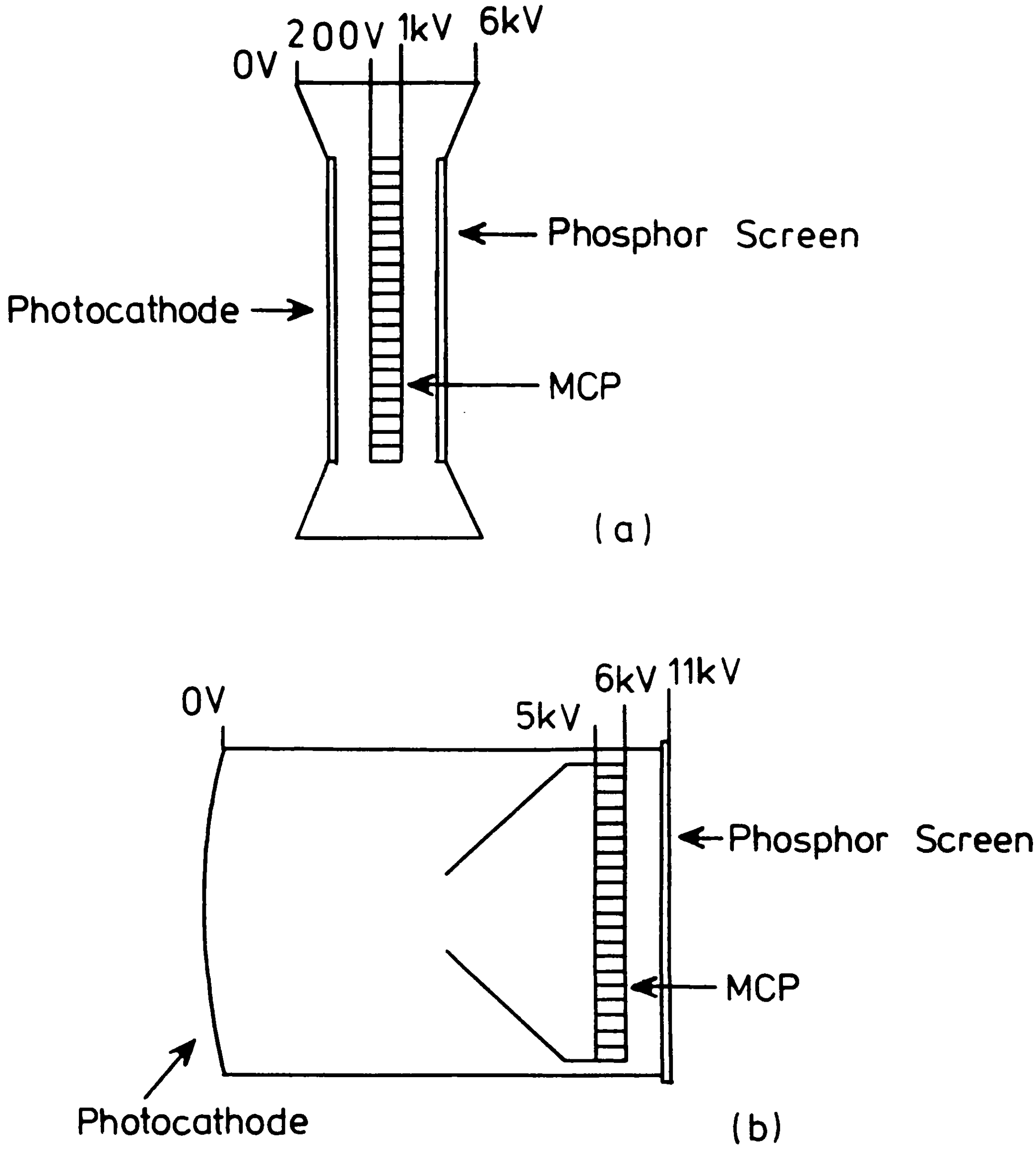

1.2. Typical image intensifiers incorporating MCP's. Incident radiation, normally visible light, releases electrons from the photocathode which are detected and amplified by the MCP. The resulting 10^3-10^4 electrons are accelerated into a phosphor screen to produce a visible image.

(a) Proximity focused tube. Electrons from the photocathode are accelerated across a small gap to produce an electron image on the MCP. Allows production of very small image tubes but requires inversion of image for normal viewing.

(b) Electron focused tube. Electrons are focused onto the MCP by an electron lens. Slightly longer image tube than (a) but no further inversion is necessary (adapted from ref.[4]).

intensifier is exposed to bright light, however, the MCP saturates, i.e. above a given input level no increase in output is observed. In contrast to previous image intensifiers, this allows faint detail to be observed even when there is a bright source in the field of view. These MCP image intensifiers are lighter and more compact than their predecessors, and for MCP's of 15 μm channel pitch, resolutions of 30 line pairs mm^{-1} are possible. The high MCP gains allow operation at very low light levels and they are extensively used in military night vision devices.

MCP intensifiers can also be used in scientific experiments where very low light yields are present. By using suitable photocathodes these devices can be adapted to image other wavelengths, e.g. X-ray and infra-red radiation.

The small size of an individual channel, combined with the intense electric fields that exist inside the channel (1-2 V μm^{-1}), means that electron transit times are short and pulse jitter is small. MCP output pulses have rise times of less than 0.5 nsec and widths of order 1 nsec. The compact photomultiplier tubes constructed using MCP's are also very much less sensitive to magnetic fields [6]. The very fast response of MCP's have been used in areas such as plasma diagnostics [7] and nuclear physics [8].

MCP's have also been used to produce high bandwidth (~ several GHz) oscilloscopes [9,10], to measure the differential scattering cross section of electrons from helium [11] and to reduce specimen damage in electron microscopes [12].

1.3. MCP's in X-ray Astronomy

MCP's have been successfully used in X-ray astronomy as focal plane detectors for spectrometers [13,14,15,16] and imaging telescopes [17,18, 19,20]. The turning point for cosmic X-ray astronomy was the development of grazing incidence X-ray telescopes [21], which could produce two-dimensional images of X-ray sources. These images could then be detected by Imaging Proportional Counters (IPC's) or MCP's. The combination of MCP's and grazing incidence optics was able to produce very high spatial resolution images over useful fields of view. These high resolution images were supplemented by the lower spatial resolution, wider field of view images, obtained using IPC's. This gave a great boost to astrophysics since before this imaging could only be achieved by using mechanical collimators, with a rather poor angular resolution, together with an imaging proportional counter [22,23,24].

The most important imaging X-ray astronomy mission to date has been the HEAO-2 (Einstein) observatory [19]. This carried the first large area grazing incidence telescope, and provided an improvement in sensitivity of order 10^2-10^3 times over previous nonimaging missions. As part of the focal plane instrumentation Einstein had a High Resolution Imager (HRI) which incorporated a chevron MCP detector. The angular resolution of the HRI image was limited by the telescope optics to $\sim 4''$ over a $25'$ field of view. The HRI produced very high resolution images of supernova remnants, globular clusters, galaxies and provided much improved positions for a large number of point sources [25].

These results were obtained despite major deficiencies in the performance of the HRI MCP's; (1) Low quantum detection efficiency, 27% at 0.28 keV falling to 3.5% at 3 keV. (2) No intrinsic soft X-ray energy resolution. A limited amount of energy resolution was available on the HRI by using the absorption filters of the broad band filter spectrometer.

The HRI can be compared with the other imaging focal plane detector aboard Einstein, an IPC providing a much larger field of view ($75' \times 75'$) and significant energy resolution ($E/\Delta E \gtrsim 1$ between 1.5 and 4 keV). Although the IPC possessed a higher quantum detection efficiency (55% at 0.28 keV, 65% at 1.24 keV [26]) it had a significantly poorer angular resolution ($\sim 1'$). The remaining focal plane instruments, the solid state spectrometer and the focal plane crystal spectrometer, both had very high energy resolution but no spatial resolution.

Other alternatives as X-ray imaging detectors are Gas Scintillation Proportional Counters (GSPC's) [27] and Charge Coupled Devices (CCD's) [28]. The GSPC produces better (times ~2) energy resolution than the IPC but can at best only hope to equal the IPC's spatial resolution. CCD's promise to offer simultaneously very good spatial and energy resolution along with high detection efficiencies. They are, however, still in the development phase and as yet cannot match the active areas of existing MCP detectors (12 x 12 mm^2 for current CCD's as opposed to ~50 mm diameter for current MCP detectors).

The MCP detector therefore remains the only detector able to provide large area X-ray images whose resolution is limited by the telescope rather than the detector.

1.4. Future Satellite Mission in X-ray Astronomy

Future X-ray astronomy satellites that propose to use MCP detectors at the focus of grazing incidence telescopes include; ROSAT [29], Advanced X-ray Astrophysics Facility (AXAF) [30], X-ray Multi-Mirror (XMM) mission [31], High Throughput Spectrometer (HTS) [32].

ROSAT is a German national satellite intended to produce the first imaging sky survey in the 0.1-2 keV energy range. Focal plane instrumentation for the main telescope consists of 2 IPC's and a copy of the Einstein HRI supplied by the Americans. Being launched as part of ROSAT is a coaligned British piggy-back experiment, the Wide Field Camera (WFC), which will observe the unexplored 0.04-0.21 keV energy range. The sky surveys will be followed up with detailed, pointed observation, using both instruments.

Further in the future (>1990) the proposed American satellite, AXAF, will provide very high quality, long focal length, optics for detailed studies of X-ray sources. In this mission the high energy response of the grazing incidence optics will extend up to 8 keV, and very high angular resolution will be possible ($\frac{1}{2}''$).

Also being proposed for the 1990's are XMM and HTS which will provide high throughput optics for general astronomy and spectroscopy respectively. The basic parameters of these five optical systems are summarised in Table 1.1.

A property of all grazing incidence X-ray optics is curvature of the focal plane. An instrument incorporating a detector curved to match the focal plane will obviously have a sensitivity advantage. Initial work on the development of such a MCP detector is reported in this thesis (Section 4.2). Work on this topic is continuing at Leicester for the development of curved MCP detectors to be used on the ROSAT WFC.

The image scale and mirror resolution determine the necessary spatial resolution of the detector. From Table 1.1 it can be seen that the highest spatial resolution required is 25 μm for AXAF. The channel pitch limited resolution of presently available MCP's is less than 25 μm and therefore the spatial resolution requirements will only affect the design of the position encoding system and associated electronics.

The design and optimisation of focal plane instrumentation for a grazing incidence telescope is constrained by the basic telescope design (Fig.1.3). Grazing incidence optics produce an angular cone of X-rays with mean half angle θ and dispersion $\Delta\theta$. A focal plane instrument therefore only needs to be optimised for a narrow range of angles, $(\theta-\Delta\theta)$ to $(\theta+\Delta\theta)$, but must have a uniform response with polar angle around the channel.

1.5. Research Programme

We have seen in the preceding sections that MCP's have proved useful instruments in X-ray astronomy but that they suffer from two main problems.

Table 1.1

Comparison of the properties of future X-ray astronomy missions that use MCP detectors

Mission	Energy range (keV)	Approximate cone angle, $\theta \pm \Delta\theta$	Image scale μm per arc second	Mirror resolution FWHM on axis	MCP size (mm)
ROSAT Main telescope [29]	0.1 - 2	$8° \pm 2°$	12	$\hat{5}''$	36 (diameter)
ROSAT WFC [29]	0.04 - 0.21	$30° \pm 5°$	2.5	$\hat{1}'$	53 (diameter)
AXAF [30]	0.1 - 8	$2.5° \pm 1°$	50	$0.\hat{5}''$	100 x 100
XMM (LE telescope) [31]	0.04 - 2.5	$3.3° \pm 1°$	20	$1\hat{0}''$	80 (diameter)
HTS (LE telescope) [32]	0.06-0.3,0.45-1.8	$7.4° \pm 2°$	14.5	$2\hat{0}''$	120 x 30

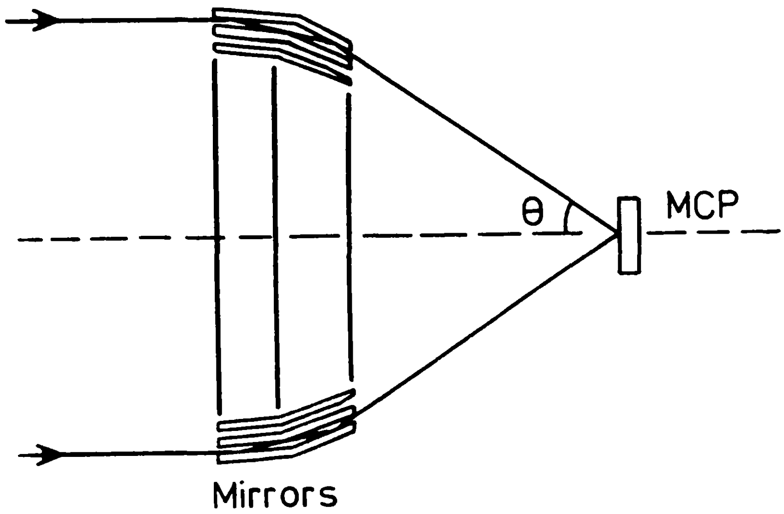

1.3. X-ray interaction geometry with a Wolter type grazing incidence telescope. Each mirror consists of two sections, which have a paraboloid or hyperboloid geometry. Incoming X-rays reflect once from each section and converge to form a cone of half angle θ at the focal plane. Only X-rays that are reflected from both mirrors reach the focal plane, all others being blocked out by baffles.

(1) Low detection efficiency. (2) No intrinsic energy resolution.
The X-ray astronomy group at Leicester University has been actively engaged in the development of MCP's in X-ray astronomy since their use was first considered. Development work was undertaken for the Einstein HRI. A sounding rocket programme in collaboration with M.I.T. in the United States is currently in progress and Leicester lead a consortium of British X-ray astronomy groups developing the ROSAT WFC.

In the following chapters we will present work carried out with the intention of producing improved MCP detectors for use in Leicester's future X-ray astronomy experiments. This will include looking at the way in which a detector is constructed (Chapters 4,6), considering means by which the quantum detection efficiency of MCP's can be improved (Chapters 4,5) and investigating the possibility of producing some form of intrinsic soft X-ray energy resolution (Chapter 7).

CHAPTER 2

BASIC MCP OPERATION

2.1 General Principles

2.1.1. Desirable properties for imaging MCP detectors

The principal use of MCP's in X-ray Astronomy (Section 1.3) is to produce high resolution images over large areas. Position coordinates are usually produced (one dimensional case) by dividing the output charge from the MCP (Q_1+Q_2), between two preamplifiers in such a way that the ratio $Q_x = Q_1/(Q_1+Q_2)$ (or $Q_2/(Q_1+Q_2)$), gives the event position (Section 2.2).

The ultimate resolution obtainable by any MCP detector is set by the channel pitch. The EXOSAT MCP detectors have a channel pitch limited resolution of 30μm over a 42 mm diameter area [18] and the ROSAT WFC will have a channel pitch limited resolution of 15 μm over an approximate 50 mm diameter area [33]. This limiting resolution is seldom attained however; the resolution of the WFC mirrors is, for example, only 150 μm which is a factor of ten worse than the MCP detector resolution. The position encoding electronics for the WFC therefore only needs to evaluate Q_x to an accuracy of one part in 350.

The achievable spatial resolution is limited by the electronics, and in any analogue readout system this limit is inversely proportional to the signal to noise ratio (S/N) of the signals fed to the ratio electronics. To produce positions accurate to one part in 350 in each axis requires a S/N = 700 (assuming equal charge division between each axis). Since the electronic noise from the WFC readout system is ~1800 electrons the output charge pulse from the MCP must be in excess of ~1.3×10^6 electrons (0.2 pC). To make full use of the intrinsic WFC detector resolution would require a S/N = 7000 and a MCP charge pulse of 1.3×10^7 electrons (2 pC).

The spatial resolution must, however, be maintained over the entire field of view, a requirement which typically gives a dynamic range of 10:1 in the magnitude of Q_1 and Q_2. On top of this variation, which is intrinsic to the readout element operation, the magnitude of the output charge pulse from the MCP (Q_1+Q_2) can vary by factors of 10-100.

In order, therefore, to avoid using very accurate and complex electronics, which will almost certainly be heavy and susceptible to interference, the MCP detector should produce charge pulses of greater than 2×10^6 electrons, with a very narrow amplitude distribution. The output charge amplitude must also be constant over the active area of the MCP. The larger and better defined that the output charge levels are, the less stringent the operating limits become on the electronics.

The detector should also have a uniform efficiency response over the entire field of view.

2.1.2. MCP manufacture

MCP's can be manufactured in a number of ways [34], the most common being by drawing, etching and reducing a composite glass rod (Fig.2.1). The outer cladding is the lead glass which will eventually form the MCP, with the inner core being soluble glass which is etched out later in processing. The composite glass rod is heated and drawn into fibres ≈0.7 mm in diameter. These fibres are then stacked in a hexagonal mould and heated to fuse them together. The hexagonal block is again drawn to produce a multi-fibre which is 0.85 mm across. The multi-fibres are then stacked in a glass container and fused together to form a boule.

This process has created the basic MCP structure. The boule is now sliced to produce MCP's with the appropriate thickness and channel bias angle. The thickness of a MCP is determined by the channel diameter, D , and required length to diameter ratio, L:D , of the channel. Common

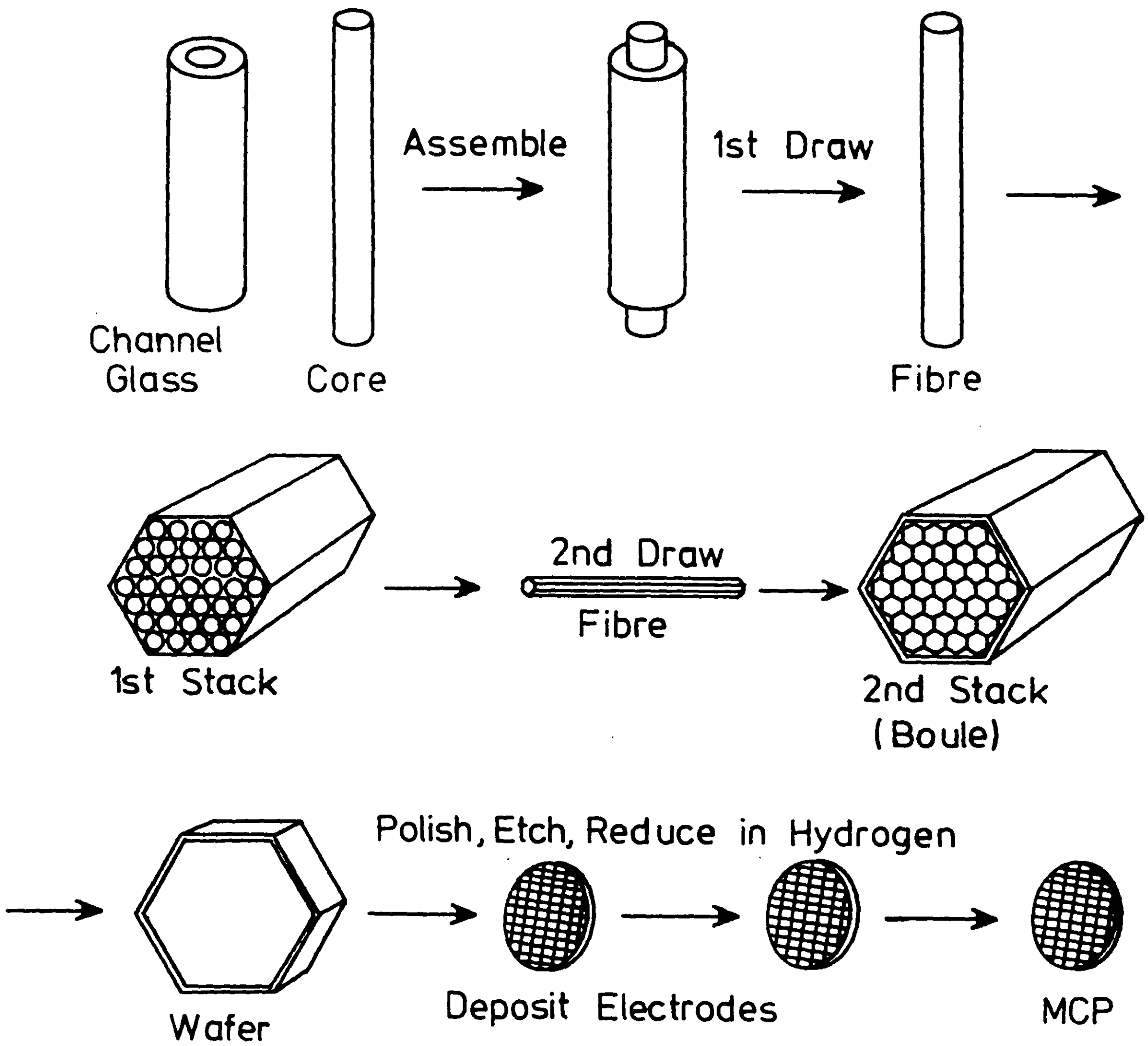

2.1. The manufacture of MCP's (Adapted from ref.[73])

commercial MCP's have D = 12.5 μm, L:D = 40:1 and hence a thickness of 0.5 mm. The bias angle, θ_B, of a MCP is the angle between the channel axis and the normal to the front surface.

The slices are polished and the inner cores etched out. They are then fired in a hydrogen reducing oven to produce channels that have a semi-conducting layer of reduced lead glass underneath a high secondary electron yield silica like surface layer. An electrode, normally a nickel-based alloy such as Inconel or Nichrome, is vacuum evaporated onto both faces of the MCP. This is normally done at an angle, to produce an electrode penetration of one or two channel diameters into the channel. The MCP is then complete.

Typical MCP's are disks of diameter 25-60 mm, containing straight channels of circular cross section. The hexagonal packing structure normally gives an open area ratio of 63% for channels with D = 12.5 μm and channel pitch p = 15 μm. MCP's have also been produced with square cross section microchannels [35]. The simplicity of the manufacturing technique allows MCP's to be made with L:D ratios very different from the standard 40:1. MCP's with L:D ratios up to 175:1 have been produced.

MCP's can be produced for special applications by changing the size and shape of the final boule; sizes up to ~100 x 100 mm are possible with D = 12.5 μm channels. If the manufacturing process is altered more radically plates with 'C' and 'J' channel curvatures can also be produced (Section 2.1.4) [36,37].

2.1.3. MCP gain mechanism

Each microchannel acts as a high gain electron multiplier, when appropriately biased (600-2000 volts depending on L:D ratio). Since electron emission takes place when ions or molecules strike the channel surface with sufficient energy, these devices must be operated under vacuum ($\lesssim 2 \times 10^{-5}$ mb) to avoid continuous excitation.

Consider an incident photon, electron or particle interacting with the channel wall (at the low potential end) to produce an electron (or batch of electrons) (Fig.2.2). This electron will have some velocity perpendicular to the channel wall and so will drift towards the opposite side of the channel. At the same time it will be accelerated downwards by the applied electric field, so that when it hits the channel wall again it will have gained sufficient energy to release several secondary electrons. Each of these secondary electrons in turn will be accelerated and release several new secondary electrons upon collision with the channel wall. In this manner the number of electrons multiplies rapidly.

The multiplication process continues until a pulse of 10^4-10^5 electrons is obtained from the MCP output. The magnitude of this output pulse is controlled by the applied voltage and by positive wall charging at the channel output [38]. At low applied voltages the gain is determined by the level of stimulation at the input, and the output Pulse Height Distribution (PHD) is exponential [10]. Initial attempts to produce peaked PHD's, like those of Channel Electron Multipliers (CEM's) [39], by increasing the applied voltage, were unsuccessful. In all cases the MCP's suffered from ion feedback before useful peaked PHD's could be obtained [40]. Ion feedback is caused by the ionisation of residual gas molecules by the passage of the electron avalanche. Under the influence of the applied electric field these ions can reach the top of the channel and initiate further avalanches. In severe cases this process can be self-sustaining and can cause severe damage in image intensifier tubes. The ions are produced from either the general background atmosphere if the vacuum is poor, or from molecules released from the MCP glass by the electron bombardment. This effect has been used to produce self-triggered ion sources [41].

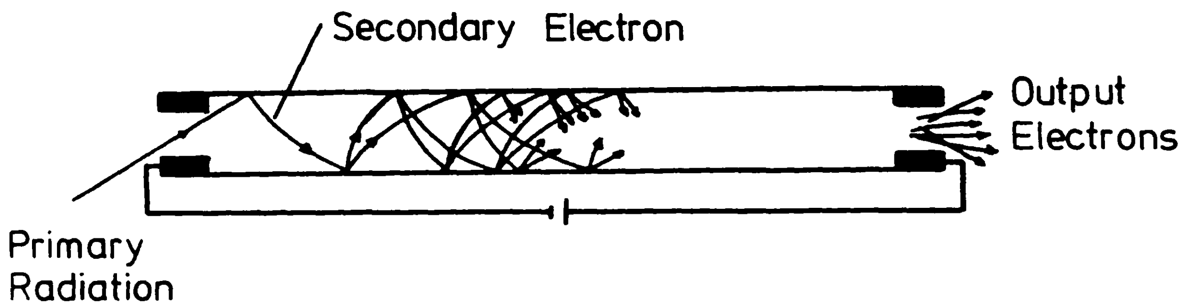

2.2. Electron multiplication in a channel (Adapted from ref.[73])

2.1.4. High gain MCP configurations

The problems encountered in attempting to produce a peaked PHD from MCP's were similar to problems found in the development of CEM's. The adopted solution for CEM's was to use a curved rather than a straight channel [2], so that ions would collide with the channel wall near the output end, thus substantially reducing the magnitude of the spurious pulse. A similar approach has been used with MCP's to produce 'C' and 'J' curved channel MCP's [36,37]. Peak gains, $G_c \sim 10^6$, and Full Width at Half Maximum (FWHM) values, $\Delta G_c/G_c \sim 34\%$ have been achieved with such devices. The production of curved channel MCP's is more difficult than that of normal straight channel devices [42] and such MCP's are only produced by a few manufacturers. The available gain from 'C' and 'J' plates is rather low to satisfy the conditions of Section 2.1.1.

A simpler solution to the problem of ion feedback is to use a "chevron" pair of MCP's [43,44] (Fig.2.3(a,b)). This comprises a pair of MCP's, operated in series, which have opposed bias angles, say 8° and 8° to produce a 16° change in channel direction (Fig.2.3(a)), or as is more commonly used in X-ray astronomy, a 0° bias front plate and a 13° bias rear plate to give a 13° change in channel direction (Fig.2.3(b)). This change in channel direction has the same effect as curving the channels of 'C' and 'J' plates and of CEM's; i.e. forcing the positive ions to collide with the channel wall sufficiently far from the input end to produce a negligible output pulse.

The 0° bias MCP is little used except in X-ray astronomy. In most applications (e.g. image intensifiers) such a bias angle has no value because a parallel, normally incident, beam of radiation or particles would pass straight through the MCP without being detected. With grazing incidence telescopes (Section 1.4) a conical beam of X-rays is produced. Hence X-rays reach the MCP at a non-zero angle to the MCP normal. If an MCP with non-zero bias angle were used as a focal plane detector, its

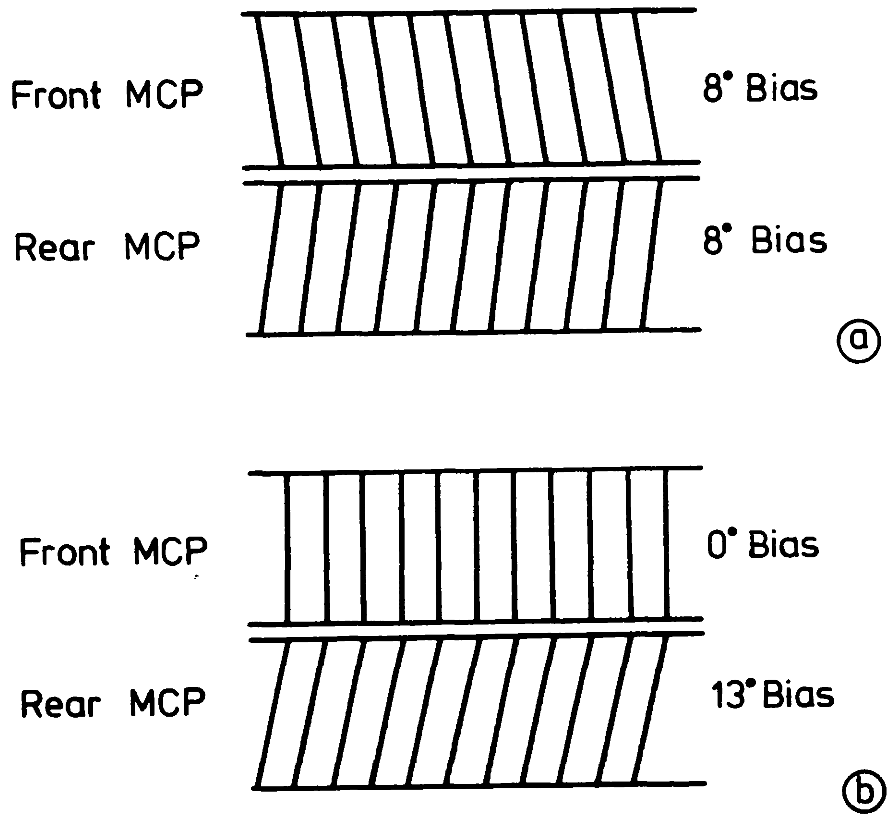

2.3. Schematic representation of two possible MCP chevrons

(a) 8° bias front and rear MCP's giving a total change in channel direction of 16°

(b) 0° bias front MCP and 13° bias rear MCP giving a total change in channel direction of 13°

response to radiation coming from different parts of the mirror would vary because the MCP efficiency response is a function of incidence angle (Section 2.3.3).

Chevron detectors (0°, 13° pair) can easily produce peaked PHD's, with values of $G_c \sim 10^7 - 10^8$ and FWHM's of 50% or less (Fig.2.4) and hence satisfy the conditions of Section 2.1.1. To produce such a PHD a chevron is operated in a saturated mode (large bias voltage), as opposed to the linear mode of operation used in image intensifiers.

It has recently been shown that a single, straight channel MCP (L:D = 160:1) can be operated in a high gain mode ($\lesssim 10^6$) practically free from ion feedback, by applying a pulsed high voltage [45]. The complexity and weight of power supplies able to produce pulsed high voltage means this is unlikely to be a sensible choice for X-ray astronomy missions.

The restricted availability of curved channel MCP's taken together with their rather low gain, and the good record of MCP chevron detectors, prompted us to concentrate on the development of the latter detector type. A drawback of this choice is the observed gain drop with accumulated counts of chevron detectors. This gain drop (reviewed by Fraser [46]) is related to the charge abstracted per unit area of the plate, although the processes involved are not well understood, and the gain drop varies from MCP to MCP. The lower gains of the 'C' and 'J' type MCP's would imply a longer lifetime in terms of accumulated counts. The fall in gain can, however, be reversed to some extent by increasing the voltage across the MCP's [37] and this problem is unlikely to be significant for X-ray astronomy.

2.2. Electronic Readout Techniques

2.2.1. Available techniques

Since all experiments in soft X-ray astronomy must be conducted from either satellites or sounding rockets, some form of electronic image encoding is required. A review of these encoding methods has been presented by

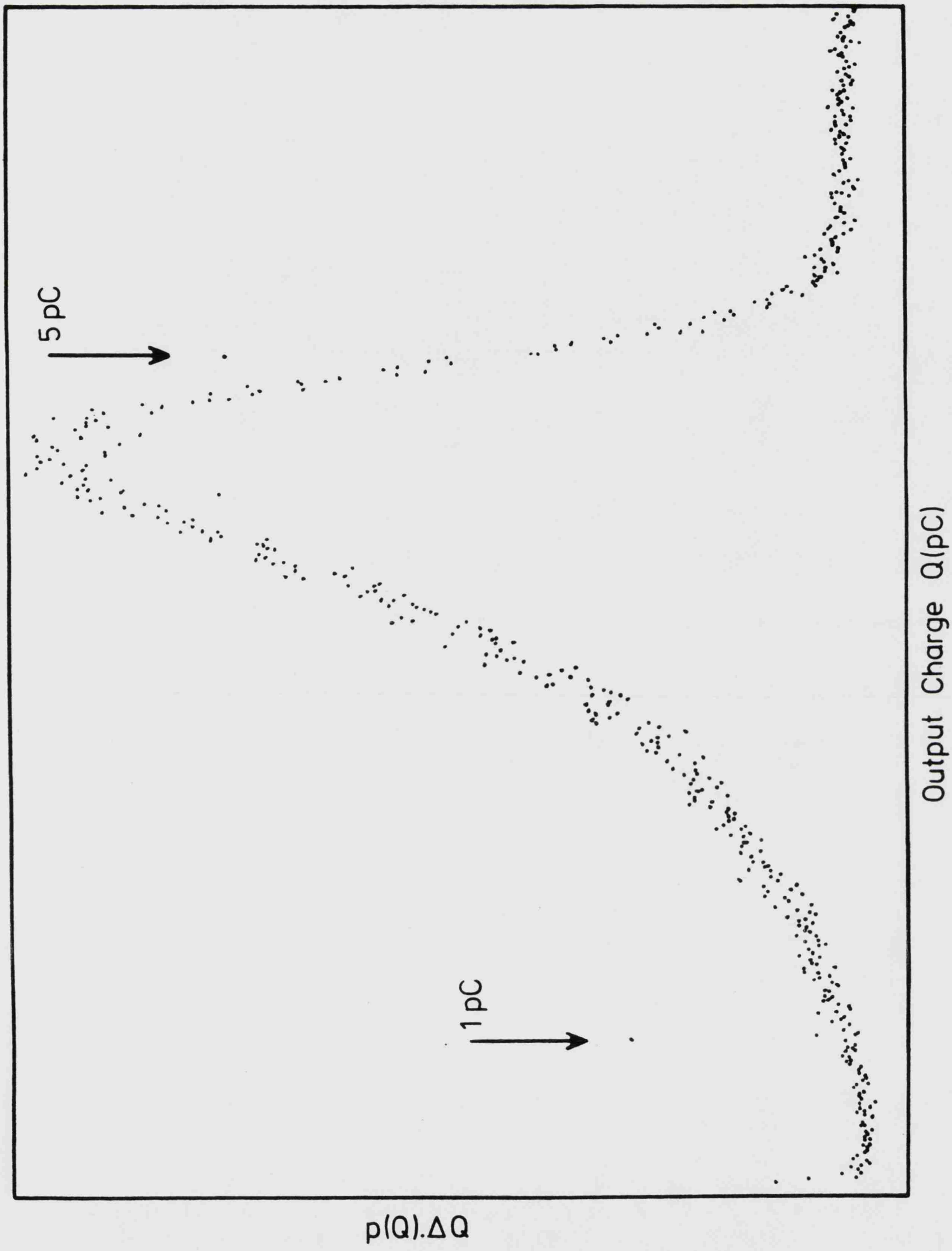

2.4 Typical PHD from a chevron detector. C-K (0.28 keV) X-rays incident at θ = 13.5° to the channel axis. Both MCP's have D=12.5 μm, L:D=120:1, 0° bias front plate, 13° bias rear plate. G_C=4.4 pC. FWHM=37%

Fraser [46] and so only brief details will be presented here.

The position encoders used in X-ray astronomy are normally analogue systems where the centroid position of the MCP output charge cloud is detected by 3 or more charge sensitive preamplifiers followed by appropriate electronics. This can be accomplished by collecting the charge on a uniform resistive anode [47,48,49], a pair of "crossed" wire grids (using various charge division methods) [50,51,52] or by an array of conductors on a solid substrate [53,54,55].

The development of one particular "crossed" wire grid technique is described in the following section.

2.2.2. Graded density electrode development

It was suggested by Mathieson et al [56,57] that a development of the Graded Density (GD) cathode used in imaging proportional counters would be a suitable readout technique for MCP's. In collaboration with Dr. G.C. Smith an experimental investigation of this possibility was carried out [52].

The principles of GD readout are described in detail in ref.[57]; only a brief description will be given here. Each graded density electrode (Fig.2.5) comprises a plane of wires of uniform pitch, connected electrically into two groups, A and B, such that the linear density of group A decreases approximately linearly across the electrode width, while the linear density of group B increases approximately linearly. Then, provided the width of the MCP charge distribution on the electrode is sufficiently large compared with the wire spacing, the charges q_A and q_B on each group will vary approximately linearly with position x, of the charge centroid across the electrode. A suitable position signal may then be obtained as

$$Q_x = \frac{q_B}{q_A+q_B}$$

In the absence of resistive noise the principal noise contribution is from the preamplifiers [57] and with suitable electronics this can be made

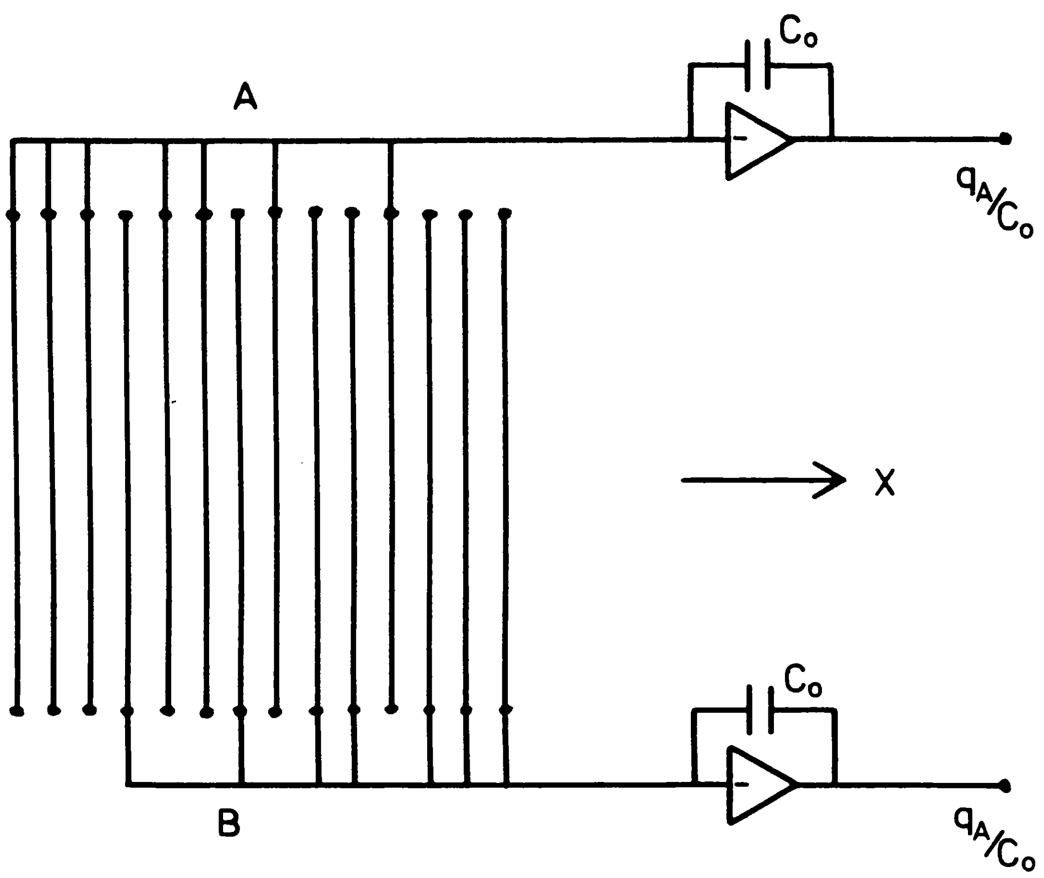

2.5. Schematic representation of a GD electrode. The electrodes were squares of side 40 mm and contained 160 copper wires at 250 μm pitch. Only the central 30 mm of the electrode was used for sensing, the remaining 20 wires on each side were connected to the adjacent group of maximum density to diminish field non-uniformities at the edges of the encoding region.

very small (~ 500 electrons rms). Since with MCP's the GD electrodes are collecting electrons, rather than the induced charge detected by GD cathodes in proportional counters, there will be an additional noise source, partition noise, given by [58]

$$\Delta x = \frac{1}{S}\left(\frac{Q_x(1-Q_x)}{n_o}\right)^{\frac{1}{2}}$$

where S = system sensitivity = $\frac{dQ_x}{dx}$, n_o = number of electrons in a charge pulse. This has a maximum value at the centre, where $Q_x = 0.5$, falling to zero at the edges of the electrode.

The GD electrode technique was tested in the detector shown schematically in Fig.2.6(a). Cu-L (0.93 keV) X-rays were used to stimulate the MCP's, the output PHD being peaked with G_C~2.5 pC for most imaging measurements.

Initial measurements were conducted using an electrode with 15 μm diameter wires on 250 μm pitch, situated in a plane 4 mm behind the rear MCP. A plane conducting plate (reflector plate) was placed a further 3 mm behind the GD electrode. Laboratory standard charge sensitive preamplifiers were connected to the two components, A and B, of the GD electrode. A bias voltage between ±30 volts could be applied, simultaneously, to both components of the GD electrode to ensure the electrodes were maintained at a well defined potential. A mask containing a row of 13 holes, 100 μm in diameter and 2 mm apart, was placed between the detector and the X-ray source, close to the front of the MCP. The line of holes was aligned parallel to the sensing axis defined by the GD electrode. The signals from the preamplifiers were processed by analogue electronics and could be displayed on a storage oscilloscope for visual inspection or examined in detail on a Multi Channel Analyser (MCA).

The important bias voltages are (Fig.2.6(b)): the voltage between the rear MCP and the GD electrode, V_1, and the voltage between the GD electrode and the reflector plate, V_{ref}. The absolute value of the bias voltage

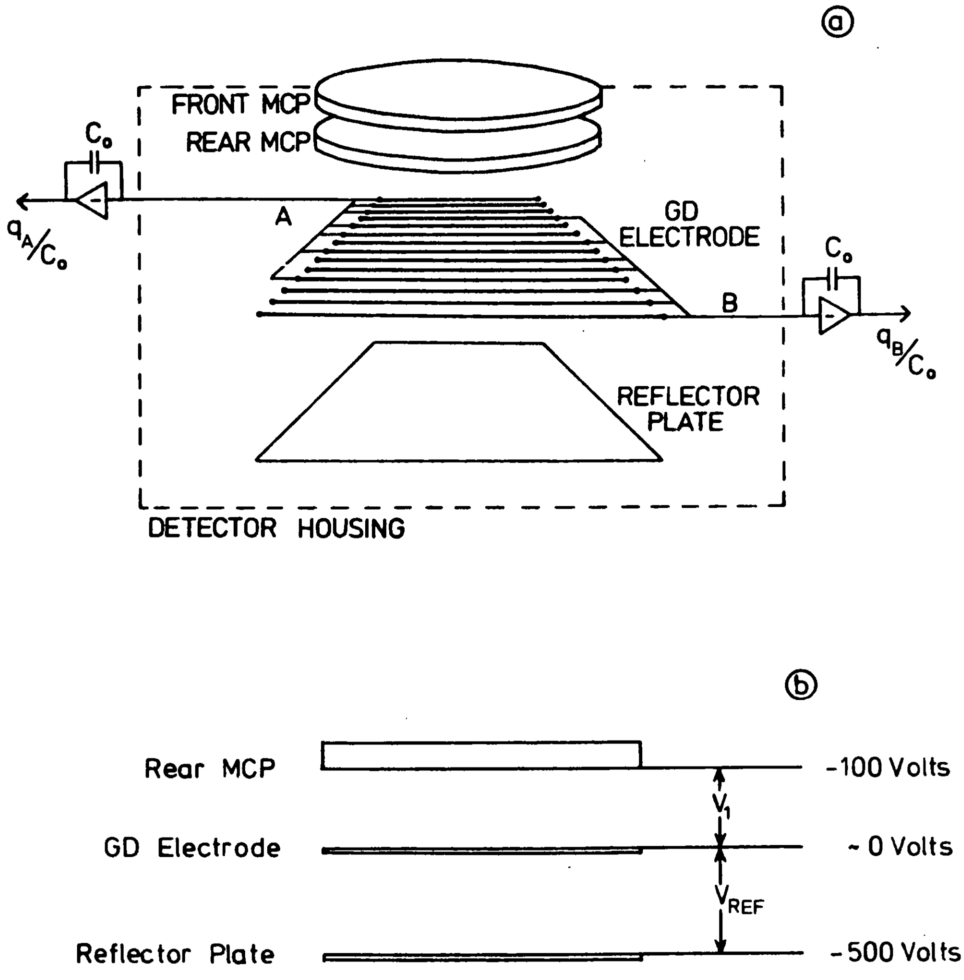

2.6. (a) Schematic representation of the MCP detector and one-dimensional GD electrode encoding system. The MCP's were 36 mm in diameter with 15 μm pitch, D=12.5 μm and L:D=120:1. Chevron arrangement as in Fig.2.3(b). The clear aperture of the detector was 30 mm in diameter.

(b) Biaising details for the one-dimensional GD electrode readout.

applied to the GD electrode had no effect on the resulting images and hence a nominal bias voltage of 1 volt was used. The GD electrode must be biased, otherwise its potential becomes ill defined and charge collection is incomplete.

The voltage V_1 is an important parameter because it determines the size of the output charge cloud at the wire plane. In practice an accelerating potential $\gtrsim 20$ volts is needed otherwise not all of the output charge is collected on the electrode, some being lost to the detector structure. No significant changes were observed in the range $-20 \lesssim V_1 \lesssim -200$ volts and V_1 was therefore set at -100 V for the remainder of the work.

The reflector plate was used to ensure that all of the charge from the MCP avalanche was collected by the GD electrode. The effect of varying V_{ref} is shown in Fig.2.7 (data from VTF detector, see Section 3.2). The most probable explanation for the behaviour is that as V_{ref} was reduced, some of the higher energy electrons reached the reflector plate and caused electron emission. This produced increased negative charge on the GD electrode and positive charge on the reflector plate. At all voltages the total charge detected remains approximately constant. This explanation is not borne out in detail by the rather small published values for the secondary electron emission coefficient (δ) of the reflector plate (Cu and Fe $\delta = 1.3$ maximum) [59]. No other explanation of the effect could be found, however, and the data of ref. [59], which is rather old, may perhaps be in error. $V_{ref} = -500$ volts was adopted for all further work.

It was noted during the above investigation that the GD electrodes were able to image on the induced charge distribution when all the electrons were being collected on the reflector plate ($V_{ref} = 0$ volts). This did not appear to present any significant improvement over direct collection of charge (except in terms of image scale, see later) and the idea was not pursued.

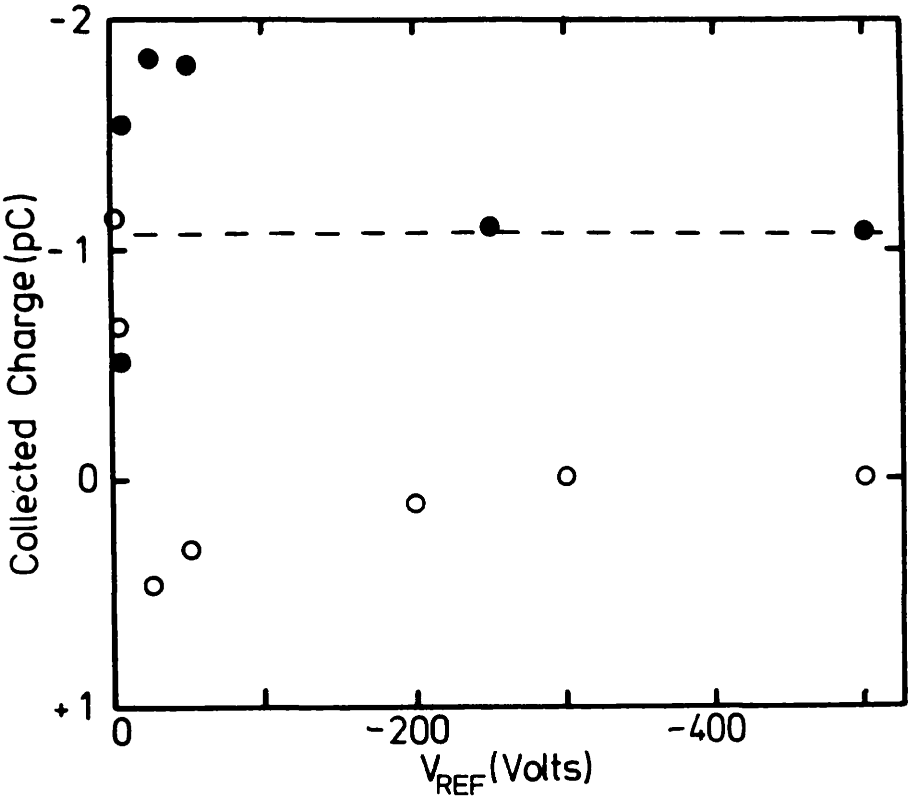

2.7. Total charge collected on the reflector plate (open circles) and the GD electrodes (filled circles) as a function of the reflector plate voltage, V_{ref}. The sum of the positive and negative charges is approximately constant (broken horizontal line).

With $V_1 = -100\,V$ and $V_{ref} = -500\,V$ images could be easily obtained. Non-linearities were visible in the centre of the field of view and considerable distortions were present towards the edges. Three field defining electrodes were added to ensure a uniform electric field existed between the rear MCP and the GD electrode. This improved the linearity but curious changes were observed in the image scale. This had always been slightly smaller than expected but could now be made even smaller by appropriate biasing of the field defining electrodes.

To aid investigation of this effect a second, identical, GD electrode was installed to produce a two-dimensional imaging detector. The second GD electrode was placed in a plane 0.5 mm behind the original, with its wires orthogonal to those of the first electrode. In order to obtain equal charge division between the two GD electrodes the rear one was biased at -0.1 V with respect to the front one. Similar analogue electronics were used to process the signal from the second electrode and the resulting two-dimensional image was again displayed on a storage oscilloscope. The mask used in this case had a square pattern of 100 μm diameter holes, spaced 2 mm apart in both axes.

The observed effect was that as the bias voltages on the field defining electrodes were changed, both the image scale and distortion changed. If the field defining electrodes were biased to produce an approximately uniform field then the resulting image did not have any large scale distortion, but it was only ~84% of its expected size (Fig.2.8(a)). If the field was non-uniform, with a high field region next the MCP and a low field region next the GD electrodes, the image possessed pronounced pin cushion distortion with an image ~95% of expected size (Fig.2.8(b)). If the field was non uniform, with a low field region next the MCP and a high field region next the GD electrodes, the image had barrel distortion and was only ~62% of expected size (Fig.2.8(c)).

a

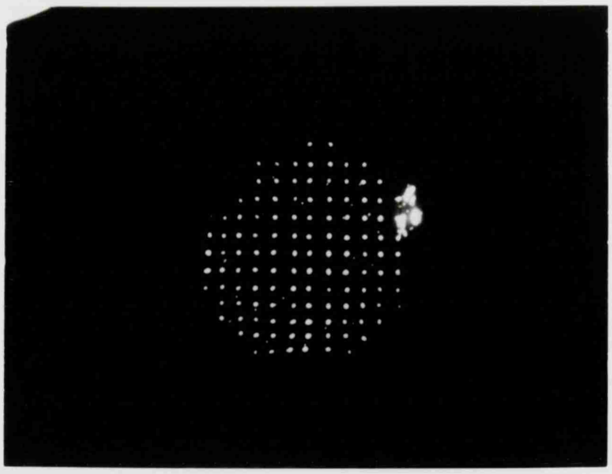

b

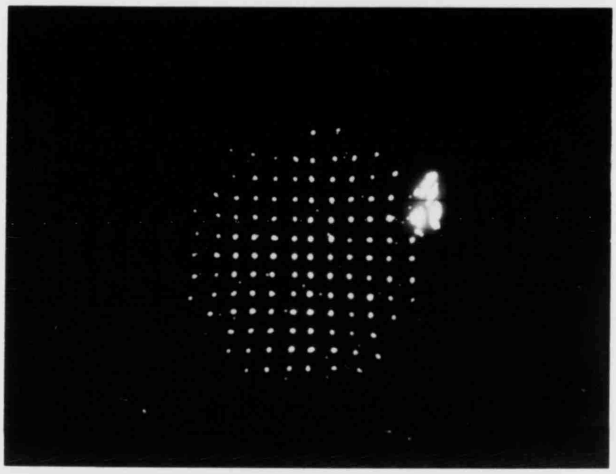

c

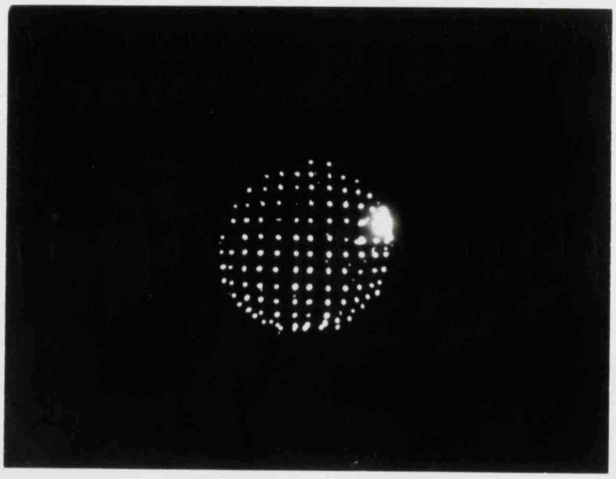

2.8. Effect of altering the bias voltages on the field defining electrodes between the rear MCP and the GD electrode. 100 μm holes on a 2 mm square array Cu-L (0.93 keV) X-rays. The noise spot was caused by a fibre on the front MCP.

(a) Uniform electric field. Image 84% of expected size.

(b) High electric field next MCP, low electric field next GD electrode. Image 95% of expected size.

(c) Low electric field next MCP, high electric field next GD electrode. Image 62% of expected size.

It was observed that increasing the field between the GD electrodes and the reflector plate increased the image scale. It had also been observed that when imaging on induced charge the image scale was of order 95% of expected. This means that the electric field between the GD electrode and the reflector plate can somehow effect the size of the electron image reaching the GD electrode. No satisfactory physical explanation could be produced for why this should happen, as computer simulations [58] indicated that field leakage through the GD electrode should be minimal.

In spite of the results of the computer simulations the most likely reason for this effect is indeed the high geometrical transparency (94%) of the GD electrodes. To test this experimentally a second pair of GD electrodes were produced, with wires of 125 μm diameter on 250 μm pitch. Since these electrodes are only 50% transparent any field leakage should be very much reduced. This was indeed the case and image scales of 95-98% were achieved without significant overall distortion.

The integral non-linearity was measured in one dimension using one of the 125 μm electrodes, and the results are shown in Fig.2.9. The result of 0.8% rms non-linearity is very encouraging as the size of the charge cloud, when it reaches the GD electrode, is rather smaller than originally thought. Using the simple formula of Wiza et al [49], which assumes that electrons emerge from the rear MCP at angles up to 45° from the normal, the diameter of the charge cloud at the GD electrode was calculated to be approx. 4 mm [52]. The experimental results of Bronshteyn et al [60], however, indicate a much narrower angular distribution and hence a charge cloud diameter of 1.0-1.5 mm would be more appropriate.

In this situation the basic requirement for using the GD electrode; that the charge cloud size be large compared with the wire pitch, is only barely fulfilled. It is reasonable to expect, therefore, that an increase in the MCP to GD electrode gap, producing a larger charge cloud, would result in improved linearity. This would of course require good electric

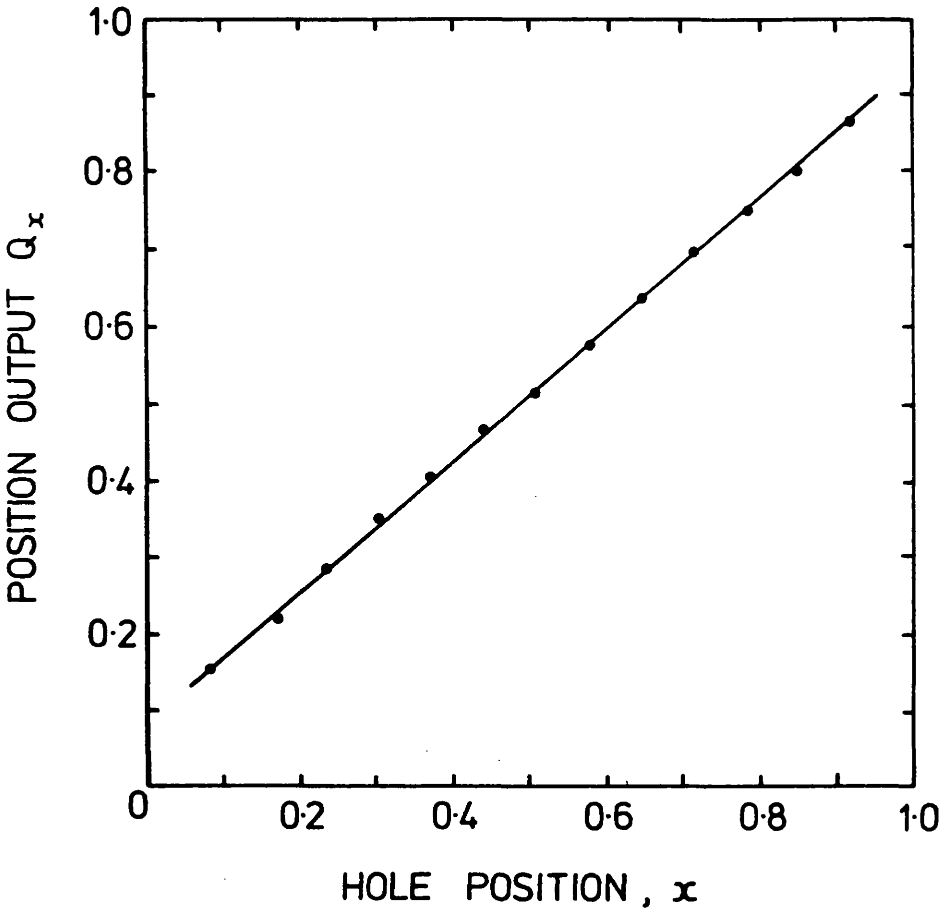

2.9. Position signal, Q_x , plotted as a function of normalised hole position (i.e. X-ray beam position), x . The rms non-linearity is approximately 0.8%.

field definition if gross image distortion were to be avoided.

These problems were also encountered in the development of the wedge and strip anode [54] which uses a similar charge division technique. A MCP electrode separation of 12.5 mm had to be used to improve linearity and field defining electrodes were required to eliminate the effect of stray electric fields.

The gradient of the line in Fig.2.9 (positional sensitivity of detection system) was 0.86. This compares very well with the predicted value [57] of 0.85, calculated from the measured dynamic input capacitance of the preamplifiers (1100 pF) and the intercomponent capacitance of the GD electrode (98 pF). This general agreement between theory and experiment indicates that these GD electrodes do not suffer from the electron focusing effects of the original 15 μm electrodes.

Fig.2.10 shows the result of imaging the test mask in two dimensions. The sensitivity is the same in both axes and is very similar to that measured in the one-dimensional case. Local non-linearities are present in both axes but there is no systematic large scale distortion present. As for the one-dimensional case the image would probably be improved by using a larger MCP-GD electrode gap, together with better electric field definition.

These results confirm that GD electrodes may be employed for one- and two-dimensional position encoding with MCP's. No attempts were made to measure the spatial resolution of the GD electrodes because this would have been completely dominated by electronic noise from the electronics then in use. This particular type of GD electrode would also be expected to suffer from substantial differential non-linearity [61], although this was not measured. Subsequent work on IPC's has shown that GD cathode performance can be substantially enhanced over that of the simple design used here [62].

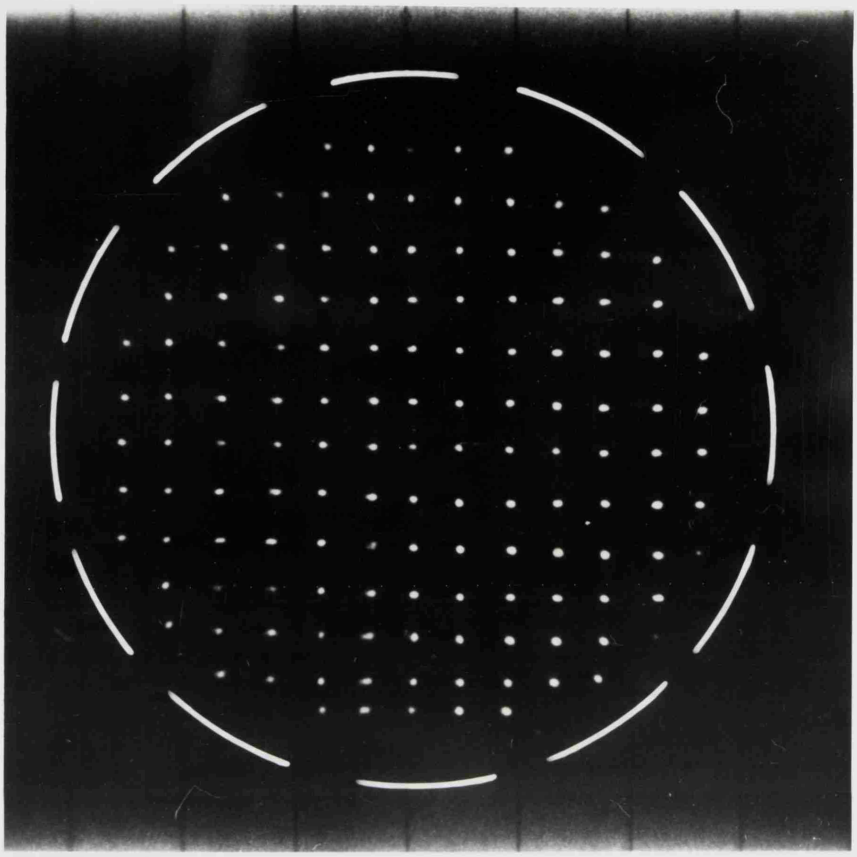

2.10. Two-dimensional image of an array of 100 μm diameter holes with 2 mm pitch in each axis. The dashed circle defines the 30 mm usable diameter of the MCP's.

2.3. Detector Operation

2.3.1. Experimental considerations

Voltages can be applied to a chevron in two ways; with the detector input held at ground or at high negative potential. For satellite experiments the input MCP is usually at a high negative potential (and the readout earthed) to provide protection against low energy electrons. The MCP detectors on the EXOSAT low energy experiment were operated with a grounded input [63] and problems were experienced with electron background. The configuration adopted here is that of a high potential input and a grounded readout, which also simplifies the mechanical and electrical connections to the readout. This electric field arrangement will of course attract positive ions, and does not exclude high energy electrons, therefore an earthed polypropylene window is placed in front of the detector to act as a shield (Section 3.2).

The performance of a chevron detector is determined by the voltage applied to the MCP's, and by the voltage across the interplate gap (V_G). Increasing the voltage across the MCP's increases the gain. Eventually a transition occurs from "linear" to "saturated" operation as the PHD changes from exponential to peaked with a large FWHM. Further increases in voltage increase the gain and reduce the FWHM of the PHD, the precise shape of which is determined by the front plate voltage, V_F , and rear plate voltage, V_R. A large rear plate voltage will produce a sharp falling edge while a large front plate voltage produces a sharp rising edge. Very high voltages can produce very narrow PHD's, FWHM $\lesssim$ 30%, but in these cases the peak lies on top of a base level that contains a significant number of counts. In this situation the FWHM figure does not give an accurage representation of the PHD. Voltages are chosen to produce a "good" PHD, which for most cases means a FWHM of ~50% (Chapter 7).

As can be seen from Fig.2.4 the output PHD may not be Gaussian, and is in general decidedly asymmetrical. A true Gaussian distribution should contain 76% of its count with the FWHM. The fraction of counts within the FWHM of an MCP PHD varies between 95% and 52%. Significant deviations from Gaussian behaviour normally occur at very low or very high gains. Consideration of the fraction of counts contained within intervals, $\pm\delta G_c$, about the peak, G_c ($\delta G_c = 0.25\ G_c$, $0.375\ G_c$, $0.50\ G_c$) , show that these behave in the same general way as the FWHM (see Figs.4.1(b),4.2). Within limitations the FWHM is therefore a useful indicator of the performance of a chevron detector.

The limiting voltage which can be applied to a MCP is often determined by the detector dark noise. MCP's normally have a dark count rate of ~1 count $cm^{-2}s^{-1}$ when operated in a saturated mode. Some of this noise may be caused by cosmic radiation or natural radioactivity in the MCP glass, but most counts are probably caused by defects in the MCP structure [3,64]. In normal operation this is not important but occasionally some MCP's will degrade and noisy areas or "switched on channels" may appear. In some cases a trade off may have to be made between dark noise and FWHM. It has been observed that some chevron detectors will produce less noise if bias voltages are increased smoothly and slowly. For the VTF detectors (Section 3.2) the voltages were normally applied over a 10-15 minute period.

Typical voltages applied across each MCP range from 1400-2000 volts depending on MCP type. The current through each MCP is continuously monitored while in operation, and we deduce typical resistances of 450-650 M Ohms for MCP's with L:D = 120:1.

The output PHD of a MCP will also be affected by very high count rates [1,45,65]. A steady decrease in gain and increase in FWHM is observed with increasing count rate (Section 7.2.5). This is not an important effect in X-ray astronomy because of low source count rates, but it is relevant in the laboratory where much higher count rates can be used.

2.3.2. Variation of pulse height distribution with angle of X-ray incidence

The gain and PHD FWHM of an MCP is a function of θ, the X-ray angle of indidence with respect to the channel axis. This is shown in Fig.2.11 where 3 PHD's (C-K X-rays (0.28 keV)), taken at different angles are compared. The basic cause of this decrease in gain and increase in FWHM at low angles is the interaction of X-rays a long way down the channel. These events are subject to much less multiplication and so have a smaller gain.

Two factors are important: (1) Geometrical transparency of the MCP, (2) Reflection of X-rays. At very small angles ($\theta \lesssim 0.5°$ for L:D = 120:1) X-rays can pass straight through the MCP. At such angles, interaction with the channel wall will occur at all possible positions along the channel length thus producing a large variation in gain. Compounding this effect the probability of X-ray reflection from the channel surface increases dramatically below a certain critical angle, θ_c, (Table 2.1). This again has the effect of making the X-rays interact a long way down the channel. These two processes are also responsible for the small angle efficiency response of MCP's (Section 2.3.3).

Reflection can still play an important part for angles of incidence $\theta > \theta_c$ because of the geometry of X-ray interaction (Fig.2.12(a,b,c)). The cylindrical nature of the channel ensures that for X-rays interacting at polar angle ψ, the grazing angle to the channel surface, α, lies between 0 and θ. This means that regardless of the angle of incidence some fraction of the X-rays will have $\alpha \lesssim \theta_c$. α, θ and ψ are related by [66]

$$\sin\alpha = \cos\psi \sin\theta .$$

The overall effect is that variations in gain and FWHM occur out to approximately twice the critical angle (Fig.2.13).

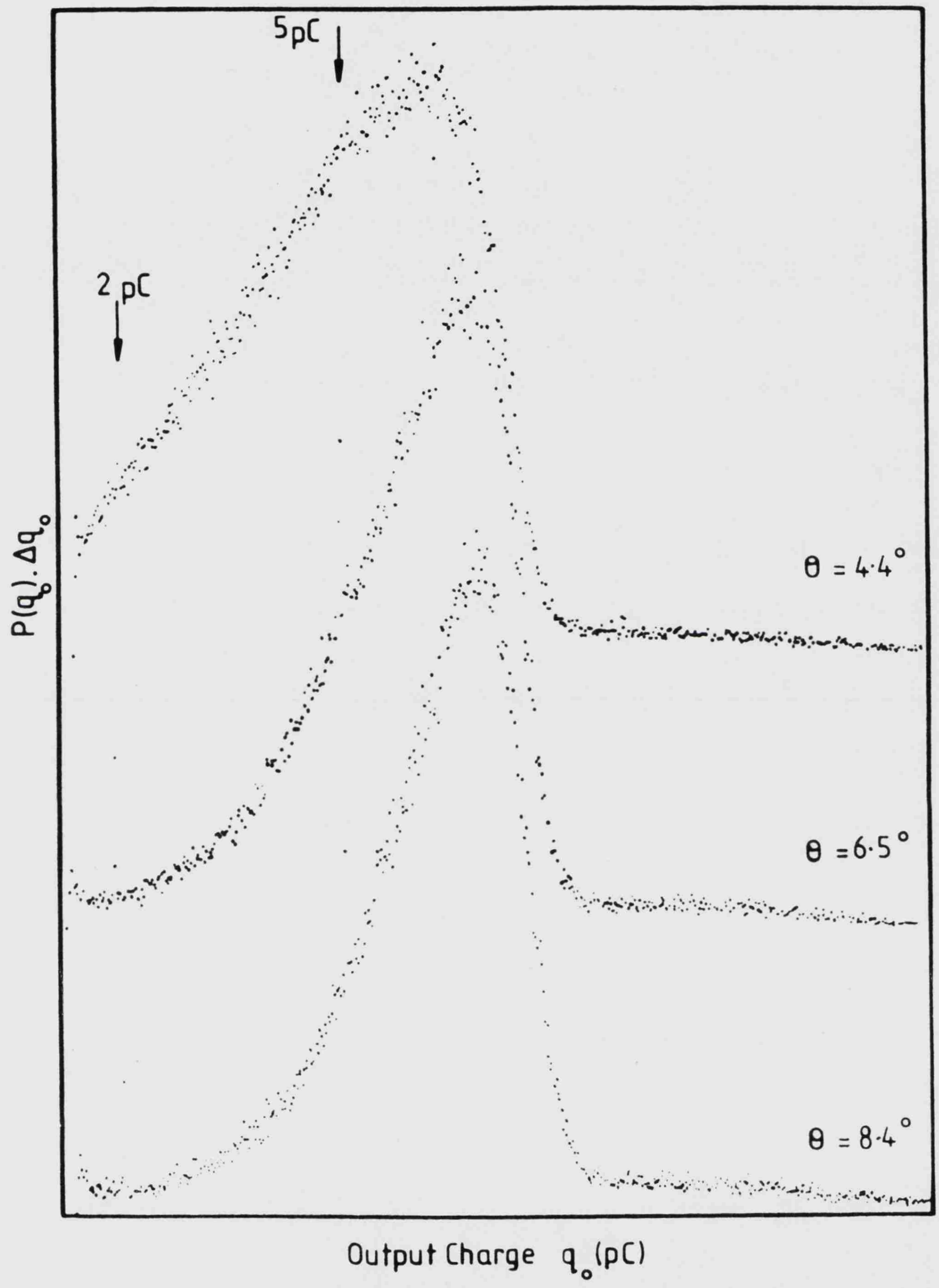

2.11. Variation of chevron MCP output PHD with C-K (0.28 keV) X-ray angle of incidence, θ. When θ is less than θ_c (6.6° for C-K X-rays incident on MCP glass [66]) X-ray reflection broadens the PHD towards low charges. Front MCP; D=12.5 μm, L:D=120:1

Table 2.1

Critical angle of reflection from MCP glass and CsI for various X-ray energies [66,72]

X-ray energy		Critical angle θ_c (degrees)	
line	keV	Bare MCP	CsI
B-K	0.18	9.68	8.50
C-K	0.28	6.96	5.22
Cu-L	0.93	2.20	1.88
Mg-K	1.25	1.64	1.60
Al-K	1.49	1.39	1.40
Si-K	1.74	1.10	1.22
Nb-L	2.28	0.91	0.95
Ru-L	2.68	0.79	0.80

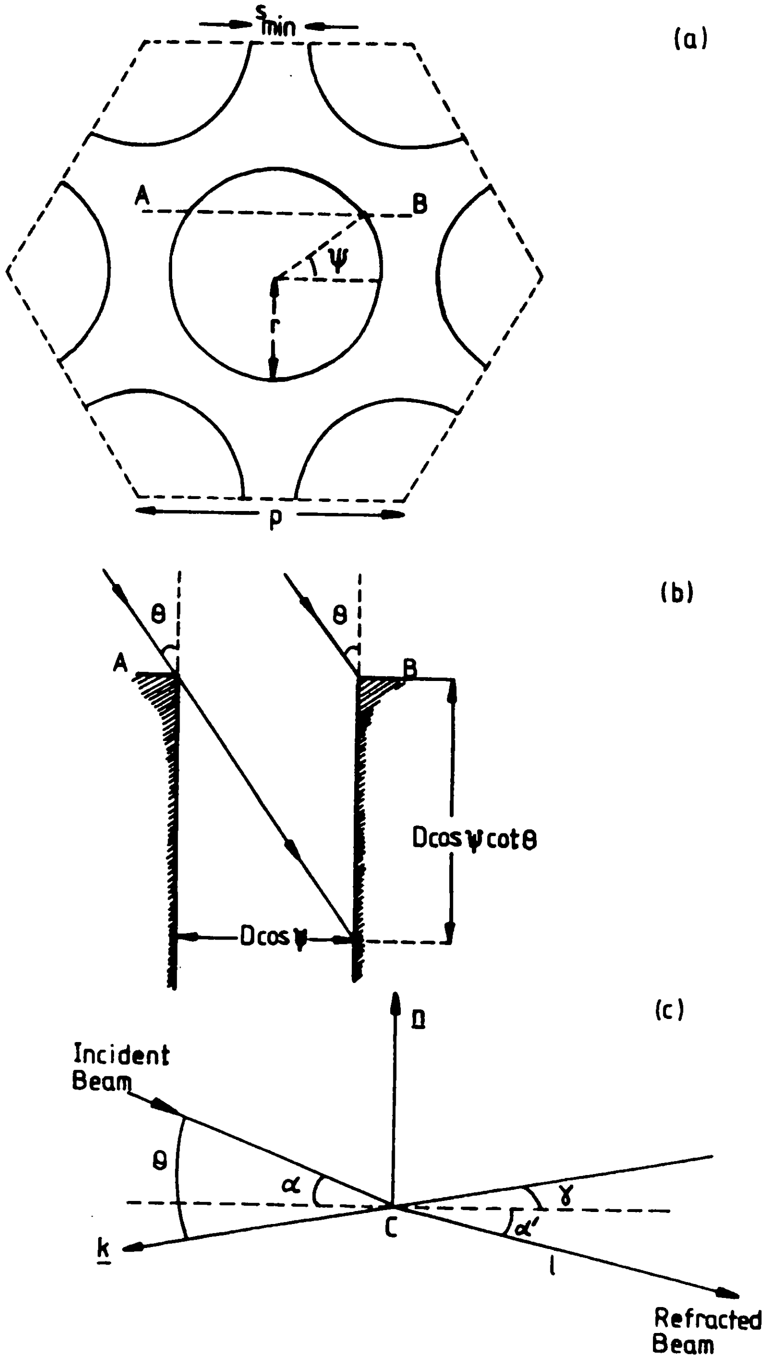

2.12. (a) Plan view of a cell of a hexagonally-packed MCP. Channel radius r, channel pitch p .

(b) Vertical section through central channel along the line AB , at polar angle ψ. X-rays incident at θ degrees to the plate normal illuminate the channel to a depth $D \cos\psi \cot\theta$, where D is the channel diameter. This figure illustrates an MCP with bias angle $\theta_B = 0$.

(c) Geometry of the X-ray interaction with the channel wall. $\underline{K}$ is the vector in the direction of the MCP surface and $\underline{n}$ is the normal to the channel wall at the point of incidence, C . θ is the incident angle of Fig.2.12(b), α is the grazing angle and α' the refraction angle. ℓ is the distance along the refracted path. The reflected beam is omitted for clarity. (Adapted from ref.[66])

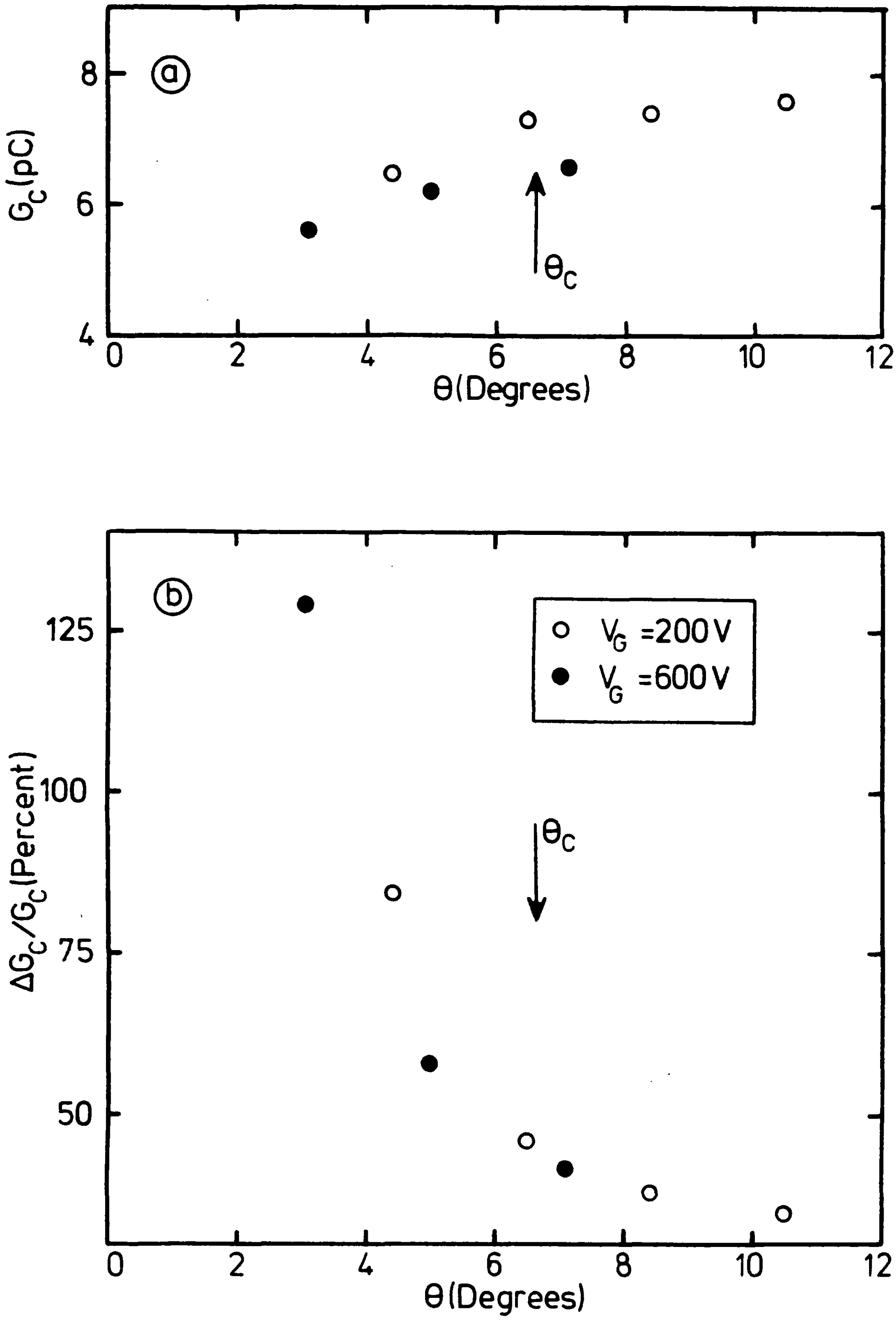

2.13. (a) Variation of peak gain, G_c , with C-K (0.28 keV) X-ray angle of incidence, for two different interplate gap voltages V_G (see Section 4.1). V_G=200 V (open circles) and V_G=600 V (filled circles). Critical angle of reflection, θ_c , marked by vertical arrow. MCP's D=12.5 μm, L:D=120:1.

(b) Variation of FWHM, $\Delta G_c/G_c$, with C-K (0.28 keV) X-ray angle of incidence. Other details as for Fig.2.13 (a).

2.3.3. Soft X-ray detection efficiency

In the soft X-ray region ($\lesssim$ 8 keV) all interactions with the MCP occur in the 100 Å thick activated layer on the channel wall [66]. This is a silica like layer, depleted of Pb and enriched with K during the final stages of MCP processing [67,68]. The basic absorption geometry is shown in Fig.2.12(c). It can be seen that as α decreases large absorption lengths are possible with the point of interaction lying only a short perpendicular distance, d , from the surface. As θ , and hence d , decreases the probability of a photo - or Auger electron getting into the channel increases, thus raising the detection efficiency, Q (Fig.2.14). The efficiency decreases at low angles because of the reflection and transmission effects discussed in the previous section. A comprehensive discussion of these processes is given by G.W. Fraser [66].

It is interesting to note that some MCP's show a more pronounced dip in efficiency at $\theta = 0°$ than others, when tested under identical conditions. This can be attributed to nominally 0° bias MCP's having small bias angles, even 0.5° having a significant effect. Slight misalignments are therefore produced between the X-ray beam and the channel axis when nominally $\theta = 0°$. Variations in the surface roughness of the channel walls may also have an effect.

The most important aspect of the "bare" MCP efficiency response is that, except for a relatively small range of angles about the peak, the efficiency is very low. This effect is accentuated at higher energies with the Si-K X-ray peak response having an angular FWHM of only ~2°. The standard method of improving this efficiency response is to coat the MCP with a photocathode material (Section 4.3).

Exposure to organic contamination, especially diffusion or rotary pump oil, can significantly reduce the detection efficiency of the MCP and change the peak gain and FWHM of the PHD [69,70]. This can be seen by

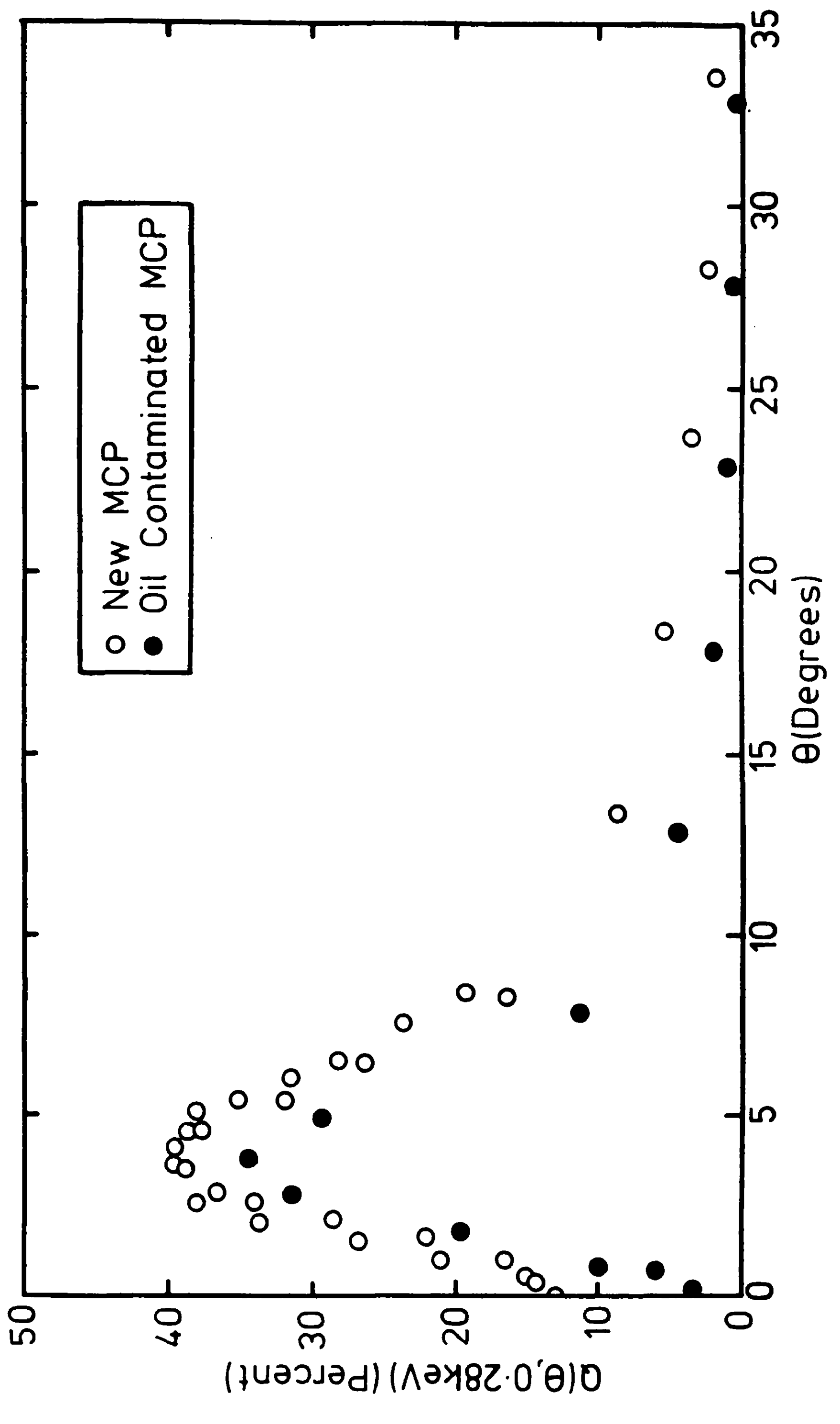

2.14. Variation of efficiency, Q , with C-K (0.28 keV) X-ray angle of incidence for two MCP chevron detectors. MCP's in good condition (open circles) and oil contaminated MCP's (filled circles). D=12.5 μm, L:D=120:1.

comparing the two data sets of Fig.2.14, which show a pronounced decrease in efficiency on the oil contaminated plate. This contamination was caused by an accident with a diffusion pump; gross oil backstreaming occurred when an operating diffusion pump was vented to atmospheric pressure. It was accidents like this which constrained the design of the VTF pumping system (Section 3.3).

Several pairs of MCP's had been contaminated in this manner at Leicester and attempts were made to remove the oil contamination and restore the efficiency. One such attempt involved ultrasonically cleaning the MCP's (36 mm diameter, D = 12.5 μm, L:D = 120:1) in propan-2-ol (IPA) followed by a wash in water at just less than 100°C. The MCP's were then air baked at 70°C for 1 hour. It is uncertain if this procedure actually removed any of the contamination, it certainly did not achieve any increase in efficiency and the PHD was largely unchanged. It is possible however that the washing procedure actually removed the contamination and reduced the efficiency is some other manner.

An attempt to recondition another pair of oil contaminated MCP's (53 mm diameter, D = 25 μm, L:D = 120:1) was made by the manufacturer [71]. This involved removing the nichrome electrodes, cleaning in water and IPA, and baking overnight at 70°C. The MCP's were then air baked at 420°C for 35 minutes (plus warm up and cool down time) and then reduced in a hydrogen furnace at 420°C for 2 hours. Nichrome electrodes were then reapplied. This process is the same as that which produces the semiconducting channel layer on new MCP's and hence might be expected to restore the detection efficiency to its original value.

The result of this processing was to double the resistance of the MCP's, reduce their gain and make them very noisy. There was no significant change in the quantum detection efficiency. The conclusion to be drawn from this work is that once a MCP becomes contaminated with vacuum pump oil its efficiency will be permanently degraded.

2.3.4. General handling and cleanliness

Mechanical damage is one of the causes of MCP noise. A simple crack or surface chip will normally give rise to a very high count rate and an exponential PHD. There is little that can be done with such MCP's. If the noise spot is near to an edge it may be possible to mask off the affected area and continue using the rest of the MCP since the performance on the undamaged surface is not usually affected.

There have been occasions when MCP's have picked up small chips, burn marks and various other disfigurements and still operated very satisfactorily. In general however despite being sturdy devices, MCP's should not be subjected to gross mechanical stress.

The actual handling of MCP's should always be done with gloved hands to avoid organic contamination. Tweezers can also be used and are very effective in positioning and removing MCP's in restricted spaces. The MCP is either picked up edge on, with the front and rear faces gripped by the tweezers, or the tweezers are opened out and the MCP picked up by the edges. Care must be taken in both cases to prevent damage to the edges of the MCP which can result in noise.

MCP's should always be stored in dry conditions, as it is known that they degrade in a damp atmosphere. All MCP's used at Leicester are stored under dry nitrogen in a desiccator and only removed for assembly into a detector. Assembly of a detector should always be done in a clean area, since fibres and dust particles that settle on the front MCP surface can be a major source of noise. Fibres and particles show up as isolated hot spots and the resultant noise can increase until normal operation is impossible. Additional precautions are necessary for some forms of photocathodes (Section 4.4).

CHAPTER 3

DESIGN AND CONSTRUCTION OF A MCP TEST FACILITY

3.1 MCP Test Facility Definition

In order to support investigations into the improvement of chevron MCP X-ray detectors (Section 1.5) it was necessary to design and build a new laboratory test system. To produce a flexible piece of equipment, all possible future uses of the test system were considered. The major concerns were the improvement of MCP quantum detection efficiency and the study of MCP output PHD's. Also of interest was the study of how such an improved chevron's characteristics change with age. Possible future work would involve the development of two-dimensional imaging systems.

The test system was to be constructed so that modification of its basic configuration could be made simply and easily if the experimental emphasis changed. Economic considerations dictated that the basic detector be constructed using standard, 36 mm diameter, circular MCP's. The overall design, however, took into account the possibility of very large MCP's being tested for future X-ray astronomy missions, (Section 1.4).

It was considered impractical to produce one detector body that could be easily adopted for use with other, unspecified, sizes of MCP's and types of image readout. The solution adopted was to use a simple mounting system and build separate detector bodies for each MCP-readout combination. The present detector uses 36 mm diameter MCP's and two-dimensional graded density electrode readout (15 μm diameter wire type, see Section 2.2.2).

All work on MCP photocathodes was to be carried out with photocathodes deposited on one half of the MCP only (Fig.3.1), to provide an uncoated reference surface. Many of the photocathodes of interest (Section 4.4) are deliquescent or hygroscopic and therefore should be disturbed as little as possible during detector operation. Certain life test

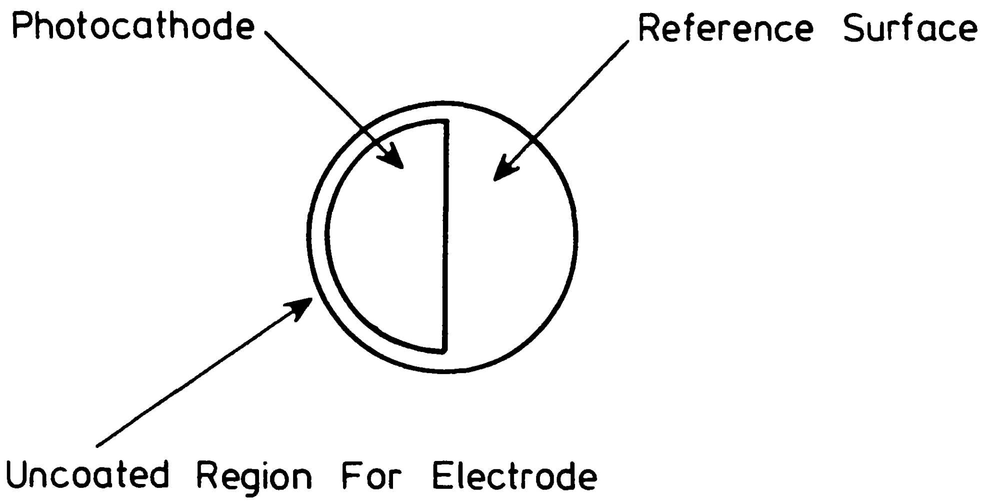

3.1 Coating pattern for test MCP's.

configurations, with the detector operated continuously, also demand that the system should be able to run undisturbed for extended periods.

The above scientific objectives, operational requirements and general MCP characteristics (Chapter 2) define the basic properties of a MCP test facility:-

(A) A clean chamber capable of holding the MCP detector at high vacuum ($\leq 5 \times 10^{-6}$ mb) for prolonged periods.

(B) An X-ray source of appropriate energy range and collimation.

(C) A reference detector to allow the calculation of MCP efficiencies.

(D) The ability to rotate and translate the MCP detector relative to the incident X-ray beam.

(E) An electronic processing system which allows accurate pulse counting, pulse height analysis and basic X-ray imaging.

(F) Adaptability.

These requirements and their implementation in terms of the MCP Vacuum Test Facility (VTF) will be described in detail in the following sections.

3.2. MCP Detector Construction

The 36 mm diameter MCP's for this detector have 12.5 μm channels on 15 μm pitch. Their thickness depends on the channel length-to-diameter (L:D) ratio. Normally we choose L:D = 120:1 which implies a thickness of 1.5 mm, but the detector was constructed to allow easy use of 0.5 mm (40:1 MCP) to 2.5 mm (plano - concave MCP (Section 4.2)) thick plates.

The detector was designed to allow the insertion of various imaging masks, windows and field defining electrodes in front of the MCP's. This involved restricting the maximum usable X-ray angle of incidence, θ , to approximately 40°. This is not a serious restriction since even a CsI-coated MCP (Section 5.4) has its peak response at angles $\lesssim 10°$. No present or foreseeable mission in X-ray astronomy would demand angles of incidence as large as 40°.

A sectional view of the detector is shown in Fig.3.2. The axis of rotation lies in the plane of the front surface of the front MCP. All components were shaped to provide adequate outgassing paths from the MCP to the vacuum system.

The detector assembles in two parts, with the MCP assembly being inserted from the top and the GD electrodes from the bottom. Sufficient space was left for future developments of the GD electrodes, e.g. increased electron drift space (Section 2.2.2).

Since the detector must be assembled in a clean, dry environment all electrical connections are mechanical rather than soldered. The MCP assembly is held together by four screws through the detector top plate.

Electrical contact is made to the MCP's using three gold plated copper electrodes (Fig.3.3). The front and middle electrodes are castellated and are assembled out of phase so that each channel in the front MCP is open to vacuum at one end. In accordance with industrial practice [42] and previous experience at Leicester [17], the internal diameter of the rear electrode is smaller than that for the front and middle electrodes. This is done to prevent the readout element picking up noise which can be generated along the edges of the first two electrodes. The internal diameter of the rear electrode determines the usable diameter of the detector.

Various types of middle electrode are available, all using the same pattern but differing in thickness. The most commonly used electrode is double sided, consisting of two layers of copper separated by a layer of kapton, all three layers being ~50 μm thick. Such electrodes allow a potential difference to be established between the MCP's (Section 4.1).

A grid was made from 95% transparent tungsten mesh for use between the macor spacer and the leaf spring. This allows control of the electric field strength and direction in the region immediately in front of the MCP (Chapter 6).

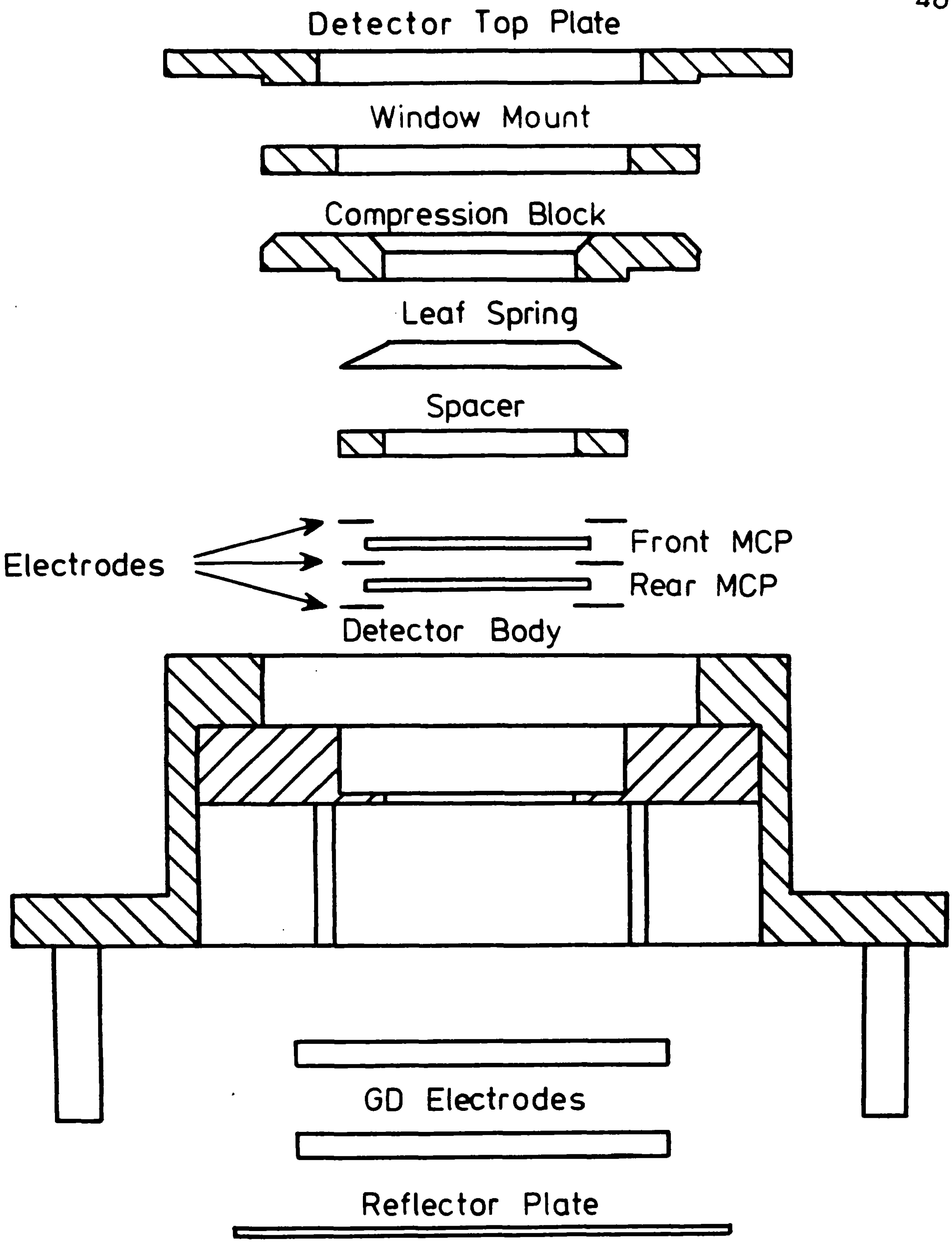

3.2. Sectional, exploded view of the VTF MCP detector. Compression block, spacer and internal detector body are Macor [115]. Leaf spring is Cu-Be. GD electrode frame - G10 fibreglass. All other components are stainless steel.

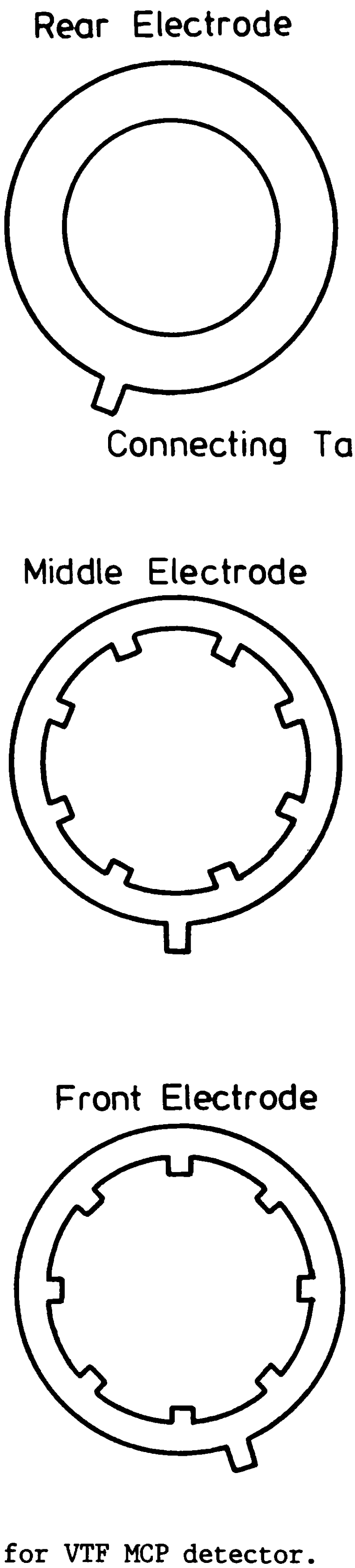

3.3. Electrode patterns for VTF MCP detector. Correct orientation is achieved by use of locating channels for the connecting tabs.

It was originally intended to operate the detector without any form of window between the MCP's and the vacuum system. This did not prove to be possible, however, because the detector was sensitive to positive ions (or possible high energy electrons) present in the system. This sensitivity was sufficient to increase unpredictably the detector dark noise and make this mode of operation unsatisfactory. A thin carbon coated polypropylene window was therefore fixed to the spacer and window mount. Great care must be taken to produce a window of uniform thickness in order to avoid errors due to variations in X-ray transmission across the window.

3.3. VTF Pumping System

There are a number of different pumping systems available for the production of high vacuum [74]. Candidate systems which satisfy the conditions of Section 3.1 are:

(1) Oil filled diffusion pump backed by an oil sealed rotary pump.

(2) Turbomolecular pump backed by an oil sealed rotary pump.

(3) Sputter ion pump. Initial pumpdown by sorption pumps or diffusion pump - rotary pump unit.

(4) Cryopump. Initial pumpdown by sorption pumps.

The basic operation of these pumps is well covered in the literature [74-81] and will not be described here. The operational characteristics of the pumps will be discussed, in Sections 3.3.1 - 3.3.5, only where these are important with respect to the VTF. Section 3.3.6 summarises the final selection process.

3.3.1. Diffusion pump

The combination of an oil filled diffusion pump backed by an oil sealed rotary pump, often operated with a liquid nitrogen trap on top of the diffusion pump, is one of the most common ways of producing a high vacuum. The diffusion pump is inexpensive to buy, run and maintain, is quiet and easy to operate, and provides high and constant pumping speeds in the pressure range 10^{-2} mb to $< 10^{-9}$ mb .

The biggest danger with a diffusion pump is the possibility of oil contamination reaching the vacuum chamber. This will happen to a certain, small, extent during normal operation, although with modern single structure pumping units backstreaming is very small [82]. Problems are more likely to occur because of equipment failure or operator error, when gross oil contamination can occur. This can happen, for instance, if the chamber inadvertently comes up to atmospheric pressure while the diffusion pump is operational. This form of contamination has been observed to reduce significantly the efficiency of MCP's (Section 2.3.4). Rigorous precautions, both in design and operation would be required to prevent such contamination in the VTF. Properly operated diffusion pumps can run for several years between maintenance periods.

3.3.2. Turbomolecular pump

A turbomolecular pump (TMP) backed by an oil sealed rotary pump is an established system for producing very clean high vacuums. Being a purely mechanical pump the TMP has no pumping fluid to cause contamination by backstreaming. The only possible source of contamination is the grease or oil from the pump bearings, together with any contamination in the fore vacuum line. When the TMP is operating, however, it has an extremely high ($> 10^{10}$) compression ratio for high mass molecules and so virtually no contamination will be able to migrate into the vacuum chamber [83,84].

Contamination can take place when the TMP is switched off and left under vacuum. In this situation bearing lubricant and fore vacuum contamination may reach the vacuum chamber. To avoid this problem the TMP should always be vented to at least 200 mb before it comes to rest.

The major disadvantages of the TMP are the high initial cost and the cost of maintenance should anything go wrong. TMP's also require periodic

(3000-5000 hours) bearing lubrication. This normally involves stopping the pump and venting it to atmospheric pressure. A minor inconvenience is the high pitched noise produced by a TMP while operating.

TMP's have been produced which do not use oil or grease lubricated bearings. These are generally larger units and were not under consideration for the VTF.

3.3.3. Oil sealed rotary pump

Both the diffusion pump and the TMP are continuous ejection vacuum pumps and require a minimum fore vacuum pressure of 10^{-1} mb and 10^{-2} mb respectively. The vacuum chamber must also be evacuated to $\sim 10^{-1}$ mb before they begin to pump effectively.

The pump that is used almost exclusively in the role of roughing pump is a single or double stage oil sealed rotary pump. The advantage of the double stage pump is that ultimate vacua of $\sim 10^{-3}$ mb are obtainable (as opposed to $\sim 10^{-2}$ mb for single stage pumps), and they give higher pumping speeds and less backstreaming at low pressure.

It is accepted that to produce a clean high vacuum great care must be taken when operating rotary pumps [82,84,85,86], and that the major contamination in many systems is actually rotary pump oil.

In the context of the VTF a rotary pump would have to be operated so that the risk of contamination is reduced to a minimum [87,88]. Since backstreaming increases with decreasing pressure, one way to proceed is to always operate the rotary pump at the highest pressure consistent with the required result. To allow the rotary pump pressure to be controlled a leak valve can be placed just before the pump to admit gas into the fore vacuum line. To reduce the contamination further a foreline trap, filled with a molecular sieve or activated alumina, can be fitted between the rotary pump and vacuum system.

3.3.4. Ion pump

The ion pump has the advantages of being completely silent in operation requiring no form of backing pump and offering complete freedom from oil contamination. The ion pump does however require a rather better starting vacuum ($\lesssim 10^{-3}$ mb) than either the diffusion pump or the TMP and is in general rather slower to start.

The starting pressure can be produced by a sorption pump system. Rotary pumps are not used in general because they struggle to produce the required pressure and also because any oil contamination can badly damage the ion pump. An alternative method is to use a rotary/diffusion pump combination. The lower pressures obtained by this technique may be required for some types of ion pump.

There are several disadvantages to ion pumps. They have a very poor performance when pumping the noble gases, especially argon. Also being a closed pump (i.e. storing pumped gas rather than ejecting it from the system) there is a limit to the amount of material that can be pumped.

These considerations were of great importance since the VTF was to include a proportional counter equipped with a thin plastic window and filled with an argon-methane gas mixture (Section 3.6). This would give both a high total pressure and a very high argon partial pressure. Measurements made on the completed VTF gave pressures of order 5-10 x 10^{-6} mb, 99% of which was due to leakage from the proportional counter. The argon partial pressure was 50% or 90% of the total pressure, depending on the gas mixture used.

The presence of argon in such large proportions would have given a very unstable pumping performance, and the very high total pressures would have meant an ion pump lifetime of only 1-2 years. With present and foreseeable thin window technology, the ion pump was not considered a suitable pump for use on the VTF.

3.3.5. Cryopump

The cryopump has a very high pumping speed and can produce very clean, completely oil free high vacua. Starting pressures of $\sim 10^{-2}$ mb are required; these can be easily produced by a sorption pump system. The cryopump itself is silent in operation and requires very little maintenance, but vibration can be a problem. A compressor is also required, but this can be distant from the pump itself.

Like the ion pump, this is a closed pumping system and needs periodic regeneration when a large amount of material has been pumped. This period is typically of order a few weeks to a few months for a system like the VTF and might cause problems for long term performance and life tests.

The pump requires 1-2 hours to cool down and must be operated continuously until regeneration is possible. Regeneration takes 2-4 hours after which the pump must be cooled down again.

Cryopumps tend to be economic only for very large pumping speeds ($\gtrsim 800\,\ell\,s^{-1}$) and so were not a sensible choice for the VTF.

3.3.6. Final choice

The choice of pump for the VTF was made on grounds of suitability and cost. The only one of the four options that proved impracticable was the ion pump, because of the high gas throughput and argon instability. Probably the best way to produce a very clean high vacuum is the cryopump/sorption pump combination. There was however a question mark against its flexibility with respect to prolonged pumping times and this, together with economic considerations, ruled it out.

In operational terms there is very little to choose between a single structure diffusion pump and a TMP. The TMP was the preferred choice here because it produces a slightly cleaner vacuum and when properly installed is less likely to produce contamination through failure or human error.

The higher initial cost of a TMP was offset by the availability of an unused TMP within the X-ray astronomy group. The TMP was backed by a two stage rotary pump, with a foreline trap and leak valve as detailed in Section 3.3.3. Provision was made for automatically venting the TMP to atmospheric pressure (with dry nitrogen), whenever the pump stopped.

3.4. General Vacuum System

Consideration of Section 3.1 and a desire to construct a high quality vacuum system led to the decision that whenever possible the VTF should be constructed to Ultra High Vacuum (UHV) standards. This meant that all materials used should have a low outgassing rate and that sources of organic contamination, e.g. rubber gaskets, oils, grease, should be avoided whenever possible.

In general to achieve pressures below $\sim 5 \times 10^{-7}$ mb it is necessary to heat (bake) the vacuum system. This removes adsorbed gas, reduces the outgassing rate and can also remove unwanted contamination. The VTF was therefore designed to withstand a moderate bakeout.

To provide adaptability it was decided to have a modular system constructed from standard stainless steel vacuum components using the conflat [89] sealing principle (identical knife edges compressed into a copper gasket). As far as possible all components inside the vacuum system were also constructed from stainless steel, with certain specialised parts made from copper, glass, ceramic and PTFE. PTFE was used in preference to PVC since PVC has been found [90] to produce contamination by evaporation of plasticiser. Two viton [91] rubber gaskets were used in the vacuum system itself with a third being used in the proportional counter (Section 3.6). Sample outgassing rates are given in Table 3.1.

The chosen vacuum components were tubular with an internal diameter of 150 mm, allowing sufficient space to install the MCP detector (Section 3.2), proportional counter (Section 3.6) and filter wheel (Section 3.5).

A schematic diagram of the vacuum system is shown in Fig.3.4. The

Table 3.1

Sample material outgassing characteristics

Material	Degassing rates (mb ℓ/sec / cm^2) Before bakeout	After bakeout
Aluminium	10^{-9}	10^{-13}
OFHC copper	10^{-8} - 10^{-10}	10^{-11} - 10^{-14}
Gold		3 x 10^{-11}
Nilo K		10^{-11} - 10^{-12}
PTFE	10^{-9}	10^{-12}
Pyrex	10^{-6}	10^{-10}
Quartz	10^{-5} - 10^{-7}	10^{-9} - 10^{11}
Stainless steel	10^{-8} - 10^{-10}	10^{-11} - 10^{-14}
Viton A	10^{-7}	10^{-9}

Values from Vacuum Generators information sheet
"Materials for clean and ultra high vacuum applications"
See also ref.[75] page 142 for further information.

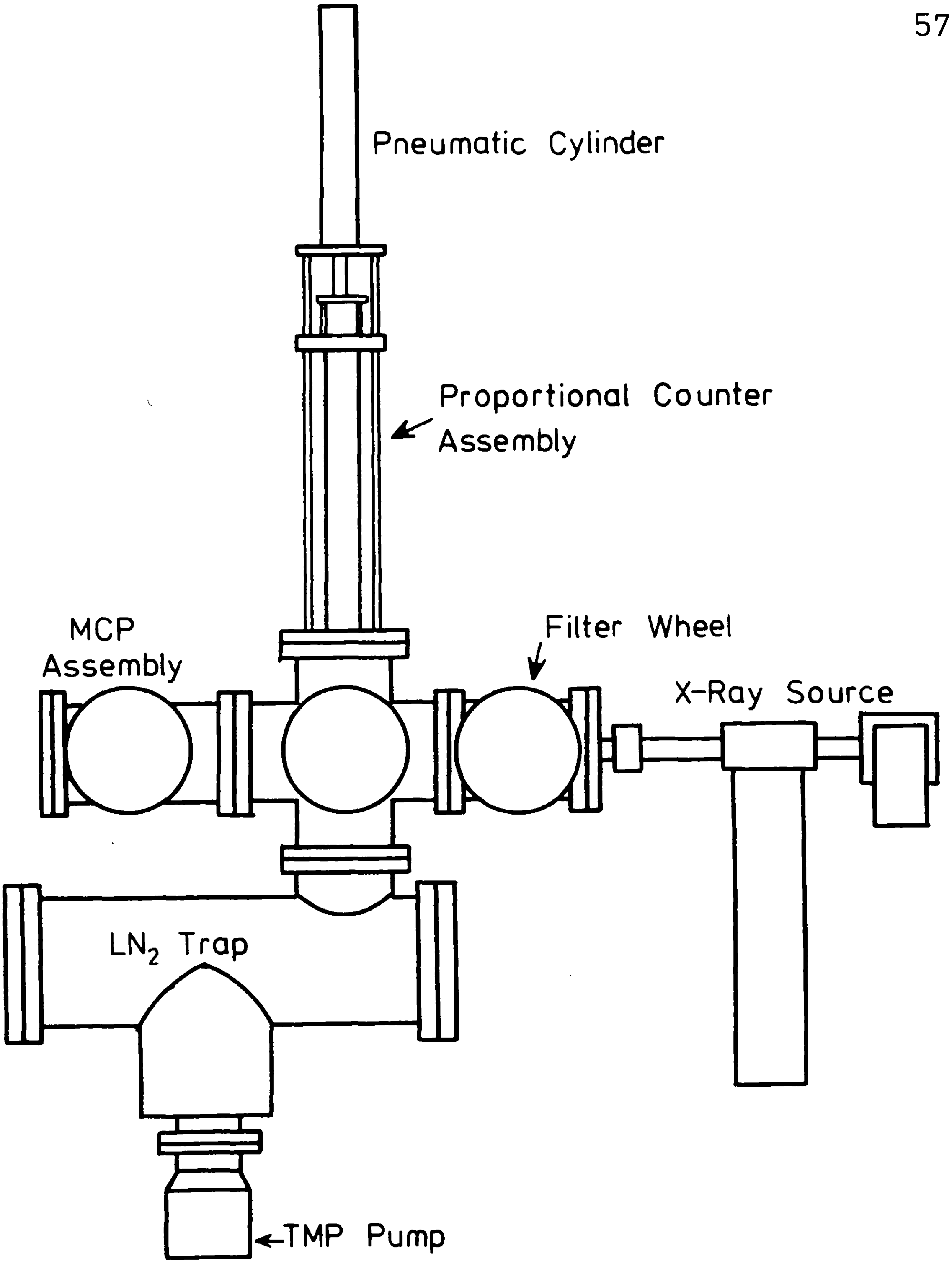

3.4. Schematic side view of completed VTF.

TMP was interfaced to the vacuum chamber proper by means of a high quality liquid nitrogen trap. This provides a large increase in the pumping speed for water vapour and allows the possibility of installing a diffusion pump at some future time. The cold trap also contains an isolation valve and ports for the installation of pressure gauges.

Provision was made for isolating any one of the three main experimental sections; (1) MCP assembly, (2) X-ray source, (3) reference detector, by the addition of gate valves. Economic considerations dictated that only the most important, (2), was actually installed (Section 3.5).

To provide the required dry environment (Section 3.1) the VTF was designed to backfill with dry nitrogen rather than air.

The pressure inside the VTF can be monitored from atmospheric pressure to $\sim 10^{-10}$ mb by use of several standard vacuum gauges; thermal conductivity, penning and ion gauges. The pressure and residual composition can also be measured using a quadropole mass spectrometer. This is placed immediately behind the MCP detector and can detect the presence of organic contamination and evolution of material from the MCP's or their photocathodes.

The entire system, including pumps and control units, was mounted on an easily movable, custom built frame.

3.5. X-ray Source

3.5.1. Energy range

The energy range which the X-ray source must cover is determined by the requirements of future X-ray astronomy missions (Section 1.4). The present principal region of interest is 0.02-3.0 keV (300-4 Å) with a longer term need for energies up to ~ 8 keV.

It is not possible to produce X-rays over this entire energy range with only one type of source. A simple electron bombardment or fluorescent source [92,93] is able to generate characteristic energies $\gtrsim 0.1$ keV, but to produce lines in the 0.04-0.1 keV range a penning discharge source is needed [94].

Since the development of a penning source and its required monochrometer is itself a considerable task it was decided to develop an electron bombardment type source only, in the first instance. The bombarding electrons excite atoms of selected elements on the anode which then decay, producing characteristic K and L X-ray lines. This is achieved by coating the anode of the X-ray source with a compound containing the desired element. Low energy radiation is cut out by the use of transmission filters (Section 3.5.5). Table 3.2 gives details of the X-ray energies, compounds and filters used.

The X-ray source should be able to produce after collimation (Section 3.5.6) a minimum of 500-700 counts s^{-1} at the MCP detector ($\geq 2 \times 10^{8}$ counts s^{-1} steradian^{-1}). Any count rate variation should preferably be small, changes being gradual rather than abrupt, and therefore the power supply must be emission stabilised

3.5.2. X-ray source construction

The major consideration in the construction of the X-ray source was the provision of access to the anode to allow the coating to be changed easily. The comments of Section 3.1 show that it is desirable to do this without disturbing the MCP detector and therefore the X-ray source must be separately pumped. Separate pumping also allows the X-ray source to be operated in a higher vacuum than the MCP detector thus improving filament lifetime and count rate performance.

In order to minimise spectral contamination of the desired X-ray lines the vacuum chamber should be constructed to UHV standards. (The principles and design philosophy of Section 3.4 were followed throughout.) This is especially important with respect to organic contamination, which tends to be broken down by the electron beam to produce a layer of carbon on the anode. A carbon layer has two effects, (1) it cuts down the intensity of the line being produced and (2) the X-ray beam is contaminated

Table 3.2

X-ray energies and filters for characteristic lines used

Line	KeV	Å	Filter	Anode Material
Boron K	0.183	67.6	NONE	BN
Carbon K	0.277	44.7	2 μm Lexan	SiC
Copper L series (mean)	0.924	13.41	4 μm Al	CuO
Magnesium K	1.25	9.89	20 μm Al	MgO
Aluminium K	1.49	8.34	20 μm Al	Al_2O_3
Silicon K	1.74	7.13	1 μm Ag	SiC
Niobium L series (mean)	2.28	5.44	1 μm Ag	Nb_2O_5
Ruthenium L series (mean)	2.68	4.63	1 μm Ag	Ru O_2

with C-K X-rays (0.28 keV).

A schematic view of the X-ray source is shown in Fig.3.5.

In operation the X-ray source is separated from the main vacuum chamber by a thin (~ 1 μm) polypropylene window. This transmits all the energies of interest and provides effective separation of the two vacuum chambers. Windows of this type used on proportional counters, and subjected to cycling from high to low pressure differentials, fail after relatively few cycles [95]. To allow the X-ray source to be let up to atmospheric pressure while the main vacuum chamber is under vacuum, or vice-versa, a gate valve is used to separate the two chambers. The dead volume between the window and the gate valve is pumped via the bypass line. This means that there is never any significant pressure differential across the window and so very little danger of window failure.

Flexible bellows provide sufficient movement of the bypass line to remove the window support if the window does fail.

3.5.3. Pumping system

The comments of Sections 3.3.1-3.3.5 apply to the choice of pump for the X-ray source. Major differences are the absence of argon from the source chamber and a very much smaller gas throughput, which means that the achievable vacuum will be very much better. Also to be considered is that analysis of existing, diffusion pumped, X-ray source anodes, by electron microscope easily shows the products of cracked rotary pump and diffusion pump oil [96,97].

With the diffusion pump excluded on contamination grounds and the cryopump on economic grounds, the choice lies between a TMP and an ion pump. An ion pump was chosen because of its ease of operation once the pump has been started. An old ion pump/sorption pump system was available within the Physics Department and so this was also an economically sensible choice.

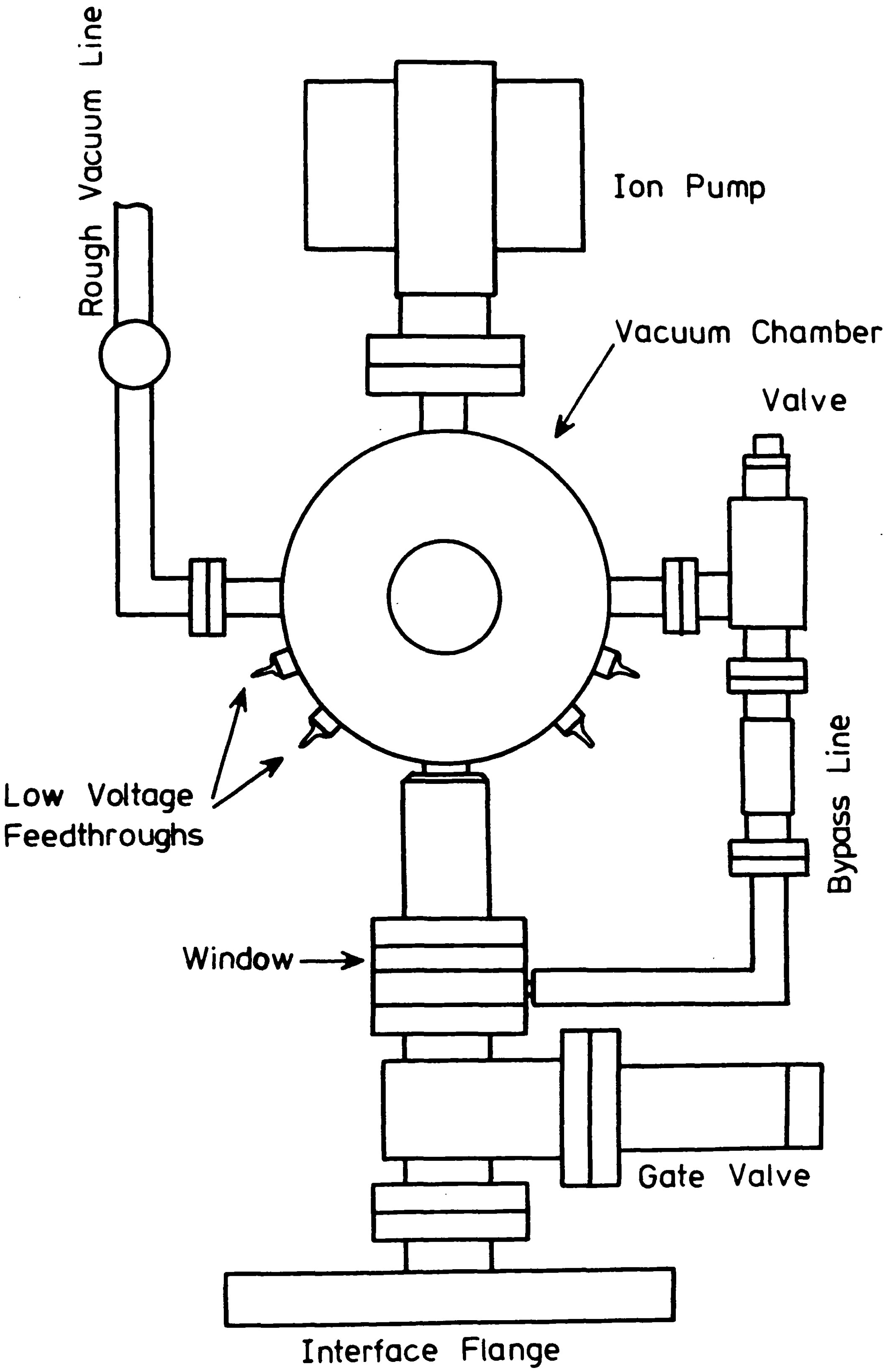

3.5. Schematic plan view of the X-ray source and its interface to the VTF.

An ion pump/sorption pump system will give a very clean high vacuum (pressures of $\lesssim 10^{-8}$ Torr have been obtained) and is ideal for a system like the VTF that is not cycled "very often". If the source were to require altering more frequently than approximately once every two days the increased gas throughput, and time spent starting the pump might make this combination a poor choice.

3.5.4. Anode and filament assembly

Fig.3.6 shows a schematic view of the anode and filament assembly of the X-ray source. The source uses a filament at ground and a high voltage, water cooled copper anode. The problem of having water at high voltage was solved by having the water flow through a long length of coiled PVC pipe to a section of grounded metal pipe. The use of distilled water and a long column, ensures that the current flow through the water is very small (0.1 mA/kV, $\lesssim$ 10% of true emission current) and stable and so does not affect the emission stabilising characteristics of the power supply.

The anode is a copper cylinder 18 mm in diameter with its surface cut at an angle of 15° to the horizontal. The filament is 25 mm of 110 μm diameter tungsten wire and is mounted on top of a ground plane, positioned so that a 5 mm hole is aligned with the centre of the anode. As shown in Fig.3.7 this produces a crude electron lens. As the filament tip is moved relative to the bottom face of the ground plane the diameter of the region of heavy electron bombardment changes.

The regions of electron impact were well determined because of the appearance of a dark contamination spot on the anode (Section 3.5.7). The observed X-ray count rate was correlated with the size and position of the contamination spot and therefore the spot could be used to determine the size and the position of the electron beam. Collimation alignment and filament positioning were thus easily achieved. It was found that

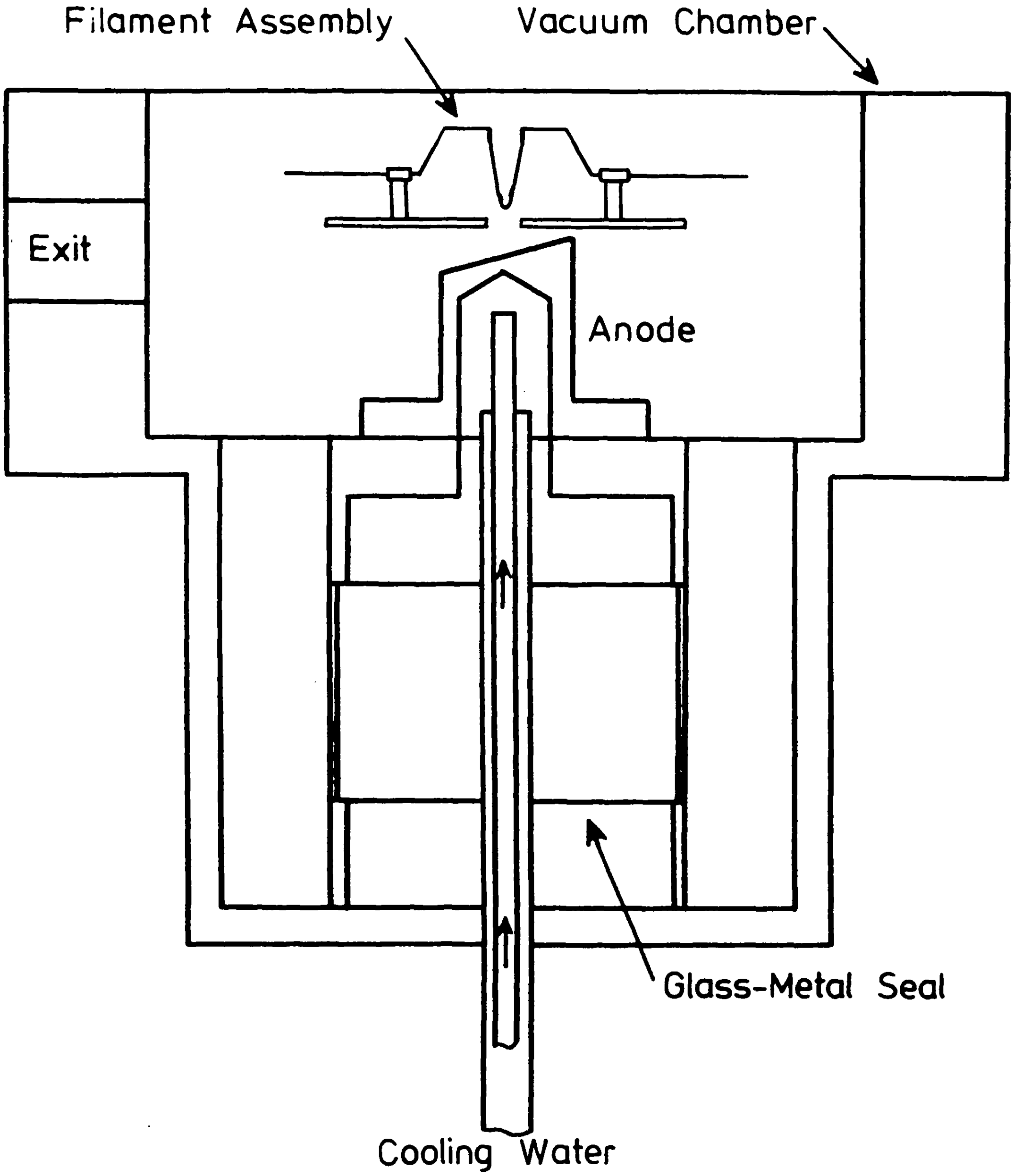

3.6. Schematic, sectional side view of the X-ray source interior.

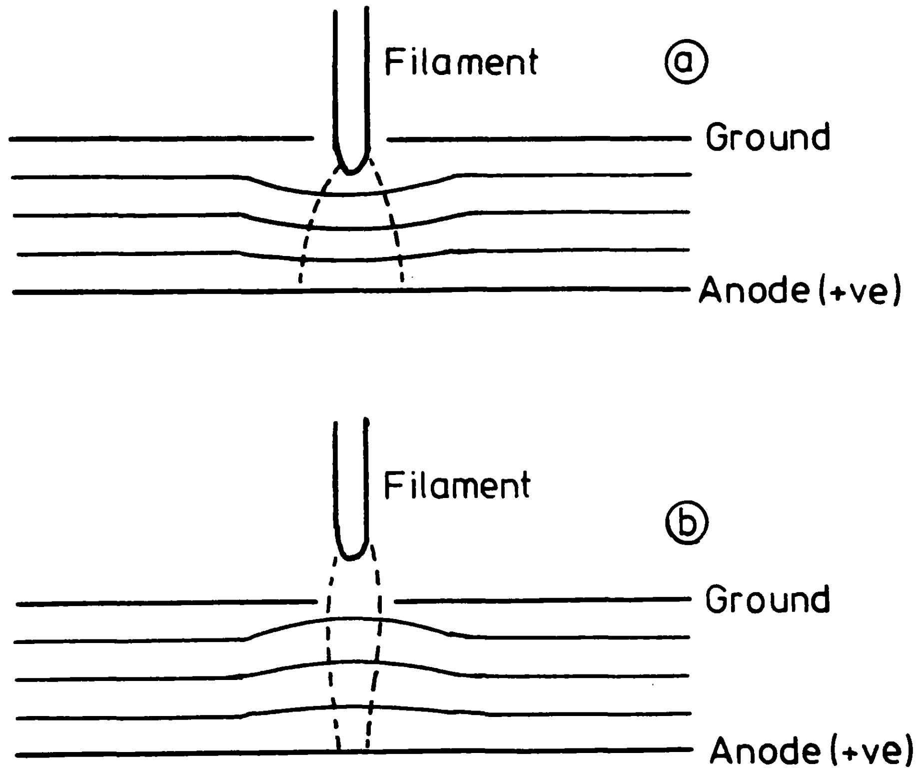

3.7. Crude electron focusing arrangement for the X-ray filament
(a) Filament protrudes through ground plane. Electric field configuration produces a large electron beam.
(b) Filament above ground plane. Electric field configuration focuses electrons onto a narrow spot.

if the filament tip was ~ 1 mm above the 1 mm thick ground plane, the majority of the electrons were focused onto a 2-3 mm diameter spot.

The geometry of the anode (Fig.3.11(a)) means that a circular output beam will be produced from an elliptical area on the anode surface. Since the focusing arrangement described above excites a circular area on the anode this geometry is not optimum. The present arrangement gave sufficiently high count rates for all commonly used X-ray energies, however, and so no further development was undertaken.

3.5.5. X-ray filters

When attempting to produce characteristic X-ray lines at a given energy all lines of lower energy will also be excited, possibly with higher efficiency. An electron bombardment source will also produce a continuous spectrum generated by the decelerating electrons. For the study of MCP's described in Section 3.1 it was necessary to remove this unwanted radiation and isolate the required spectral line.

The best way to produce a spectrally pure line is to use some form of X-ray monochrometer, based either on a grating [98] or a crystal [99]. This option was considered but rejected because it was too complex mechanically and required a stronger X-ray source than was available. The method adopted was to use thin films or foils to absorb the unwanted low energy radiation and transmit the higher energy characteristic line of interest [100]. The filter materials used are listed in Table 3.2 and their transmissions are shown in Figs.3.8(a-d).

These filters are mounted in the X-ray beam line (see Fig.3.4) on a rotatable wheel which can accommodate six filter sets. Filters with clear diameters of 20 mm could be installed but in practice the filter material was normally glued to the collimating hole using Evo-Stick*.

---

* manufactured by Evode Ltd., Common Road, Stafford, England.

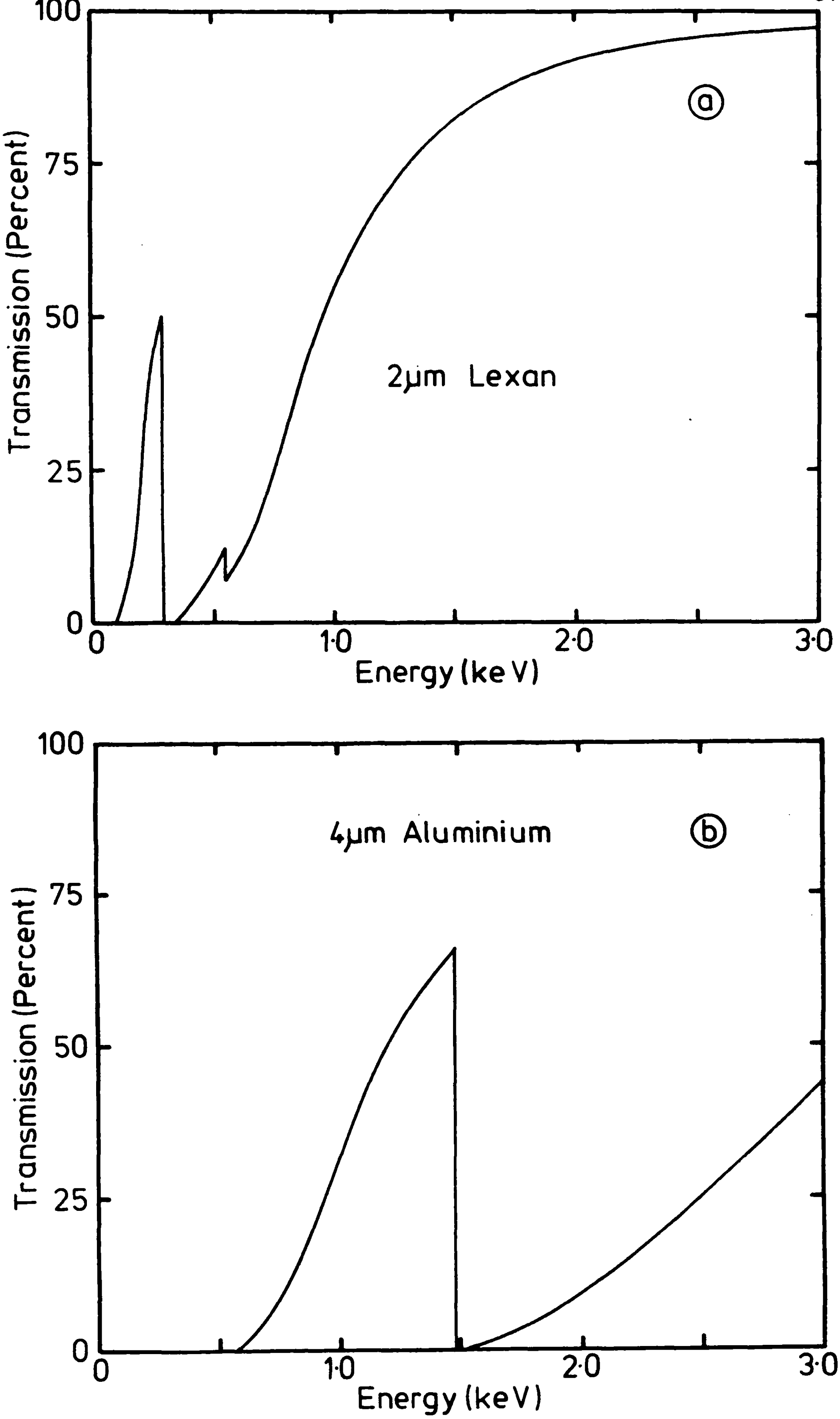

3.8. Transmission of the X-ray filters used on the VTF.
(a) 2 µm thick Lexan
(b) 4 µm thick Aluminium
(c) 20 µm thick Aluminium
(d) 1 µm thick Silver (mounted on 3.5 µm thick mylar)

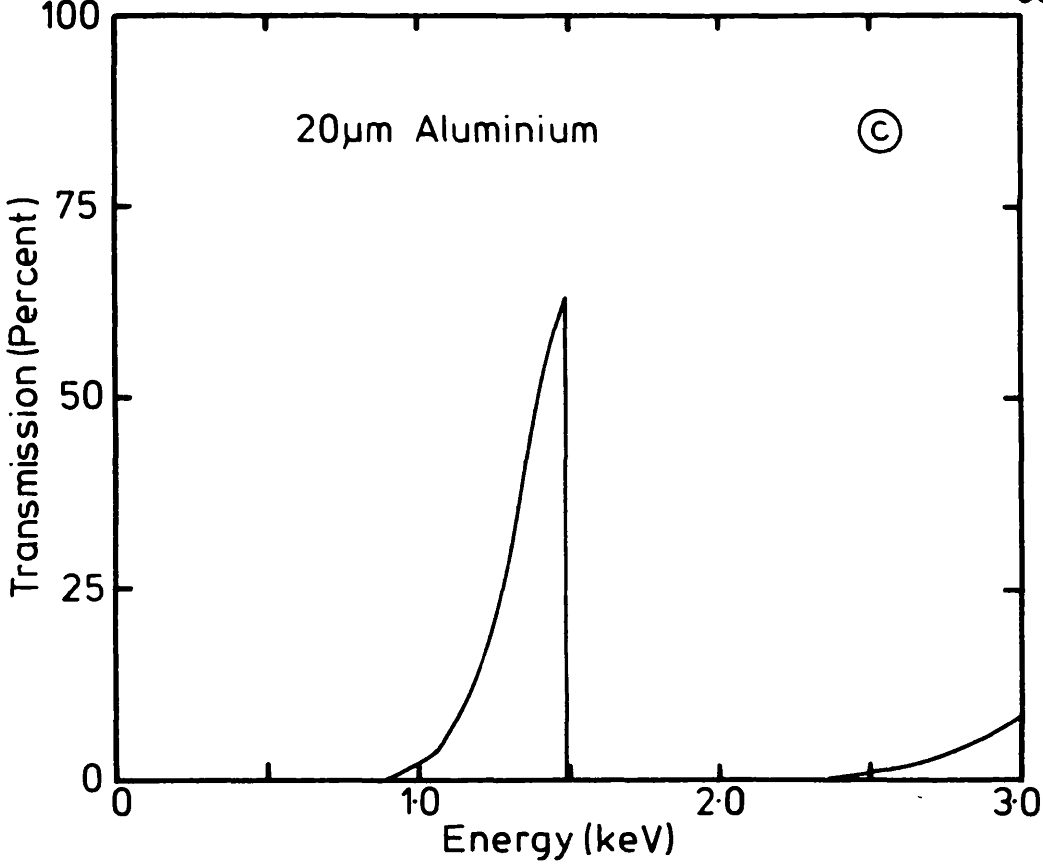
20μm Aluminium
ⓒ
Transmission (Percent)
100
75
50
25
0
0
1·0
2·0
3·0
Energy (keV)

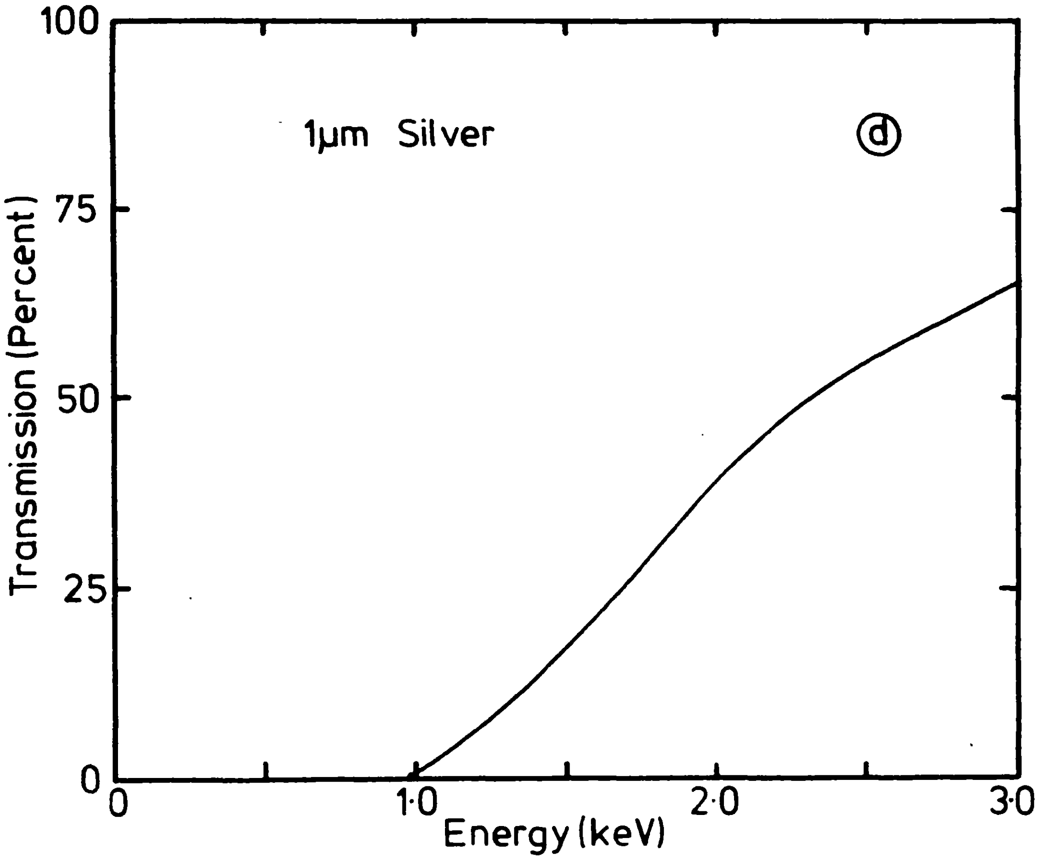
1μm Silver
ⓓ
Transmission (Percent)
100
75
50
25
0
0
1·0
2·0
3·0
Energy (keV)

3.5.6. Collimation

Collimation of the X-ray beam is required for two reasons, (1) the beam must fit onto one half of the MCP (Section 3.1, Fig.3.1), (2) the beam must have a small angular divergence since the MCP quantum detection efficiency is very strongly dependent on X-ray incident angle (Section 2.3.3.). The beam collimation should not however be significantly better than is required for efficiency measurements because of the consequent reduction in X-ray count rate. A range of beam divergences should therefore be possible with $\pm$ 0.25° being a suitable maximum value. Constraint (1) requires the beam diameter at the MCP to be less than 7-8 mm.

Other constraints which must be considered are: (3) no scattered radiation should reach the detector, (4) it is desirable to be able to illuminate uniformly a 30 mm diameter MCP detector with a simple change in the collimating arrangement.

The X-ray beam is collimated using small holes in two stainless steel plates. One of these is situated inside the X-ray source and the other is mounted on the filter wheel. A complete set of six collimating plates, one for each filter type, is therefore required for the filter wheel. This allows the collimation to be set as appropriate for each energy.

The geometry of the collimator is shown in Fig.3.9. The overall size of the X-ray beam, x_D , is given by

$$x_D = \frac{\ell_3(d_2+d_1)}{\ell_2} + d_2 \tag{3.1}$$

where d_1 and d_2 are the hole diameters and ℓ_2 and ℓ_3 the spacings as shown in Fig.3.9.

The diameter of the central "core" of the beam, x_2 , is given by

$$x_2 = \frac{\ell_3(d_2-d_1)}{\ell_2} + d_2 \tag{3.2}$$

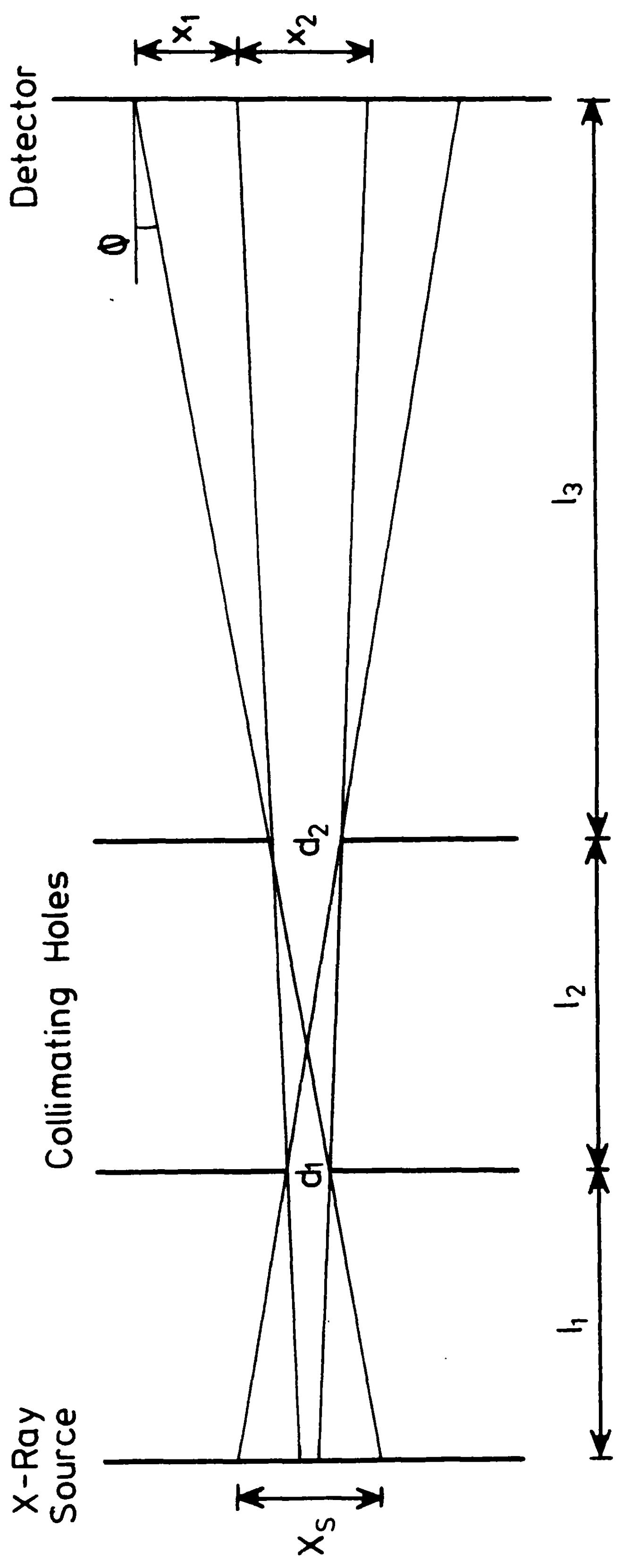

3.9. Geometry of the VTF X-ray source collimation.

The diameter of the spot on the anode, x_s , that contributes to the X-ray beam is given by:

$$x_s = \frac{\ell_1(d_2+d_1)}{\ell_2} + d_1 \tag{3.3}$$

The maximum beam divergence, ϕ , is given by

$$\phi = \tan^{-1}\left(\frac{d_1+d_2}{2\ell_2}\right) \tag{3.4}$$

The actual system parameters used for the measurements reported in Chapters 5, 6, 7 are given in Table 3.3(a) while Table 3.3(b) illustrates the possible variation in X-ray beam collimation which can be obtained by varying d_1 and d_2 (calculated using eqns.(3.1)-(3.4)). x_{pc} is the diameter of the beam at the proportional counter and is calculated using eqn.(3.1).

The above arrangement, with d_1=0.85 mm and d_2=2.0 mm, satisfies constraints 1 and 2. Also by removing the collimation plate from the filter wheel it is possible to illuminate a 30 mm diameter MCP using only the central core (x_2>30 mm) of the X-ray beam. Thus, constraint 4 can be satisfied.

It is possible, however, for radiation to be reflected from the sides of the tube connecting the X-ray source to the main vacuum chamber and reach the MCP's. To reduce this risk an additional baffle plate was installed between the two collimating plates. The hole in this baffle plate was limited by constraint 4, in that the collimation produced by the baffle plate and hole d_1 should produce x_2=30 mm.

For reflected radiation to get through this baffle it must be reflected from the stainless steel of the tube at angles of at least 6° and have been generated outside an 8.5 mm diameter spot on the anode. From the X-ray reflection data of Lukirskii et al [101] it can be seen that only C-K (0.28 keV) and B-K (0.18 keV) X-rays have any significant reflection coefficient at 6° grazing angle. For these lines a reflection coefficient of 25-50% might be expected. Considering that at least two

Table 3.3(a)

System parameters used for present series of measurements

ℓ_1	= distance between source and first collimating hole	=	50 mm
ℓ_2	= distance between the two collimating holes	=	460 mm
ℓ_3	= distance from second collimating hole to MCP detector	=	490 mm
ℓ_3'	= distance from second collimating hole to PC detector	=	156 mm
d_1	= diameter of first collimating hole	=	0.85 mm
d_2	= diameter of second collimating hole	=	2.0 mm

Table 3.3(b)

Beam collimation can be changed by altering the diameter of the collimation holes (d_1,d_2). The possible variation in beam collimation presently available is shown.

d_1(mm)	d_2(mm)	x_2(mm)	x_D(mm)	x_s(mm)	ϕ (degrees)	x_{PC}(mm)
0.50	0.85	1.23	2.30	0.64	0.08	1.31
0.85	2.00	3.23	5.05	1.16	0.18	2.97
2.00	2.00	2.00	6.28	2.44	0.25	3.36

reflections are required for the detector to "see" scattered radiation and that the electrons from the filament are tightly focused onto a spot 3-4 mm in diameter on the anode, it is unlikely that any significant amounts of scattered radiation will reach the MCP detector.

3.5.7. Performance

Initial development of the X-ray source was undertaken with an uncoated anode generating Cu-L (0.93 keV) X-rays. High X-ray count rates could be obtained from the source but could not be sustained for long periods. As shown in Fig.3.10 the count rate decayed very quickly to a baseline level a factor of 5-10 below its starting value.

This fall in count rate was correlated with the appearance on the anode of a dark, approximately circular, contamination spot. The position and size of the spot depended on the position and size of the electron beam incident on the anode and this was used to help position the filament (Section 3.5.4).

The spot could be removed by lightly abrading the anode surface and cleaning with IPA. The subsequent X-ray count rate characteristics then followed the previous fall off. These results were repeatable and subsequent exposure to atmosphere or prolonged periods under vacuum did not produce any changes.

Analysis of the contamination spot by scanning electron microscope produced several surprising results. The actual contamination spot could not be detected by the electron microscope; there were no gross differences, either of composition or surface structure, between the contaminated and uncontaminated regions. Traces of carbon and oxygen with very small traces of tungsten were found within the spot. None of the several experienced electron microscopists consulted were able to identify the contamination and none could explain why the mark did not show up easily under examination.

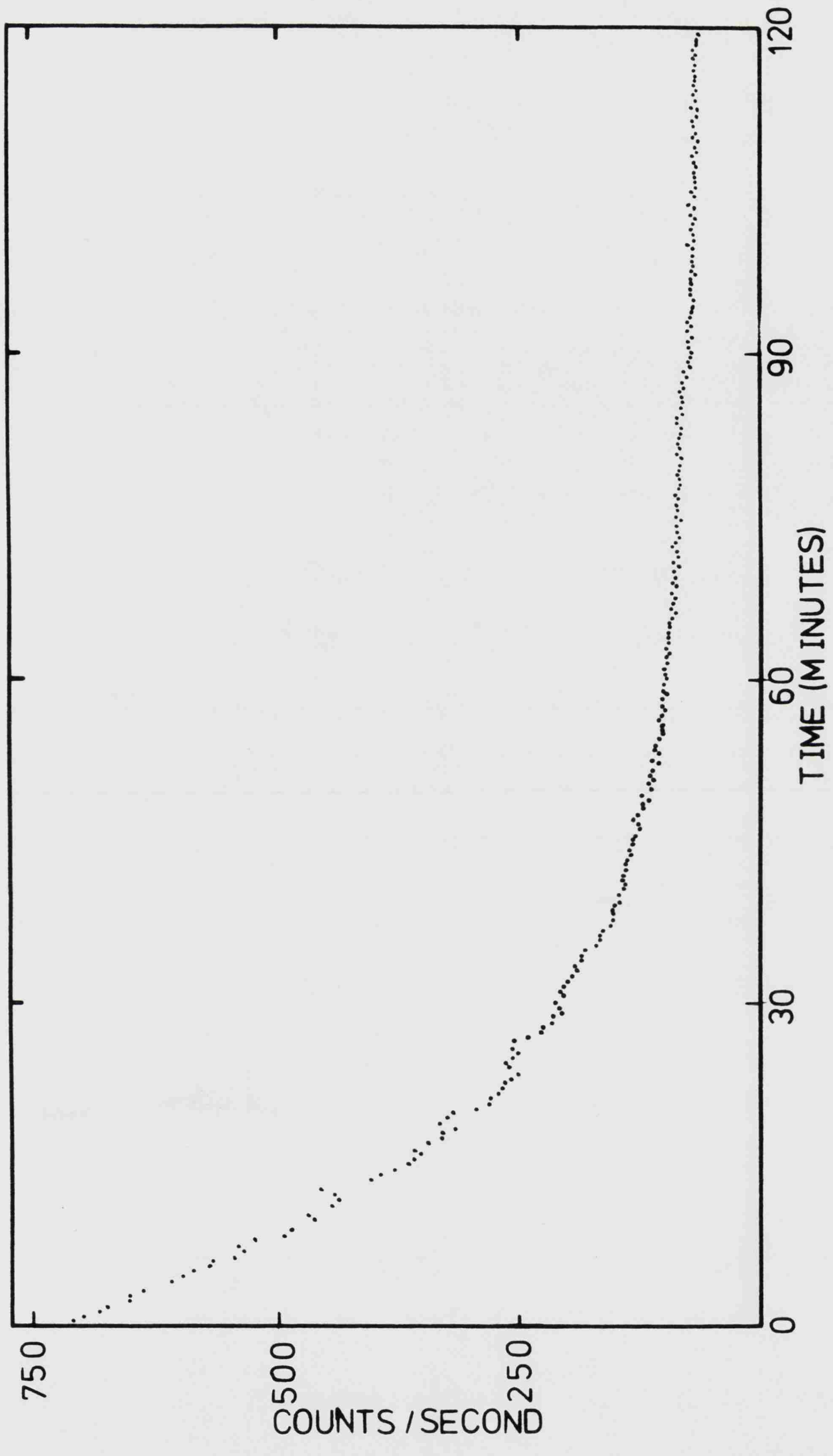

3.10. Variation of Cu-L (0.93 keV) X-ray count rate with time. Uncoated copper anode.

Possible sources of the contamination were considered. (1) Emission from the filament, (2) contamination present within the vacuum chamber, (3) contamination within the copper anode itself.

Several filaments were carefully cleaned before assembly and degassed using high currents once installed. This produced no significant change in the decay characteristics, and taken together with the very small quantities of tungsten detected by the electron microscope indicated that the filament was not the source of the contamination.

As the vacuum chamber had been constructed to UHV principles, and has achieved pressure of less than 10^{-8} Torr on several occasions, there is unlikely to be any significant source of contamination present.

This leaves the anode material itself as the contamination source which would seem to be consistent with the observed pressure increase when the anode is bombarded (and hence heated) by electrons.

Initial observations had been made using accumulated operating times of 4-6 hours. This was increased to ~ 24 hours in an attempt to induce further effects. After 8-10 hours of operation the X-ray count rate started to increase. This increase continued over a period of 3-4 hours until the count rate recovered to its high starting level. This count rate was then constant for the remainder of the test period.

On examination of the anode it was found that the small area directly below the filament was again a bright copper colour. A large proportion of the surrounding area was still contaminated, some of it heavily. There seems little doubt therefore that the increased count rate was due to the central anode area again becoming free of contamination.

A possible explanation of this behaviour is that the "contamination" spot is actually some form of surface roughness effect. Molecules liberated from the anode, when it is heated by electron bombardment, cause the surface to become jagged by some sputtering effect (Fig.3.11). The observed X-ray count rate will drop because only a fraction of the incident

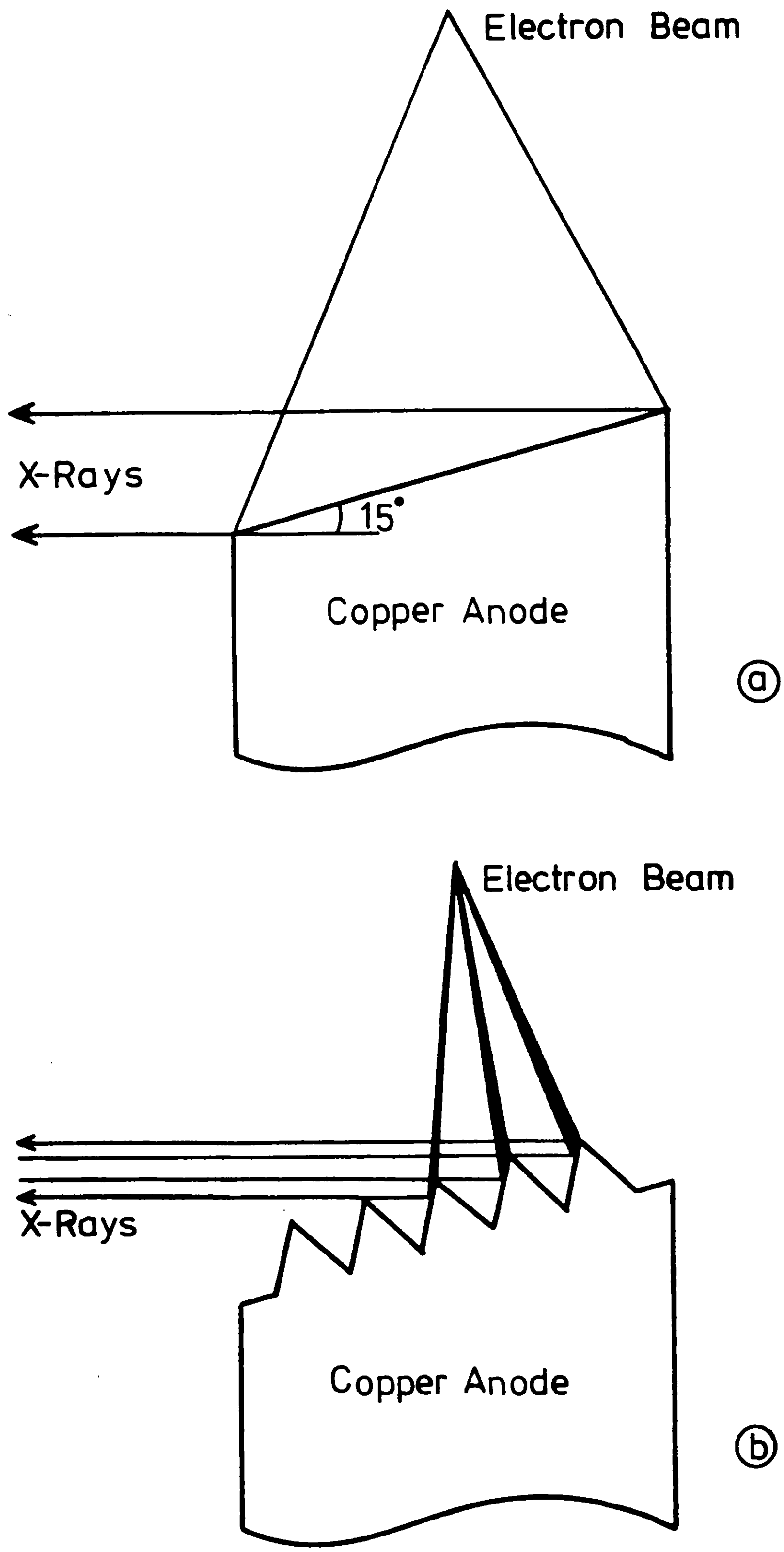

3.11. Schematic representation of an anode surface structure which could cause the observed decay in count rate.

(a) Normal smooth anode. All the incident electrons contribute to the output X-ray beam.

(b) Rough anode structure. Only electrons from the three shaded beams contribute to the output X-ray beam thus reducing the output flux.

electrons can now generate X-rays that contribute to the output beam (Fig 3.11(b)). The black discolouration may be a thin layer of cupric oxide caused by trapped pockets of air on the machined anode surface reacting with the copper. Once the anode has been sufficiently outgassed by continuous operation the sputtering will stop and local surface melting could again produce a smooth copper surface.

The small scale irregularities (~ few thousand Å) would not have been detected by the electron microscope because the anode surface was irregular on a larger scale. To investigate the model in depth would require subjecting a highly polished anode surface to detailed electron microscopy.

Subsequent tests using compounds applied to the anode to generate other characteristic lines showed the count rate to be stable over long periods of operation. This provides additional support for the above theory, and so Cu-L was subsequently generated using a cupric oxide coating rather than from the bare anode.

The problems with Cu-L count rate instability might have been avoided if the anode had been subjected to a high temperature vacuum bake before use.

The stability of the count rate over 30 second counting intervals was determined with C-K (0.28 keV) X-rays. 140 sequential 30 second integrations were made using the proportional counter. These integrations were then considered in groups of 3; denoted n_1, n_2, n_3. It was found that the value of n_2 could be predicted, with an rms deviation of less than 1%, by using $(n_1+n_3)/2$. No improvement in the predictions were observed by using a straight line fit to points n_1, n_3, n_5, n_7 to predict n_4. These tests established the feasibility of predicting the X-ray count rate during an efficiency measurement on the MCP, by averaging proportional counter measurements made before and afterwards.

3.6. Reference Detector

3.6.1. Use of a proportional counter

In order to measure the quantum detection efficiency of a MCP detector it is necessary to know in absolute terms the X-ray flux incident upon the detector. This means that a reference counter, with an accurately known and stable quantum detection efficiency at all wavelengths in use, must be able to move into the X-ray beam when required.

There are a limited number of such detectors; possibilities are (1) channel electron multiplier [102], (2) microchannel plate [1], (3) windowless diode [103,104], (4) thin window proportional counter [105]. Of these 1,2,3 would all need initial calibration against some absolute standard and would also require periodic recalibration. All three detector types are sensitive to organic contamination and hence after accidents in use, installation or storage they would require recalibration. This could produce delays at inconveneint times and therefore these detector types were rejected as reference detectors for the VTF.

A simple single wire proportional counter (PC) is a sturdy detector which can be easily calibrated in the lab and fulfills the above requirement. Many workers have made use of the single wire proportional counter as a reference detector [102,106,107,108], and such a detector was chosen for the VTF.

Proportional counters are limited in application, however, by the transmission and strength of the thin plastic entrance windows [109] required for low energy work. These windows cut off all very low energy radiation. Stretched polypropylene for example (Fig.3.12) can only be used down to ~ 0.1 keV (~ 125 Å). For study extending further into the XUV band (up to ~ 400 Å) a proportional counter would not be suitable and a windowless diode would probably have to be used.

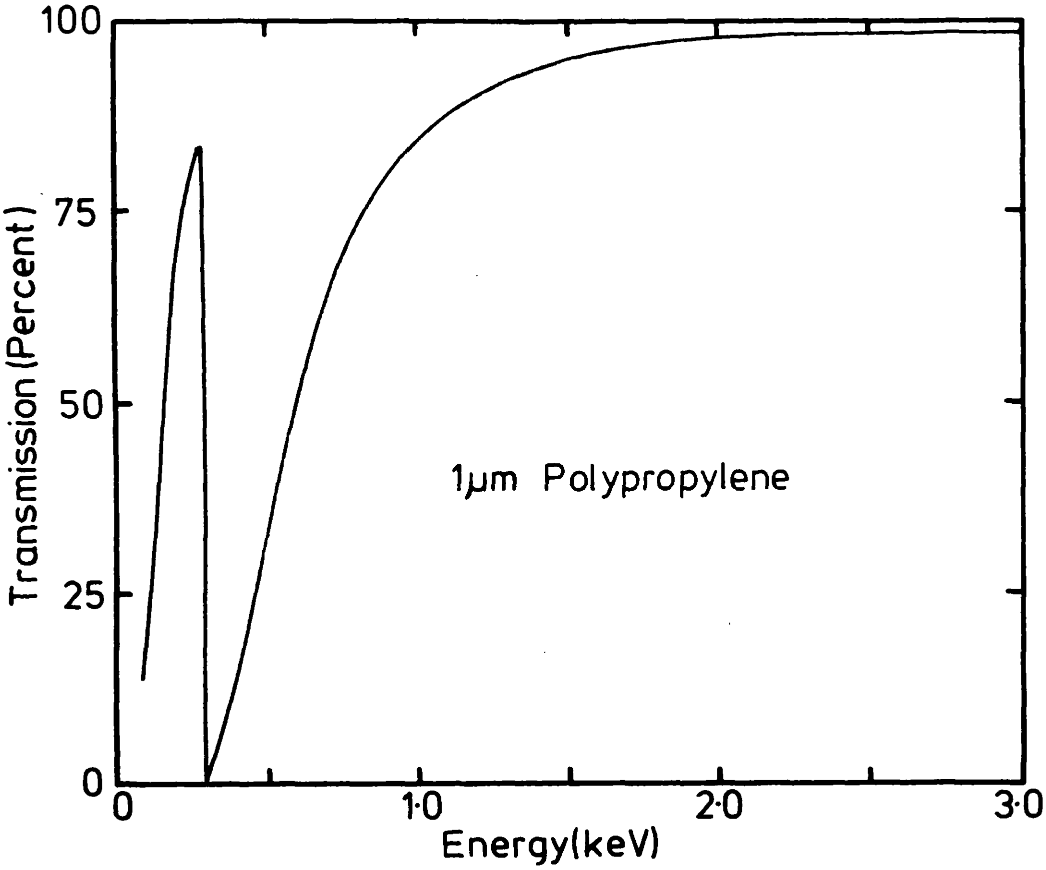

3.12. Transmission of a 1 μm thick polypropylene window as used on the VTF proportional counter.

Gas leakage through the proportional counter window will limit the pressure attainable in the vacuum system (Section 3.3.4).

3.6.2. Proportional counter design and construction

An existing proportional counter design was adapted for use in the VTF. A 40 mm absorption depth was provided to allow for the detection of high energy ($\lesssim$ 8 keV) X-rays.

The detector body was machined from a block of stainless steel with two gas flow pipes providing the mechanical mounting (Fig.3.13). The 25 μm diameter tungsten anode wire is supported by two glass-to-metal seals. Protection from mechanical damage and electrical interference is provided by two stainless steel cans (shown on plan view, Fig.3.13(b)).

The design of the window assembly was chosen to give leak free operation and allow easy replacement of windows. The window should be able to accept all the incident X-ray beam, with an allowance for small errors in position of the counter with respect to the X-ray beam. From Table 3.3(b) the largest X-ray beam diameter at the proportional counter is less than 3.4 mm and therefore a window diameter of 10 mm was chosen. A larger window would have been possible but this would have increased the leak rate from the detector and produced a poorer ultimate vacuum.

The window support structure consisted of a thin stretched stainless steel mesh sandwiched between a 1 mm stainless steel plate and a thin (0.1 mm) Cu-Be annulus. A carbon coated stretched polypropylene window was then glued to the Cu-Be using Evo-Stick. This assembly was sealed to the counter body by clamping it to a viton 'O' ring with the lid. The 'O' ring seals against the window material to reduce the possibility of small leakage paths existing between the window and the Cu-Be. When in place the carbon coating (Section 5.3.1) on the inside of the window makes contact with the proportional counter body. This earths the window and prevents gain variations occurring because of window charging.

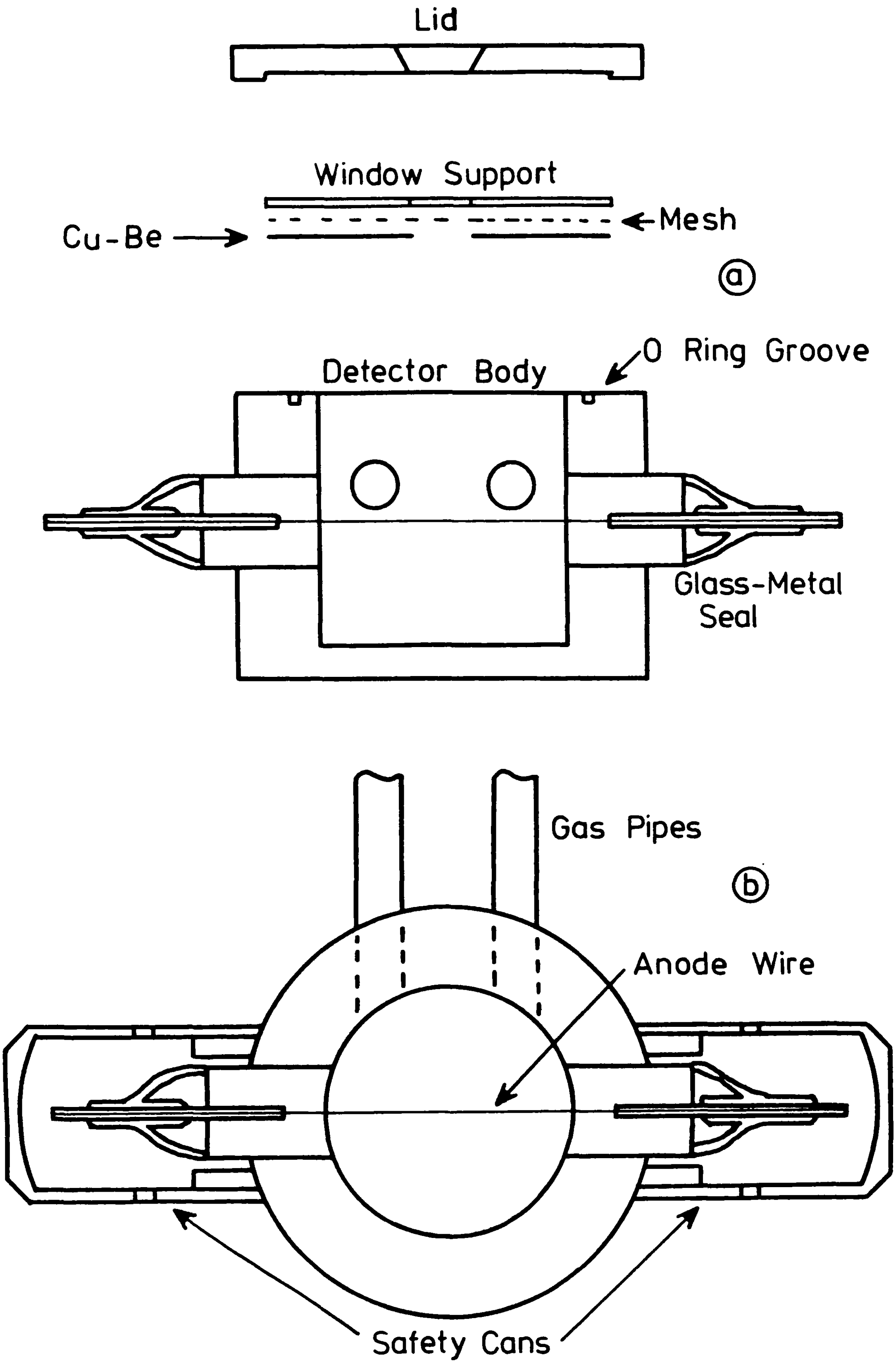

3.13. Schematic sectional view of the VTF proportional counter
(a) Side view showing window support and lid.
(b) Plan view showing protective cans for the glass-metal high voltage feedthroughs.

The proportional counter was moved in and out of the beam line by a pneumatically operated edge-welded bellows system. Sufficient travel was provided to allow for the installation of a gate valve (Section 3.4, Fig.3.4).

High voltage was supplied to the proportional counter via a stainless steel conductor mounted on a ceramic feedthrough. This was connected to the anode wire with a short length of coaxial cable. A machined PTFE block was used to support the stainless steel conductor.

3.6.3. Proportional counter operating techniques and performance

The proportional counter was originally operated using P10 gas (90% argon, 10% methane), a mixture which proved quite adequate with both Cu-L (0.93 keV) and Al-K (1.49 keV) X-rays. The output PHD (gain and FWHM) was consistent with that produced by similar detectors and the background noise was low (~ 1 count per second). The PHD at C-K (0.28 keV) X-rays, however, was very broad and quite unacceptable (Table 3.4).

Table 3.4

Comparison between using P10 and P50 in the proportional counter. Absorption coefficients calculated from basic atomic data[118]

		FWHM (%)		Depth at which 99.9% of X-rays are absorbed (mm)	
Line	Energy (keV)	P10	P50	P10	P50
Al-K	1.49	42	-	37	59
Cu-L	0.93	58	60	11.0	16.5
C-K	0.28	120	70	0.78	1.32

When the operating gas was changed to the less dense P50 (50% argon, 50% methane) the FWHM was reduced from 120% to ~ 70% - a much more reasonable figure.

The most probable explanation for these observations is the "window" or "wall" effect [110]. This occurs when a significant number of interactions occur very close to the boundaries of the detector, causing some fraction of the liberated charge to be intercepted by the detector body rather than being multiplied and collected on the anode wire. The counter gain will be reduced for such events, broadening the FWHM of the output distribution. In a severe case, the gain may be reduced so much that the event is lost below the lower level discriminator

An attempt was made to calculate the magnitude of the window effect for the VTF proportional counter. The range of the photo or Auger electron released by the incoming X-ray is very difficult to calculate for these energies and only empirical formulae exist. The formula used by Bateman et al [111] was developed for high energy electrons (~ MeV) in aluminium and therefore a very approximate formula [58] devised for use with low energy electrons in gases was used. The range, R_p , in microns is given by:

$$R_p = 44\ E_o^{1.7} \rho$$

where E_o = energy of photo electron in keV

ρ = density of gas in grams per litre.

The calculated ranges for electrons produced by C-K (0.28 keV) X-rays are; R_p (P50) = 4 μm, R_p (P10) = 3 μm. The depths at which 1% of the incoming X-rays are absorbed are, P50-0.3 μm, P10-0.5 μm. These results are in qualitative agreement with experiment since they show that charge is more likely to be lost in the P10 gas mix than in P50. The figures also suggest that a small fraction of the incoming X-rays may produce very low gain events and hence fall below the lower level discriminator.

Examination of C-K PHD's produced in P50 indicates, however, that the wall effect is not important for the present application. The FWHM may be affected to a certain extent but there is no evidence for an excess of low charge level events which would signify counts being lost below the lower level discriminators. Estimates based on the observed PHD indicate that $\lesssim 0.5\%$ of events are lost in the electronics. This does not compromise the suitability of the proportional counter as a reference detector. A typical C-K (0.28 keV) PHD is shown in Fig.3.14.

The wall effect is also potentially important at the top of the energy range (~ 3 keV), where there is insufficient path length to absorb all the X-rays within the counter. As for the low energy X-rays this can reduce the counter gain for X-rays absorbed close to the walls. There is no evidence of events being lost beneath the lower level discriminator, however, and so the wall effect can again be neglected.

Those X-rays that pass through the gas are absorbed by the stainless steel walls of the detector. The low photoelectric yield of metals means that these X-rays are not detected and the proportional counter becomes less than 100% efficient.

Several authors [112,113] have "tuned" their proportional counters, by adjusting the type and pressure of the operating gas, to give detectors which only absorb 85-95% of the incident X-rays. This has been partially to improve the energy resolution of the detectors. Since energy resolution is not a factor for the VTF detector, and there is no evidence of "lost" counts, the only changes made in the VTF proportional counter involved the operating gas (P10 and P50). Table 3.5 gives a summary of the proportional counter operating characteristics.

The observed PHD at the three higher energies is degraded compared to expectation. Some of this degradation may be due to multiple line combinations, e.g. Nb-L and Ru-L, but it is also observed that the PHD degrades with count rate. This is a strong indication that window charging is taking place, possibly because the carbon coating on the window is too thin. This would significantly impair the energy resolution of the proportional counter but the effect is not significant for the present purpose.

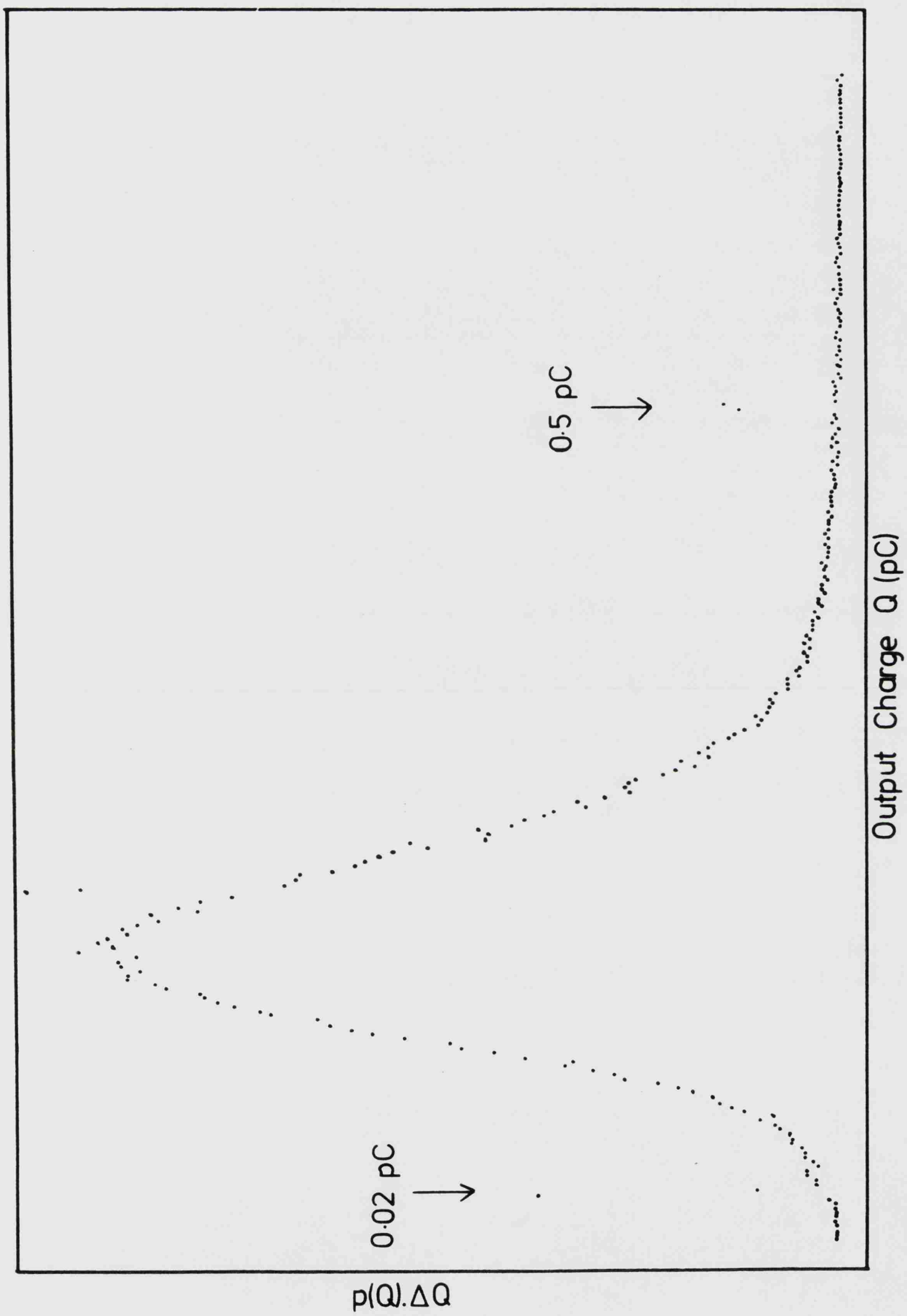

3.14. Typical proportional counter PHD from C-K (0.28 keV) X-rays using P50 gas. Gain markers were obtained by injecting charge into the preamplifier via a capacitor. No correction has been made for differing signal time constants.

Table 3.5

Proportional counter operating characteristics.
Window support mesh transmission constant (≈ 46%).
For derivation of gas detection efficiency see Section 5.3.

Line	Energy (keV)	Gas detection efficiency (%)	Typical FWHM (%)	Operating gas
B-K	0.18	100	-	P50
C-K	0.28	100	82	P50
Cu-L	0.93	100	73	P10
Mg-K	1.25	100	49	P10
Al-K	1.49	100	44	P10
Si-K	1.74	99.2	45	P10
Nb-L	2.28	89.3	52	P10
Ru-L	2.68	76.4	56	P10

Window charging may also be the cause of an observed increase in the FWHM of the C-K PHD from 70% to 82%. This effect occurred over a period of a few weeks during initial operation of the PC. No further degradation has occurred.

3.7. MCP Detector Interface and Transport Assembly

The MCP detector interface and transport assembly (ITA) must provide rotational and translational movement, together with high voltage and signal feedthroughs. The structure should be simple, sturdy and as compact and adaptable as possible.

For ease of operation the whole assembly including MCP detector was designed to be removed from the VTF in one piece and disassembled in the lab. To achieve this all feedthroughs were mounted on a single vacuum flange (Figs.3.15,3.16). Linear motion of ± 25 mm about the centre is available together with a rotation of $\pm 60°$.

The detector rotation is limited by the electrical connections; the rotary drive being a direct drive 360° rotation device. The drive is rather coarse. Although it is possible to read the angular scale to ± 0.1-$0.2°$, for repeatable measurements to 0.1° accuracy it is inadequate. To achieve such accuracy a more complex drive system would be required.

The ITA also provides two seven-way instrumental feedthroughs and six high voltage feedthroughs. This allows six possible detector high voltage levels to be varied independently from outside the tank. The instrumental feedthroughs serve to connect the GD electrodes to the preamplifiers which are outside the vacuum system (Section 3.8).

All electrical connections inside the vacuum system were made using PTFE insulated cables which are long enough to absorb the possible amount of rotation and translation.

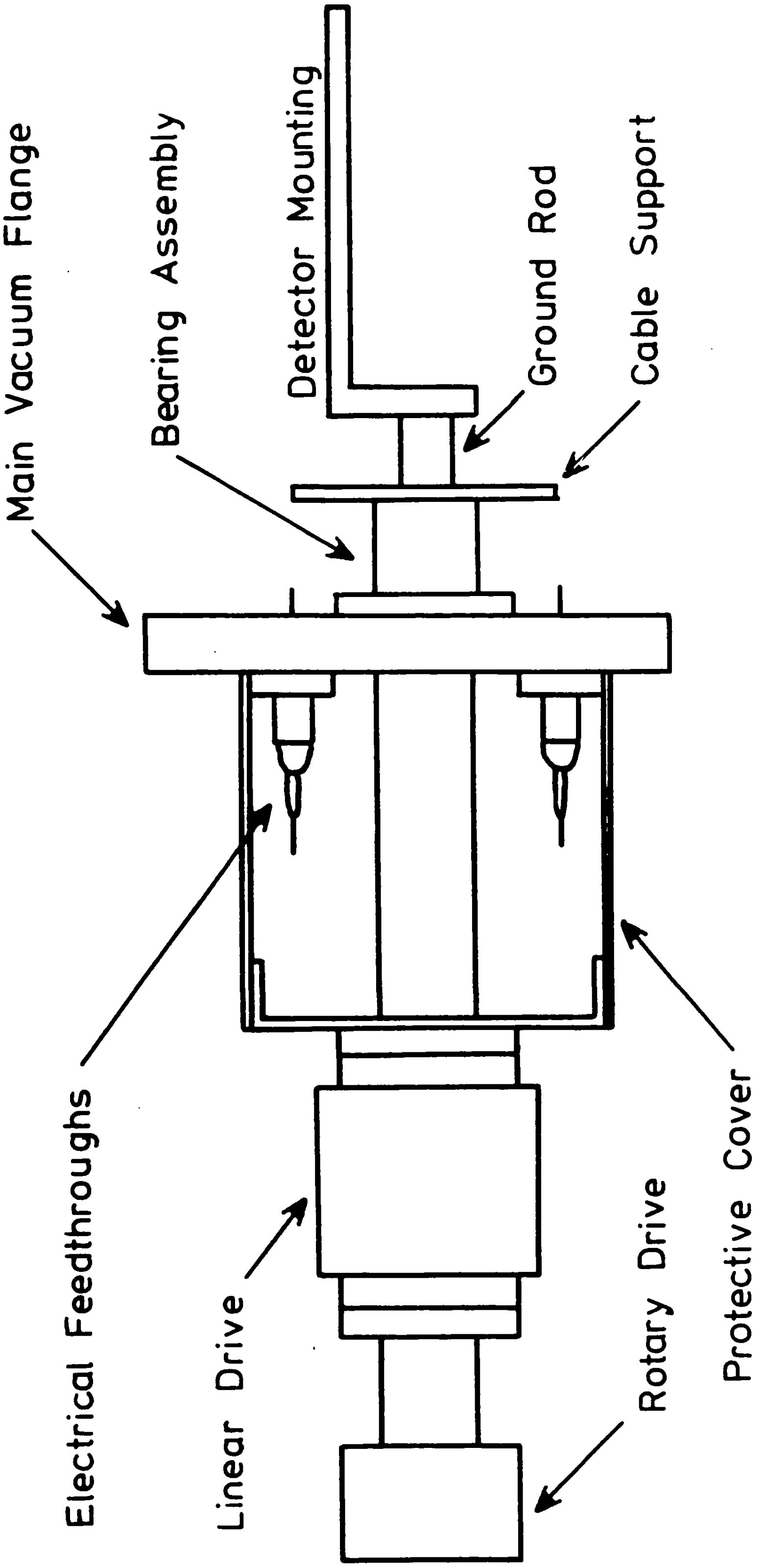

3.15. Schematic view of the MCP detector interface and transport assembly.

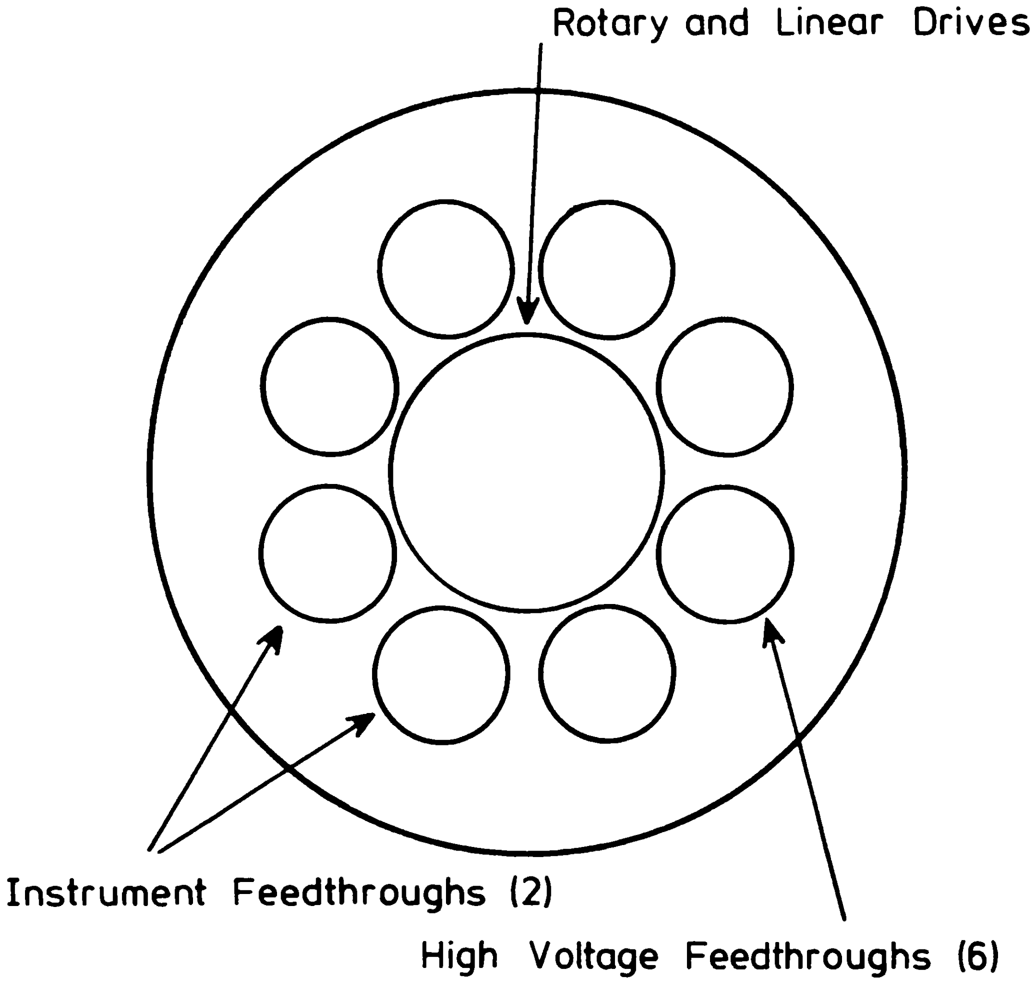

3.16. Feedthrough locations on the main vacuum flange of the ITA.

3.8. Electrical and Electronic Systems

3.8.1. Preamplifier location

To produce two dimensional images using GD electrodes four charge sensitive preamplifiers must be used (Section 2.2.2). To provide low noise operation these preamplifiers must be located as close to the GD electrodes as possible. It must be decided if the preamplifiers should be placed inside or outside the vacuum system.

If the preamplifiers are located inside the vacuum chamber they will need only short connections to the GD electrodes, giving low capacitive loading and hence low intrinsic noise levels. They will also be protected from externally generated radiative interference. This situation would be ideal if extremely low noise operation was needed, e.g. for high resolution imaging.

Disadvantages are that preamplifiers are inaccesible and may cause contamination of the vacuum chamber. Additional space within the chamber must also be provided to house the preamplifiers.

With preamplifiers outside the vacuum chamber the longer cables between them and the GD electrodes will give a higher capacitive loading and hence an increased intrinsic noise. They will also be susceptible to the pick up of external radiative interference. The great advantage is that the preamplifiers are accessible and can be tested and repaired without disturbing the vacuum system.

Consideration of Section 3.1 shows that externally situated preamplifiers are preferable for the VTF, provided that the resultant noise count rate can be reduced to acceptable levels.

A separate charge sensitive preamplifier is also used for the proportional counter, and similar comments apply.

3.8.2. Electrical connection of external preamplifiers

Typical lower level thresholds for each MCP preamplifier are ~0.02-0.03 pC, giving a threshold for the total pulse size of ~0.08-0.12 pC. These thresholds are well above the intrinsic noise level of even basic preamplifiers (3000 electrons rms) and so the only consideration is the pick up of external electrical interference. Since in practice detector counts will be integrated for 30 second periods the noise level must be stable and preferably very low over successive periods.

Initial connection of the preamplifiers using coaxial cable outside the vacuum chamber, plain cable inside and with the detector body earthed to the vacuum chamber proved unsatisfactory. Bursts of several hundred counts were recorded at irregular intervals, with some of the counts being well over 0.5 pC in magnitude. An actual measurement using a 0.025 pC threshold gave 3469 counts in 60 minutes, approximately 1 count per second. Only 2 counts were recorded in the last 11 minutes, however, showing that it was not possible to average the noise out.

There was no single identifiable source of this noise; most of the electrical equipment in the Physics Building contributing. This made suppression of the noise at source impractical and so the only solution was better shielding at the preamplifier and detector.

The configuration finally adopted for the VTF is shown in Fig.3.17. In this configuration the MCP detector body was isolated from the vacuum system earth by PTFE spacers. Typical results, using a 0.025 pC threshold, gave 161 counts in 14 hours, with the largest recorded burst being 10 counts. Such performance was quite adequate for the VTF.

The configuration of Fig.3.17 would also be the preferred connecting system for the proportional counter. The method adopted to support the proportional counter (Section 3.6.2) precludes the possibility of isolating the detector body from vacuum system earth. Fortunately by shielding the ends of the anode wires with metal cans (Fig.3.13(b)) and the use of a

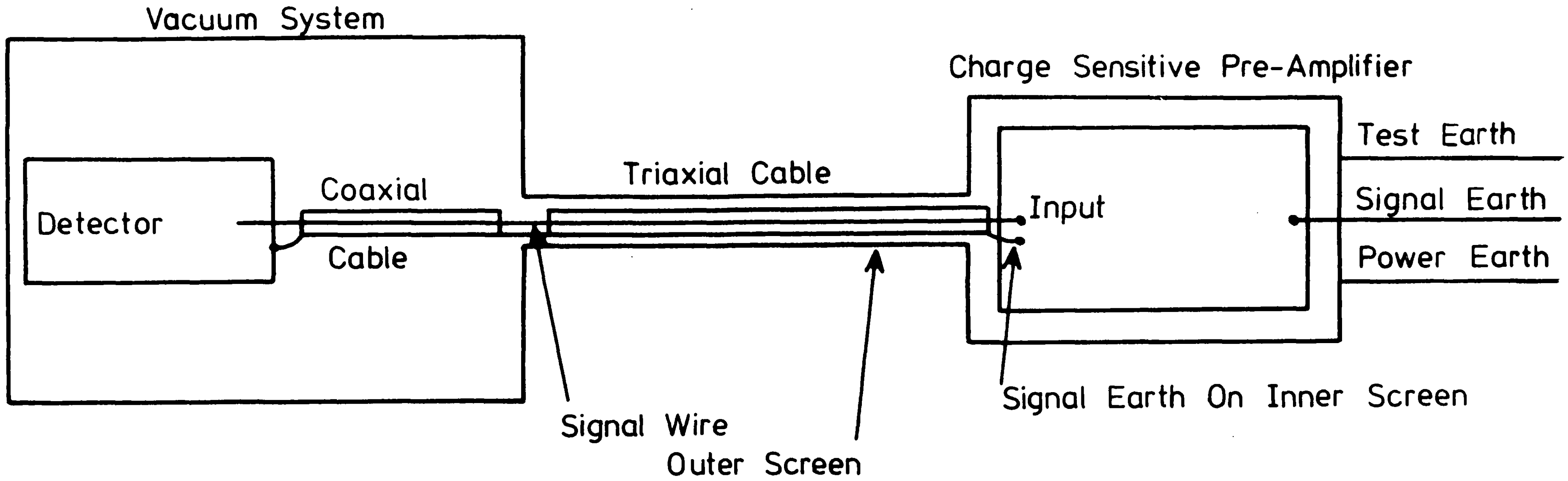

3.17. Schematic diagram of the optimum method of connecting an external preamplifier to a detector readout element.

short length of coaxial cable to connect the anode wire to the stainless steel feedthrough, satisfactory PC operation was achieved. The external connection to the preamplifier used double screened coaxial cable rather than triaxial. Induced noise over a 0.02 pC threshold was negligible.

3.8.3. Pulse counting electronics

A block diagram of the processing electronics is shown in Fig.3.18. The signals from the four MCP charge sensitive preamplifiers are fed through an interface module to a fast summing amplifier and hence to a unipolar shaping amplifier of 1 μsec time constant. These signals are then fed to an Ortec Single Channel Analyser (SCA). The output of the SCA is then taken simultaneously to an Ortec counter and overflow counter, a ratemeter and an Ortec counter-timer, counter combination. This allows up to 10^{12} accumulated counts to be recorded while a check can be kept on the instantaneous count rate at the same time as recording the number of counts arriving in various preset intervals.

Signals from the proportional counter are processed by a similar chain and counted using the same electronics. This involves changing the input cable to the SCA. The counter recording accumulated MCP counts is switched off while the proportional counter is connected. This does not invalidate the accumulated count since only noise counts are lost and these represent an insignificant part of the total count.

System calibration is provided by feeding a known voltage pulse into a known test capacitor (1 pF) on each preamplifier, thus allowing the electronics to process a signal of known charge level.

The PHD produced by either the MCP or proportional counter can be collected and analysed on a Canberra series 30 multi-channel analyser and printed out using an analogue graph plotter.

There is no requirement in X-ray astronomy for very high count rate capabilities and so no exceptionally fast electronics are needed. All

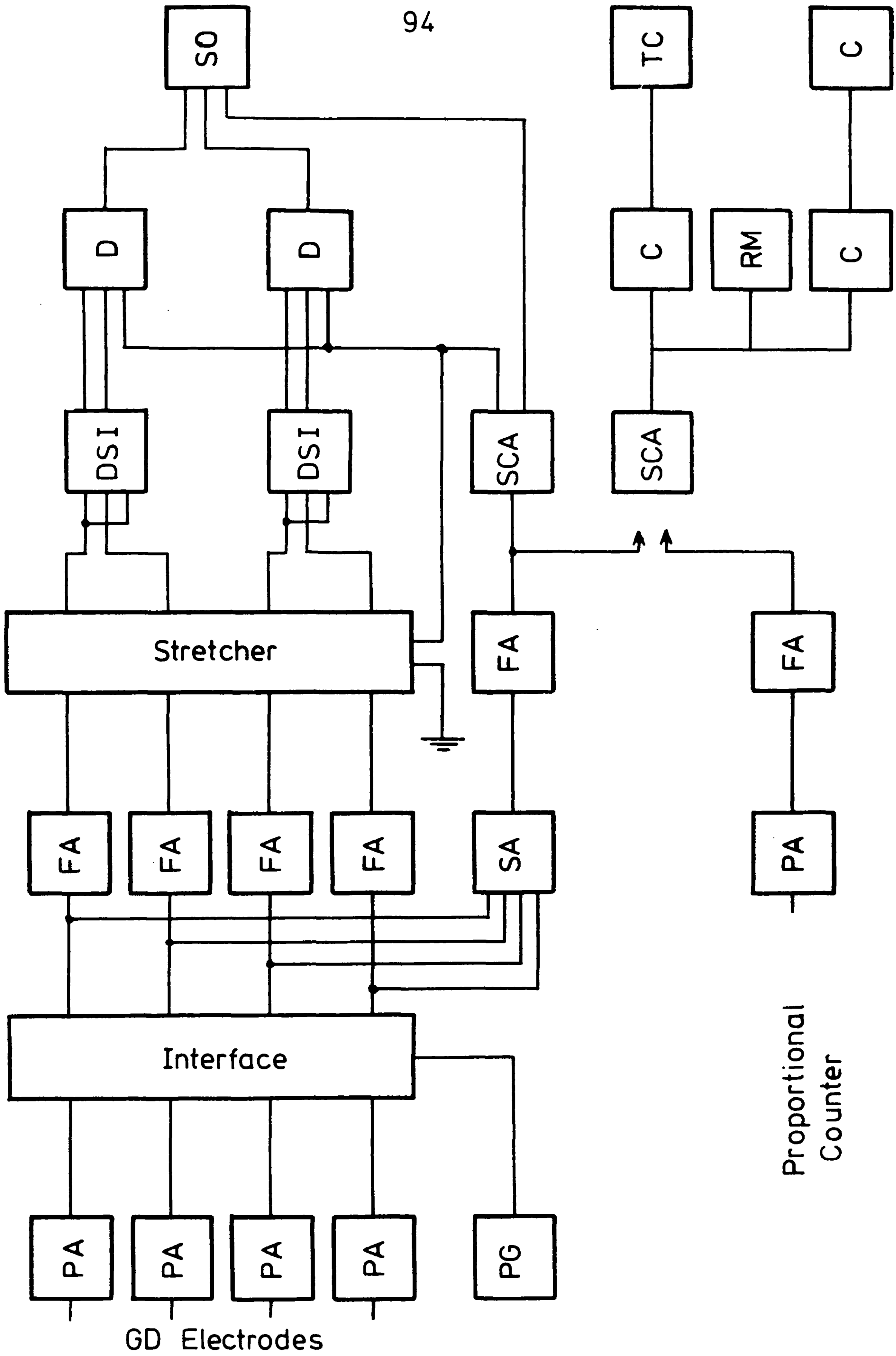

3.18. Block diagram of signal processing electronics. PA - Preamplifier, FA - Filter amplifier, PG - Pulse generator, SA - Summing amplifier, DSI - Dual sum and invert, D - Divider, SO - Storage oscilloscope, SCA - Single channel analyser, C - Counter, TC - Timer counter, RM - Rate meter.

units are NIM standard devices.

3.8.4. Imaging electronics

The imaging electronics used (Fig.3.18) is an analogue system developed at Leicester and is relatively simple with many limitations. A usable image is produced, however, and allows the position of the X-ray beam to be determined and aids the location and diagnosis of excess noise.

The preamplifier signals are fed into four bipolar shaping amplifiers of 1 μsec time constant. The resultant signals are then stretched and fed in pairs into a dual sum and invert unit (one for each axis). Each unit produces two signals which are the inverses of q_A and q_A+q_B (Section 2.2.2) for the X and Y axes. Amplitude ratio units then produce the ratio $\frac{q_A}{q_A+q_B}$ to give the X and Y coordinates of the event. These signals are then displayed on a storage oscilloscope.

This system will only work reasonably over a restricted dynamic range of 15-20. A special SCA is therefore used to gate the two ratio units and provide a bright up signal for the storage oscilloscope.

3.8.5. High voltage production and measurement

Operation of MCP chevron detectors require high voltage power supplies which can deliver up to 5kV . As less than 5 μA is drawn in normal operation standard NIM type units are ideal.

Measurement of the actual current flowing through each MCP is accomplished by using 2 digital, battery powered, ammeters which are floated to the same potential as the MCP. These provide measurements accurate to ± 0.01 μA.

The voltages applied to the MCP's are determined using a voltage divider (Fig.3.19). A resistor-capacitor filter network is provided to smooth out any supply irregularities. An accurately calibrated chain of high stability resistors provide a reduction ratio of 1000:1. A digital

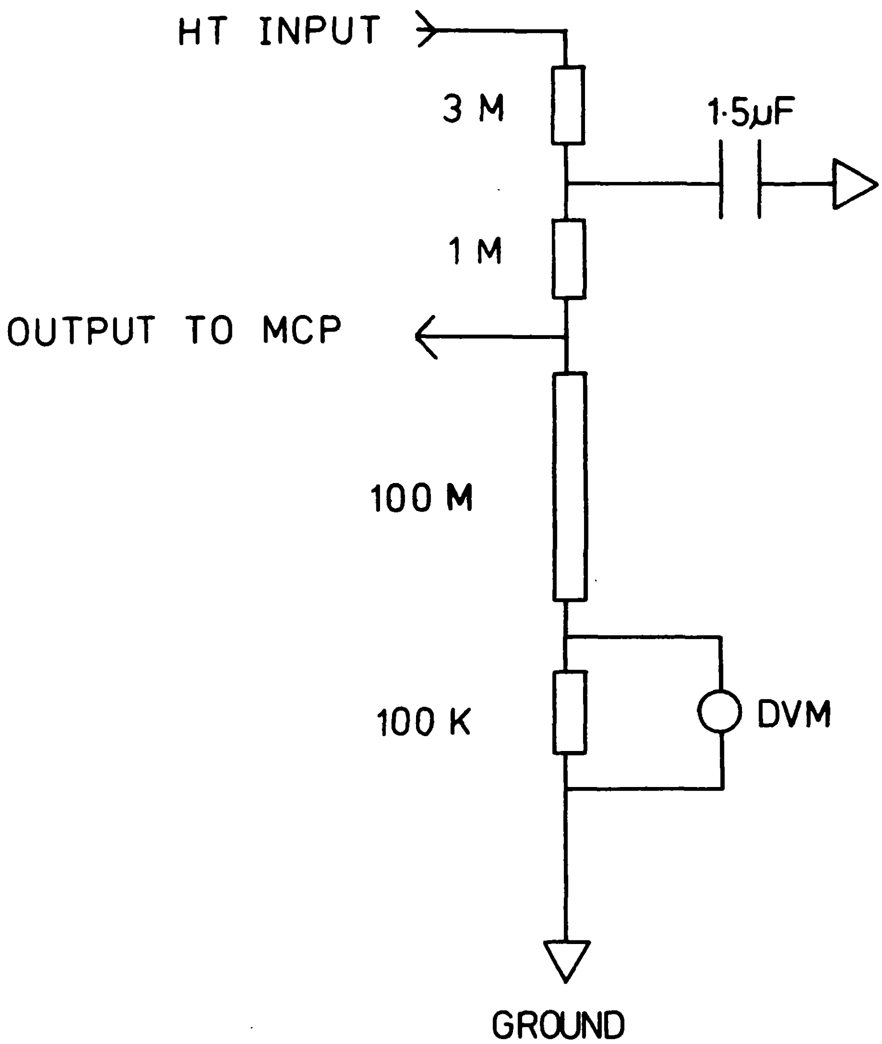

3.19. Schematic diagram of voltage measuring system using a resistor dividing chain.

voltmeter is then used to measure the 0-5 V output from the chain.

3.8.6. Mains power and VTF earth

All mains power to the VTF was filtered using a high quality RF interference filter. This was found to be necessary to stop the detectors picking up mains borne interference. Power to selected systems was supplied through high power relays. This allows the system to "fail safe" in the event of equipment malfunction, vacuum failure or power failure. In particular high voltage can be automatically removed from the detector if the pressure rises above a preset limit.

When earthing the VTF two things had to be considered. (1) Safety. (2) Detector noise. The ideal situation is to have each item earthed independently to a central point which is solidly bonded to earth [114]. This was not consistent with the requirement of safety, however, as for practical reasons the VTF itself must be the central earthing point, and to produce an ideal pattern would require disconnecting mains earth wires. In practice this does not cause a problem with the VTF. The metal of the vacuum system was also connected to the main earth separately, and hence was not solely earthed through mains powered equipment connected to it.

For minimal noise, detectors should be earthed through the electronics (see Section 3.8.2).

CHAPTER 4

DETECTOR OPTIMISATION

4.1 Effect of an Interplate Gap Bias Voltage

As mentioned in Section 3.2 the VTF MCP detector was normally operated with a "double-sided" middle electrode, which separated the two MCP's by 160 μm and allowed potentials of up to 600 volts to be applied between the rear of the front MCP and the front of the rear MCP. This can substantially improve the PHD by increasing the level of saturation in the rear MCP and thus reducing the FWHM. This is illustrated in Figs.4.1(a,b) which show the variation of peak gain, G_c , and FWHM, $\Delta G_c/G_c$ with accelerating interplate bias voltage V_G . (Fig.4.2 illustrates the proportion of counts within $\pm\delta G_c$ of the peak (as discussed in Section 2.3.1) for the same data set as Fig.4.1.) An improvement in the PHD FWHM is also observed if a chevron is operated with a (160 μm thick) double sided electrode rather than a thin single electrode. A chevron (L:D=120:1, $V_F=V_R=1550$ volts) operated with $V_G=300$ volts produced a gain $G_c=4.1$ pC and a FWHM=68%. When operated with a 38 μm thick single electrode the same detector had a gain $G_c=2.8$ pC and a FWHM=137%.

The results of Figs.4.1(a,b) can be interpreted [38,49,116] in terms of a reduction in the number of channels, N_c , in the rear MCP excited by the output charge cloud from a single channel in the front MCP. From ref.[38] we have:

$$G_c = G_F^{1-\alpha}\ G_R\ N_c^{\alpha}$$

G_F and G_R are the single electron gains of the front and rear MCP's respectively and G_c is the chevron peak gain as before. α is a parameter which depends on channel diameter, D . ($\alpha \simeq 0.6$ for the D=12.5 μm MCP's used here [38]).

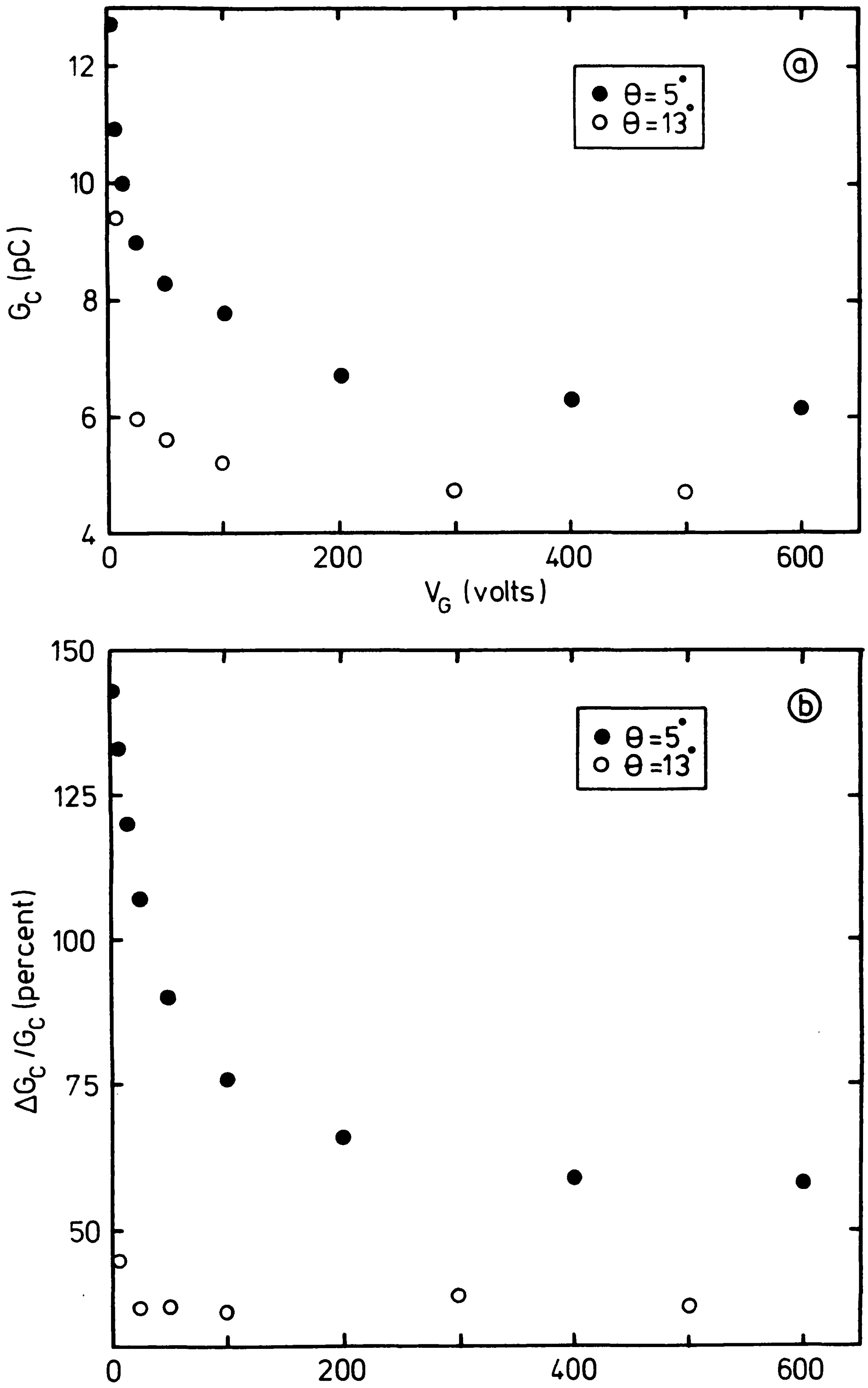

4.1. (a) Variation of gain, G_C, with interplate bias voltage V_G.
(b) Variation of FWHM, $\Delta G_C/G_C$, with interplate bias voltage V_G. C-K (0.28 keV) X-rays incident at θ=5° (filled circles) and θ=13° (open circles) MCP chevron, both MCP's L:D=120:1, D=12.5 μm. Interplate gap 160 μm.

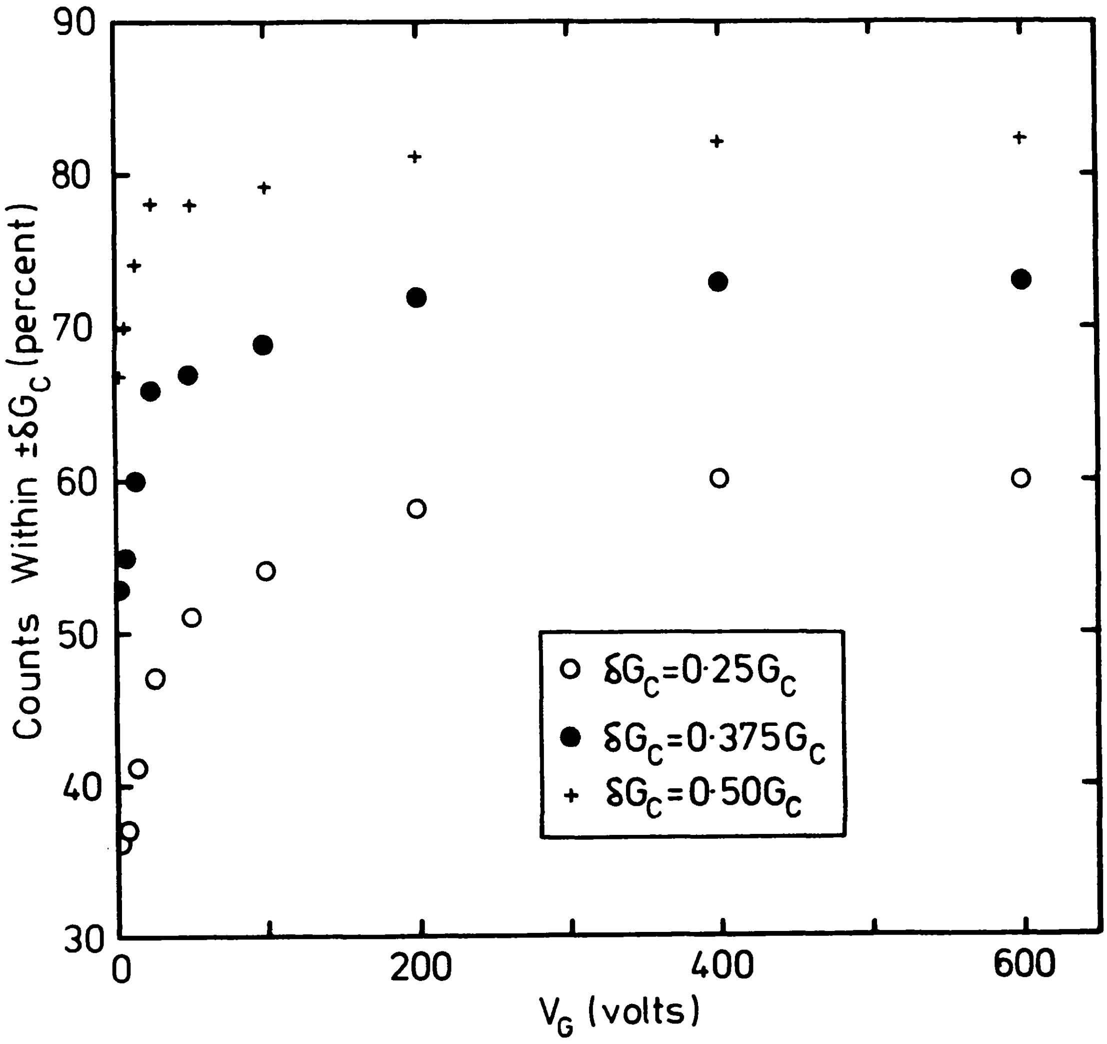

4.2. Variation with interplate voltage, V_G , of the fraction of counts which lie within a given interval, $\pm\ \delta G_C$, about the peak G_C , of the PHD's reported in Fig.4.1 (θ=5°). Open circles δG_C=0.25 G_C , filled circles δG_C=0.375 G_C , crosses δG_C=0.50 G_C .

The applied accelerating electric field reduces the transit time of the charge cloud between the two MCP's, hence limiting its lateral spread, reducing the value of N_c and hence reducing G_c. Values of N_c can be calculated using Equation 6 of Ref.[38]. This equation gives $N_c \approx 25$ when $V_G = 3$ volts and $N_c \approx 4$ when $V_G = 600$ volts. A smaller FWHM would be expected at high values of V_G as the same number of electrons are entering fewer channels. This increased level of stimulation will produce saturation closer to the input end of the channel and give a more stable multiplication process.

There is a significant variation in the energy of the electrons [60] as they emerge from the front MCP. Distinct high energy (100-300 eV) and low energy (~ 10 eV) peaks are observed in the energy distribution curves of the output electrons (peak position varies with emission angle relative to the channel axis). The accelerating potential, V_G, increases the average energy of the electrons incident on the rear MCP and allows them to be detected with maximum efficiency [117]. This increased electron detection efficiency will again increase the level of saturation and thus reduce the FWHM.

Another possible, although marginal effect, is the reduction in the spread of electron transit times across the interplate gap. With no applied electric field the transit times for electrons of 5 eV and 600 eV (limiting values from [60]) are 120 psec and 11 psec respectively. Since the multiplication time for the whole detector is of order 1 nanosecond [73] this time difference may be significant. Electrons arriving after the initiation of an avalanche will encounter a channel of much reduced gain because of the finite recovery time of an MCP [1]. Such electrons will therefore have only a small effect on the overall gain, but this may be sufficient to produce a broadening of the FWHM. The applied electric field will reduce the time spread between the arriving electrons and hence cause the rear MCP to produce a more well defined pulse height.

Fig.4.1(b) shows that the effect of V_G depends on the incident angle of the input radiation. Much lower values of V_G are required to achieve the plateau value for the FWHM when $\theta=13°$ than are needed when $\theta=5°$. This can be explained in terms of the lower degree of saturation in the front MCP which is produced by X-rays interacting further down the channel, because of X-ray reflection and a longer length of illuminated channel (Section 2.3.2.). The poorer PHD's obtained at low angles will correspond to a relatively higher proportion of high energy electrons in the output charge cloud because the channel is not fully saturated [38]. Higher interplate gap voltages are therefore required to produce the limiting charge cloud diameter on the rear MCP. There will also be an even larger range of transit times and again larger voltages are required to reduce them.

The results of Figs.4.1(a,b) are similar to those of Wiza et al [49], obtained using positive ions. The PHD FWHM's shown in Fig.4.1(b) are somewhat smaller than these reported in Ref.[49] but this can be explained in terms of the L:D ratios of the respective MCP's (L:D=120:1 for Fig.4.1, L:D=40:1 for Wiza et al). The larger L:D ratio MCP's will intrinsically produce a higher degree of saturation and hence a smaller FWHM.

The results presented by Rogers and Malina [116] show a very different variation; with G_c increasing as V_G increases. The MCP's used had L:D values of 50:1 and they would therefore be expected to produce similar results to these reported in Ref.[49]. The basic gain of the detector described in Ref.[116] is, however, a factor of 10 lower than the gains of Ref.[49] and Fig.4.1(a), and even the best FWHM values obtained were very large (270%). This indicates that the detector was being operated with a very low bias voltage and hence was probably not saturated. The behaviour of the FWHM is qualitatively the same as shown in Fig.4.1(b) and Ref.[49].

Use of an interplate accelerating voltage allows very narrow FWHM's to be obtained under optimum conditions. Such a voltage is most useful, however, when the system characteristics are such that the MCP's cannot be operated in a fully saturated mode, since under these conditions the possible improvements in FWHM are much more significant. This is illustrated in Fig.4.1(b), where a much larger decrease in FWHM is obtained with $\theta=5°$ than $\theta=13°$. An interplate bias voltage is therefore potentially very important for any AXAF MCP detector because of the very small X-ray incidence angles, $\sim 2.5°$ (Table 1.1). Non-saturated operation could also occur if the voltages applied to the MCP's were limited by the onset of noise.

4.2. Plano - Concave MCP

4.2.1. Description

As noted in Section 1.4 the focal planes of all grazing incidence X-ray telescopes are curved. A sensitivity advantage therefore accrues to any telescope incorporating a detector curved to match its focal plane. No such imaging detector has been produced to date. Curvature would be very difficult to achieve with IPC's and GSPC's. Over a large field of view, it would be possible to approximate a curved surface by using a mosaic of detectors, each having a flat input face, but this would produce dead spaces along the detector boundaries. A MCP detector is one imaging device that could conceivably be curved using existing glass working techniques. In the case of the ROSAT WFC (Section 1.4) a detector spherically curved with a radius of 165 mm, confers a sensitivity advantage of $\sim$ 2.5 times, compared with a flat detector in focus at the centre of the field of view [118]. The possibility of producing a curved surface MCP for use on the ROSAT WFC was therefore investigated.

Five surfaces need to be examined when considering a MCP chevron as a curved surface detector; the four MCP surfaces and the readout plane.

The front surfaces of the front MCP must be curved to match the focal plane. It is important to discover what consequences this has for the slope of the other four surfaces.

The simplest solution mechanically, would be to produce a chevron with a normal (i.e. flat) rear MCP and readout element and a Plano - Concave (P-C), (i.e. curved front surface, flat rear surface) front MCP. The feasibility of such a detector was investigated using a 36 mm diameter MCP, with D=12.5 μm and bias angle θ_B=0°, whose L:D ratio varied from 120:1 at the centre to 175:1 at a radius of 15 mm. This was a good approximation to the required ROSAT WFC MCP which would have an L:D of 120:1 at the centre and 190:1 at the edge.

The P-C MCP was produced [119] by optically grinding and polishing the front surface, before etching out the glass cores. The shaped MCP block was then processed in the normal way.

4.2.2. Results

The P-C MCP was operated with an L:D=80:1, θ_B=13° rear MCP to form a chevron. The experimental configuration is shown in Fig.4.3. The measurements were not made in the VTF, hence the need for the movable mask to control the position of the X-ray beam. Cu-L (0.93 keV) X-rays incident at θ=13° were used for all measurements.

The PHD peak gain and FWHM was measured, for a number of voltages, at four radial positions across the plate; X_R=0, 5 mm, 10 mm and 14 mm from centre (V_G=500 volts). The results are shown in Figs.4.4(a,b). The variation in gain and FWHM across the radius of the detector, for a given voltage across the P-C MCP, is shown in Figs.4.5(a,b) (rear plate voltage V_R=1300 volts). Similar results were obtained with V_R=1400 V.

In order to produce a viable imaging detector the variation in detector output pulse size must be as small as possible (Section 2.1.1). Figs.4.5(a,b) show that for a given front plate voltage, a region of relatively uniform gain exists in the central region of

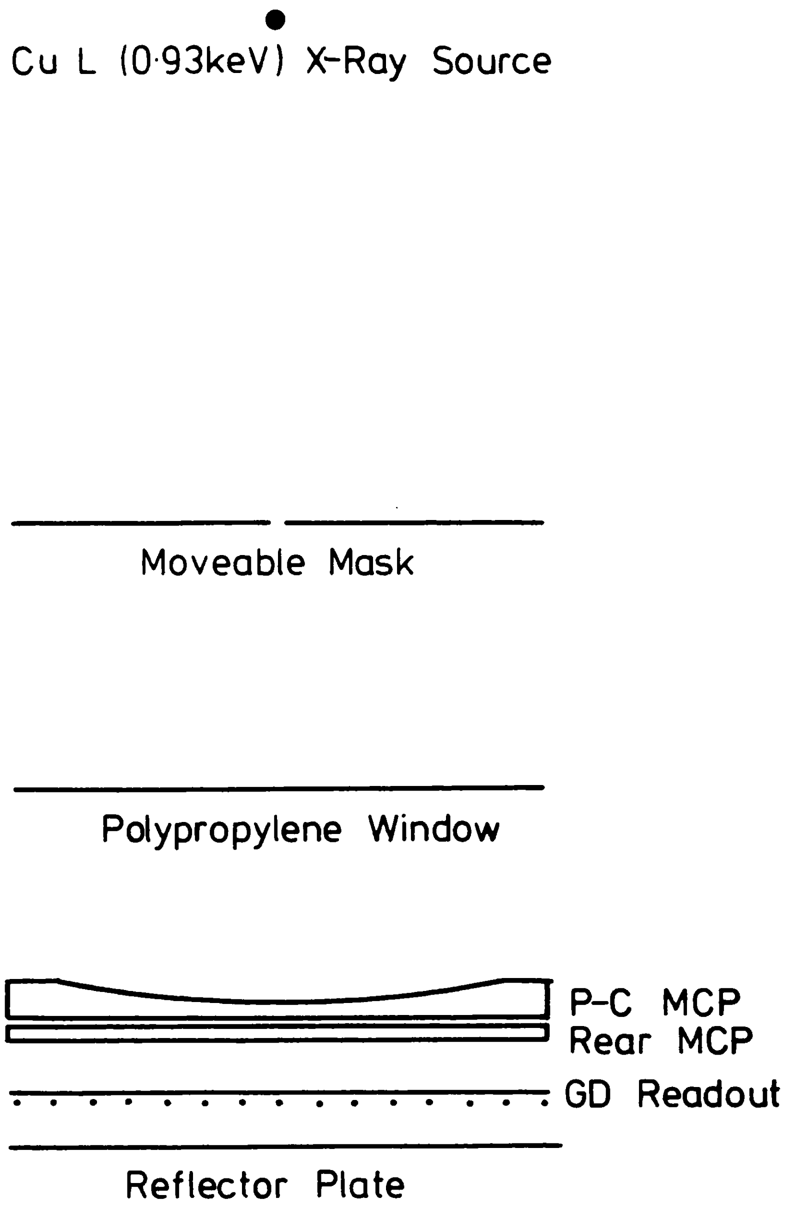

4.3. Experimental arrangement used to test the P-C MCP.

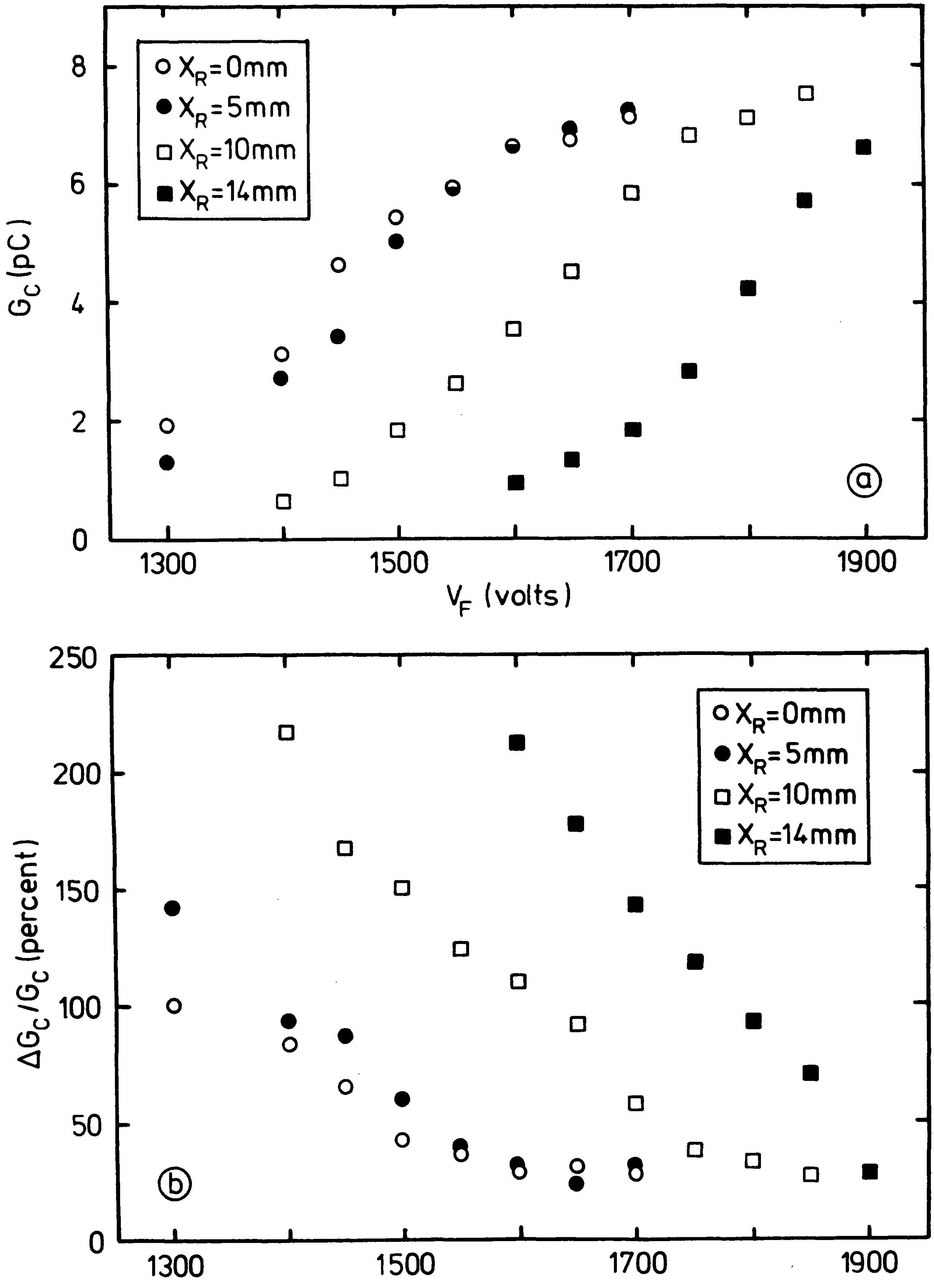

4.4. (a) Variation of gain, G_C, with voltage applied across the P-C MCP, V_F.

(b) Variation of FWHM, $\Delta G_C/G_C$, with voltage applied across the P-C MCP, V_F. Cu-L (0.93 keV) X-rays incident at θ=13°. Radial positions from centre X_R=0 mm (open circles), X_R=5 mm (filled circles), X_R=10 mm (open squares), X_R=14 mm (filled squares).

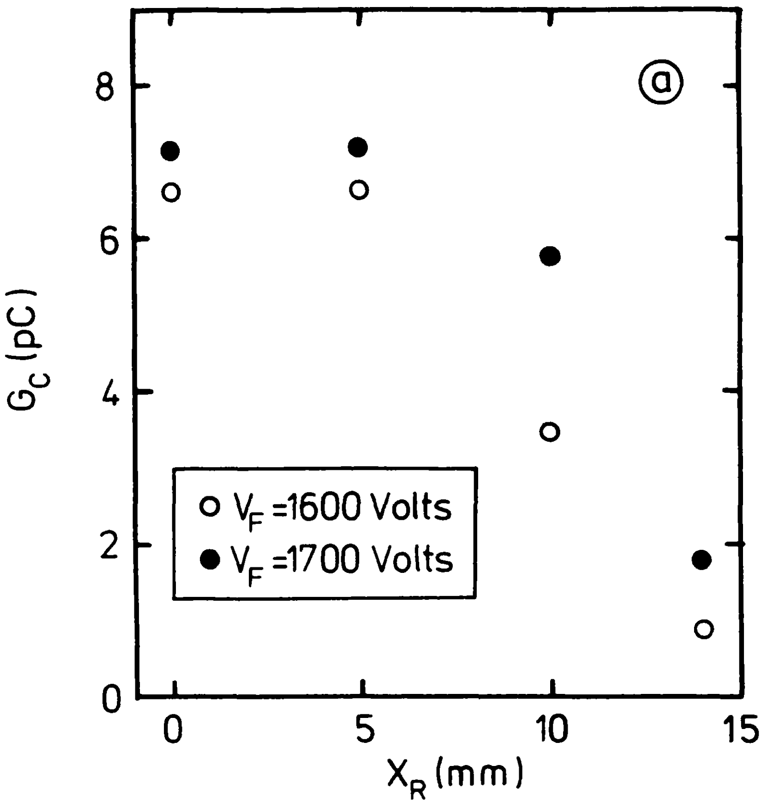

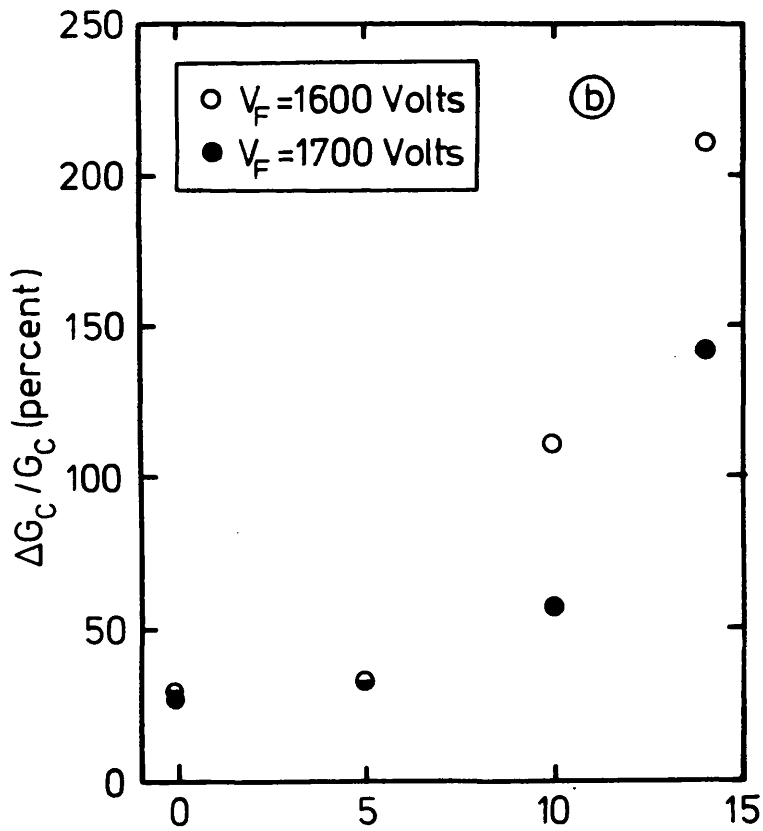

4.5. (a) Variation of gain, G_C , with radial distance, X_R , across the P-C MCP.

(b) Variation of FWHM, $\Delta G_C/G_C$, with radial distance, X_R , across the P-C MCP. Cu-L (0.93 keV) X-rays incident at θ=13°. Voltage across P-C MCP V_F=1600 volts (open circles), V_F=1700 volts (filled circles).

the P-C MCP, but that the gain falls off rapidly towards the edge. Figs.4.4(a,b) indicate, however, that with ~2000 volts across the P-C MCP its saturation characteristics would produce a relatively small radial gain variation. At these voltages, however, the shorter central channels are very badly affected by ion feedback which produced pulses approximately five times larger than normal. Fig.4.6 shows the development of ion feedback (i.e. proportion of very high gain events) at the centre of the P-C MCP (X_R=0), with increasing voltage.

These characteristics can be understood in terms of the variation of gain with L:D ratio. It is well established that gain in the linear regime is proportional to L:D [120]. Recent calculations have also shown [38] that even when saturated, the MCP peak gain , at a given voltage, will depend on the L:D ratio. This can be understood qualitatively since, for a given voltage, the longer channels have a lower accelerating electric field and hence the electrostatic balance which produces saturation, will undoubtedly be changed.

To produce a usable focal plane detector either the ion feedback must be eliminated or the saturation characteristics of the rear MCP altered. Since ion feedback is caused by the ionisation of residual gas it could, in principle, be eliminated by a combination of a better operating vacuum and a high temperature vacuum bake of the MCP's. Previous experience, e.g. the initial development of chevrons, argues that this might be difficult to achieve. There would also be the danger of a significantly reduced lifetime for the shorter central channels because of the higher levels of saturation. Practical difficulties in obtaining a suitably high vacuum together with the lifetime uncertainty, ruled out this approach.

Parameters which can be varied to alter the saturation characteristics of the rear MCP are the middle electrode gap size and voltage, and the rear MCP type and voltage. Typical results for varying V_G , and hence N_C , have been presented in Section 4.1. These show that optimum performance

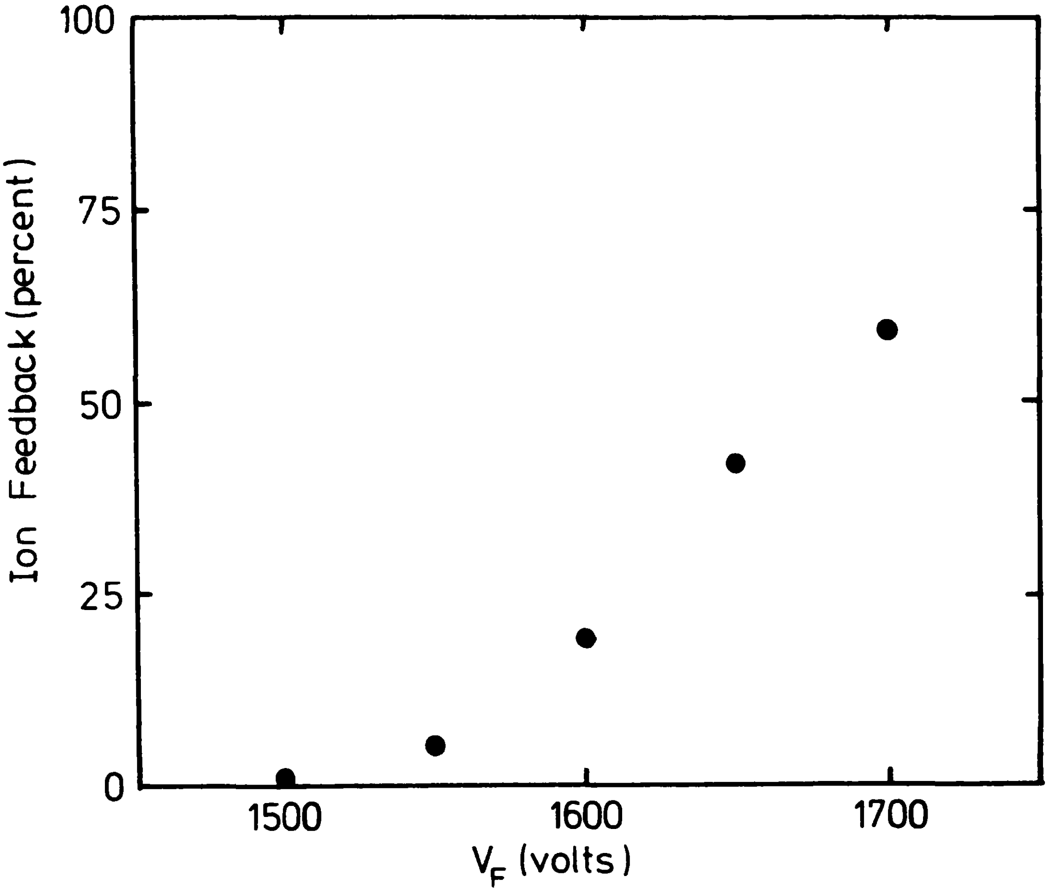

4.6. Variation of proportion of events causing ion feedback as a function of front plate voltage, V_F . Cu-L (0.93 keV) X-rays incident at θ=13°, X_R=0 mm.

is achieved with a high value of V_G , and since the results of Figs.4.4(a,b) were obtained with V_G=500 volts, no further improvements would be expected by varying the interplate spacing or voltage. This was borne out by trying middle electrodes of varying thickness.

The effect of varying V_R was to produce a linear increase in gain with voltage. There was no evidence of any plateau in the curve which could be exploited to level off the varying input from the P-C MCP. Similar results were obtained with two different (L:D=120:1) rear MCP's, data from one of which is shown in Figs.4.7(a,b). It does not seem possible, therefore, to produce a uniform gain across the P-C MCP.

The conclusion to be drawn from these results is that the P-C MCP is of no practical use for imaging X-ray astronomy. It has been shown, however, that the basic principle of using a curved input face does not degrade the performance of any individual section of the MCP. No operational problems were encountered in terms of excess noise, dead spots or electrical contact problems. The actual process of curving the MCP was found, by the manufacturers, to be easy, relatively inexpensive and not to affect the final stages of MCP processing.

The results imply that to produce a viable detector the MCP must have an approximately constant L:D ratio across the MCP diameter. To do this requires a MCP curved on both front and rear surfaces. The technique adopted for the ROSAT WFC detector was that of curving all five surfaces to avoid the possible effects of non-uniform electric fields. The final configuration consists of two MCP's in chevron configuration, with all four surfaces curved to a radius of 165 mm, and a resistive anode readout curved to the same radius. No tests have been made on this detector to date, although both curved MCP's and curved resistive anodes have been successfully manufactured.

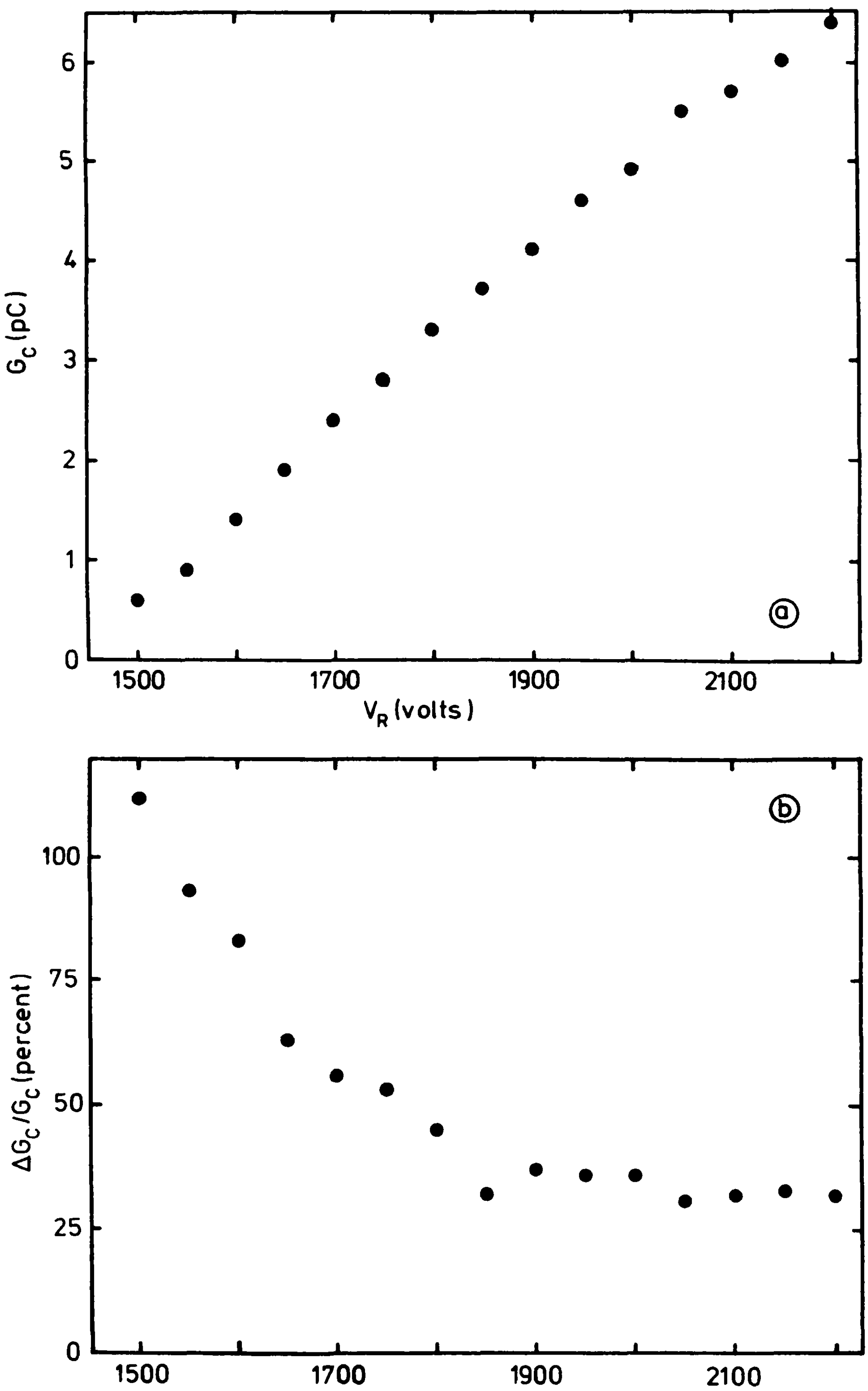

4.7. (a) Variation of gain, G_C , with rear plate voltage, V_R .
(b) Variation of FWHM, $\Delta G_C/G_C$ with rear plate voltage, V_R . Cu-L (0.93 keV) X-rays incident at $\theta=13°$. P-C front MCP, L:D=120:1 rear MCP, D=12.5 μm. X_R=0 mm.

4.3. Methods of Improving MCP Quantum Detection Efficiency

4.3.1. Basic MCP limitation

As already noted (Section 1.3) one of the principal drawbacks of MCP's is their poor quantum detection efficiency relative to competing detectors. The basic response of MCP's to soft X-rays is now well understood [66,121] in terms of a physical model. There is therefore little scope for improvement in the response of the MCP itself, the only obvious possibility being to obtain some contribution from the interchannel area, ~ 37% of front surface area (Chapter 6).

To produce any substantial (factors of 2-10) increase in efficiency it is necessary to provide the MCP with a high yield photocathode. This can be achieved in one of two ways; (1) reflection photocathode (Section 4.3.2), (2) transmission photocathode (Section 4.3.3).

4.3.2. Reflection photocathodes

Reflection photocathodes are normally produced by the vacuum evaporation of a suitable material onto the front surface of the MCP, so that a thin layer is applied to the front surface and the tops of the channel walls (Section 5.1). X-rays then interact with the photocathode in the same manner as they interact with the bare glass of uncoated MCP's (Fig.4.8(a)).

A useful photocathode is one in which the probability, per incident photon, of the initiation of an electron avalanche in the channel is greater than that for bare MCP glass. A material that has been widely used as such in X-ray and EUV astronomy [64,122] is MgF_2. This material has been chosen more because of its stability under laboratory conditions [102, 123] than its effectiveness as a photocathode. Substantial improvements in efficiency were reported for MgF_2 by Henry et al [64] (from 5.5% to 9% for 1.49 keV X-rays at $\theta=4°$, a factor of 1.64), but no increase was observed

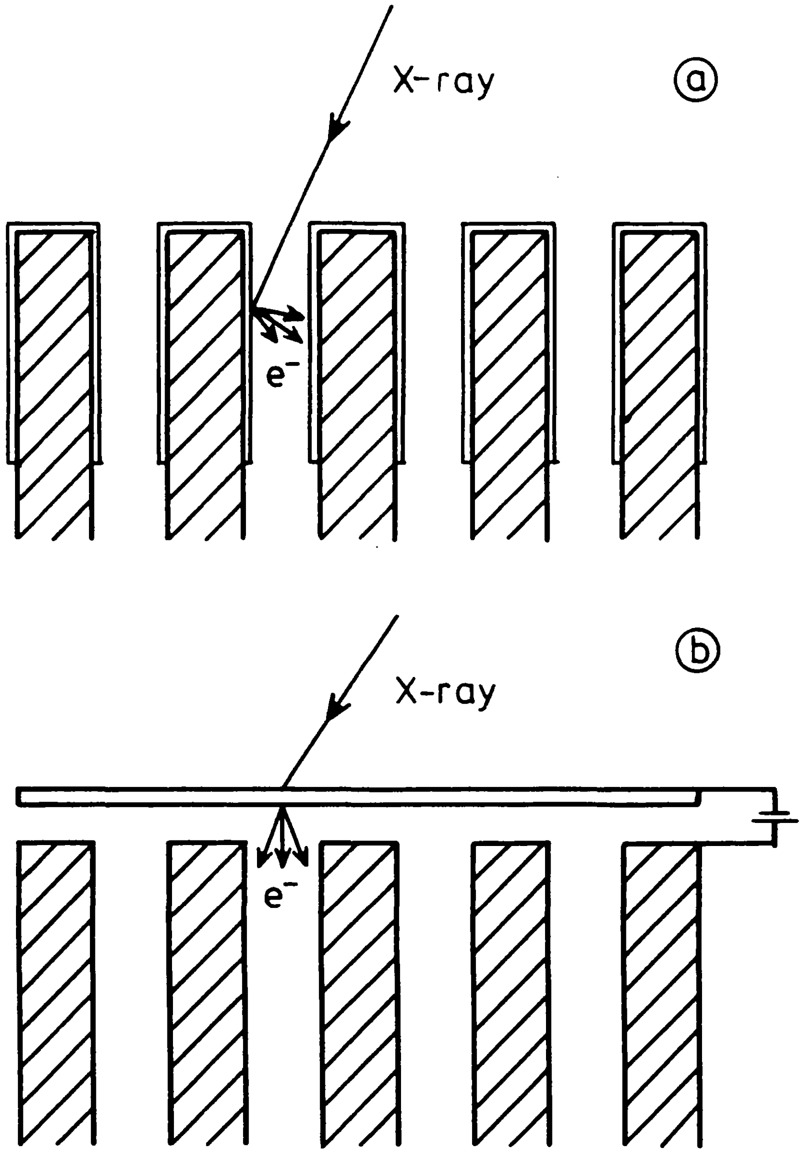

4.8. (a) Interaction of an X-ray with a reflection photocathode applied to a θ_B=0° bias MCP. Liberated electrons are accelerated down the channel.

(b) Interaction of an X-ray with a transmission photocathode. Liberated secondary electrons are accelerated towards the MCP by a small potential (~100 V).

by Fraser et al [106]. Measurements made at Leicester suggest that MgF_2 will only produce a useful increase in efficiency when used in conjunction with a MCP with degraded efficiency response.

A comprehensive theoretical study of the behaviour of reflection photocathodes has been undertaken by G.W. Fraser [121,124]. This shows quite clearly (Fig.4.9) that MgF_2 is far from optimum in the 1-10 Å range. CsI and CsCl are predicted to be by far the best photocathodes among those materials studied. Preliminary experiments with CsI [106] tended to confirm this (Chapter 5).

A good photocathode is usually one that has a very high secondary electron yield. In terms of the characteristics of the material this translates to a low excitation energy for secondary electrons combined with a large escape length [124]. This can lead to the situation where a large number of electrons are produced for relatively few X-rays giving high current quantum yields (in electrons photon^{-1}). More important for MCP photocathodes, the creation of a large number of secondary electrons also increases the pulse quantum yield of the photocathodes (in "counts" photon^{-1}), which of course must always be less than one. It is this factor that is important in determining the efficiency of MCP's since only one electron is needed to initiate an output pulse.

Although materials like GaAs P [125], exist that have very much better secondary electron parameters than CsI, they tend to be stable only under high vacuum (~ 10^{-10} Torr). The characteristics of CsI are such that it lies on the boundary which separates photocathodes that are stable when exposed to air and those that are not [124]. CsI can therefore be regarded as the optimum photocathode for work in the soft X-ray region where the detector must be periodically exposed to air.

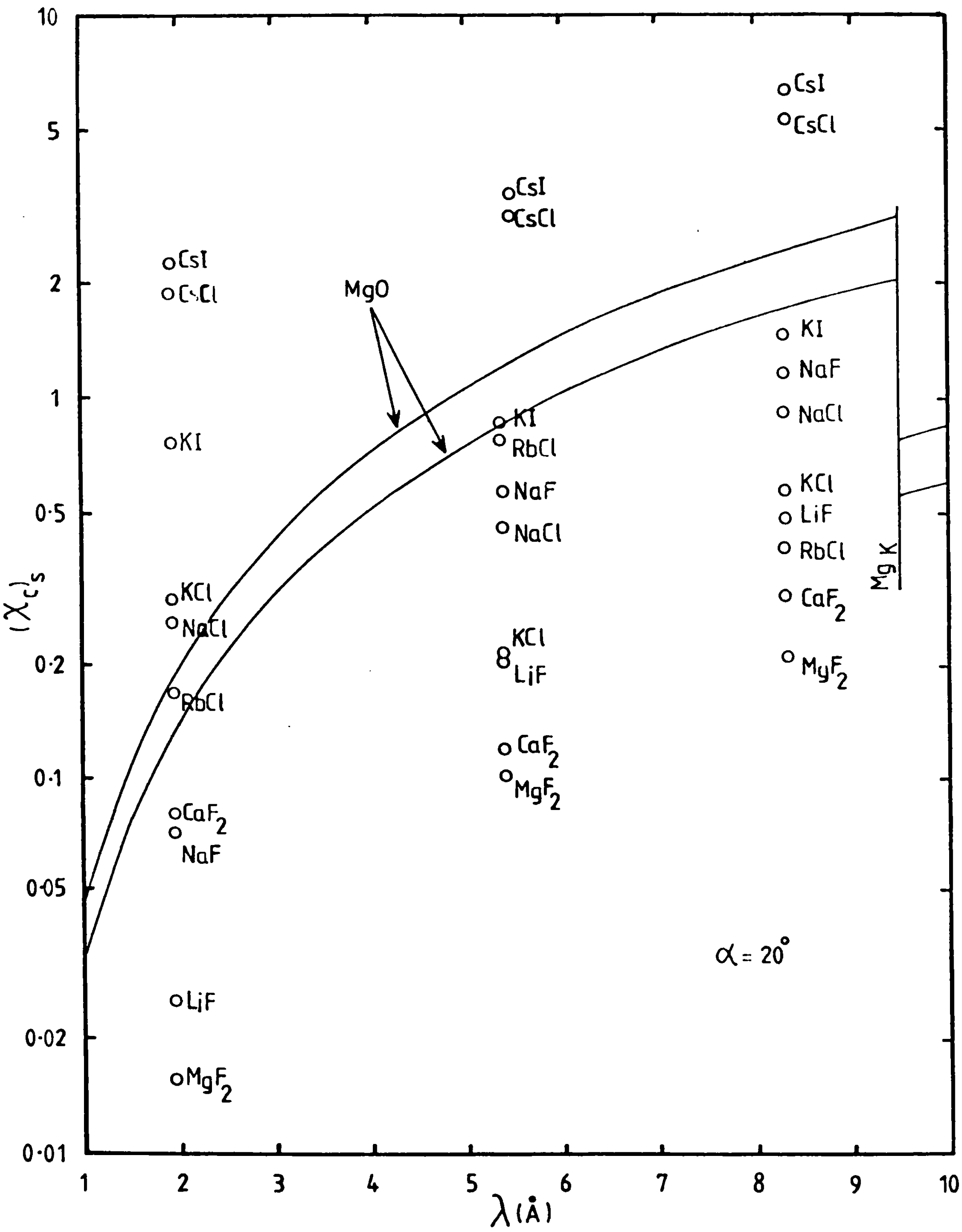

4.9. The ranking of insulating photocathodes at 1.94, 5.4 and 8.3 A° X-ray wavelength. Secondary photocurrents measured at grazing angle α=20° except for Mg F_2 and Mg 0 which are calculated values. (From Fraser [124]).

4.3.3. Transmission photocathodes

An alternative to the reflection photocathode is the transmission photocathode. This would normally be prepared by vacuum evaporation of the photocathode material onto a thin, X-ray transparent, substrate. This is then mounted in front of the MCP, with the substrate towards the X-ray source, and a moderate bias voltage (~ 100 volts) applied to the substrate to ensure collection of the electrons (Fig.4.8(b)). Photocathodes mounted with the substrate towards the MCP would not be very effective since the substrate would be practically opaque to the low energy (~ 1 eV) secondary electrons liberated from the photocathode.

The model developed in Refs.[66,121,124] has been applied to normal density transmission photocathodes. Excellent agreement [126] has been obtained between this model and published [107] experimental current quantum yields for CsI. For operation with MCP's however the important quantity is the pulse quantum yield rather than the current quantum yield. The important difference between the two is that the pulse quantum yield cannot be greater than the absorbed fraction of X-rays.

Unlike reflection photocathodes, transmission photocathodes have an optimum thickness for each X-ray energy. There is a trade off between absorbing the incident X-rays and allowing the resulting secondary electrons to escape from the photocathode towards the MCP. As the escape length for secondary electrons in CsI is of order 200-250Å, only electrons liberated close to the surface of the photocathode next to the MCP, will contribute to the detection process.

In practice the optimum photocathode thickness does not vary by large factors in the 0.28 keV to 8 keV energy range. The factor which limits efficiency is that beyond optimum thickness the pulse quantum yield starts to fall. The thicker photocathode absorbs more X-rays but not all of the secondary electrons can escape from it. The nett result of this [126] is that the expected efficiency from transmission photocathodes is less than has been measured for reflection photocathodes (Fig.4.10). This is especially true at higher energies since the transmission photocathode works best when the X-ray absorption lengths are small compared with the electron escape lengths.

For the detection of higher energy X-rays, however, the technique of Bateman et al [127] is of interest. This consists of using a 0.2-0.5 mm thick, low density (~ 5% of bulk), layer of CsI and applying a high electric field across it. The thick layer provides the large absorption depths required and the electric field produces field enhanced secondary electron emission. This internal multiplication allows electrons to escape from a much greater depth than is possible with a high density photocathode.

Best case efficiencies of ~ 50% at 5.9 keV have been produced with these low density photocathodes, much better (times 2-3) than would be expected from reflection photocathodes. There are, however, considerable practical problems. The 200-500 μm thick CsI layer is mounted on a thin metallic substrate and tends to be rather fragile. Also very high electric fields (~ 1 kV mm^{-1}) are necessary for efficient secondary electron production and these may flex the substrate sufficiently to dislodge the photocathode [128]. Problems have been encountered with the reproducibility of the efficiency of the low density photocathodes [128] and these will undoubtedly increase for the very large areas that would be required in a practical detector (e.g. 100 x 100 mm for AXAF). Noise, both intrinsic, and background from the detection of high energy particles, could also cause problems.

4.3.4. Adopted technique

The method selected for further development was the reflection photocathode (Section 4.3.2) using CsI. This promised maximum improvement in the present area of maximum interest (Section 1.4) and also provides a

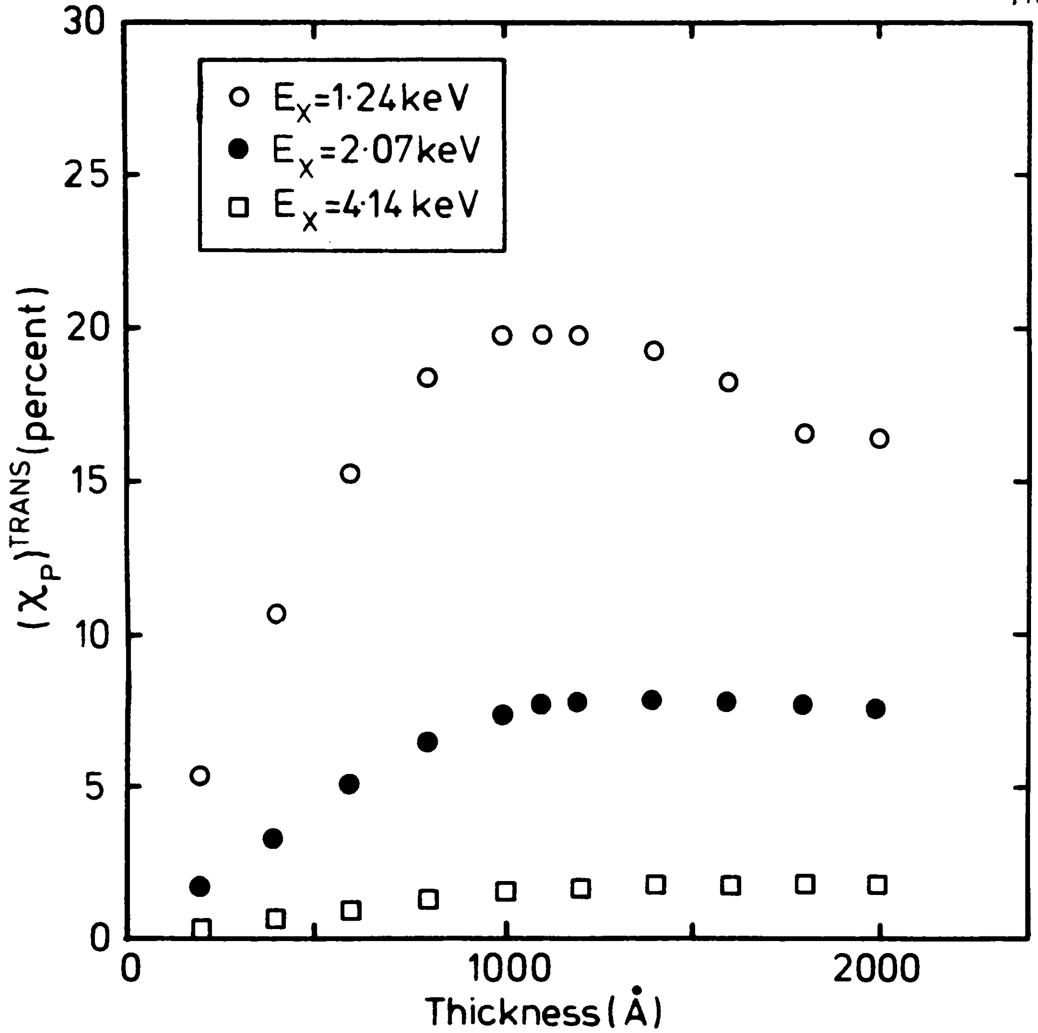

4.10. Calculated pulse quantum yield, $(x_p)^{Trans}$, as a function of planar CsI transmission photocathode thickness. Normal illumination, E_X=1.24 keV (open circles); E_X=2.07 keV (filled circles), E_X=4.14 keV (open squares). Data from G.W.Fraser - private communication.

natural progression from already established techniques for applying MgF_2 photocathodes. The added complications of attempting to develop low density transmission photocathodes were not considered worthwhile at the time.

The use of CsI requires drastic revision of previous operating procedures; this is described in the next section.

4.4. Practical Consequences of Using a CsI Photocathode

4.4.1. Characteristics of CsI

CsI is a deliquescent material and must therefore be protected from all sources of water vapour. There have been reports in the literature [129-132] of substantial degradation in the performance of CsI photocathodes after exposure to normal humidity laboratory air. The best solution to this problem would be to seal permanently the MCP detector under vacuum once the photocathode had been applied. This is not practical, however, since the development programme may involve changing the physical arrangement of the detector.

The adopted solution was to store all CsI coated surfaces under dry nitrogen in a desiccator, with all detector assembly work being done in a dry nitrogen filled polythene bag. When it was not possible to keep the CsI totally within a dry nitrogen atmosphere, dry nitrogen was flowed over the CsI surface. These procedures ensure minimal exposure of CsI coated MCP's to atmospheric humidity.

These precautions are sufficient since it has been determined [106] that exposure of a few hours to relative humidities of order 50% does not affect the X-ray response of the CsI. These findings are in agreement with the results of Salomon et al [133] but differ somewhat from other evidence [129-132]. Considerable uncertainty therefore still exists as to the precise ways in which CsI photocathodes degrade. The allowable exposure to moisture will probably depend on previous history, general handling procedures, temperature, relative humidity and may vary from sample to sample.

4.4.2. Water content of MCP's

In common with other glass structures MCP's contain large amounts of water vapour [134]. The water content of MCP's is enhanced by the final stage of processing which involves reducing the lead oxide glass surface in a hydrogen atmosphere. Also, despite its small size, a 36 mm diameter MCP, with D=12.5 μm diameter channels, has approximately 0.5 m^2 of surface area.

If CsI was evaporated onto such a substrate its effectiveness as a photocathode would inevitably degrade with time as water vapour was absorbed from the glass. The level of water vapour in the MCP must therefore be drastically reduced. This is a common problem in the attainment of high vacuum and the standard solution is to bake the item at high temperature under vacuum.

The procedure adopted, after considering the processing received by MCP's incorporated into commercial image tubes, was a 48 hour vacuum bake at a temperature of 275°C. This bakeout reduced the partial pressure of H_2O in the vacuum furnace by a factor $\sim 10^3$ giving a final value of $\sim 10^{-10}$torr (at room temperature) comparable with the partial pressures (as revealed by mass spectrometry) of secondary products, CO, N_2, and CO_2.

This is not necessarily the optimum procedure; it is, however, a sensible adaptation of industrial practice, and has so far proved to be adequate. It is important that once a MCP has been baked in this manner it is never exposed to significant amounts of water vapour since moisture is absorbed very easily onto baked surfaces.

4.4.3. Effect on MCP's of high temperature bakeout

Several authors [134,135,136] have reported the effect on MCP's of a high temperature vacuum bakeout. This normally produces a non-reversible increase in the MCP's resistance and a corresponding decrease in gain. Experience from the processing of MCP's in commercial image intensifiers also shows that a small fraction of MCP's will go noisy after this treatment [42].

A batch of 10 36 mm diameter, D=12.5 μm, L:D=40:1, MCP's were baked out as described in Section 4.4.2. Comparison of resistances before and after bakeout showed an increase of 10-30% afterwards [137]. This is somewhat lower than the increases of Ref.[135]. These MCP's were manufacturers rejects and therefore used only for resistance tests.

A more extensive series of tests were carried out on 3 other MCP's in two configurations. A rear MCP, L:D=120:1 was used in turn with two front MCP's, L:D=80:1** and 120:1, in a chevron detector (all three plates with D=12.5 μm). Both front MCP's were subsequently coated with CsI (see Chapter 5). The resistance of the 80:1 MCP increased by a factor of ~ 3 on bakeout, from 400 mΩ to ~1150 mΩ, vastly more than any previously reported figure. The overall performance did not seem to be degraded but precise comparisons before and after bakeout could not be made because it was fully coated with CsI immediately after bakeout. (For a comparison between the two front MCP's after coating with CsI see Section 5.4.) The reason for this massive change in resistance is unknown. The only factor that may have had an effect was the MCP's age. This particular MCP was left over from development of the Einstein HRI [138] and therefore was approximately 6 years old.

The effects of bakeout could be studied in more detail on the 120:1 MCP as this was only half coated with CsI (Section 3.1). Before useful measurements could be made a noise spot on the front MCP had to be screened off by using a larger rear electrode. The noise source was a chip on the front surface of the MCP that must have been caused either

** L:D=80:1 MCP supplied by Dr. M. Zombeck, Harvard Smithsonian Centre for Astrophysics, for coating with CsI. The MCP was to be used in testing the AXAF Technology Mirror Assembly.

by the bakeout itself or by improper handling procedures. In contrast to that of the 80:1 MCP, the resistance remained unchanged at ~ 610 mΩ. The resistance of the rear MCP had increased by $\sim 10\%$ to ~ 620 mΩ. The PHD from C-K (0.28 keV) X-rays is also practically unchanged. A comparison of efficiency at C-K before and after bakeout (Figs.4.11(a,b)) shows that there is very little difference between the two, with if anything the efficiency after bakeout being slightly higher than that before. There was no measurable increase in noise on the uncoated half of the front MCP.

The results would seem to indicate that the ~ 3 times increase in resistance of the 80:1 MCP is anomolous. The overall conclusion is that the bakeout of Section 4.4.2 does not affect the ability of MCP's to detect X-rays.

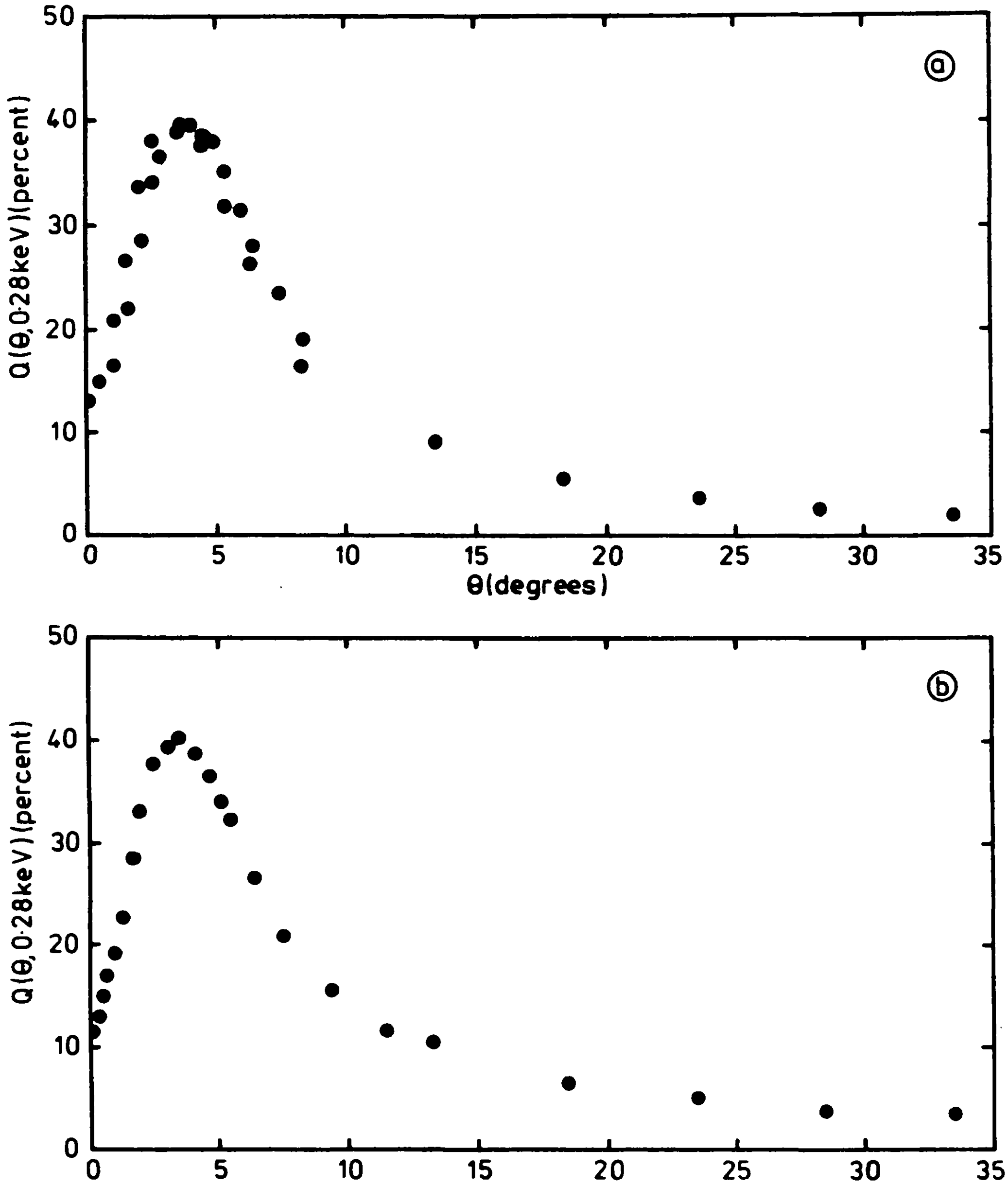

4.11. (a) MCP quantum detection efficiency versus C-K (0.28 keV) X-ray angle of incidence. Uncoated, unbaked MCP, L:D=120:1, D=12.5 μm (same data as for Fig.2.15).

(b) As for Fig.4.11(a) after MCP bakeout (Section 4.4.2).

CHAPTER 5

MCP EFFICIENCIES WITH A CsI REFLECTION PHOTOCATHODE

5.1. Production of a Reflection Photocathode

5.1.1. Coating geometry

Reflection photocathodes are prepared by vacuum evaporation, from a molybdenum boat, of the photocathode material onto the MCP input surface (Section 4.3.2.). By suitable arrangement of the relative positions of the MCP and boat (Fig.5.1(a)) the characteristics of the deposited photocathode can be altered. The maximum size and uniformity of the photocathode are constrained by the inside diameter (12 inches) of the round topped, cylindrical, glass bell jar of the evaporation plant. Since deposition occurs in line of sight of the boat, the degree of penetration of the photocathode into the channels can be changed by adjusting the coating angle $\hat{\alpha}_o$. As the depth of penetration increases, however, the thickness of the material deposited on the channel walls decreases, relative to that deposited on the surface of the MCP.

Even with the most favourable electric field for the collection of photoelectrons from the MCP front surface, most detected X-rays interact with the channel walls (see Chapter 6). It is therefore the thickness and depth of penetration of the photocathode into the channels that principally determine the MCP efficiency. The thickness of the layer applied to the channel wall may be calculated from the thickness deposited on the MCP front surface. Photocathode thickness is monitored experimentally by an Edwards FTM4 quartz crystal film thickness monitor, with the crystal placed close to and in the same plane as the MCP surface (Fig.5.1(a)). Since CsI has a secondary electron escape length of 200-250 Å sufficient material must be evaporated to produce a wall thickness of this order.

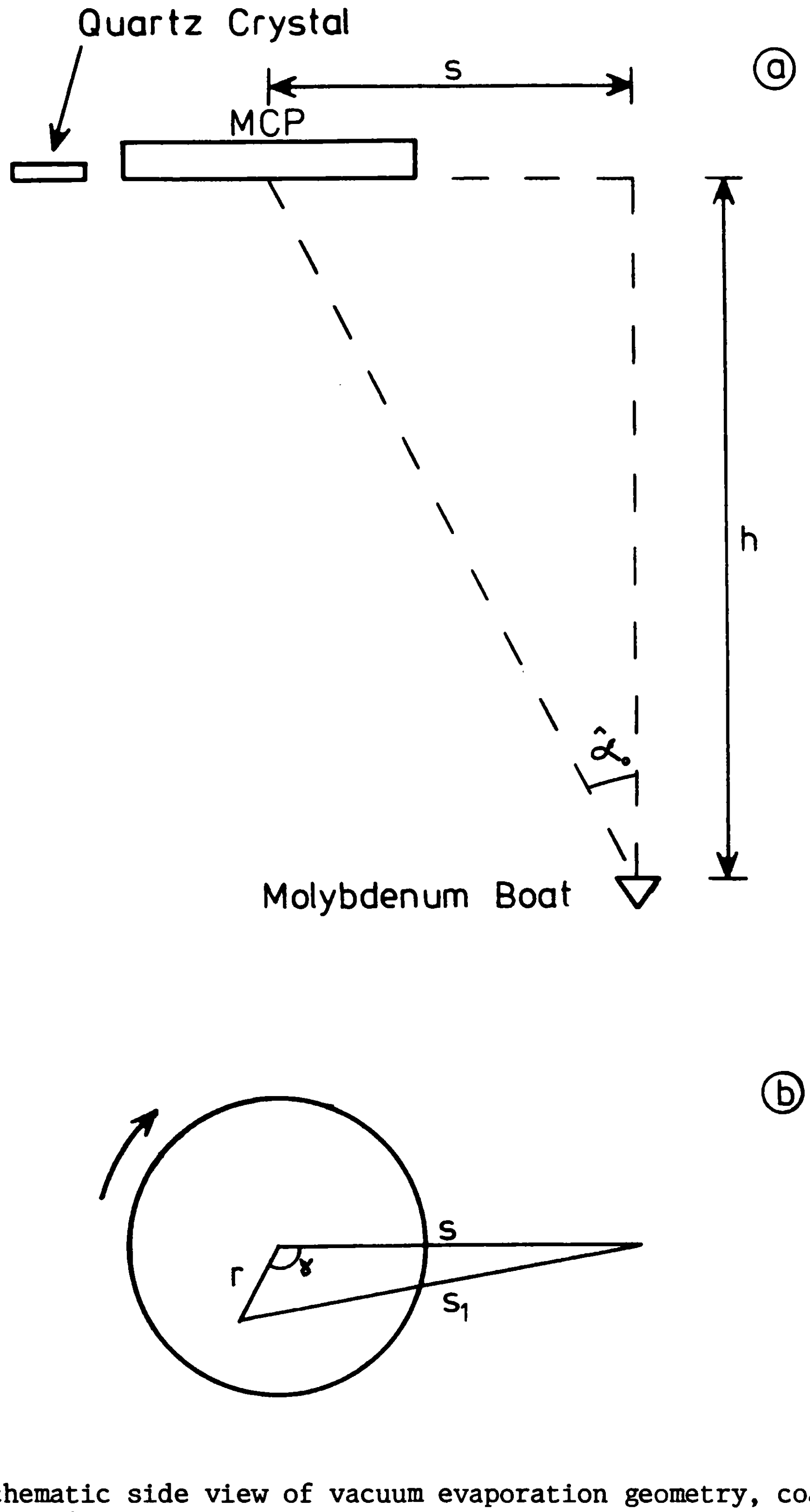

5.1. (a) Schematic side view of vacuum evaporation geometry, coating angle $\hat{\alpha}_0$.

(b) Schematic top view of a MCP during evaporation illustrating the effect of rotation on an off axis channel at radial distance r .

The choice of $\hat{\alpha}_o$ depends on the X-ray incidence angle, θ , for which the detector is to be optimised. Previously reported work [106], orientated towards the ROSAT WFC (Section 1.4), used $\hat{\alpha}_o=15°$. For the present work a much smaller coating angle was desirable, to produce results relevant to the higher energies and lower incident angles produced by the ROSAT main telescope and AXAF (Section 1.4). Theoretical calculations [139] for C-K (0.28 keV) X-rays incident at $\theta=5°$ indicated that $\gtrsim 75\%$ of the maximum attainable efficiency could be produced with wall thicknesses of order 350 Å. This thickness also provided a sufficiently thick absorbing layer for all other energies accessible from the present X-ray source. The chosen coating angle was therefore the smallest angle at which the required 350 Å wall thickness could be produced. Tests were carried out to determine the mechanical stability of CsI layers of varying thickness (Section 5.2). These tests indicated a maximum achievable coating thickness of 14,000 Å, dictating a coating angle $\hat{\alpha}_o=4°$ (Section 5.2.5).

In order to produce an even coating all the way round each channel the MCP was rotated about an axis perpendicular to its input surface. If this was not done the geometry of Fig.5.1(a) would produce a full depth coating at one side of each channel and none at all at the other. Rotation only completely corrects this effect for channels at the very centre of the MCP, however, since for a channel at non-zero distance, r , from the centre (Fig.5.1(b)) the coating angle, $\hat{\alpha}$, will vary around the channel such that:

$$\hat{\alpha} = \tan^{-1}\left(\frac{s_1}{h}\right) \qquad (5.1)$$

where

$$s_1^2 = r^2 + s^2 - 2rs\cos\gamma \qquad (5.2)$$

The depth to which the channel is coated thus varies with polar angle, γ , around the channel as shown in Fig.5.2(b). This variation can be minimised by making s large compared with the maximum value of r . For a given $\hat{\alpha}_o$ this means a large MCP-boat separation, h , which in turn requires a larger evaporation chamber and larger quantites of photocathode

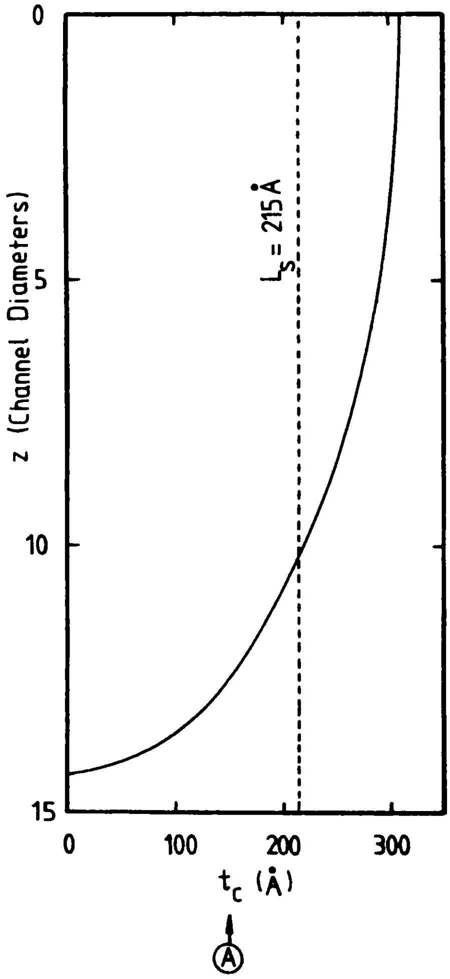

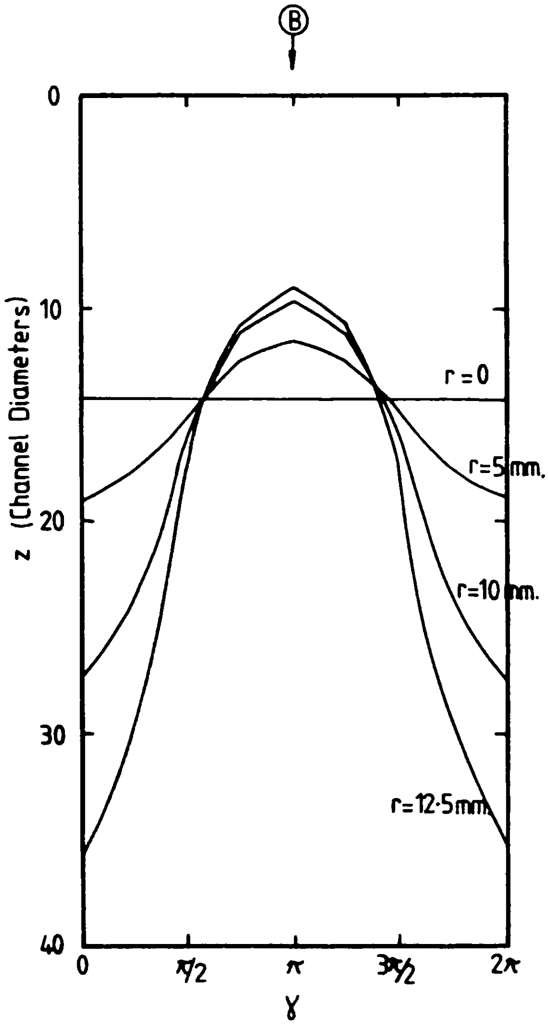

5.2. (a) Variation of the wall coating thickness, t_c , with depth into the channel, z , at MCP centre. Secondary electron escape length for CsI indicated by the broken vertical line. $\hat{\alpha}_0$=4°, front surface thickness 14000 A°.

(b) Variation of maximum penetration depth of the CsI coating with polar angle γ around individual channels sited at radial distances r from the MCP centre. $\hat{\alpha}_0$=4°, front surface thickness 14000 A°.

in the molybdenum boat. The quantity of material required goes up with the square of the MCP-boat separation, and hence the boat differs significantly from a point source (~ 40 mm long by 8 mm wide). The decrease in coating angle variation because of increased h must therefore be traded off against the increase in variation caused by the larger evaporation source.

For the present work, using a coating angle $\hat{\alpha}_o=4°$, the maximum attainable value of h was 360 mm. The variation in $\hat{\alpha}$, for a channel at the edge of the coated area, r=15 mm, was therefore $1.6° \lesssim \hat{\alpha} \lesssim 6.3°$. The variation of $\hat{\alpha}$ at the position where measurements were made, r=6.5 mm, was $2.9° \lesssim \hat{\alpha} \lesssim 5.0°$.

The variation of the photocathode thickness with depth down a channel at the MCP centre is indicated in Fig.5.2(a). The calculations were carried out for an ideal point source, $\hat{\alpha}_o=4°$ and a 14,000 Å front surface thickness; the true profile will be modified because of the extended nature of the molybdenum boat.

5.1.2. Evaporation techniques

The precautions outlined in this section were developed after carefully considering the comments of Section 4.4. The evaporation plant used was a rotary pump/diffusion pump system, NGN model 12 SG-2 with a 12 inch glass bell jar. A liquid nitrogen cold trap was used in conjunction with the diffusion pump.

Before using the evaporation plant all components were cleaned and checked. The plant was then pumped down to its ultimate vacuum, ~ 10^{-6} Torr, and the empty MCP holder heated to ~ 100°C. The inside of the system was also given an HT glow discharge clean. The object of this procedure was to remove as much water vapour as possible from the inside of the evaporation plant along with any forms of organic contamination.

After this clean up the coating plant was flushed with dry nitrogen while the MCP and CsI filled molybdenum boat, loaded and transferred in a dry nitrogen atmosphere, were installed. The evaporation plant was then pumped down to $\sim 10^{-5}$ Torr at which point the MCP was heated to 100°C and given a 10 minute HT glow discharge clean. The maximum temperature of the MCP was limited by mechanical factors to ~ 100°C. This may be rather lower than required to produce ideal films of CsI (Section 5.2). The glow discharge produces high energy ions which bombard the MCP, removing surface contamination and leaving a good clean surface for the photocathode to adhere to. The photocathode was then deposited with the MCP at 100 $\pm$ 5°C (Section 5.2). The CsI had previously been heated to just below the sublimation temperature for two minutes in an attempt to reduce the amount of intrinsic water vapour present.

The evaporation rate was normally kept between 20 and 40 Å s^{-1}. All quoted thicknesses are nominal since the calibration of the film thickness monitor was not checked by optically measuring sample films. Since the same monitor was used throughout, although not the same crystal, the accuracy of the measurements, relative to each other, should be quite good (few per cent).

After evaporation the MCP was allowed to cool below 95°C under vacuum before the bell jar was filled with dry nitrogen. It was then allowed to cool further to ~ 35°C before being transferred, in a dry nitrogen filled sealed polythene bag, from the coating plant to the detector assembly area.

5.2. Determination of Maximum Coating Thickness

5.2.1. Preparation of CsI films

Initial tests with CsI evaporated onto both glass blanks and MCP's, established the suitability of CsI for vacuum evaporation [137]. Initial results from CsI coated MCP's [106] and longer term tests to establish CsI's storage characteristics [140] showed CsI to be a suitable photocathode material. Of interest for the present work was the maximum achievable deposition thickness (Section 5.1.1) and optimum coating techniques.

There were indications that the temperature of the substrate during deposition could radically change the storage characteristics of the CsI layer. A CsI layer applied to a glass blank at room temperature turned "milky" while one applied at 100°C remained clear. There are also reports in the literature [141,142,143] that CsI layers deposited onto a hot substrate have better mechanical and electron emission properties than cold-coated layers.

To determine adequately the secondary electron emission parameters, and hence choose between hot/cold deposition and thick/thin films, would have required a photoelectron spectrometer. Such equipment was not available and therefore the CsI films could only be characterised by their visual appearance (Section 5.2.2), scanning electron microscope photographs of the surface structure (Section 5.2.3) and mechanical stability (Section 5.2.4). Comparisons were then made between the 6000 Å thick layers (i.e. similar thickness to those used in initial work [106]) and the other thicknesses to determine the suitability of the thicker layers as photocathodes. The mechanical stability of the CsI layer was a very important factor, since if the photocathode were to break up, loose particles might lodge in the channels and produce noise spots. Previous experience with MgF_2 photocathodes showed that layers thicker than ~ 6000 Å (deposited at room temperature) became powdery after a few days storage in air.

Twelve glass blanks were vacuum baked as described in Section 4.4.2. These were split into two groups, one group being coated at room temperature and one at 100°C. Each group of six blanks had deposited on them, test layers of 4,6,8,10,12,14 thousand angstroms of CsI. Two other unbaked glass blanks were coated with 11350 Å and 13250 Å of CsI. The evaporation technique used was identical to that of Section 5.1 except that a coating angle $\hat{\alpha}_o=0°$ was used.

After deposition of the CsI the blanks were stored in sealed, nitrogen filled polythene bags along with 5 silica gel desiccant capsules. These bags were kept in a desiccator jar.

5.2.2. Changes in visual appearance of CsI films

All the CsI coated blanks were examined by eye on removal from the coating plant. Almost all the CsI films were clear and blemish free; only the 12,000 Å and 14,000 Å films coated cold showed any slight signs of a milky appearance.

The blanks were visually examined, at intervals of between 3-4 days and a month, until they were 120-130 days old. This examination consisted of; (1) holding the blank up to a light and observing the transmitted colours, (2) rotating the blank and observing the colours reflected from the film, (3) observing the film against a dark background. All examinations were made with the blanks still sealed in their polythene bags to prevent water vapour contamination.

In transmission the films normally appeared grey. The thinner films showed tinges of green and pink when new but these faded with time. The thicker layers gave a somewhat darker grey, probably because the thicker film absorbs more light, and there was also a slight increase in greyness with time for all films.

All films showed very distinct colours in reflection when viewed at the correct angle. The cold coated films gave a deeper, more distinct colour at all times. As the films aged the reflected colours changed. A typical sequence was bright green, pale green, red, indistinct combination of colours, no colour at all (reflected white light). While these changes took place the angle in which the colours could be observed became steadily narrower. The thicker films changed fastest and gave no distinct colour after ~120 days, while the thin films still showed some effect after ~130 days.

When viewed against a dark background the films tended to change from clear, to slightly cloudy, to very cloudy. This occurred fastest with the cold coated and thick films. Initially there were considerable differences between hot and cold coated films of the same thickness. These differences largely disappeared over the first ~ 40 days. The variation in appearance with thickness also gradually disappeared until at ~ 120-130 days, there was no significant difference between any of the films.

The two films deposited on unbaked glass blanks exhibited very similar behaviour. In fact on many occasions these two films looked "better" than the others, although this may have been because they were the last films produced and hence were the youngest. The final appearance of these films was very similar to these on the baked blanks except for more distinct colours being visible on reflection.

These results show that the CsI films certainly change their structure with time and then seem to stabilise at some standard condition irrespective of thickness or coating conditions. A possible cause of this effect is the films absorbing some of the residual water vapour in their immediate environment. The important factor for future use of CsI is that on long time scales there is no difference in the characteristics of the 6000 Å thick layer and the 14000 Å thick layer. A MCP coated with a 6000 Å layer of CsI has been stored and tested for more than a year, with no degradation in efficiency. From the above similarity in stability between the 6000 Å and 14000 Å layers, we can therefore predict, with some confidence, the long term stability of the 14000 Å layer.

5.2.3. Scanning electron microscope studies of CsI surface structure

When the two 4000 Å thick films were 15 days old they were overcoated with a 100 Å thick layer of Al to allow them to be examined in a Scanning Electron Microscope (SEM). This was done to see if there was any difference in the surface structure of the hot and cold coated films.

The 4000 Å films were selected because they were expected to suffer least from mechanical instability, and were not therefore necessary for vibration testing (Section 5.2.4.).

Extreme difficulties were encountered in obtaining good images with the available SEM, and high magnification, > 5000 times, images were very poor. A view of the hot coated surface at X 5000 magnification is shown in Fig.5.3 [144]. This shows a surface roughness of order 0.5 μm and is typical of views obtained on both hot and cold coated films. The variation in depth of the film is difficult to judge but must be less than 0.4 μm, the thickness of the film.

Fig.5.3 was obtained using back scattered primary electrons. Attempts to analyse the surface using the emitted secondary electrons showed a curious banded structure. Within these bands a paving stone structure could be easily observed, with characteristic dimensions again of order 0.5 μm. What little structure was visible outside these bands was consistent with the structure observed within them. The banded structure may have been caused by irregularities in the thickness of the Al coating, with scratches, either in the original glass blank or on the CsI film, showing up as bands.

5.2.4. Vibration tests

The basic structural integrity of the CsI films had been demonstrated by the ability to examine and store the glass blanks without the CsI falling off. Some form of mechanical test was, however, needed to quantify this. It was considered that careful handling procedures would prevent the photocathode making any direct mechanical contact in normal MCP use. This ruled out any form of surface friction test. In a practical X-ray astronomy application the most severe test of equipment is normally the vibration levels encountered during launch. It was decided therefore to vibrate some of the blanks and collect and count any particles that were dislodged.

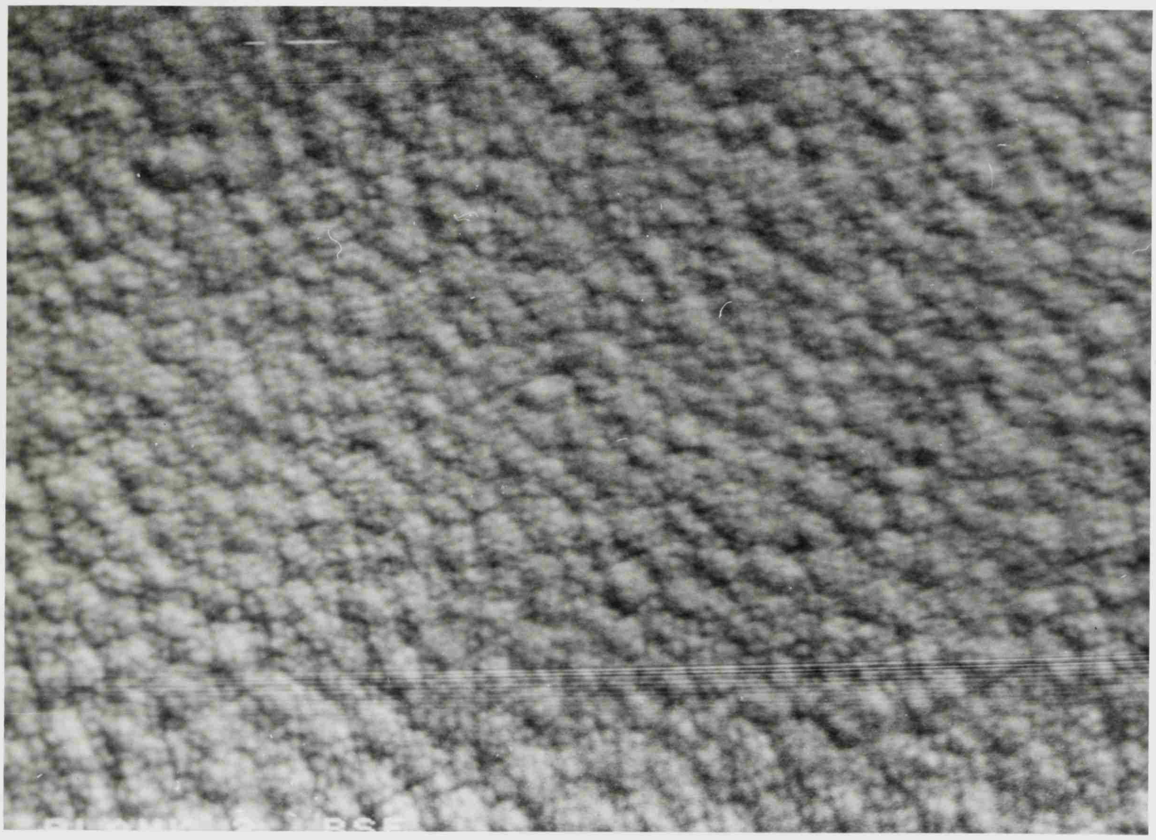

5.3. Scanning electron microscope photograph of a 4000 A° thick, hot coated (100°C) CsI film. Image obtained using back scattered electrons. Magnification 5000 times.

For vibration the blanks were mounted (in a dry nitrogen atmosphere) in a purpose built sealed jig (Fig.5.4). Four vibration runs were made on each blank tested (Table 5.1). For each vibration level the jig was subjected to both increasing and decreasing frequency runs. The available equipment limited the maximum accelerations used and also dictated that a sinusoidal rather than a white noise vibration pattern was used.

Table 5.1

Acceleration and frequency limits used for vibrating the CsI films

Acceleration (g)	Frequency range (Hz)
5	50-2500
15	50-2500
21	50-2500
30	800-2500

Particles which vibrated loose were collected on a glass plate coated with a thin oil layer (the CsI film being inverted during vibration). The oil film was produced by applying a few oil drops to the plate and smearing them out into a film. This technique proved somewhat unreliable as it was very difficult to produce an oil film free from small air bubbles. The method was still usable however, as the number of particles in each area examined was counted before and after vibration.

To examine the oil film the bottom half of the vibration jig, containing the oil coated glass plate, was installed on an X-Y table. Five 1.5 mm wide strips were then scanned using a high quality zoom microscope. Tests indicated that particles of ~ 5 μm and over should be easily visible. Each strip was scanned before vibration and the number of observed particles noted. After vibration the same strips were scanned and the particle count repeated. The increase in number of particles was generally only 20-30% of the initial "noise" level, an average ~ 7 particles per strip. Vibrating the jig alone, without any blank present, produced an increase of ~ 4 particles per strip. There were therefore ~ 3 particles per strip coming from the CsI coated blank.

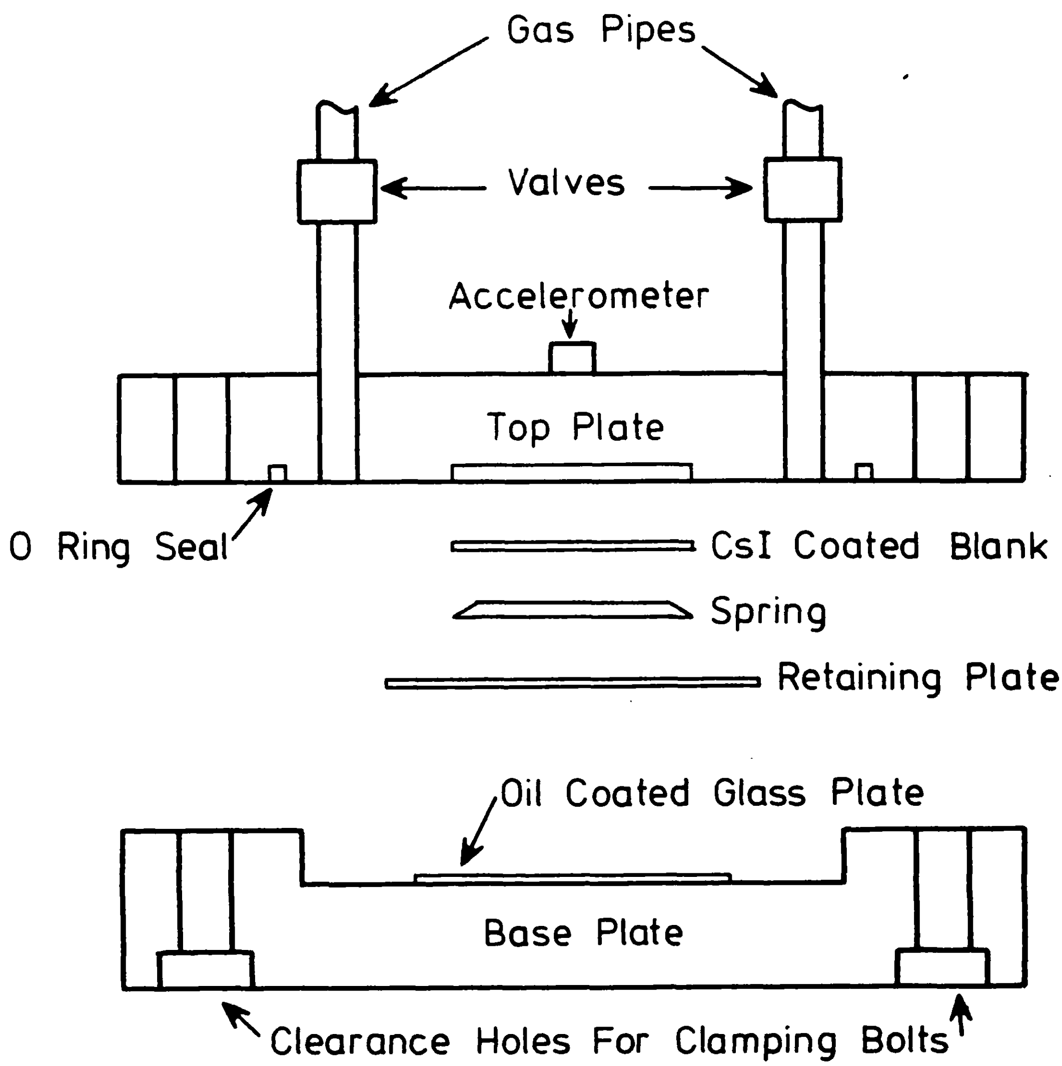

5.4. Schematic, sectional side view of jig used to vibrate CsI coated glass blanks. Spring used to hold glass blank was identical to that used to hold MCP's in detector body (Fig.3.2). Main body machined from aluminium.

Three sets of blanks were tested; the 6,10,14 thousand angstroms CsI films coated hot and cold, all approximately 130 days old. There was no significant variation in the number of particles coming from the hot and cold coated films, and there was no observed increase in particles with increasing thickness. No large portions of the films broke free. All observed particles were of order 10-20 μm in size. The gross mechanical stability of the films was therefore quite good.

Around ~ 120 particles were collected from each CsI film during vibration. This number can only be regarded as an upper limit to the number of particles that would come off an ideally handled photocathode. The decision to vibrate the films was not taken until after the blanks had been coated and stored and they had not been stored in an optimum manner for this type of test. The scanning electron microscope images showed that the two CsI films examined were scratched and had particles adhering to the surface. If dislodged these would serve to increase the particle count above that of a properly handled film. The important factor, however, is that the 14000 Å and 10000 Å layers gave essentially the same results as the 6000 Å layer.

5.2.5. Conclusion

The results of Section 5.2.2 and 5.2.4 are qualitative rather than strictly quantitative. Our conclusions rely on comparing the thick film performance with that of the 6000 Å layers. This can be done because a MCP detector with a 6000 Å CsI photocathode has been successfully used in the lab with a combined use and storage time of more than a year. Since during the present investigation the performance of the 6000 Å layer and the 14000 Å layer on glass blanks were very similar it would seem reasonable to assume that the 14000 Å layer is usable as a microchannel plate photocathode.

While these tests are sufficient for the present laboratory program, the vibration test in particular was insufficient to qualify a 14000 Å thick layer for a satellite experiment. For these purposes much higher standards of handling and storage would be required. The acceleration levels used here were also rather low for satellite qualification. Also because of the very large open area of a MCP (63%) there will be a significant difference between the planar CsI layer studied here and the layer actually applied to a MCP. On an MCP the thickness of the photocathode will be of the same order as its local width and there will be a large number of "edges" around the channel entrances. To overcome these problems tests would need to be done with CsI actually deposited on MCP surfaces.

In these present measurements there was no prolonged difference between films coated hot and coated cold. It was decided, however, to coat MCP's at 100°C to take advantage of any possible increase in the secondary electron emission coefficient that this might bring [143], and also of the higher degree of substrate cleanliness this would produce.

The maximum safe coating thickness as determined here was 14000 Å. This was in many ways a practical limit imposed by the charge of CsI which the molybdenum boat would hold (Section 5.1.1).

The two 0° bias MCP's of Section 4.4.3 were coated with 14000 Å layers of CsI at $\hat{\alpha}_o$=4°. This procedure resulted in a channel wall thickness of between 310 Å and 550 Å, the uncertainty being caused by the extended nature of the evaporation source (Section 5.1.1). The L:D=80:1 MCP was coated with a 25 mm diameter disk central to the MCP while the L:D=120:1 MCP was half coated as in Fig.3.1.

5.3. Measurement Techniques and Errors

5.3.1. Efficiency measurement technique

The MCP efficiency, Q , is calculated using:

$$Q = \frac{2\ N_m\ Q_{pc}\ T_p\ T_w}{(N_{n1}+N_{n2})(T_p)^{\sec\theta}} \tag{5.3}$$

where N_m is the MCP X-ray count rate and $(N_{n1}+N_{n2})/2$ is the average proportional counter (PC) X-ray count rate (see below). θ is the angle of X-ray incidence, Q_{pc} is the proportional counter quantum detection efficiency, T_p the transmission of the carbon coated polypropylene PC and MCP windows and T_w the transmission of the PC window support mesh.

The detector count rates, N_m and N_n , are determined by taking consecutive 30 second counts with the MCP and PC detectors and then subtracting the relevant noise count rates. N_{n1} is the PC count rate measured immediately before N_m and N_{n2} is the PC count rate measured immediately after N_m . This averaging process allows the X-ray source count rate to be determined to within ~1% (Section 3.5.7.).

The noise count rate of the MCP detector was checked before and after each series of measurements by making four consecutive 100 second noise counts. Since the PC noise count rate is both lower and more stable a single set of four consecutive 100 second noise counts were used to calculate the noise count rate. These noise counts were taken either before or after the measuring sequence.

The quantum detection efficiency of the PC, Q_{pc} , was assumed to be equal to the proportion of X-rays absorbed in the PC gas. X-rays that pass through the gas and are absorbed by the stainless steel walls of the PC are not detected (Section 3.6.3). The efficiency with which X-rays were absorbed in the gas was calculated from the absorption coefficient of the PC gas. These absorption coefficients can be calculated from basic atomic structure data using a computer model [118].

Two 1-2 μm thick carbon coated polypropylene windows were used. One served as the entrance window for the PC and the other was used to exclude ions and electrons from the MCP. Thin polypropylene windows were produced by the heating and stretching of thicker polypropylene sheet. A number of samples were stretched until a portion of uniform thickness ~150 mm in diameter was produced. This was then repeatedly dipped in a solution of carbon and alcohol to produce a thin layer of carbon on both sides of the polypropylene, one side of which was carefully wiped clean. Five samples are taken from each portion: 1 x PC window, 1 x MCP window, 3 x calibration samples. Great care had to be taken to ensure that all five samples were of near uniform thickness as their transmissions were assumed to be identical during calibration. (Thickness was determined by observing the interference colours of the thin material.)

Each polypropylene sample was calibrated using two pieces of source filter material appropriate to the X-ray energy being used. First the relative transmission of the two filters was checked using the PC. Then the polypropylene sample was placed in line with one of the filters and the two transmissions were again compared. The transmission of the polypropylene at that energy could then be calculated.

The transmission of the polypropylene window used with the MCP detector appears in Equation 5.3 to the power of $\sec\theta$. This geometrical factor takes into account the increased path length through the polypropylene when X-rays are incident at angles $\theta > 0°$, since the polypropylene is fixed with respect to the channel axes (Fig.3.2). This factor is important only for low energies, $\lesssim 1$ keV, and large angles where the transmission is lowest.

The transmission of the PC window support mesh, T_w, was measured in exactly the same way as that of the polypropylene windows.

5.3.2. Errors

The overall error in the measured efficiency is determined by the errors in each factor of Equation 5.3.

The errors in the MCP and PC count rates depend only on the counting statistics and noise stability over the measuring period. PC noise was stable at ~ 1 count s^{-1} ($\equiv 0.002$ of total count rate) for all measurements undertaken. Within any given set of efficiency measurements the MCP noise count rate was stable to within $\pm$ 2 counts s^{-1} ($\equiv \sim 0.005$-0.05 of total count rate) although the noise level could vary between different sets of measurements. With the exception of the B-K measurement the statistical uncertainty in MCP count rate varies from 1% at high efficiency to 2.5% at low efficiency. For B-K the figures are 3.5% and 6% because of the much lower flux available from the X-ray source.

The major error in the PC count rate was the uncertainty in the true X-ray source flux. The averaging technique used (Section 5.3.1) allows the true count rate to be determined with an rms error of $\pm$ 1-1.5%.

The calculated efficiency of the PC may be considerably in error within a few eV of any absorption edge of the gas mix. Of the X-ray lines used only C-K is close to an absorption edge. The model has been extensively checked, and found to be accurate, in this region [118] however, and therefore errors in the calculation may be disregarded. The most significant errors involve the gas density used in the absorption calculations. Variations in atmospheric pressure produce variations in the PC gas density. The resulting variations in absorption lengths were unimportant for all energies used here except Nb-L (2.28 keV) and Ru-L (2.68 keV), since these are the only energies for which the PC has an appreciable transmission. Relative errors in Q_{pc} of up to $\pm$ 2% are possible at Nb-L and Ru-L because of the normal variation in atmospheric pressure.

The transmission of the window support mesh, T_w , has been measured at 5 X-ray energies and is essentially independent of energy. The measured transmission, T_w=0.46, was equal to the nominal open area ratio and is accurate to better than $\pm$ 1%.

The method of calibrating the polypropylene windows was rather poor since the transmission is assumed constant over considerable areas of plastic. Tests conducted on five test samples using C-K (0.28 keV) X-rays showed relative variations of $\pm$ 2% across a 150 mm diameter sample. For the range of T_p values measured, this produces a maximum relative error (at θ=33.5°) in $T_p^{1-\sec\theta}$ of $\pm$ 1% at B-K and $\lesssim$ 0.5% at other energies.

Considering all these factors the relative uncertainties in efficiency for C-K, Cu-L, Mg-K, Al-K and Si-K will be $\pm$ 4% for the highest efficiencies rising to $\pm$ 5.5% for the lowest measured efficiencies. For Nb-L and Ru-L the relative errors are $\pm$ 6-8% and for B-K $\pm$ 8.5-11.5%.

5.4. Results

5.4.1. Operating characteristics of the experimental MCP's

It is interesting to compare the general operating characteristics of the two detector configurations used (front MCP L:D=80:1 and L:D=120:1 Sections 4.4.3 and 5.2.5). The two configurations were identical except for the front MCP. The basic shape of the output PHD from the CsI coated MCP showed no significant change over that from the uncoated MCP. The CsI coated surfaces do however produce a significantly higher gain than the uncoated ones. Precise comparison between the two configurations was not possible because there was no reference surface left on the 80:1 MCP. To produce a gain equivalent to that of the pre-baked 80:1 MCP, 200 V less needed to be applied across it. A similar although slightly smaller effect was observed with the 120:1 MCP.

A significant variation from previously observed behaviour is that the gain of the detector after CsI coating is now energy dependent. Significantly different gains were obtained from C-K (0.28 keV) and Si-K (1.74 keV) X-rays. This effect is described in detail in Chapter 7. Since the measured efficiency was not particularly sensitive to front plate voltage all efficiency measurements on the CsI surfaces were obtained at the optimum voltages for energy resolution. Higher voltages were used when measuring efficiencies on the uncoated half of the 120:1 MCP since otherwise a significantly degraded PHD was obtained.

The 80:1 MCP showed no significant increase in noise count rate after coating with CsI which contrasts with an increase of 2-3 times for the 120:1 MCP. (Measurements made at same applied voltages before and after coating.) Two dimensional images of the noise pattern showed quite clearly that the increase on the 120:1 MCP came from the CsI coated area. The reason for this difference between the two MCP's is unclear but may be related to the much larger increase in resistance of the 80:1 MCP on bakeout than the 120:1 MCP.

The measurements described here and in Chapter 7 were irregularly interrupted by very high count rate, low level noise which would "switch on" within a second. This effect was thought to be due to a design fault within the detector which allows a coronal discharge to occur. Since the problem was not due to the MCP's themselves, and no measurements were made in the noisy state, this will not have affected the accuracy of the efficiency measurements or PHD parameters.

5.4.2. Efficiency measurements using an L:D=80:1 MCP

Since this MCP was being coated and calibrated for delivery to the Harvard-Smithsonian Centre for Astrophysics only a brief investigation was possible. The results of measurements made with C-K (0.28 keV) and Al-K (1.49 keV) X-rays are shown in Figs.5.5(a,b). Efficiencies measured on the CsI coated MCP show considerable increases over measurements made before coating. The double peak structure in the CsI curve (filled circles) of Fig.5.5(b) is due to the difference between the coating angle, $\hat{\alpha}_o$, and the critical angle of reflection, θ_c , for Al-K X-rays from CsI. For $\theta > \hat{\alpha}_o$ the response is due entirely to the CsI and the efficiency will increase as θ decreases. For $\theta < \hat{\alpha}_o$ however a significant proportion of the incident X-rays will interact with the MCP glass rather than with the CsI photocathode. In this angular region the MCP efficiency response will be a combination of the CsI response and the bare MCP response. The detection efficiency for X-rays interacting with the CsI will continue to rise until $\theta \approx \theta_c$. The overall detection efficiency, however, starts to decrease because of the much lower detection efficiency of the glass.

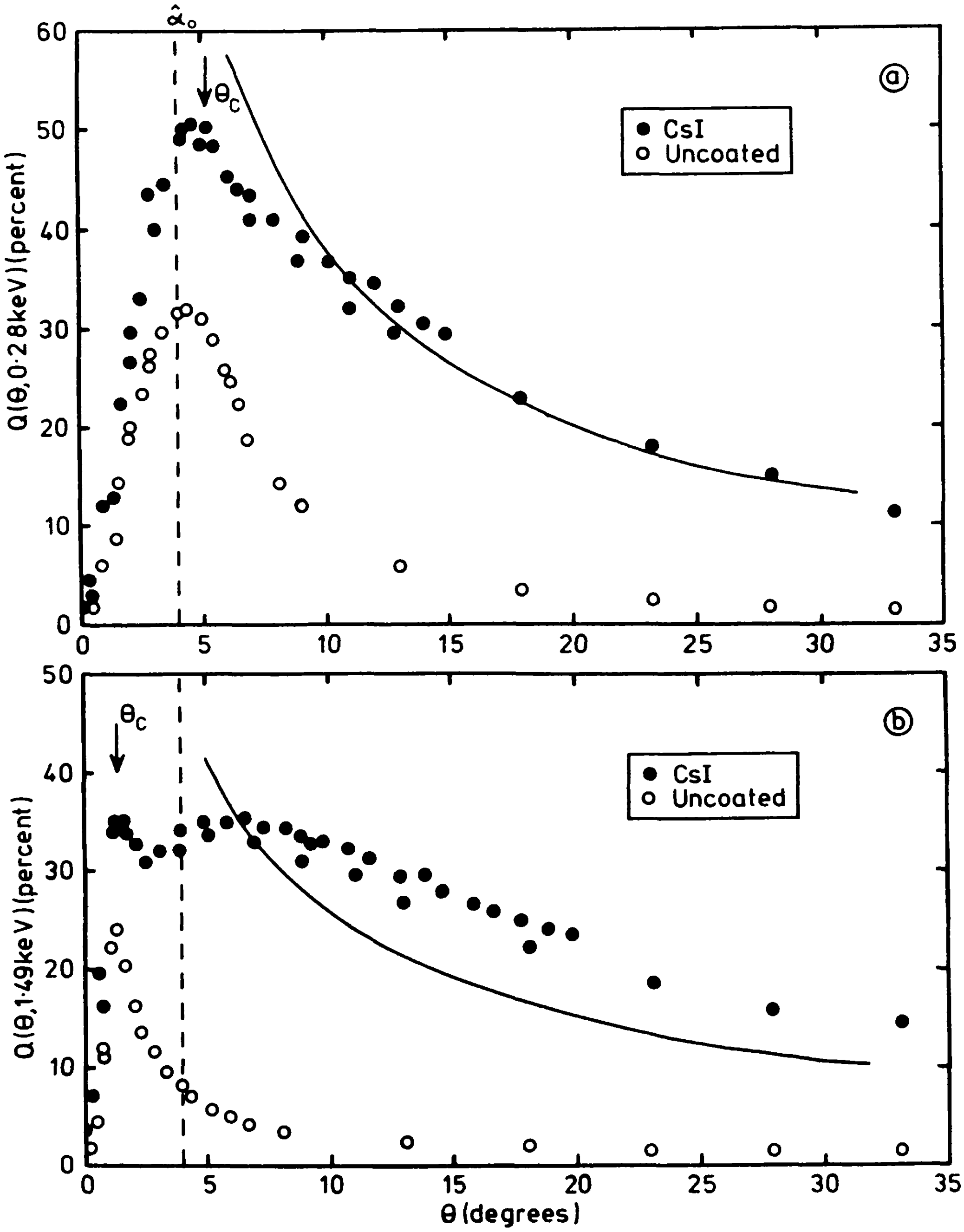

5.5. (a) MCP quantum detection efficiency versus angle of X-ray incidence before (open circles) and after (filled circles) CsI coating. C-K X-rays, energy E_X=0.28 keV. Coating angle indicated by vertical line. L:D=80:1. Full curve - calculated efficiency of CsI coated MCP at those angles where the efficiency response is wholly determined by the coating.

(b) As Fig.5.5(a) except Al-K X-rays, E_X=1.49 keV.

This produces a peak at $\theta \approx \hat{\alpha}_o$. Then as θ approaches θ_c the increase in the glass response produces an increase in the overall efficiency to give a peak of $\theta \approx \theta_c$. For $\theta < \theta_c$ significant amounts of reflection reduce the detection efficiency in the same way as for uncoated MCP's (Section 2.3.3.).

The solid curves in Figs.5.5(a,b) are theoretical predictions using a model developed at Leicester [124,139]. The model produces excellent agreement with the C-K results above θ=10° . For θ < 10° the model overestimates the response, mainly because it assumes a uniform photocathode thickness (d=300 Å) rather than using the actual profile shown in Fig.5.2(a). The model is less successful at Al-K, but agreement with the data is still quite good.

5.4.3. Efficiency measurements using an L:D=120:1 MCP

A comprehensive set of measurements at eight energies (Figs.5.6 (a-h)) were made on the L:D=120:1 MCP. These results, like those of Figs.5.5(a,b), show a large increase in efficiency on the CsI coated half of the plate. Increases in peak efficiency for this MCP were less spectacular because of its higher uncoated efficiency. Table 5.2 lists the efficiency enhancement factors resulting from CsI coating. Even at Ru-L (2.68 keV) the efficiency at θ=5° exceeds 20%, and this confirms earlier claims for the superiority of CsI over MgF_2 as an MCP reflection photocathode [106].

The peak efficiencies measured by Henry et al [64] for the MgF_2 coated Einstein High Resolution Imager (HRI) at 0.28 and 1.49 keV are shown for comparison with the data of Figs.5.6(b,e). That these efficiencies fall below our peak efficiencies even on the uncoated plate half is probably explicable in terms of the L:D values involved (120:1 here 80:1 for the HRI), the larger value allowing the maintenance of a narrow output PHD down to smaller θ values hence avoiding loss of counts below a low level noise discriminator.

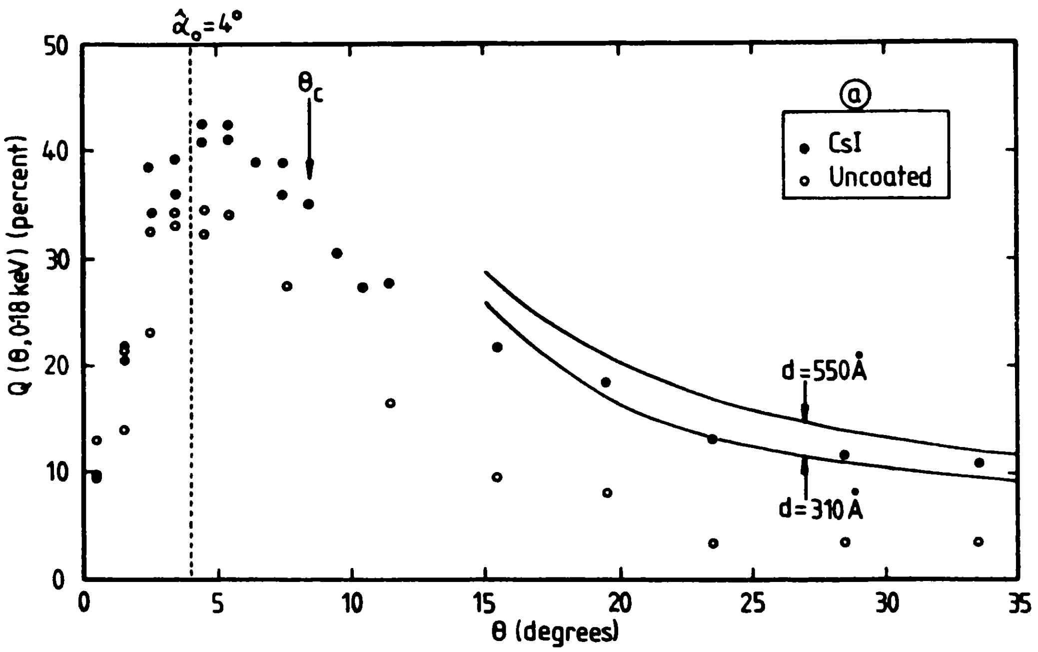

5.6. (a) MCP quantum detection efficiency versus angle of X-ray incidence for both CsI coated (filled circles) and bare (open circles) MCP halves. B-K X-rays, energy E_x=0.18 keV. Coating angle indicated by broken vertical line. Critical angle for X-ray reflection from CsI indicated by vertical arrow. Full curves - calculated efficiency of CsI coated MCP for stated channel wall coating thicknesses. Curves extend over those angles at which the efficiency response is wholly determined by the coating. L:D=120:1. Measurement positions x=19 mm (uncoated half) and x=32 mm (CsI coated half).

(b) As Fig.5.6(a), except E_x=0.28 keV. Peak efficiency of $Mg F_2$ coated MCP of Henry et al [64] - square symbol. C-K X-rays.

(c) E_x=0.93 keV. Cu-L X-rays.

(d) E_x=1.25 keV. Mg-K X-rays.

(e) E_x=1.49 keV. Peak efficiency of $Mg F_2$ coated MCP of Henry et al [64] - square symbol. Al-K X-rays.

(f) E_x=1.74 keV. Si-K X-rays.

(g) E_x=2.28 keV (mean energy of the Nb-L series obtained from a $Nb_2 O_5$ coated source anode).

(h) E_x=2.68 keV (mean energy of the Ru-L series obtained from a $Ru O_2$ coated source anode).

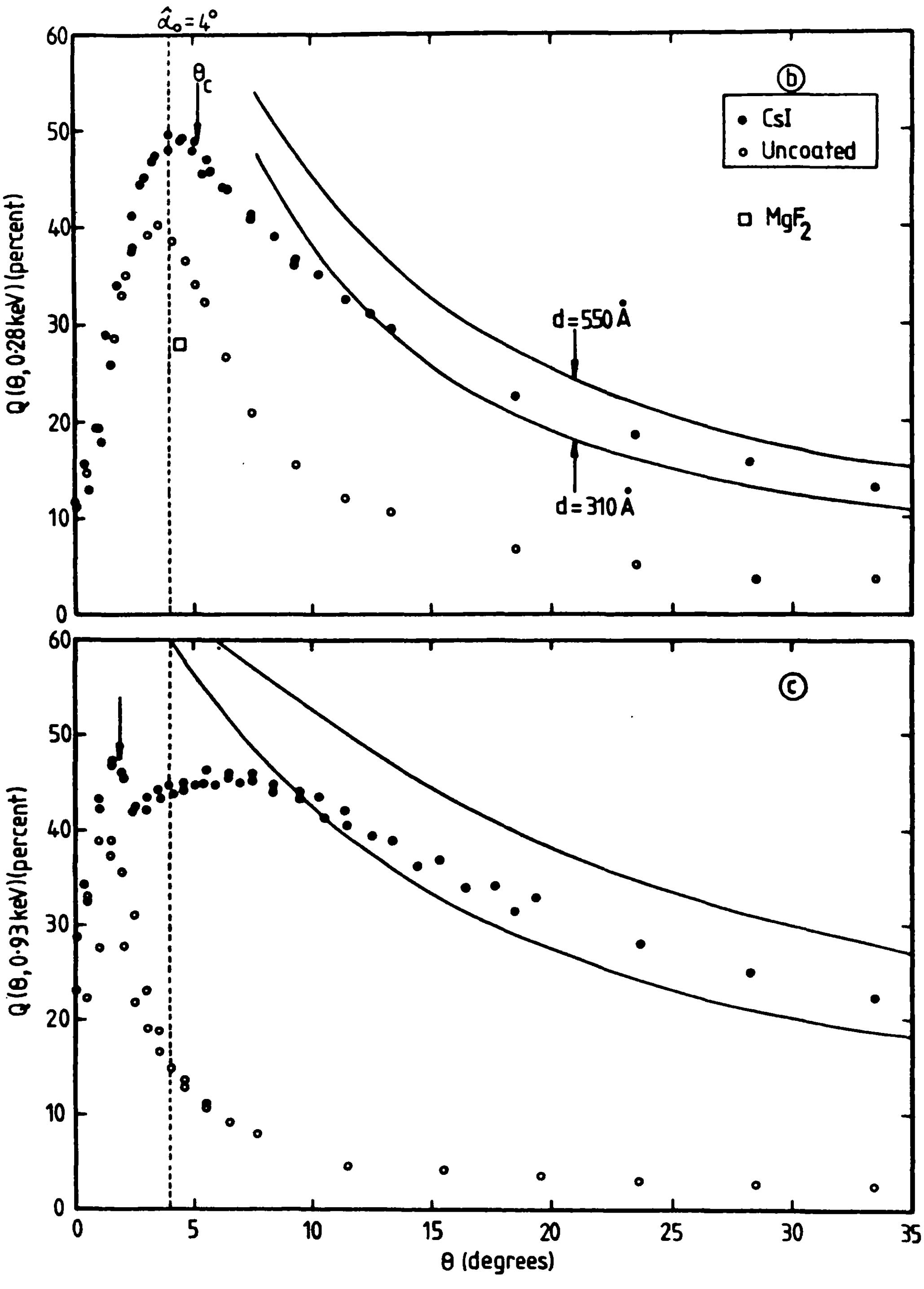

$\hat{\alpha}_0 = 4°$
θ_c
b
CsI
Uncoated
MgF_2
d=550 Å
d=310 Å
Q (θ, 0·28 keV) (percent)
c
Q (θ, 0·93 keV) (percent)
θ (degrees)

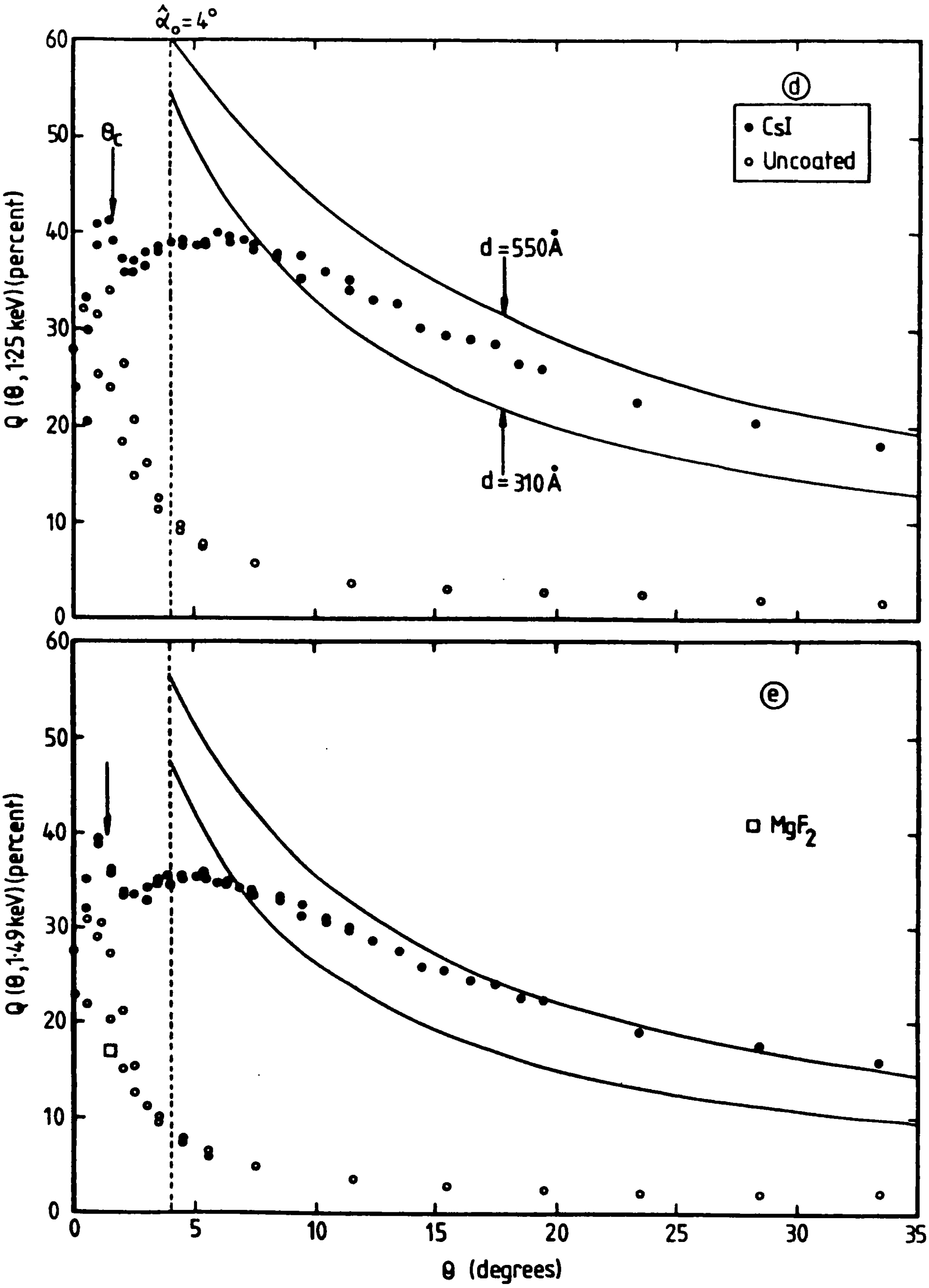

$\hat{\alpha}_o = 4°$
60
50
40
30
20
10
0
θ_c
Q (θ, 1·25 keV) (percent)
ⓓ
• CsI
∘ Uncoated
d = 550 Å
d = 310 Å
60
50
40
30
20
10
0
Q (θ, 1·49 keV) (percent)
ⓔ
□ MgF_2
0
5
10
15
20
25
30
35
θ (degrees)

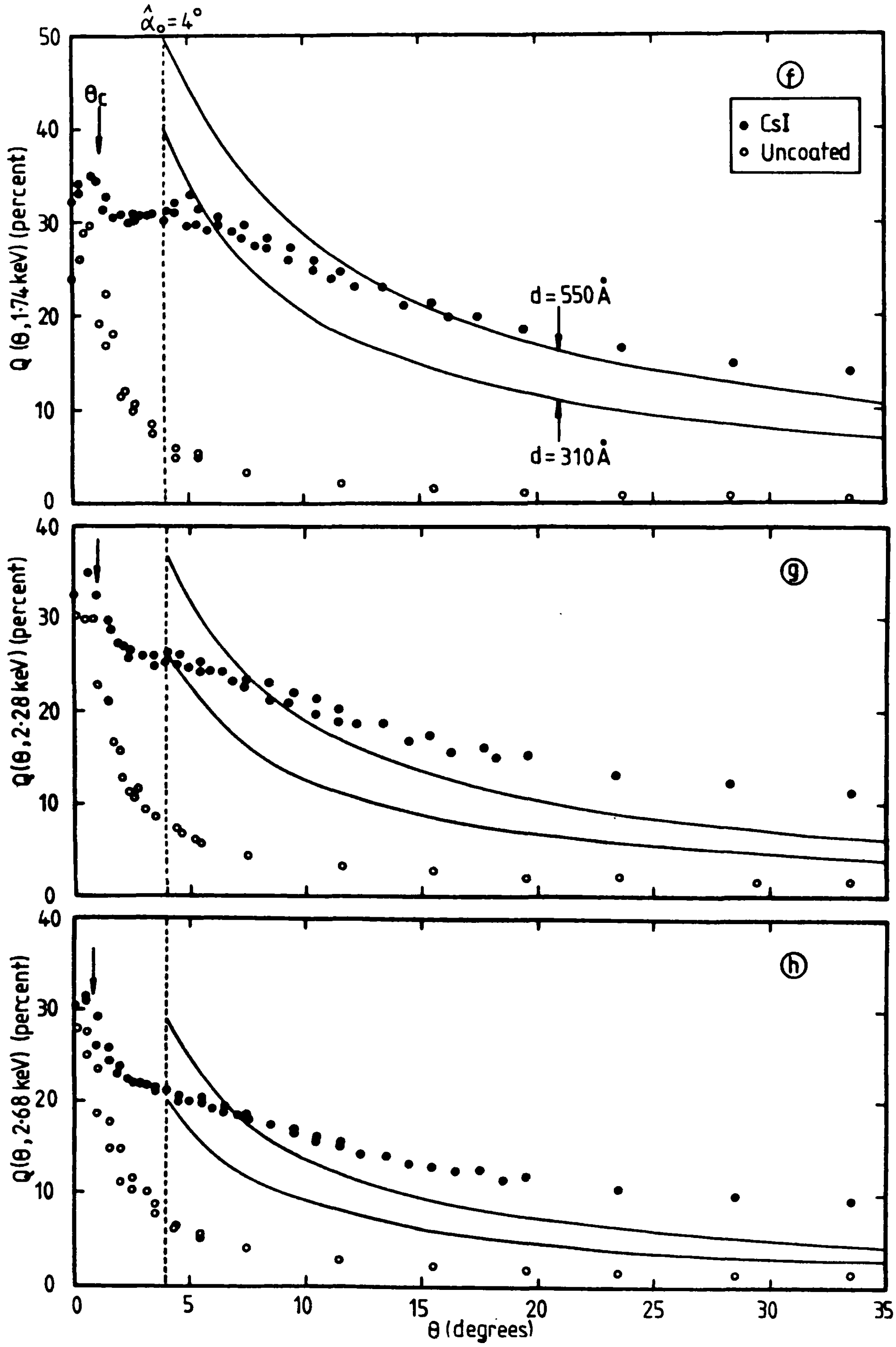
$\hat{\alpha}_o = 4°$
θ_c
(f)
• CsI
∘ Uncoated
d = 550 Å
d = 310 Å
Q (θ, 1·74 keV) (percent)
(g)
Q (θ, 2·28 keV) (percent)
(h)
Q (θ, 2·68 keV) (percent)
θ (degrees)

The double peak structure of Fig.5.5(b) is again obvious in Figs. 5.6(c-f). This structure does not occur in Figs.5.6(a,b) because $\theta_c \gtrsim \hat{\alpha}_o$ for these X-ray energies. In Figs.5.6(g,h) the second peak has degenerated into a plateau region. The plateau indicates that the decreasing contribution to the efficiency from the CsI is being matched by the increasing contribution of the bare glass.

The solid curves of Figs.5.6 (a-h) are again theoretical predictions [124,139]. Overall the model's performance is very good although it is noticeable that there is a systematically increasing error as the energy increases. This effect may be attributable to an inaccurate description of the geometry of the CsI photocathode layer, or to X-rays penetrating through the channel walls to interact with more than one channel [126].

<u>Table 5.2</u>

Measured MCP efficiency enhancement due to CsI coating, as a function of X-ray energy and angle of incidence, for the 120:1 L:D MCP

E_x (keV)	θ (Degrees)			
	5	10	20	30
0.18	1.2	1.5	2.4	3.4
0.28	1.4	2.4	3.5	4.1
0.93	3.9	6.8	9.3	9.6
1.25	4.9	8.4	10.0	10.1
1.49	5.2	8.0	9.8	8.9
1.74	4.8	7.9	9.8	9.1
2.28	4.1	6.4	8.3	7.9
2.68	3.8	5.2	7.0	7.3

CHAPTER 6

MCP FRONT SURFACE DETECTION EFFICIENCY

6.1. Principle of the Repeller Grid

6.1.1. Electrostatics

For an MCP detector operated with a high negative front plate voltage (as described in Chapters 2,4,5), X-rays will only be detected if they interact with the surface of a channel. This happens because the surrounding detector body is at earth potential and hence the electric field changes direction at the channel input (Fig.6.1(a)). Any electrons liberated from the front surface, and also from the very top of the channel, will therefore be accelerated away from, rather than into, the channel. In this configuration the MCP detection efficiency is limited by the open area fraction (≡ 63% for hexagonally packed D=12.5 μm channels on 15 μm pitch).

If, however, a plane conducting surface is placed in front of the MCP and biased to produce an electric field that does not change direction at the MCP surface (Fig.6.1(b)) then photoelectrons can be collected from the front surface [37,145]. The same result can, of course, be achieved by changing the polarity of the MCP bias voltages. If the front surface of the front MCP is operated at a positive potential, then the electric field at the channel input has the same configuration as when a field defining plane is used with "negatively biased" MCP's [146,147].

As mentioned in Section 2.3.1 the latter solution is not particularly suitable for X-ray astronomy because of the danger of detecting the large numbers of background electons which exist in orbit. Some form of field defining plane (repeller grid) is therefore the preferred solution. The overall increase in efficiency will be a balance between the contribution from the front surface and the reduced X-ray transmission because of the

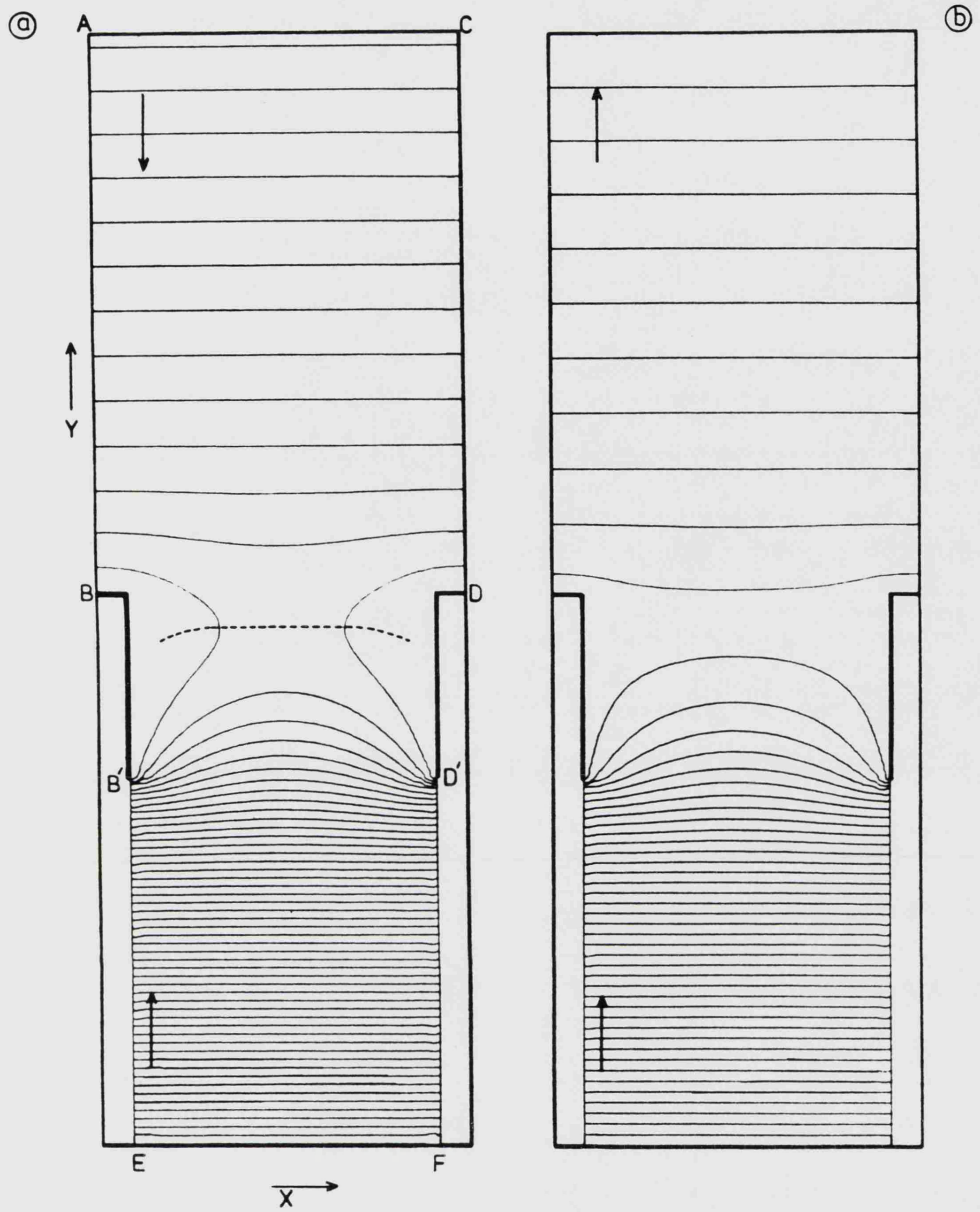

6.1 (a) Potential distribution at MCP input, U(x,y). Finite differences calculation. Contour plot represents section across the diameter of a microchannel, extending 3D above and below the channel entrance plane. The plot is compressed by a factor 1.6 in the y direction. The heavy black lines BB' and DD' represents the end spoiling electrode which penetrates one channel diameter down the channel. U is assigned the value unity along BB' and DD' and its values on the other two equipotential surfaces, AC and EF, adjusted to give any desired ratio of channel electric field strength to input electric field strength ($\mathcal{E}$). Here the ratio is 4:1 and the field vectors are in opposite senses (arrows) as in normal MCP operation ($\mathcal{E}$ negative). The broken line indicates the contour of zero electric field (Courtesy G.W. Fraser).

(b) Potential distribution at input of MCP operated with a field defining plane. Channel and input electric field vectors (arrows) in the same sense ($\mathcal{E}$ positive). Ratio of field strength again 4:1. Note the presence of a weak field region at the channel entrance, due to electrode penetration (Courtesy G.W. Fraser).

non-unity transparency of the repeller grid.

6.1.2. Initial operation

A repeller grid was constructed from tungsten mesh of 85% transparency, and placed approximately 6 mm in front of a chevron MCP detector. The effect of varying the potential of the repeller grid by $\pm$ 400 volts relative to the front MCP (Fig.6.2(a)) was to produce a large change in the output count rate, implying a change in quantum detection efficiency. The maximum count rate variation was obtained at large angles (Fig.6.2(b)). At these angles a large proportion of the X-rays are interacting at the top of the channel and the liberated electrons are therefore sensitive to the external electric field. It should be noted, however, that the MCP efficiency at high angles was very low (typically Q (25°) $\lesssim$ 1%) and hence the errors on the relative count rates are correspondingly high. The results of Fig.6.2(a) are normalised to the results obtained with $V_{grid}=0$ (ie repeller grid potential equals the potential of the front MCP), and give no information as to whether an absolute efficiency increase is produced by the grid.

Subsequent calibration of the data of Fig.6.2(a) indicated an increase in efficiency, due to the repeller grid, from 0.7% to 0.9% at $\theta=32°$ and 1.1% to 1.2% at $\theta=22°$, with a reduction in efficiency from 17.9% to 15.7% at $\theta=2°$. This confirms [37,145,146,147] that the changed electric field improves the detection efficiency by allowing the collection of electrons liberated from the front surface. To obtain maximum benefit from a repeller grid, however, a mesh of higher transparency is required together with a photocathode to increase the secondary electron yield of the front surface.

6.2. MCP with a Modified Input Electrode Geometry

6.2.1. Background

Consideration was given to any properties, other than grid

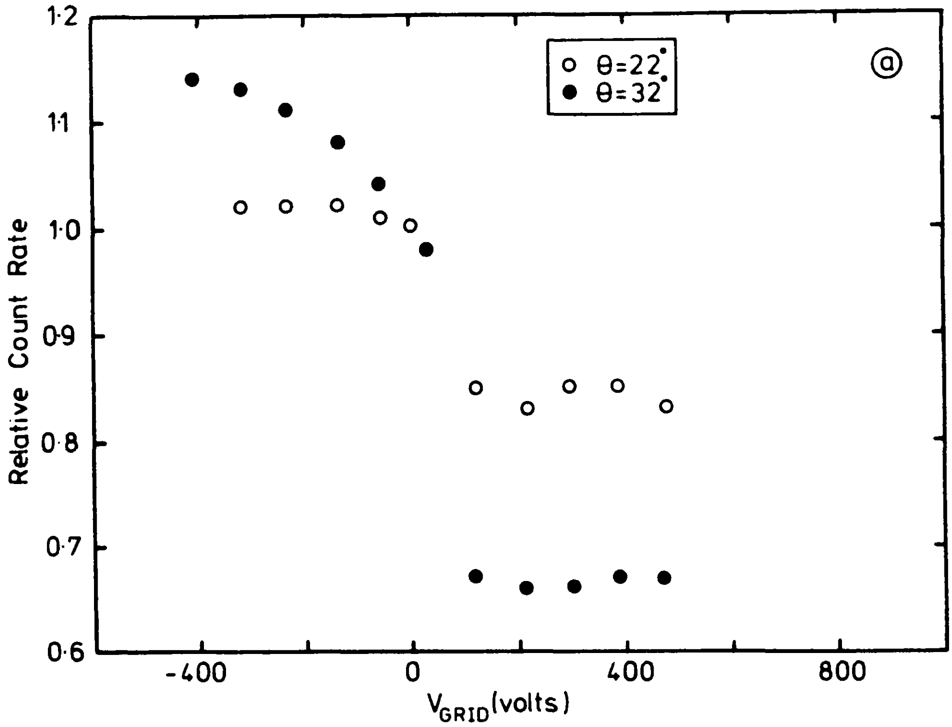

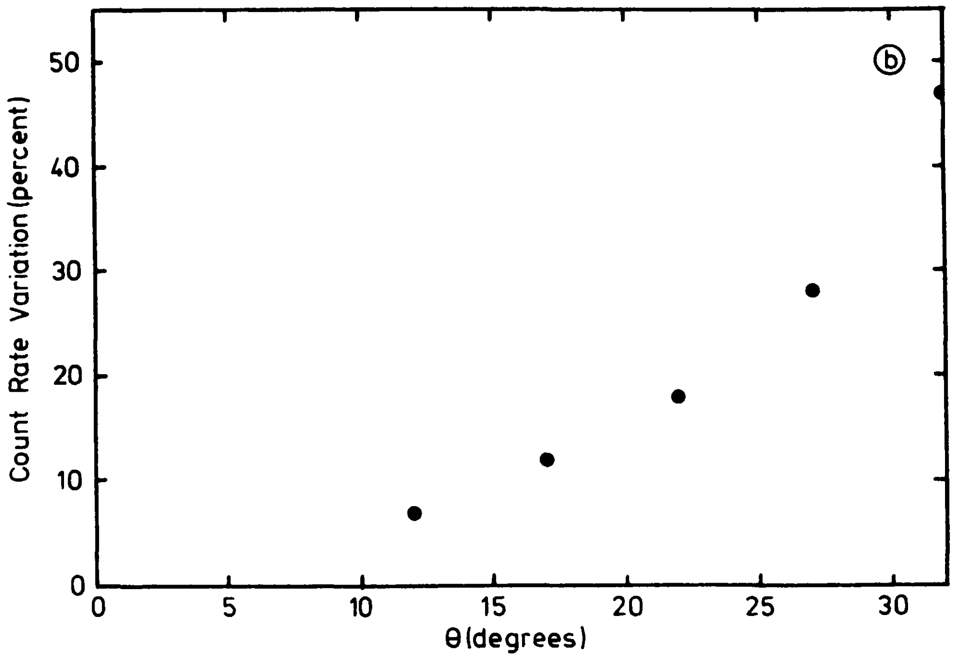

6.2. (a) Variation of output count rate as a function of V_{Grid} (Voltage difference between the repeller grid and the front MCP) for Cu-L (0.93 keV) X-rays incident at θ=22° (open circles) and θ=32° (filled circles) on an uncoated MCP. Output count rate normalised to 1.0 for V_{Grid}=0.

(b) Maximum observed variation in count rate induced by varying V_{Grid} (high negative V_{Grid} minus high positive V_{Grid}) as a function of angle, θ. Cu-L (0.93 keV) X-rays incident on an uncoated MCP.

transparency and front surface secondary electron yield (Section 6.1.2), that might effect the front surface efficiency. Since the basic conversion efficiency (X-rays to electrons) depends only on the geometry (which is fixed) and the photocathode material, the only possible factor that can be changed is the probability of the liberated secondary electrons reaching the channels. A possible influence is the distortion of the electric field by the penetration into the channel of the nichrome electrode. This would have the effect of reducing the probability of an electron liberated from the front surface getting into a channel because of compression of the electric field lines.

To evaluate properly the possible effect of the electrode penetration requires a numerical model. The real situation, however, must lie between the two extremes of; (1) plane with a slot (Fig.6.3(a)), (2) ideal parallel plane (Fig.6.3(b)), both of which have simple analytical solutions [148]. If we consider the trajectories of electrons coming in from infinity in each of these two cases, we will have a measure of the extent to which the electrode penetration may reduce the efficiency. In Fig.6.3(b) electrons that hit the very edge of the channel originate at a radial distance r from the channel axis and hence the probability of an electron entering the channel is just the geometric open area ratio, A_{open}. In Fig.6.3(a) however the same electrons originate at a radial distance $r/2$, because of the differing electric field configuration. The probability of an electron, coming from infinity, entering a channel is therefore reduced to $A_{open}/4$.

If Fig.6.3(a) is a good representation of a normal MCP with a 1 diameter electrode penetration, and Fig.6.3(b) is a good representation of a MCP with no electrode penetration, then the probability of a liberated secondary electron being detected may be up to four times higher for a MCP with no electrode penetration than for a normal MCP.

Since the front surface intercepts 37% of the incoming X-rays, the

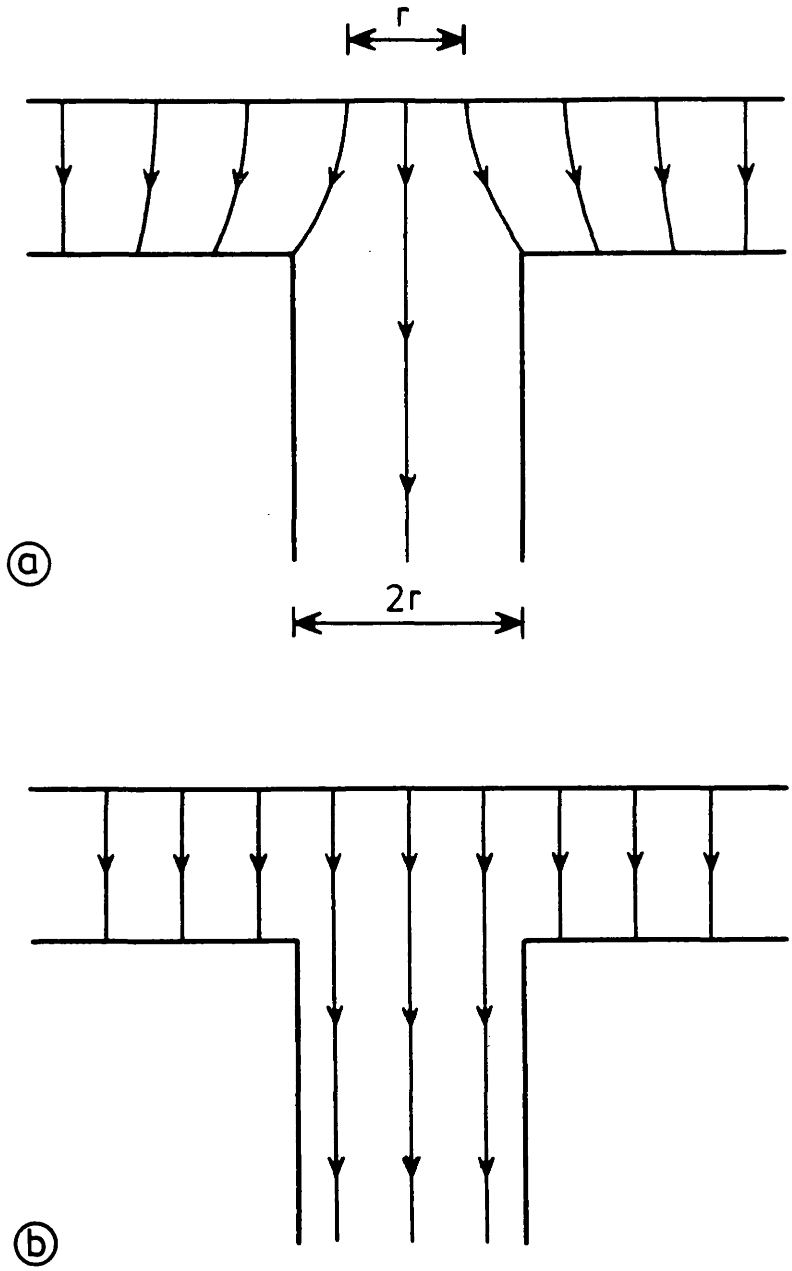

6.3. Simple analytically soluble models of the electric field at the entrance to a microchannel.

(a) A microchannel with a normal 1 D electrode penetration, modelled by a plane with an infinitely long conducting slot. The lensing probability for electrons is reduced by a factor of 4 over the open area ratio (see text).

(b) A microchannel with no electrode penetration, modelled by assuming the field lines are undisturbed by the channel. The electron lensing probaiblity equals the open area ratio.

possible front surface contribution is significant compared with the efficiencies measured in Section 5.4. The possibility of increasing the collection efficiency, for electrons liberated from the front surface, by a factor of order four is therefore worth investigating. The results of an attempt to produce a Zero Depth penetration Nichrome (ZDN) electrode MCP are described in the following sections.

6.2.2. Coating Geometry and Procedures

An L:D=120:1 MCP with bias angle $\theta_B=0°$, a normal one diameter penetration rear electrode and no input electrode, was purchased. This allowed the input electrode (nichrome alloy; 7 parts nickel, 3 parts iron, 2 parts chromium) to be applied to our specification. There are two ways of attempting to produce an electrode that does not penetrate into the channels (Figs.6.4(a,b)). The oblique incidence method illustrated in Fig.6.4(b) is the best way of ensuring that no nichrome penetrates the channels, but because of the large coating angle, $\hat{\alpha}_O=90-\delta$ (δ small), a very large quantity of nichrome is needed to produce the necessary ($\gtrsim$ 250 Å) electrode thickness. Trial evaporations showed quite clearly that this geometry was unusable in the available evaporation plant.

The adopted geometry was therefore that which was suggested by the manufacturer (Fig.6.5(a)), of placing the nichrome wire directly underneath the MCP to give $\hat{\alpha}_O=0°$ (see below). This arrangement gave rise to a range of small coating angles ($\hat{\alpha} \lesssim 2.5°$), and hence large penetrations into the channels. It was hoped that the resulting layers would be too thin (< 10 Å) to act as effective conductors even at the edges of the MCP.

The nichrome coating was deposited by vacuum evaporation in the same coating plant as used for CsI evaporation (Section 5.1). The MCP substrate was heated to ~100°C and cleaned by a high tension glow discharge. A 200 mm length of 0.5 mm diameter nichrome wire was evaporated from a tungsten filament to give an electrode thickness of ~380 Å on the MCP

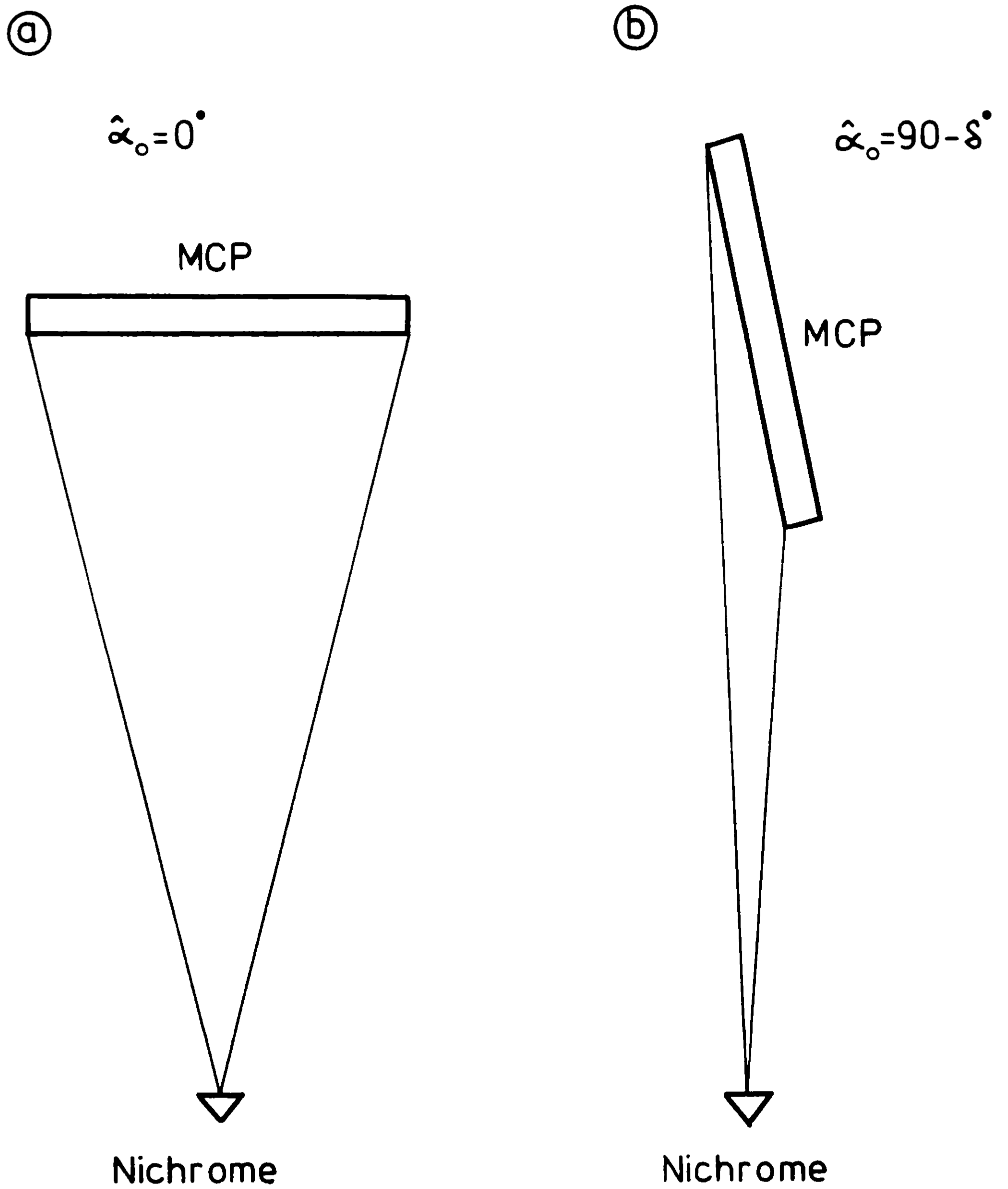

6.4. (a) Evaporation geometry used to produce the ZDN MCP (see text), $\hat{\alpha}_0=0°$ and MCP-filament separation maximised.

(b) Alternative geometry producing minimal electrode penetration. The very large coating angle, $\hat{\alpha}_0=90-\delta$, requires a prohibitive amount of nichrome to produce a suitable electrode thickness.

front surface as measured by an Edwards FTM 4 film thickness monitor.

6.2.3. Operating characteristics

The ZDN MCP was paired with a 13° bias angle L:D=120:1 rear MCP (the same rear plate used for efficiency measurements in Chapter 5), and operated as a chevron detector in the VTF. All investigations were carried out using C-K (0.28 keV) X-rays. Initial measurements were carried out with an X-ray incident angle $\theta=6°$. The detector produced a good PHD with peak gain G_c=4.3 pC, FWHM=42% (V_F=1600 volts, V_G=200 volts, V_R=1500 volts).

Measurements of the quantum detection efficiency of the ZDN MCP (Fig.6.5 filled circles) were, however, anomalous in comparison with previous uncoated plate data (Fig.5.6(b)). The low angle response, $\theta<\sim 5°$ is quite similar in the two cases but the efficiency of the ZDN plate falls off very rapidly as the angle increases. The behaviour is unlike anything that has been previously observed.

The possibility existed that this was a consequence of operating a ZDN plate without a field defining plane. A repeller grid, made from 95% transparent tungsten mesh, was therefore installed 4.3 mm in front of the MCP. The variation of efficiency with grid bias voltage is shown in Fig.6.6. A set of efficiency measurements (Fig.6.5 open circles) were then taken with V_{grid}=-200 volts. Some slight improvement was visible at large angles but nothing of the order required to bring the ZDN efficiencies up to previously observed bare MCP levels.

Another peculiarity was the variation of the PHD gain and FWHM with the interplate gap voltage, V_G (Fig.6.7), which contrasts somewhat with the behaviour described in Section 4.1. The variation of the FWHM is similar to that observed previously but there is no significant trend in the behaviour of the gain (typical errors in G_c being $\pm$ 0.2 pC).

The non-standard behaviour could either have been an intrinsic

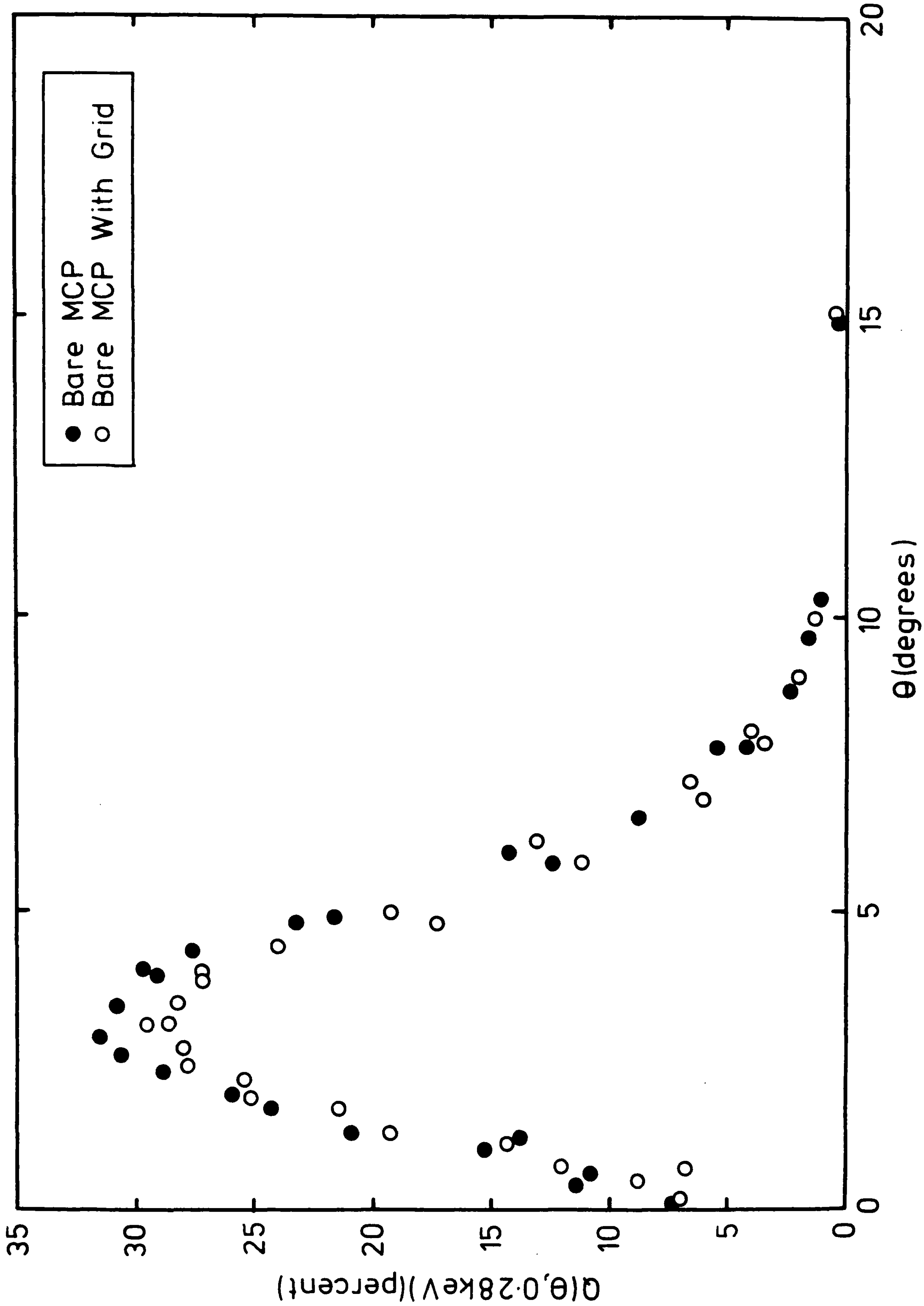

6.5. MCP quantum detection efficiency versus angle of X-ray incidence, θ, for the ZDN MCP without repeller grid (filled circles) and with repeller grid (open circles). V_{Grid}=-100 volts, repeller grid transmission 95%, C-K (0.28 keV) X-rays.

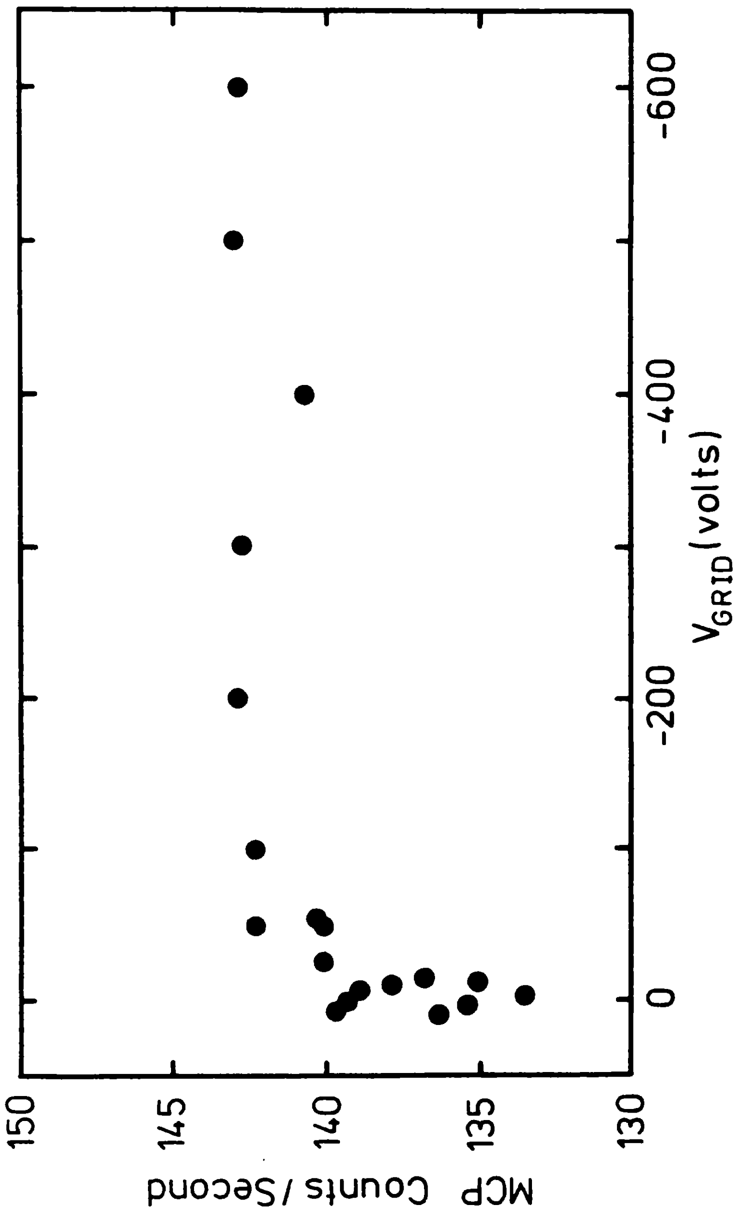

6.6. Variation of count rate (≡ efficiency; constant input X-ray flux) from the ZDN detector as a function of voltage between repeller grid and front MCP, V_{Grid}. C-K (0.28 keV) X-rays. Scatter caused by X-ray source instability.

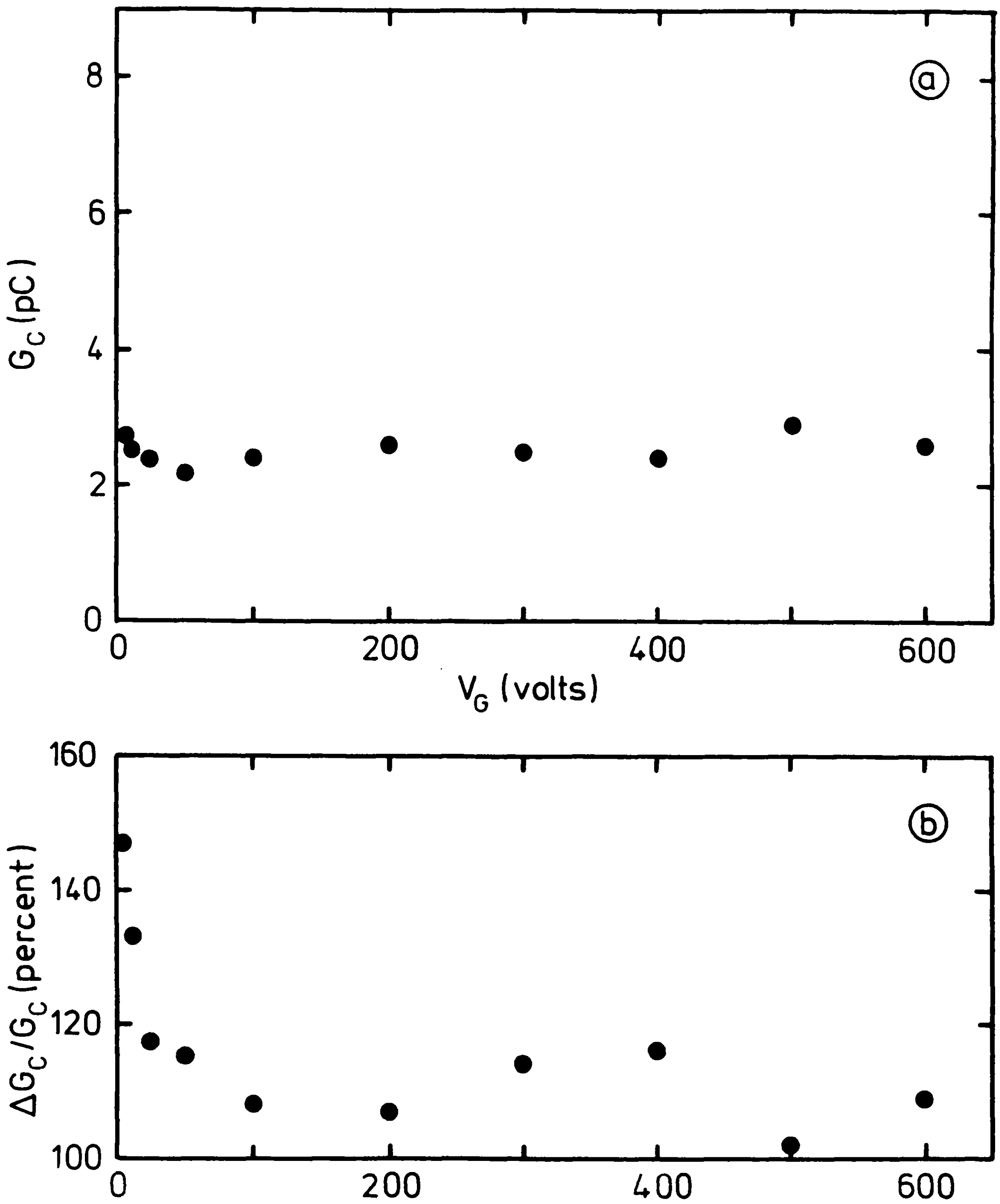

6.7. (a) Variation of peak gain, G_C , with accelerating bias voltage, V_G , for the ZDN detector.

(b) Variation of FWHM, $\Delta G_C/G_C$, as a function of V_G for the ZDN detector. $\theta = 6°$ C-K (0.28 keV) X-rays.

property of this particular MCP or a characteristic of the special nichrome electrode. To test the general operation of the MCP it was turned over and inserted into the detector with the ZDN face as the output face . The input face then had a normal one diameter penetration electrode. In this reversed mode the peak gain dropped by ≈ 35% and the FWHM increased slightly. The detection efficiency for the reversed mode of operation is shown in Fig.6.8(a) and the variation of the peak gain, G_c , and FWHM with V_G in Figs.6.9(a,b). The behaviour shown in both of these figures is what would be expected from a normal MCP; the special nichrome electrode must therefore be the cause of the anomalies described above.

Another curious difference between the operation of the detector in the two modes was the variation in the current drawn by the rear MCP. If the rear MCP was biased to full operating voltage, (V_R=1700 volts) and the ZDN plate bias voltage was raised from 1000 volts to full operating voltage (1550 volts) the current drawn by the rear MCP increased by 0.1 μA (4% increase). When the ZDN plate was reversed this increase was only 0.01 μA, which was within the measuring error of the ammeters. Both variations were very reproducible, with the behaviour of the reversed ZDN plate being the same as normal MCP's.

6.2.4. Discussion

A possible interpretation of the anomalous behaviour is that the nichrome deposited on the channel walls (Section 6.2.2) acts as an effective conductor to a depth of many channel diameters. To test this hypothesis consider a very simplistic model where efficiency is proportional to the channel length illuminated by the X-ray beam. Let the efficiency of the reversed ZDN plate, $Q_R(\theta)$ be given by:

$$Q_R(\theta) \propto D \cot\theta \tag{6.1}$$

This produces a reasonable fit to data in the large angle regime [102], although the fit is less good at the angles of interest here. Then let

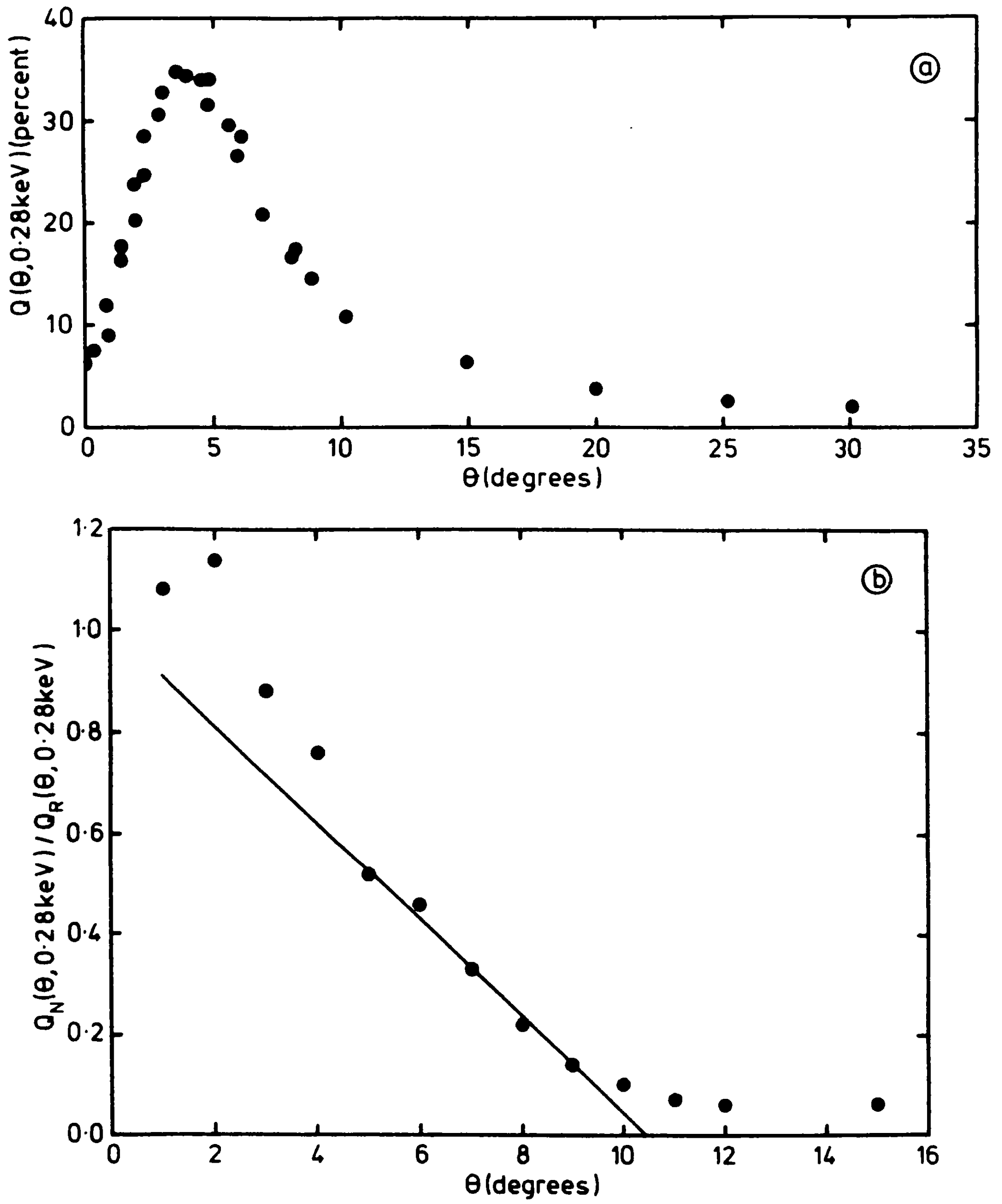

6.8. (a) MCP quantum detection efficiency versus angle of X-ray incidence, θ, for the reversed ZDN MCP with repeller grid. V_{Grid}=-200 volts. C-K (0.28 keV) X-rays.

(b) Ratio of ZDN MCP efficiency with repeller grid, Q_n (Fig.6.5) to efficiency of reversed ZDN MCP with repeller grid, Q_R, (Fig.6.8(a)) (filled circles). The solid curve represents the best fit of equation 6.3 using n=5.4.

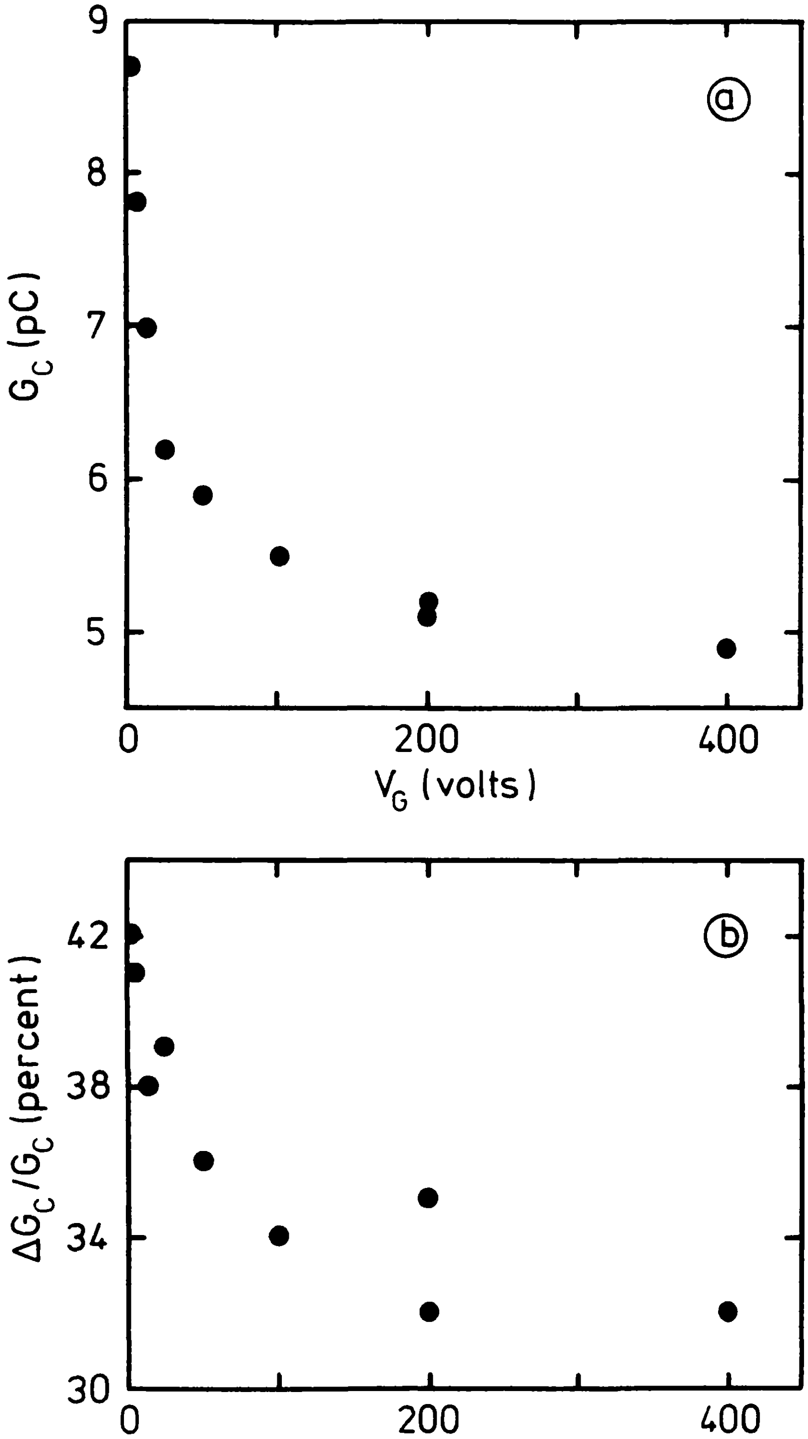

6.9. (a) Variation of peak gain, G_C , with interplate bias voltage, V_G , for the reversed ZDN detector. $\theta = 11°$, C-K (0.28 keV) X-rays.

(b) Variation of FWHM, $\Delta G_C/G_C$, as a function of V_G for the reversed ZDN detector.

the efficiency of the ZDN plate be given by $Q_N(\theta)$:

$$Q_N(\theta) \propto D\ (\cot\theta - n) \qquad (6.2)$$

where D is the channel diameter and n is the length of "dead" channel, in channel diameters. The dead region at the top of the channel could be caused by the nichrome electrode in two possible ways. The electrode will alter the electric field configuration at the mouth of the channel to produce a very weak field region and hence the probability of an ejected electron initiating an avalanche will be reduced. Secondly calculations indicate that the quantum detection efficiency of the nichrome in the θ=10°-30° range is a factor of ~ 2 lower than for MCP glass, which would again reduce the high angle efficiency of the ZDN plate.

Combining equation (6.1) and (6.2) we get:

$$\frac{Q_N}{Q_R} = \frac{\cot\theta - n}{\cot\theta} = 1 - n\tan\theta \qquad (6.3)$$

Measured Q_N/Q_R ratios together with the best fit prediction from Equation 6.3 (n=5.4) are shown in Fig.6.8(b). The errors in the experimental ratios are large for $\theta \lesssim 4°$ because the efficiency is changing very rapidly with angle. The model also has a limited range of validity since above θ=10.5° the predicted ratio Q_N/Q_R goes negative. Within the angular range 4°-10° both model and data set should be quite good and a best fit to the data gives n=5.4. Now since a normal MCP with a one diameter electrode penetration does not produce any dead area, it would seem likely that the effective electrode penetration for the ZDN plate is $\sim$ 6.5 D.

The large electrode penetration should not affect the MCP's performance when it is reversed, because the electron multiplication has already taken place and the weak accelerating field at the output still allows the charge cloud to exit from the channel. Figs.6.9(a,b) show the variation of G_C and FWHM with V_G for the reversed ZDN plate. The results indicate that the overall effect of having a large diameter electrode penetration on the output face was to produce either a wider output beam or higher energy electrons since a larger than normal value of V_G was required for G_c to reach its asymptotic value. The reason for the flat curve shown in Fig.6.7(a) is unknown.

The observed increase in current drawn by the rear MCP, as the ZDN plate bias voltage was raised from 1000-1550 volts is rather difficult to explain. A major difference between this and other MCP's is the existence of very thin nichrome layers on the channel wall and this may be a source of field emission. With the special electrode as the input there might be sufficient multiplication to produce a significant input to the rear MCP but not enough to produce counts over the lower level discriminator. When the MCP was reversed the front plate gain for these events would be very low and hence would not produce a significant load on the rear MCP.

The above explanation is rather weak, however, because there is no supporting evidence from high X-ray count rate behaviour. It would be expected that a very high X-ray count rate would also be able to stimulate the rear plate sufficiently to produce an increase in the current drawn by it, and this has not been observed. An increase may be observed however if the whole MCP active area was bombarded with X-rays instead of just the one small area that has been tried.

The overall conclusion to be drawn from this work was that it was not possible to produce an MCP with a zero penetration electrode using the technique of Fig.6.4(a). The presently available ZDN MCP is inferior in operation to MCP's with normal electrode geometry.

The alternative coating geometry Fig.6.4(b) would have been very difficult to implement. A more detailed theoretical study of the electric field, using a two dimensional numerical model, was therefore undertaken. The results of this study for a normal one diameter electrode penetration are shown in Figs. 6.1(a,b) and for no electrode penetration in Figs.6.10 (a,b). These show that the real situation is much closer to Fig.6.3(b)

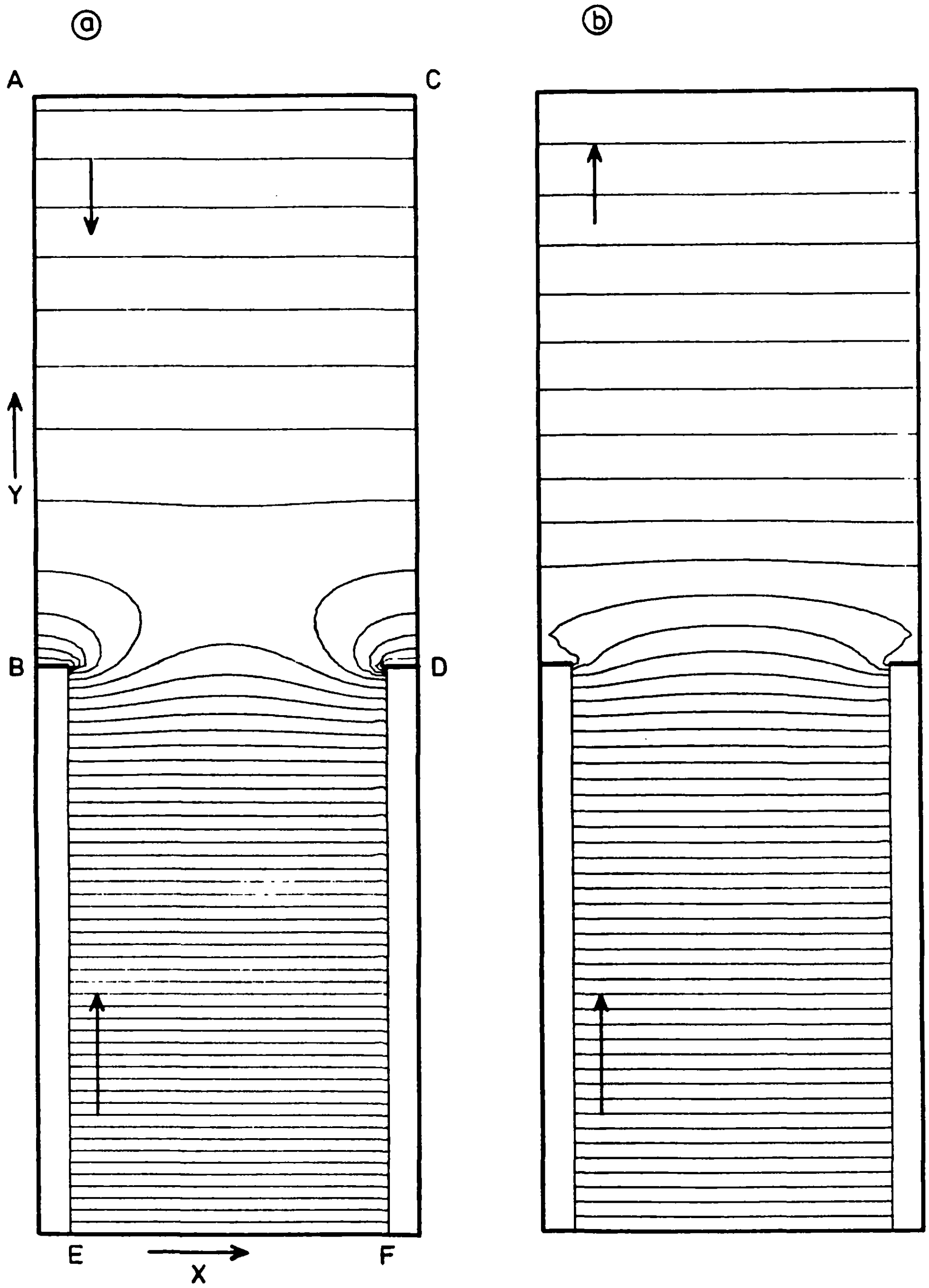

6.10. (a) Potential distribution at MCP input, $U(x,y)$. As for Fig.6.1(a) except electrode does not penetrate into channel (Courtesy G.W. Fraser).

(b) Potential distribution at MCP input, $U(x,y)$, when operated with a field defining plane. As for Fig.6.1(b) except electrode does not penetrate into channel (Courtesy G.W. Fraser).

than Fig.6.3(a) and therefore there is no great advantage in using a zero penetration electrode. A small advantage still exists but the factor of four increase in efficiency initially hoped for is not possible. The very small increases possible do not make developing the coating geometry of Fig.6.4(b) worthwhile.

The numerical model was also used to investigate the effects of larger penetration. Fig.6.11 shows the result for a 1.5 D penetration electrode and as expected a very weak field region exists at the top of the channel. This backs up the hypothesis that a 6.5 D penetration electrode would produce a large "dead" area at the top of the channel. Limitations within the model did not allow the calculation of the electric field for a 6.5 D penetration electrode.

6.3. Use of a Repeller Grid with a CsI Reflection Photocathode

6.3.1. Results

The CsI coated MCP described in Chapter 5 (L:D=120:1) was operated with the 95% transparent repeller grid described in Section 6.2.3. A series of measurements were made with C-K (0.28 keV) and Si-K (1.74 keV) X-rays to determine the effect on the efficiency of the electric field, $\mathcal{E}$, in front of the MCP. The results are shown in Figs.6.12 and 6.13. As expected from Figs.6.2(a,b) significant variation in efficiency can be produced by varying $\mathcal{E}$. More importantly considerable overall increases in efficiency can be produced compared with the results obtained without the repeller grid. This increase in effectiveness of the grid is as expected, since CsI is a much better X-ray photocathode than the nichrome of the bare MCP.

The basic shape of the efficiency curves was not changed by use of the grid, as can be seen in Figs.6.14 (a,b), 6.15 (a,b) which show the efficiency curves for both CsI coated and bare MCP with C-K and Si-K X-rays. Table 6.1 gives the measured absolute increase in efficiency on the CsI

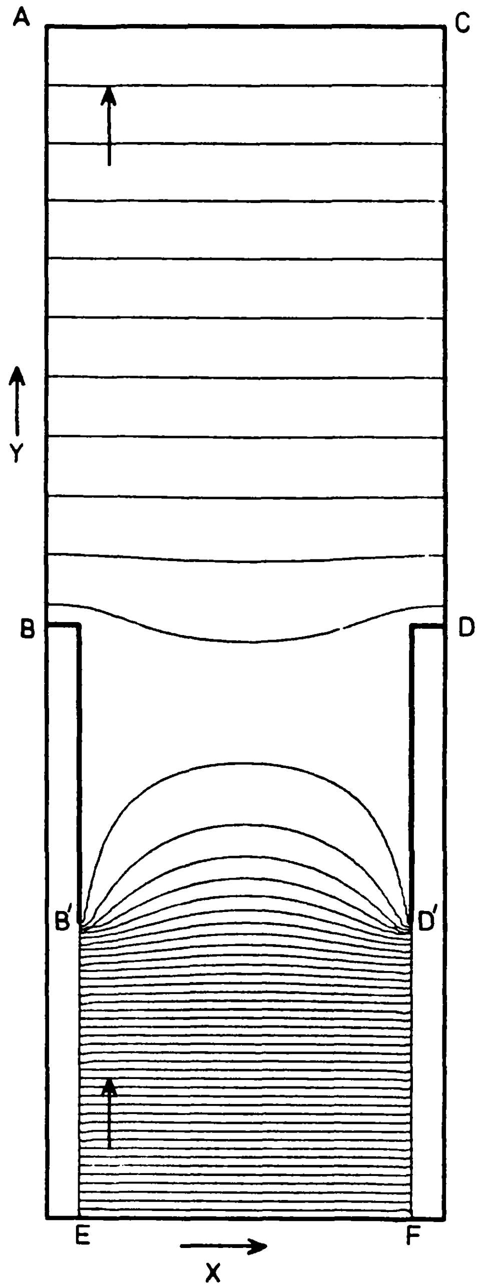

6.11. Potential distribution at MCP input, U(x,y) , when operated with a field defining plane. As Fig.6.1(b) except electrode penetrates 1.5 D into channel (Courtesy G.W. Fraser).

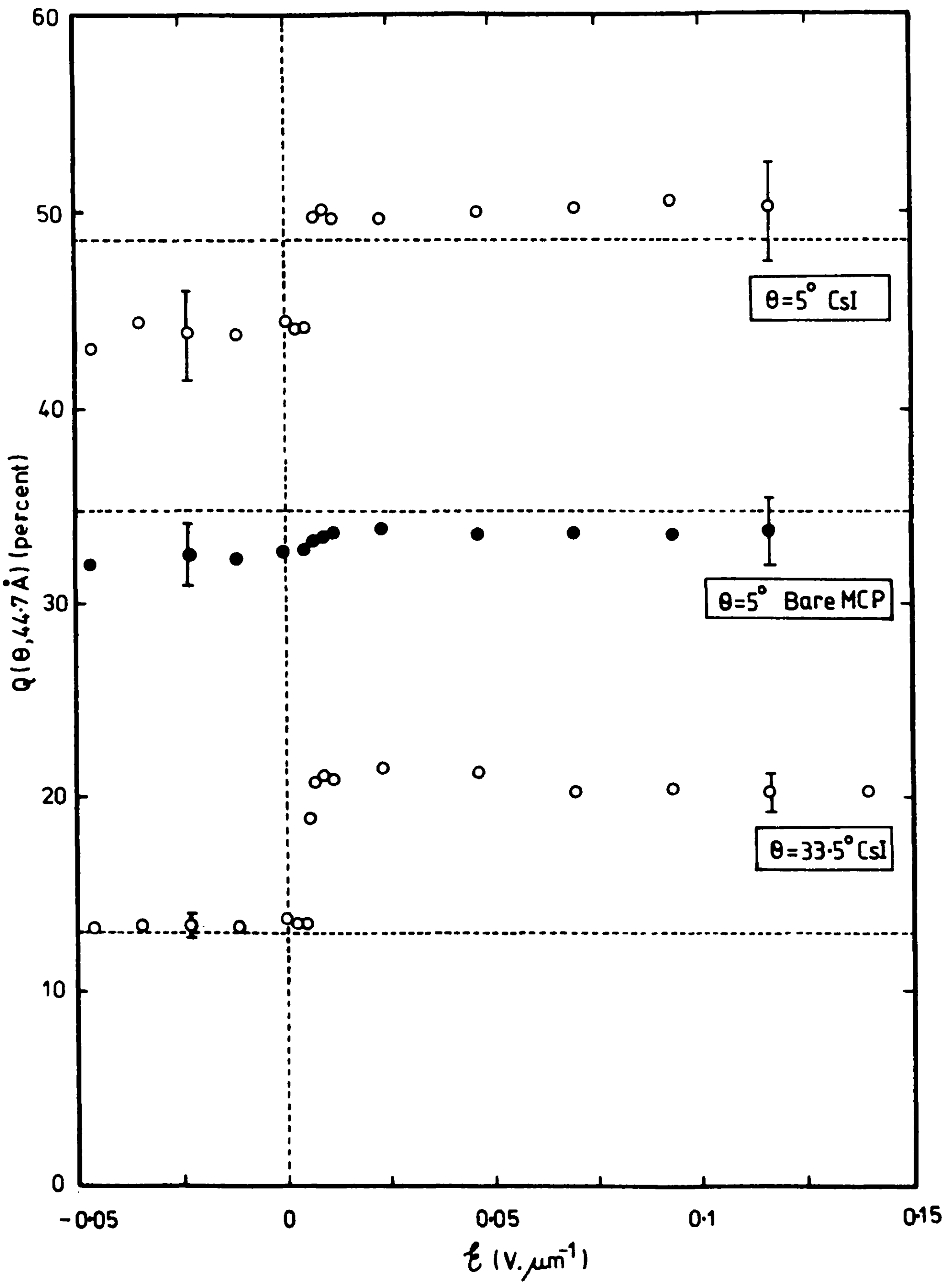

6.12. Variation of total MCP efficiency, Q(θ, 44.7 A°) with electric field at MCP input $\mathcal{E}$. Measurements made on CsI coated (open circles) and bare (filled circles) halves of the MCP. Repeller grid transparency T_0=0.95, mounted 4.3 mm in front of the MCP. The broken vertical line indicates $\mathcal{E}$=0 . The broken horizontal line indicates values of open area efficiency measured with the grid absent ($\mathcal{E}$=-0.25 V μm^{-1}) for each of three incident angle/ photocathode combinations.

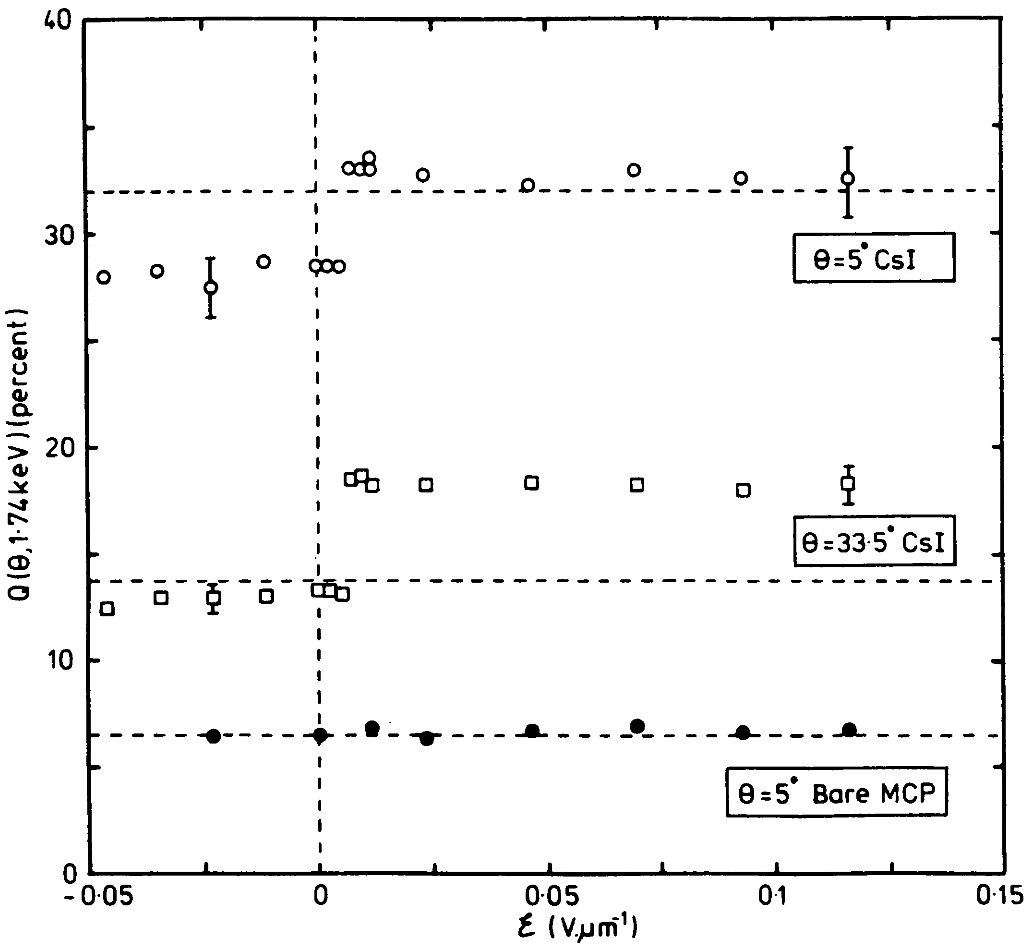

6.13. As Fig.6.12 except variation of total MCP efficiency, Q(θ, 1.49 keV) with electric field at MCP input ℰ.

half obtained by using the repeller grid. Table 6.2 compares the limiting efficiency values obtained at high positive and high negative electric fields in Figs.6.12, 6.13. The ratio Q_{G_1}/Q_{G_2} gives the expected increase in efficiency for a grid of unity transmission (compare with Q_G/Q in Table 6.1).

There was no observed change in peak gain and FWHM of the output PHD when the grid was used. The detector noise count rate was not affected by the grid. Taylor et al [145] report degradation of image resolution when using a similar grid, because electrons enter channels distant from the point of X-ray interaction. For practical reasons no attempt to investigate this degradation could be made here, but the detector was shown to operate successfully at electric field strengths which should produce relatively little degradation [145].

6.3.2. Interpretation

The results shown in Figs.6.12 and 6.13 for negative $\mathcal{E}$ values imply a repeller grid transmission of 88-103%. These values are however within experimental error of the nominal 95% transmission of the grid. Small systematic differences in the X-ray transmission of the carbon coated polypropylene window are introduced each time the detector is disassembled because it must be removed and then replaced on reassembly. Since the window does not have a locating mechanism small changes in position, and hence window transmission, will have occurred when the detector was disassembled to install the grid.

The expected front surface contribution, $(\Delta Q)_{calc}$, was calculated using a theoretical model [139] and compared with the experimental results ΔQ (Table 6.2). With typical experimental errors on ΔQ being $\pm$ 1.4% for θ=5° and $\pm$ 0.9% at θ=33.5°, agreement between theory and experiment is good at low angles but not at high angles. The qualitative behaviour of $(\Delta Q)_{calc}$ and ΔQ is very similar, however, with:

Table 6.1

Comparison of efficiencies measured with the repeller grid, Q_G , and without the repeller grid, Q . V_{grid} = -100 volts.

Energy	$\theta^{(o)}$	Q_G (%)	Q (%)	Q_G-Q (%)	Q_G/Q
C-K	5	49.4	48.5	0.9	1.02
C-K	10	37.3	35.5	1.8	1.05
C-K	15	31.5	27.2	4.3	1.16
C-K	20	27.5	22.0	5.5	1.25
C-K	25	25.5	17.0	8.5	1.50
C-K	33.5	21.1	13.0	8.1	1.62
Si-K	5	32.5	32.0	0.5	1.02
Si-K	10	28.3	26.2	2.1	1.08
Si-K	15	24.5	21.3	3.2	1.15
Si-K	20	22.0	17.7	4.3	1.24
Si-K	25	20.8	15.8	5.0	1.32
Si-K	33.5	18.8	13.9	4.9	1.35

Table 6.2

Comparison between average efficiencies measured on the CsI half, with the grid, for positive $\mathcal{E}(Q_{G_1})$ and negative $\mathcal{E}(Q_{G_2})$. $(\Delta Q)_{calc}$ is the theoretical prediction [139] for $\Delta Q = Q_{G_1} - Q_{G_2}$.

Energy	θ	Q_{G_1}	Q_{G_2}	ΔQ	$(\Delta Q)_{calc}$	Q_{G_1}/Q_{G_2}
C-K	5	50.1	44.0	6.1	4.8	1.14
C-K	33.5	20.7	13.4	7.3	5.3	1.54
Si-K	5	32.7	28.0	4.7	3.5	1.17
Si-K	33.5	18.3	12.9	5.4	4.0	1.42

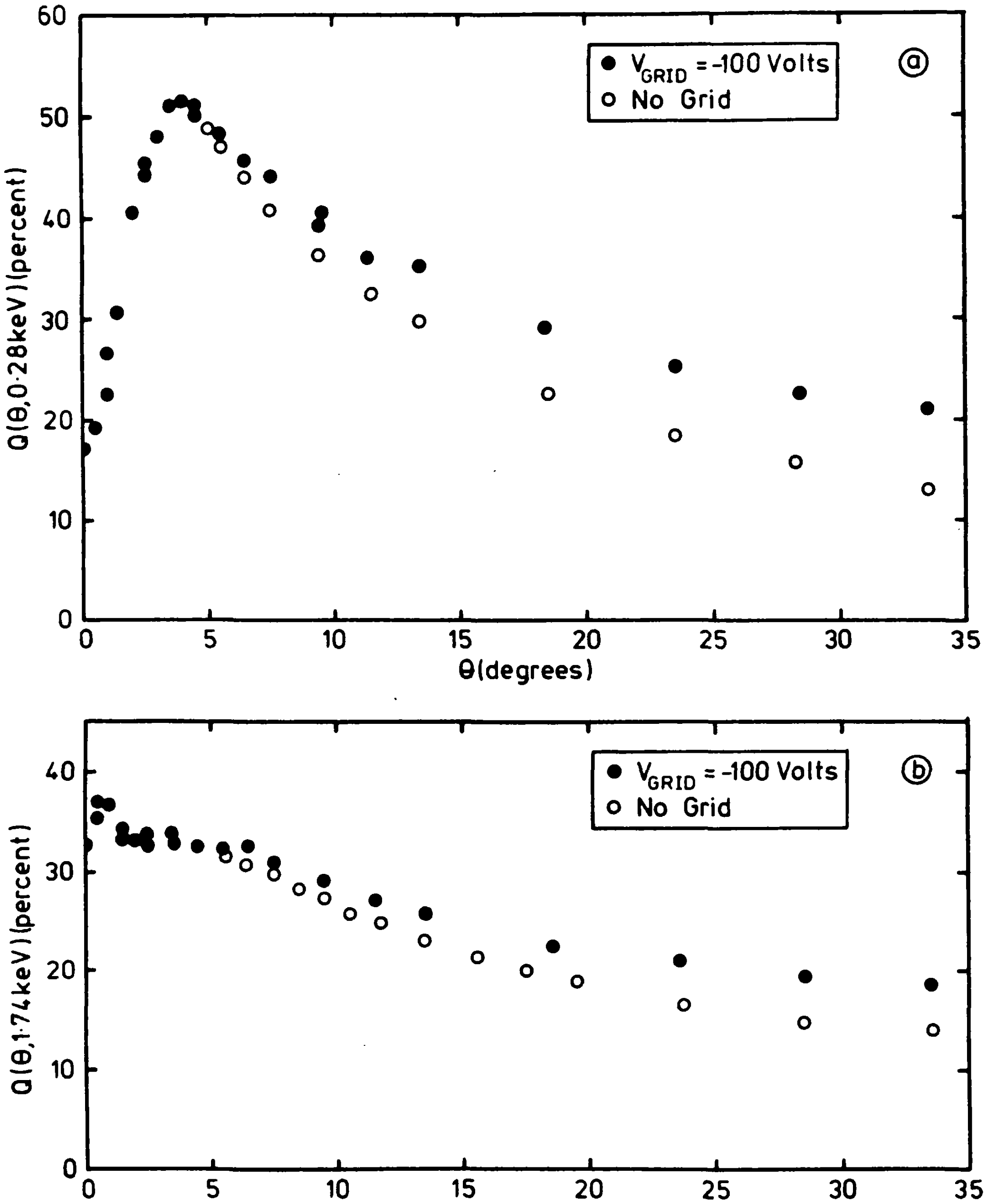

6.14. (a) MCP quantum detection efficiency versus angle of X-ray incidence for the CsI coated half, with repeller grid (filled circles) and without repeller grid (open circles). V_{Grid}=-100 volts. C-K (0.28 keV) X-rays.

(b) As Fig.6.14(a) except Si-K (1.74 keV) X-rays.

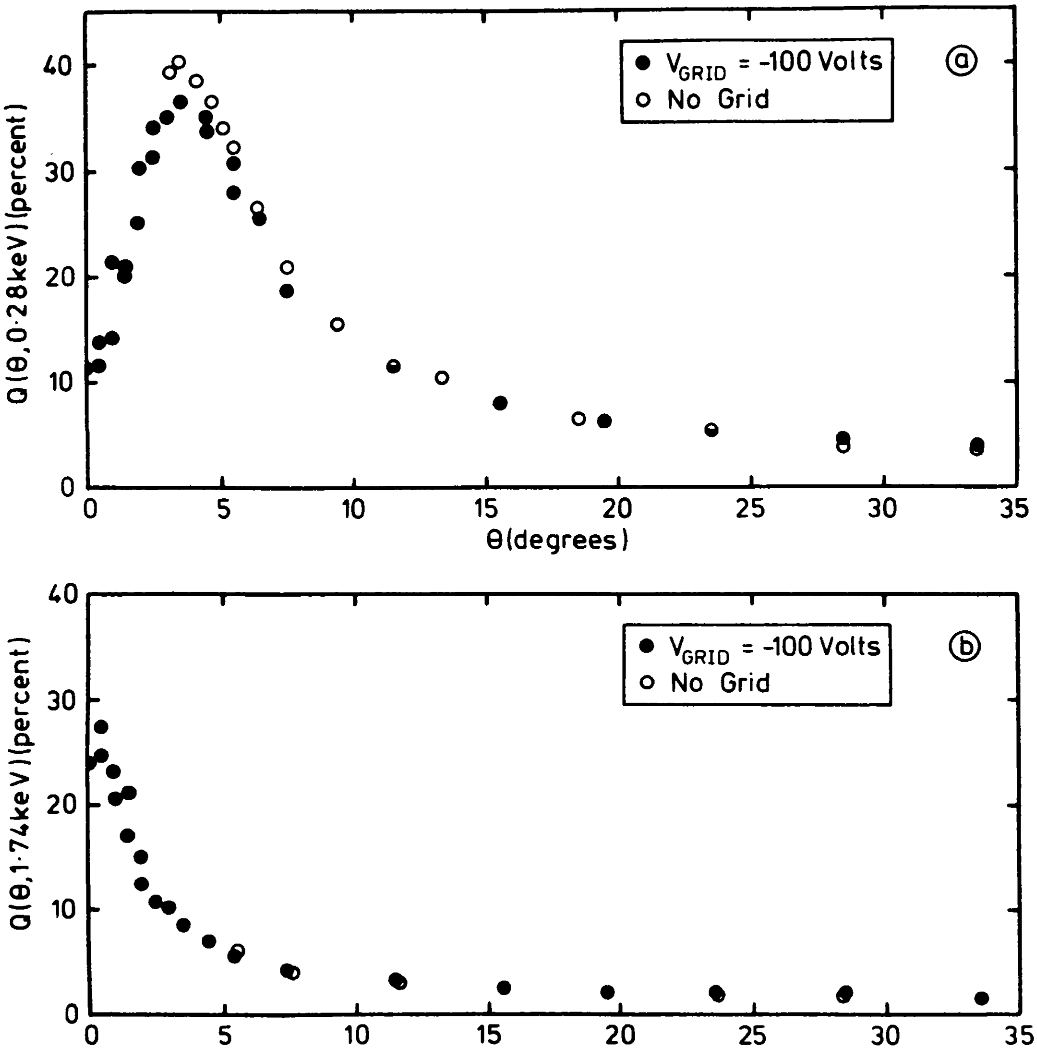

6.15. (a) MCP quantum detection efficiency versus angle of X-ray incidence for the uncoated MCP half with repeller grid (filled circles), without repeller grid (open circles). V_{Grid}=-100 volts. C-K (0.28 keV) X-rays.

(b) As Fig.6.15(a) except Si-K (1.74 keV) X-rays.

$$(\Delta Q)_{calc}(C\text{-}K,\theta) > (\Delta Q)_{calc}(Si\text{-}K,\theta) \tag{6.4}$$

and

$$(\Delta Q)_{calc}(E_x,33.5°) > (\Delta Q)_{calc}(E_x,5°) \tag{6.5}$$

These results are consistent with previous efficiency measurements (Section 5.4). The efficiency at a given angle is greater for C-K than for Si-K and hence Eqn.6.4 is reasonable , and as θ increases, the grazing angle with the front surface $\alpha=90-\theta$ decreases and hence the front surface efficiency increases, giving Eqn.6.5.

The discrepancy between ΔQ and $(\Delta Q)_{calc}$ at high angles may to some extent be caused by increased efficiency for events interacting at the very top of the channel because of the improved electrostatic configuration. By considering the electric field configuration of Fig.6.1(a) it can be seen that approximately 50% of the electrons liberated less than 0.2 D from the channel entrance will not be accelerated into the channel. A number of electrons emitted from the top 0.5 D of the channel will only experience a weak accelerating field and may not gain sufficient energy to initiate an avalanche. When the repeller grid is in place (Fig.6.1(b)) the electric field does not change direction and hence all secondary electrons liberated in the channel are captured, although some will still experience a weak accelerating field. This effect will be expected to increase as θ increases, and a larger proportion of X-rays interact near the top of the channel. The experimental data does show that $\Delta Q-(\Delta Q)_{calc}$ increases with θ although not by a large amount. A small increase is expected, however, because even at $\theta=33.5°$ the channel is illuminated to 1.5 D and the improved electric field configuration will only be really significant for the top ~ 0.5 D of the channel.

The loss of electrons from the top of the channel, when the MCP is operated without a repeller grid, will have a small effect on the accuracy of the theoretical model [139] since at present no account is taken of this loss. Unfortunately the overall result will be to produce a poorer (but only slightly) fit between the model and the experimental data of Figs.5.6(a)-(h).

The change from the low efficiency state to the high efficiency state (Figs.6.12,6.13) with changing $V_{grid}(\mathcal{E})$ is very sharp in all the CsI data, occurring over a range of less than ten volts (2×10^{-3} volts μm^{-1}). This is consistent with the narrow secondary electron energy distributions for CsI as measured by Saloman et al [133]. Of interest, however, is the fact that the mean potential at which this efficiency jump occurs is V_{grid}=-24 volts (6×10^{-3} volts μm^{-1}) while Saloman et al show that the average secondary electron energy from CsI is 0.5 eV.

The difference between the secondary electron emission energy and the grid potential at the efficiency jump, can be explained by considering the secondary electron emission coefficient, $\delta(E_e)$, for the interaction of a low energy electron with CsI [149]. $\delta(E_e)$ is very small, ~ 0.1, for electrons of $E_e < 6$ eV but rises sharply to ~ 0.95 for E_e=10 eV. Assuming a Poissonian distribution for the secondary electrons liberated from the CsI, the probability for initiation of an avalanche is given approximately by 1-(probability of no emitted electrons) which is $1-\exp(-\delta)$. The above changes in δ therefore correspond to changing the secondary electron detection efficiency of the CsI from 10% to 60%. Now because of energy conservation the secondary electrons liberated from the front surface will reach the mouth of the channel with an average energy of 0.5 eV. To have a high probability of initiating an avalanche they must therefore be accelerated through at least 6-10 volts before reaching the channel walls.

The experimental evidence suggests that the electrons will gain the required 6-10 eV only when the electric field at the top of the channel is modified by the presence of a sufficiently high external electric field. From Figs.6.12,6.13 it can be seen that a jump in efficiency occurs in the region 20 volts $\lesssim -V_{grid} \lesssim$ 30 volts. It seems reasonable to assume therefore that for V_{grid}=-20 volts, $E_e \lesssim 6$ eV , and for V_{grid}=-30 volts, $E_e \gtrsim 10$ eV, since this would produce the required increase in efficiency. Increasing the electric field $\mathcal{E}$ beyond this point will have a progressively smaller effect. Doubling the energy of the incident electron from 10 eV to 20 eV will only increase the secondary electron detection efficiency to 74%. No gradual rise in efficiency, corresponding to this increase in secondary electron detection efficiency, has been observed. Since however the actual interaction of the electrons with the CsI will be over a range of angles rather than the normal incidence geometry of ref.[149], the variation, with E_e , of the secondary electron emission coefficient may be rather different for a practical photocathode.

The effect of the grid on the bare MCP efficiencies is also shown on Figs.6.12,6.13 and Figs.6.15(a,b). No measurable effect was observed with Si-K X-rays which is reasonable considering the low photo yields of metals and the high grazing angles used, α=85°. A small effect is seen at C-K which may reflect the smaller mean depth at which the lower energy radiation is absorbed. The increase in efficiency begins at a similar electric field value but occurs over a larger range of $\mathcal{E}$ than the corresponding increase on the CsI photocathode. This indicates a larger range of emission energies and probably a less steep rise in the secondary electron emission coefficient with energy, for nichrome and glass than for CsI.

CHAPTER 7

ENERGY RESOLUTION FROM A CsI COATED MCP

7.1. Theory

7.1.1. Historical background

With the increase in efficiency demonstrated in Chapter 5 there remains only one important area in which MCP's are definitely inferior to competing imaging detectors. That is, no MCP detector possessing any intrinsic X-ray energy resolution has been reported to date. Conventionally, whatever broad-band spectral sensitivity has been possessed by MCP X-ray imagers has been provided by a combination of bandpass filters. The Einstein HRI [19], for example, was preceded by thin Be and Al foils backed by 5 microns of parylene N. Their differing X-ray transmission allowed the incident X-ray spectrum to be divided roughly into the bands $E_x < 0.25$, $0.8 < E_x < 1.5$ and $E_x > 1.5$ keV.

Intrinsic energy resolution would allow considerable simplification of detector construction by simplifying or eliminating entirely the mechanically complex filter wheels that were previously necessary. Further, the energy information would be provided on a photon-by-photon basis, and not as a result of sequential observations with different filters in place, thus providing a sensitivity advantage.

For MCP energy resolution to be observed the following are required:

(i) Proportional initiation of the electron avalanche, with the most probable number of photoelectrons released into a channel varying with the energy, E_x , of the X-ray interacting with the channel wall, and

(ii) Proportional propagation of the avalanche within the microchannel, leading to an energy dependent gain, G electrons photons^{-1}.

Prior to the use of CsI as a photocathode MCP efficiencies have been too low to encourage speculation on the first of these conditions, while condition (ii) has seemed difficult if not impossible to satisfy. In low gain operation the exponential PHD produced by MCP's would make energy information difficult to abstract. Conversely, a peaked PHD with narrow FWHM, in which G is well defined, is produced only under conditions of output pulse saturation. Any potential dependence of the gain on E_x, through the size of the photoemitted electron "batch", would therefore appear to be necessarily destroyed in the saturated mode of operation conventionally used for photon counting (Section 2.1).

Results produced during initial investigations with CsI in this laboratory [106] indicated that to a small extent gain was a function of X-ray energy. A detailed theoretical study was carried out by Dr. G.W. Fraser [72], with the important conclusion that significant soft X-ray energy resolution could be expected from a CsI coated MCP chevron pair whose bias voltages were carefully adjusted. This theoretical model is briefly described in the following two sections.

7.1.2. Secondary electron photoemission as a function of X-ray energy

A photocathode model was developed to examine the statistics of X-ray photoemission rather than the integral quantities of pulse and current quantum yields reported previously [121,124]. In particular an expression was developed for the probability, $P(n)$, that n secondary electrons are released from a planar photocathode of thickness T by an X-ray of energy E_x, incident at grazing angle α. The relative probabilities, $P'(n)$, of an emitted secondary electron batch containing $n=1,2,...$ electrons, could also be computed.

The model allows the calculation of electron number distributions for X-ray interaction geometries appropriate to bare and coated MCP's, and permits the investigation of the possibility of satisfying condition (i) above.

Figs.7.1(a,b) show calculated distributions of the secondary electron batch content for C-K (0.28 keV) and Si-K (1.74 keV) X-rays incident on a plane sample of MCP lead glass. For both energies the most probable number of emitted electrons is found to be one, a conclusion unlikely to be changed if the primary electron yield of the glass were also accounted for [66]. The average multiplicity of an electron batch, however, defined by:

$$\sum_{n=1}^{\infty} n.\ P'(n)$$

has a higher value (2.8) for Si-K X-rays than for C-K (1.8).

Figs.7.2 (a,b,c,d) illustrate the calculated variation of p(n), the probability, per absorbed photon, of n-electron emission, with X-ray energy, grazing angle and CsI photocathode thickness. Figs.7.2(a,d) are effectively the counterparts of Figs.7.1(a,b) for a 300 Å thick CsI layer. Such a T value is characteristic of the coatings experimentally deposited on a MCP's channel walls (Section 5.1).

We note:

(i) CsI electron number distributions, unlike those for MCP glass, are peaked. Further, the most probable number of emitted secondaries, n_p, increases with E_x. Fig.7.3 shows in detail the calculated increase of n_p with X-ray energy in the 0.1-3 keV range.

(ii) The peaked nature of the distribution becomes less marked as the grazing angle α increases (Figs.7.2 (a,b,c)) with T held constant.

(iii) The electron number distribution broadens towards low n as the photocathode thickness T, increases at constant α (Fig.7.2(d)).

Proportional initiation of the avalanche is thus predicted to occur in CsI coated MCP X-ray detectors. The latter two observations are explicable

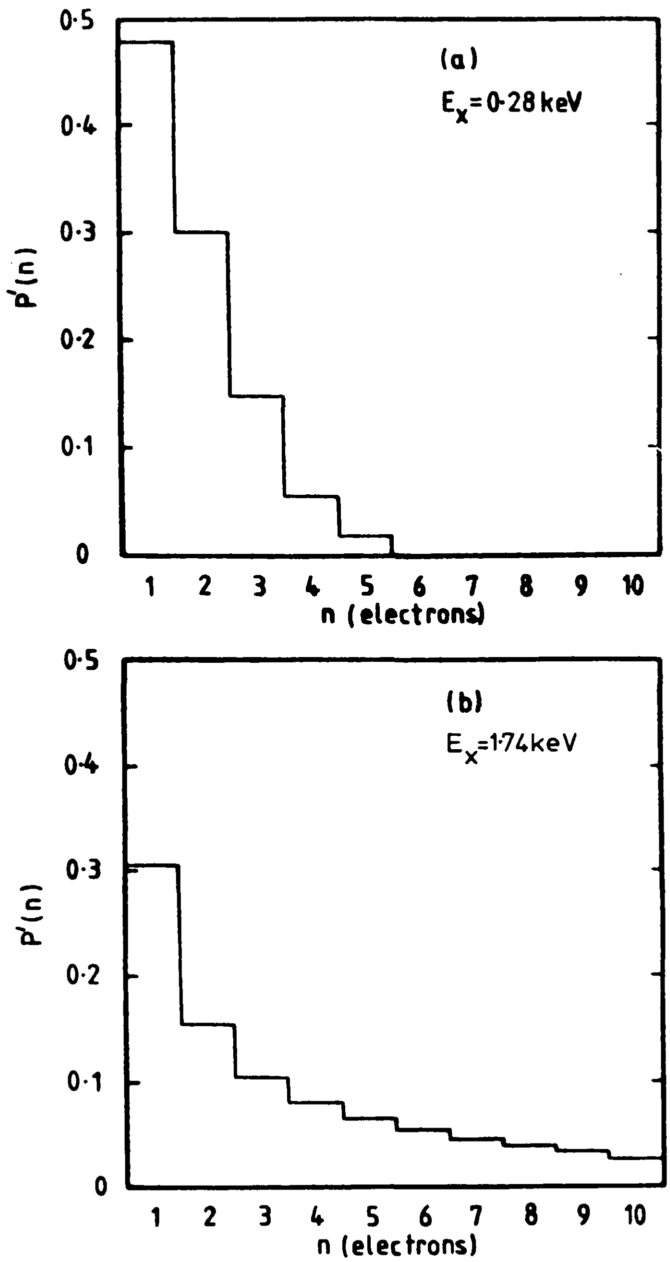

7.1. (a) Calculated relative probability distribution P'(n). C-K X-rays (0.28 keV) incident at grazing angle α=5° to a silica-like surface layer of MCP lead glass, Phillips Type 3502 [66]. p(0)=0.394.

(b) As Fig.7.1(a) for Si-K X-rays (1.74 keV). p(0)=0.965.

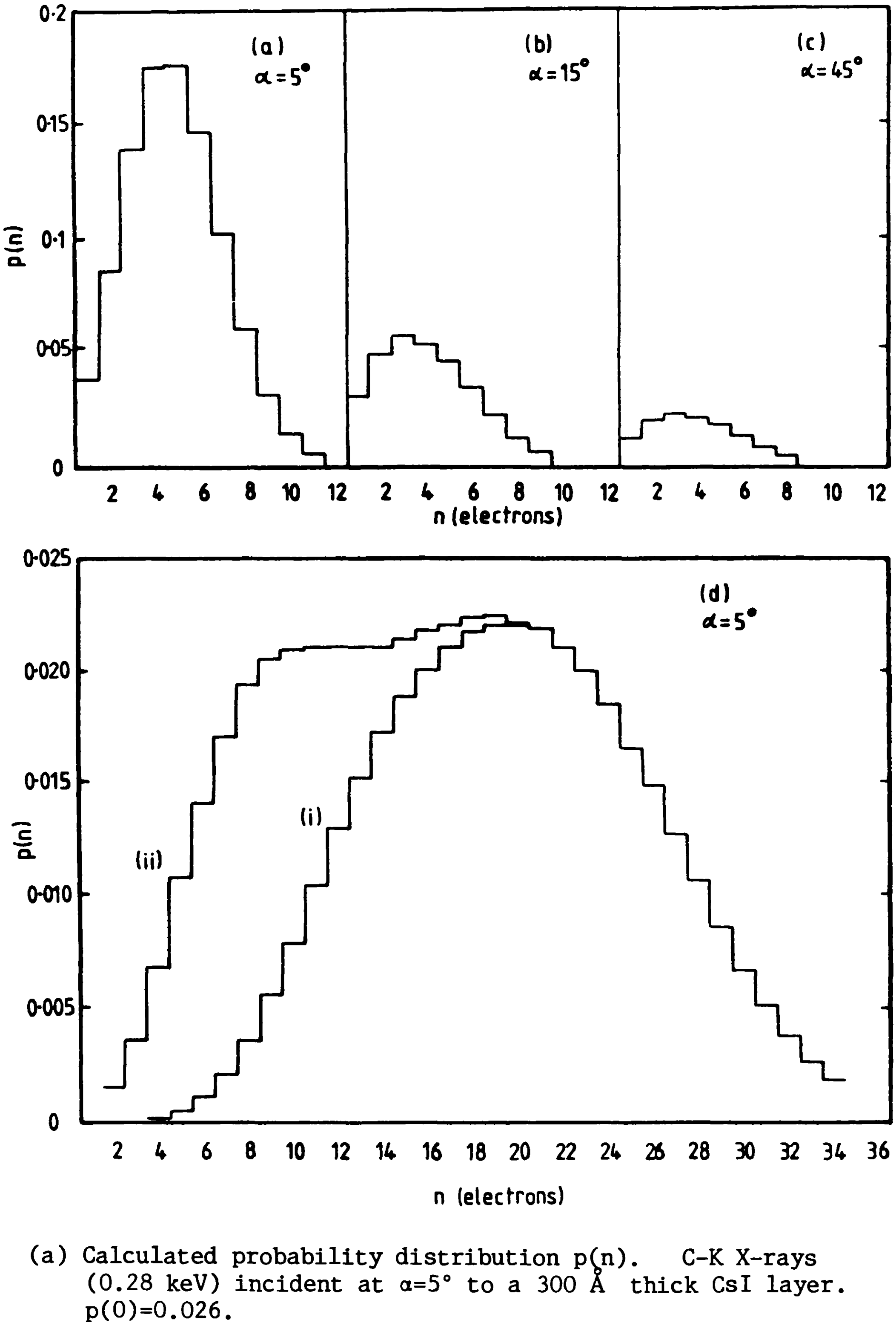

7.2. (a) Calculated probability distribution p(n). C-K X-rays (0.28 keV) incident at α=5° to a 300 Å thick CsI layer. p(0)=0.026.

(b) As Fig.7.2(a), except that α=15°. p(0)=0.684.

(c) As Fig.7.2(a), except that α=45°. p(0)=0.877.

(d) Calculated probability distribution p(n). Si-K X-rays (1.74 keV). Grazing angle α=5°. Plane CsI photocathode of thickness (i) T=300 Å (ii) T=450 Å . Probabilities, per absorbed photon, that no secondary emission occurs p(0)=0.63 (T=300 Å) and p(0)=0.50 (T=450 Å).

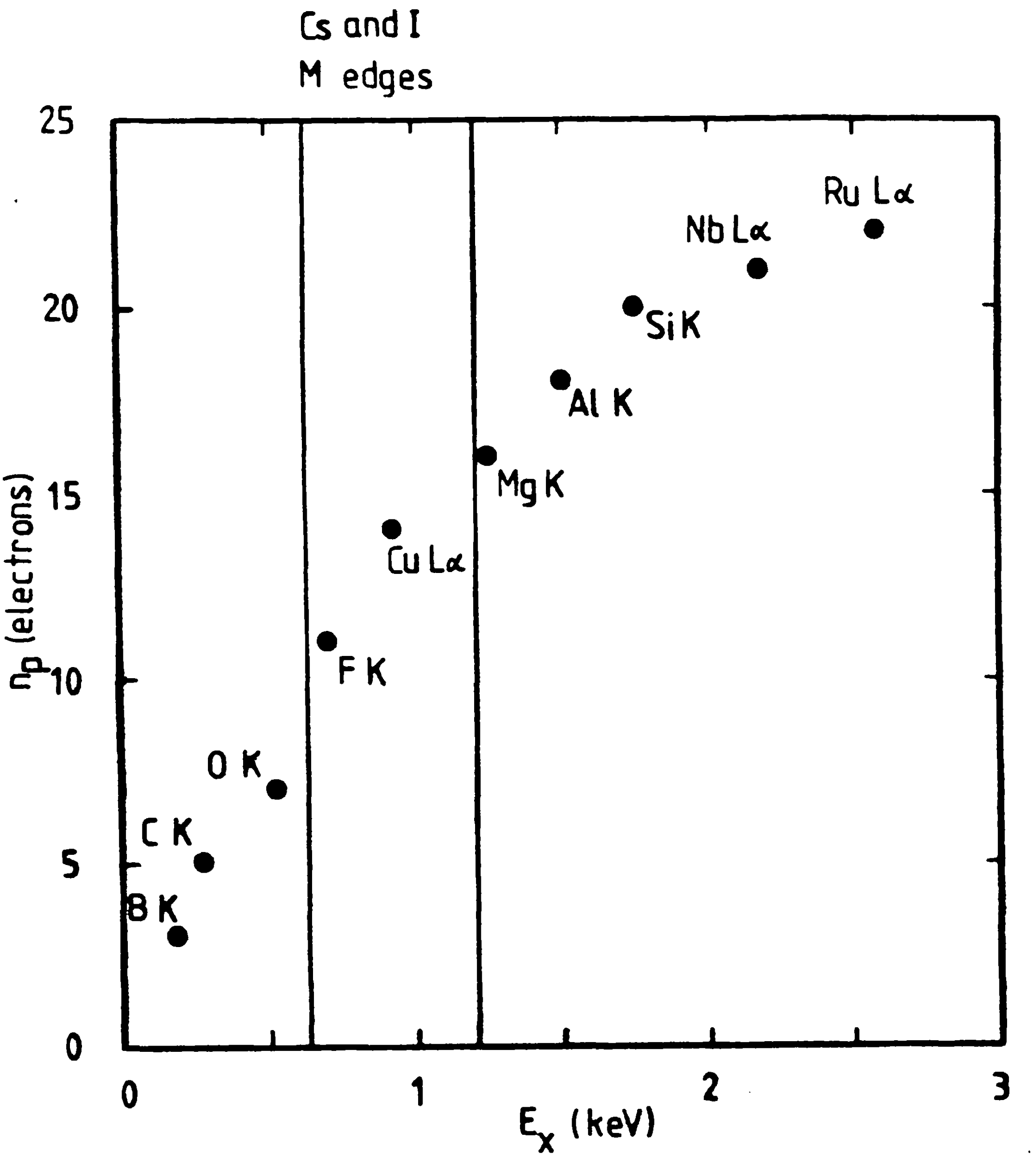

7.3. Calculated variation of n_p , the most probable number of photo-emitted secondary electrons, with X-ray energy E_x. n_p values evaluated for a series of named characteristic X-ray energies. Plane CsI photocathode, T=300 Å . Grazing angle α=5°. M edges of Cs and I lie between the vertical lines indicated.

as follows. As α is increased, the mean depth of X-ray absorption $(\mu\,\mathrm{cosec}\,\alpha')^{-1}$, increases in turn while the probability of many electrons escaping into the vacuum falls faster than for one electron. In the limit of normal incidence, the quantum yield is minimised and the most probable number of emitted secondaries is one. Increasing T increases the quantum yield [124] by virtue of few-electron events emanating from "deep" in the photocathode. This has been made obvious in Fig.7.2(d) by plotting the distribution $p(n)$ rather than $P'(n)$, whose normalisation changes with thickness.

We see that the narrowest electron number distributions occur at relatively small grazing angles and with a relatively thin photocathode layer. The trade off implied by the latter factor, between the quantum efficiency of a coated MCP (which requires the thickest possible layer of photocathode material on the channel walls) and its potential energy resolution (Section 7.1.3), cannot be quantified theoretically. Recall that the grazing angle α varies around each cylindrical microchannel between limits $0 \leq \alpha \leq \theta$ (Section 2.3.2). The calculations performed for planar photocathodes do not therefore translate exactly to the case of cylindrical MCP deposition photocathodes.

7.1.3. Chevron gain as a function of X-ray energy

In ref. [38] the following equation was developed for the peak gain of a two stage chevron MCP detector, G_C, in terms of the single electron gains of its constituent front and rear plates:

$$G_C = G_F^{1-\beta}\, G_R\, N_C^{\beta} \tag{7.1}$$

N_C is the number of channels in the rear MCP activated by electrons emanating from the single active channel of the front plate. N_C is a function of the width of the interplate gap, d_G, and the accelerating voltage across it, V_G [38]. β is a parameter expressing the sensitivity of the rear MCP to the magnitude of a brief input pulse. β appears to depend on the channel diameter D as follows [38] :

$$\beta = 0.6 : D = 12.5\ \mu m$$

$$\beta = 0.8 : D = 25\ \mu m\ .$$

We see immediately that if, at sufficiently low bias voltage V_F , the front plate were operated linearly so that its output charge distribution had a peak value

$$G_F = k\ n_p\ (E_x) \quad : \quad k \text{ constant}$$

then the chevron gain would exhibit an energy dependence of the form

$$G_c = k^{1-\beta}\, G_R\, N_c^{\beta} \,.\, (n_p(E_x))^{1-\beta} \tag{7.2}$$

Taking values of n_p from Fig.7.3 we find that the implied variation of the peak gain of a CsI coated multiplier, with channel diameter D=12.5 μm is of order:

$$(22/3)^{0.4} = 2.2$$

over the energy range 0.18-2.7 keV. The actual energy resolution to which such peak separation would correspond, of course depends on the magnitude of the chevron FWHM, $\Delta G_c/G_c$ at each energy. The intrinsic spread in chevron gain, determined by the width of the emitted secondary electron number distribution is indicated for several energies in Fig.7.4. Calculated distributions P'(n) for CsI are plotted against an ordinate $n^{0.4}$ to simulate the output PHD of a CsI coated chevron with 12.5 μm channels. Intrinsic FWHM's computed in this way range from 160% at 0.18 keV down to ~ 50% for X-ray energies above 1 keV. To attain such limiting values in practice would require no further dispersion of the gain by the channel multiplication process. This as discussed in Section 7.1.1 implies a degree of charge saturation somewhere in the multiplier chain.

The data of ref. [38] indicates that G_c varies with G_F even when

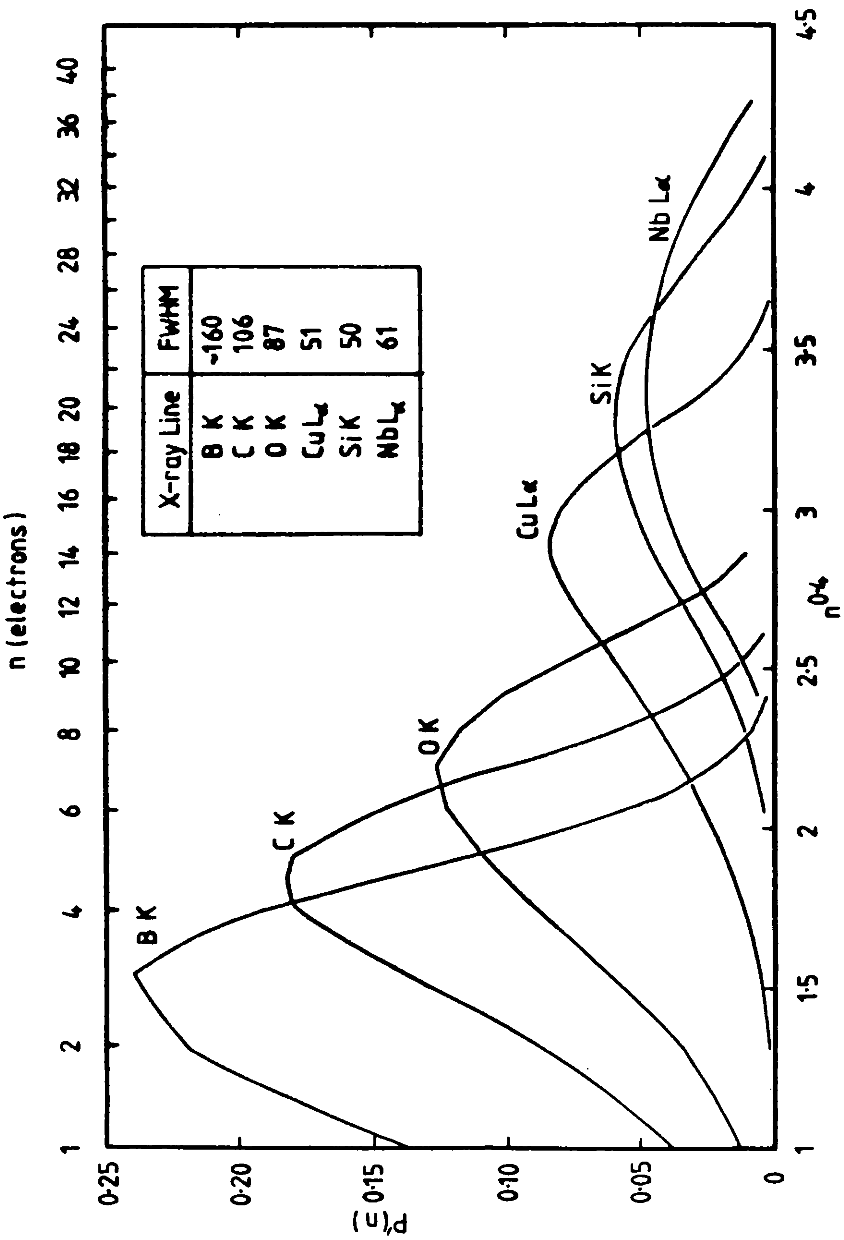

7.4. Calculated secondary photoelectron number distributions, P'(n), folded through chevron MCP gain response to yield approximations to the chevron output PHD for six named characteristic X-ray energies: B-K (0.18 keV), C-K (0.28 keV), O-K (0.525 keV), Cu-L_α(0.93 keV), Si-K (1.74 keV) and Nb-L_α (2.17 keV). CsI photocathode, grazing angle θ=5°, thickness T=300 Å. The inset table lists normalised FWHM values for each of the six distributions.

the rear MCP is operated with a sufficiently high bias voltage, V_R, to induce wall charge saturation at its output. We might therefore attempt an initial compromise between linear chevron operation (giving variation of G_c with n_p) and saturated operation (minimising $\Delta G_c/G_c$) by choosing front and rear MCP bias voltages separately such that:

$$V_F < (V_o)_S \quad : \quad V_R > (V_o)_S$$

where $(V_o)_S$ is the voltage at which the transition between unsaturated and saturated channel operation ideally occurs. $(V_o)_S$ is given approximately by [38]

$$(V_o)_S \approx 8.94\ (L/D) + 450 \text{ volts} \qquad (7.3)$$

In Section 7.2 we report successful measurements of energy resolution made with a chevron detector operated, as described above, with its front plate largely unsaturated and its rear plate in hard saturation.

7.2. Experimental Results

7.2.1. Experimental procedures

The MCP detector used for the efficiency measurements of Section 5.4.3 was used to investigate the energy dependent gain of an MCP. Measurements of G_c and $\Delta G_c/G_c$ were made at the eight X-ray energies whose efficiency curves appear in Figs.5.6(a-h). The most detailed measurements were made with Si-K and C-K X-rays. These lines, well separated in energy, but both accessible from a single anode coating of silicon carbide, were used to establish in turn the dependence of the MCP energy resolution on (i) the chevron bias voltages V_F,V_G and V_R, (ii) the angle of incidence θ, (iii) MCP output count rate N_m and (iv) beam position, x .

Since the variation of G_c with E_x is predicted (and measured) to be a non-linear function, pulse height FWHM alone is not a sufficient indicator of MCP energy resolution. We have used a figure of merit S

(E_{x_1}, E_{x_2}) to quantify the separation between output PHD's measured with X-ray energies E_{x_1}, E_{x_2} . S is the fractional area of overlap of two ideal gaussian distributions of equal area whose peaks and FWHM's are identical to those of the two measured MCP distributions. Although some of the measured PHD's are in fact appreciably non-gaussian in form (Section 2.3.1), S is a useful analytically-calculable index of MCP energy resolution, bounded by zero (for two perfectly distinct distributions) and unity (identical distributions).

The behaviour of $S\ (E_{x_1}, E_{x_2})$ turns out to be very similar to that of another figure of merit $S'\ (E_{x_1}, E_{x_2})$, which can be constructed directly from the output PHD's (Fig.7.5) :

$$S'\ (E_{x_1}, E_{x_2}) = (C_2 - C_3)/(C_4 - C_1)$$

$C_2 - C_1$ is the FWHM for the PHD produced by X-rays of energy E_{x_1} and $C_4 - C_3$ is the FWHM produced by X-rays of energy E_{x_2} . $C_2 - C_3$ is therefore a measure of the overlap between the two PHD's and $C_4 - C_1$, a measure of their total spread. S' provides a measure of the separation of the two distributions, with a small S' value implying a good separation. The very similar behaviour of S and S' (Fig.7.6) justifies the use of S despite the non-gaussian form of the output PHD's.

Calibrated PHD's obtained on both coated and uncoated halves of the detector each contained $\sim 10^5$ counts, with some 800 counts in the peak channel. Uncertainty in the peak gain, reported below in terms of an output charge per photon, is dependent on the shape of the PHD but never exceeds $\pm$ 0.1 pC. Uncertainty in the FWHM $\Delta G_c/G_c$ is of order $\pm$ 2%, while stated values of V_F, V_R and V_G are accurate to $\pm$ 5 volts.

7.2.2. $G_c(V_F)$: CsI coated MCP

Figs.7.7 (a,b,c,d) illustrate the variation of G_c and $\Delta G_c/G_c$ with front plate voltage V_F on the CsI coated half of the detector. The angle of incidence was $\theta = 5°$, with the voltages V_R and V_G set high in

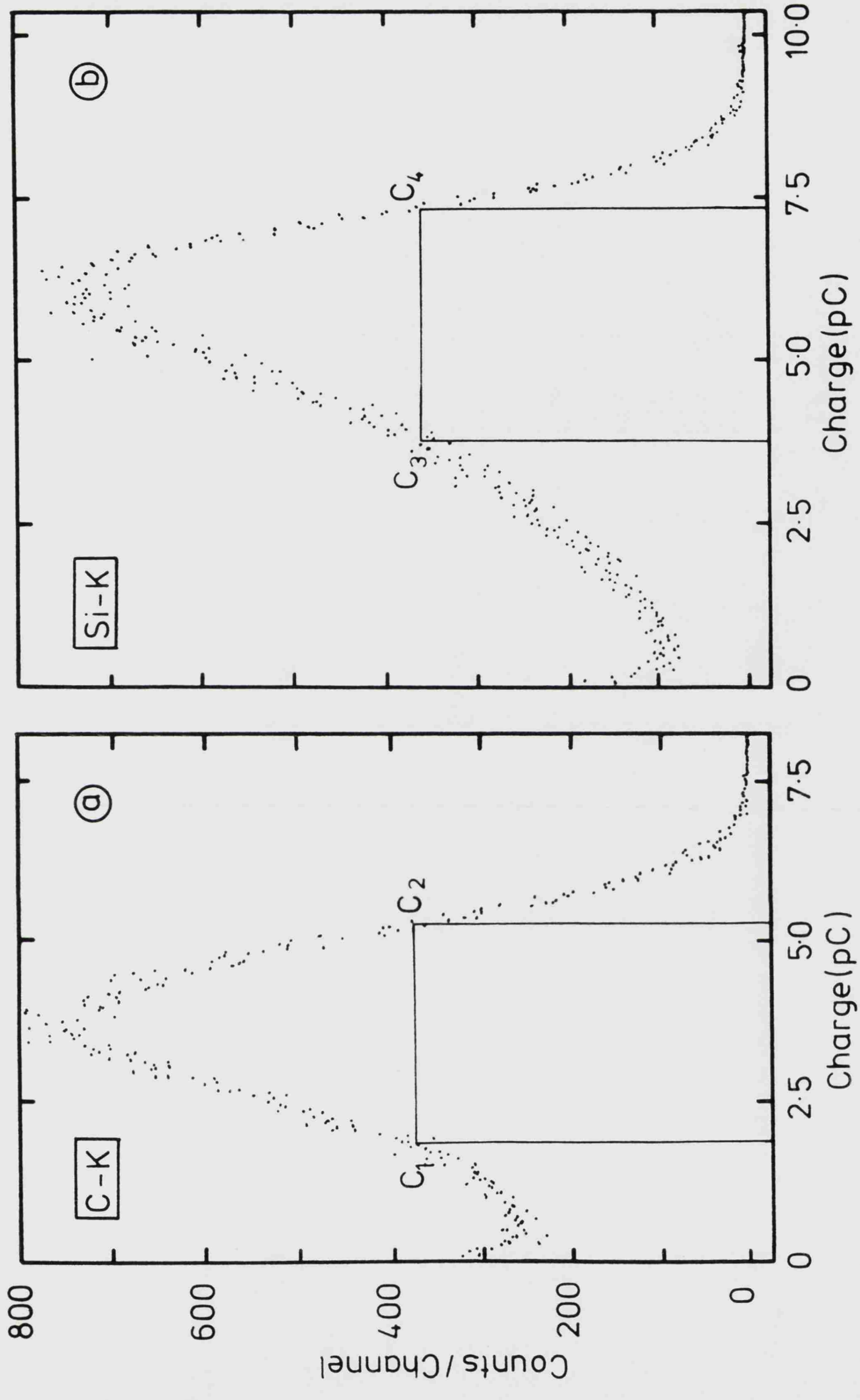

7.5. Typical PHD's used to produce S' (0.28 keV, 1.74 keV)=$(C_2-C_3)/(C_4-C_1)$. V_F=1400 volts, V_G=600 volts, V_R=1700 volts, θ=5°, x=32 mm.
(a) C-K (0.28 keV) X-rays. FWHM=C_2-C_1
(b) Si-K (1.74 keV) X-rays. FWHM=C_4-C_3

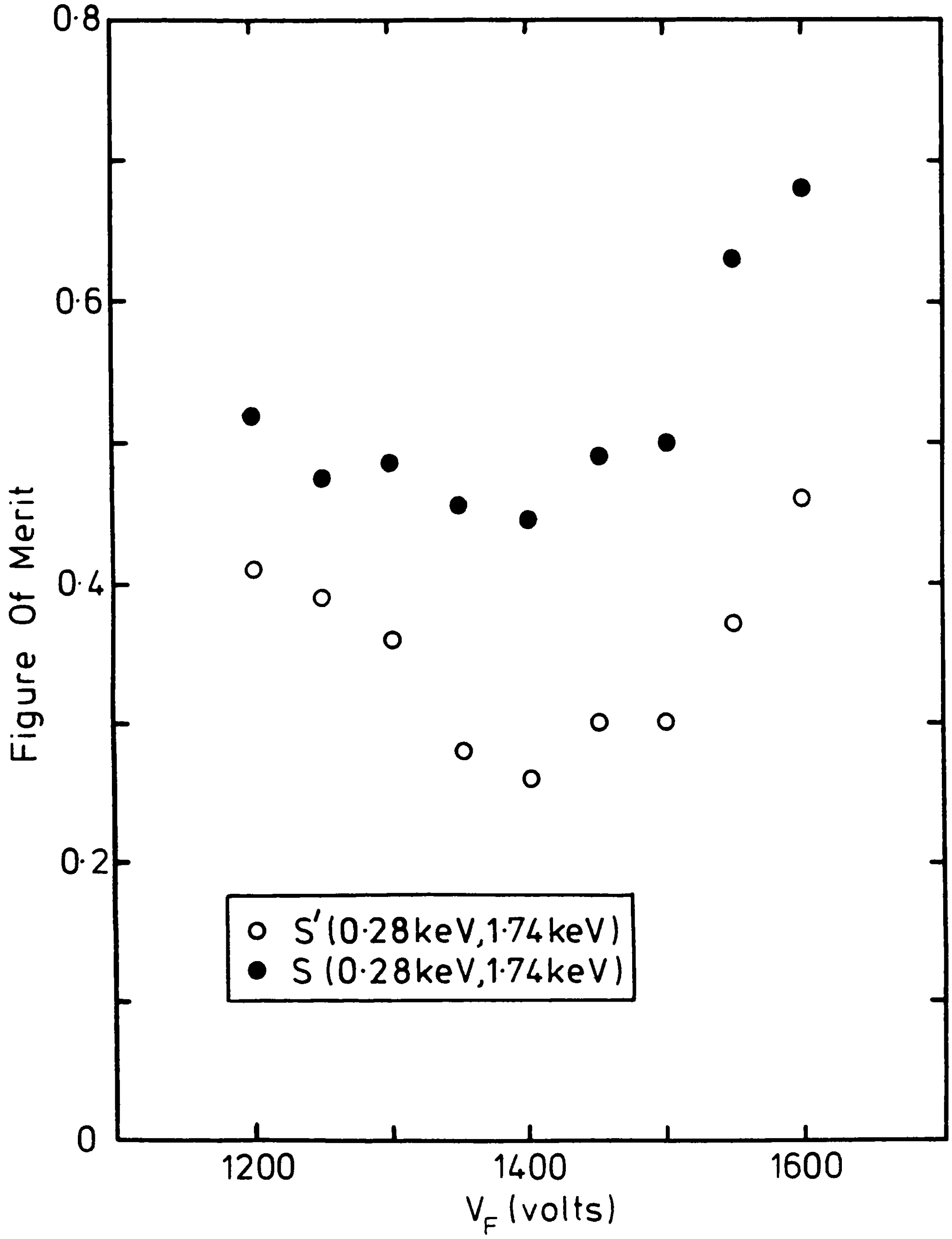

7.6. Comparison between S (0.28 keV, 1.74 keV) (filled circles) and S' (0.28 keV, 1.74 keV) (open circles) as a function of front plate voltage V_F. V_G=600 volts, V_R=1700 volts, θ=5°, x=32 mm.

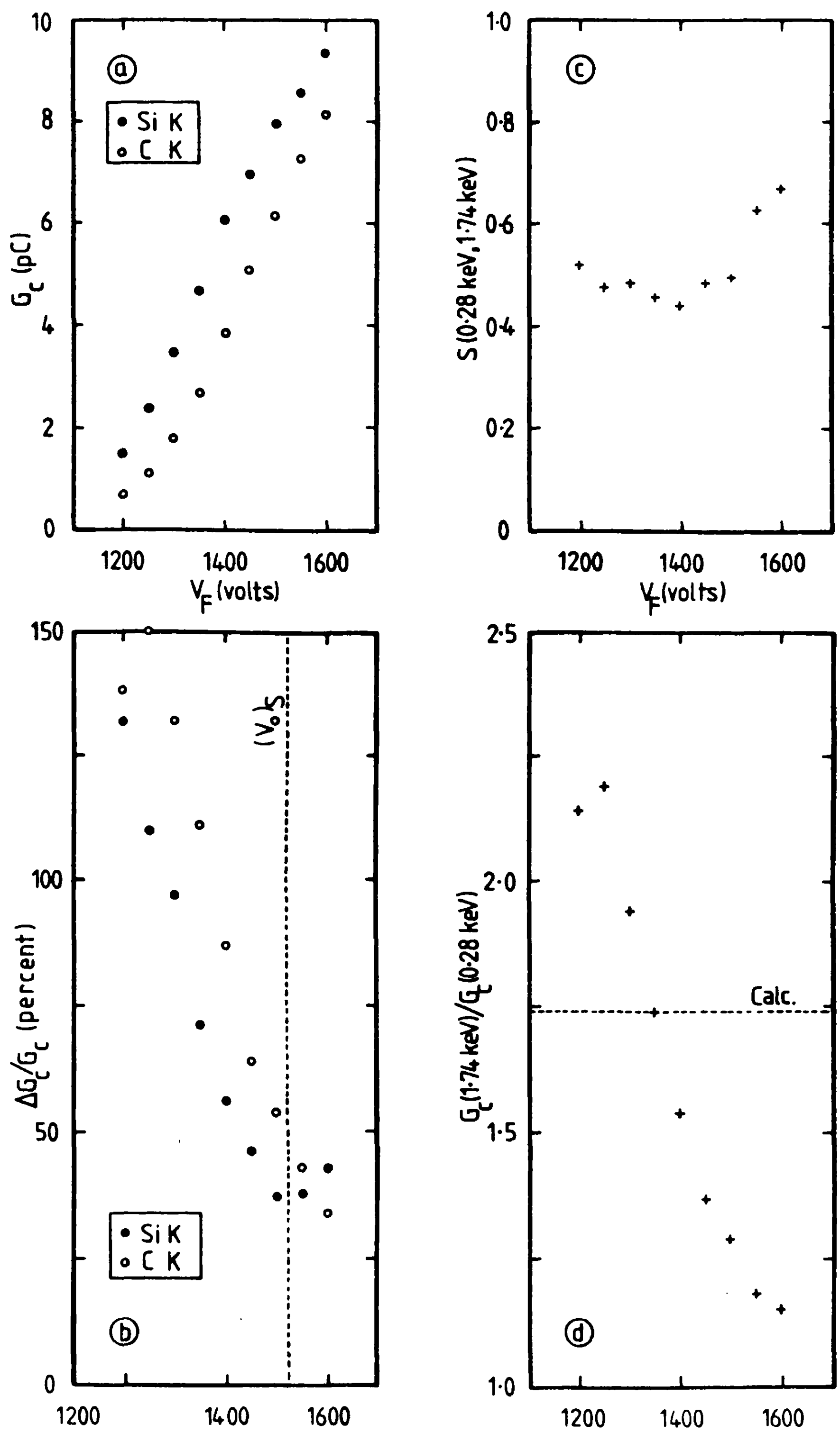

7.7. Chevron energy resolution as a function of front plate voltage V_F. Si-K (1.74 keV) and C-K (0.28 keV) X-rays. V_R=1700 volts, V_G=600 volts, θ=5°, N_m=500 s^{-1}. x=32 mm. (CsI coated detector half.)

(a) Peak gains G_c

(b) FWHM's $\Delta G_c/G_c$. Transition voltage $(V_o)_S$ (Eqn. (7.3)) indicated by broken vertical line.

(c) Separation S (0.28 keV, 1.74 keV)

(d) Ratio of peak gains G_c(1.74 keV) / G_c(0.28 keV). Theoretical estimate $(n_p(1.74\ keV)/n_p(0.28\ keV))^{1-\beta}=(20/5)^{0.4}$ indicated by broken horizontal line.

order to induce saturation in the latter part of the multiplier chain. Peak gains for the two test energies are distinct at all V_F values studied, but their ratio decreases towards unity with the onset of saturated operation. Hard saturation, judged by the stabilisation of $\Delta G_c/G_c$, occurs for front plate voltages in excess of 1500 volts, close to the value $(V_o)_S$ predicted by Eqn.(7.3). The maximum separation of the peak gains, G_c (1.74 keV) - G_c (0.28 keV) = 2.2 pC and the best energy resolution (a minimum S value of 0.45) are both obtained for an optimum V_F value of 1400 volts. In fully linear operation at lower voltages the ratio of peak gain is maximised (2.18 compared to a theoretical estimate of 1.74, based on previously calculated n_p values and a β value of 0.6) but individual PHD's are broad. As V_F is increased a progressively increasing degree of wall charge saturation reduces the dependence of G_c on n_p but also reduces the spread in output charges. The minimum value of S, as anticipated in Section 7.1.3, occurs for a front plate voltage somewhat less than that necessary to induce full front plate saturation.

V_F was fixed at 1400 volts for all further measurements on the coated side of this MCP.

A less detailed set of measurements (Figs. 7.8 (a,b,c,d)) were also obtained using the L:D=80:1 MCP used for efficiency measurements in Section 5.4.2. In this case the X-ray lines used were C-K (0.28 keV) and Al-K (1.49 keV). The general behaviour observed was very similar to that of the L:D=120:1 MCP which establishes the reproducibility of the energy resolution effect.

The maximum separation of the peak gains (1.6 pC) and the best energy resolution (S=0.41) were again obtained at the same optimum voltage, V_F=1050 volts. The minimum figure of merit value, S=0.41, is similar to that obtained from the 120:1 front MCP, despite being achieved with C-K and Al-K rather than C-K and Si-K. This S value may indicate an intrinsic difference in the energy resolution of the two MCP's, because of

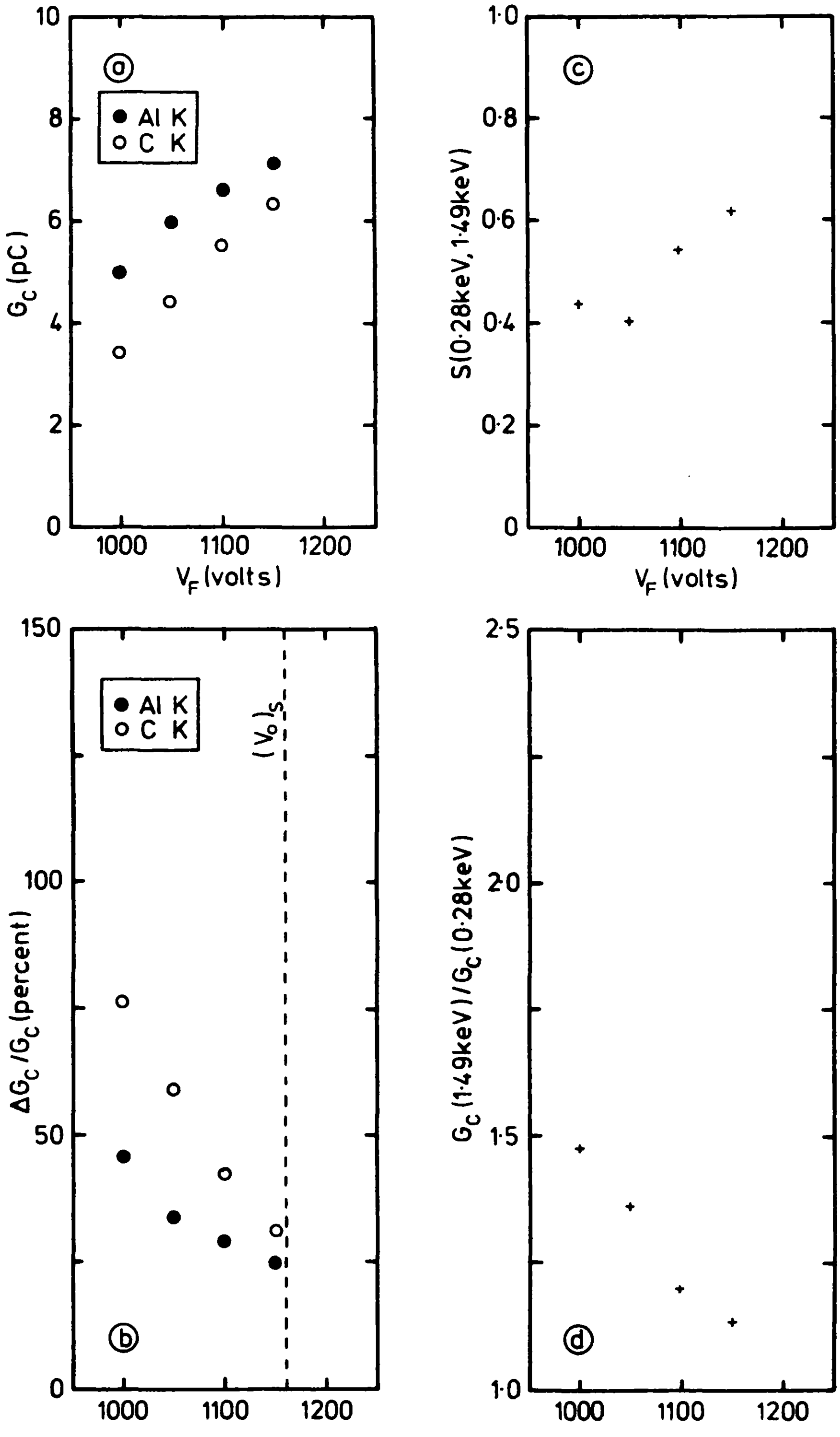

7.8. Chevron energy resolution as a function of front plate voltage V_F. Al-K (1.49 keV) and C-K (0.28 keV) X-rays. V_R=1700 volts, V_G=600 volts, θ=5°, N_m=500 s^{-1}, x=25.5 mm. (CsI coated, L:D=80:1 MCP).

(a) Peak gains G_C

(b) FWHM's $\Delta G_C/G_C$. Transition voltage $(V_o)_S$ (Eqn.(7.3)) indicated by broken vertical line

(c) Separation S (0.28 keV, 1.49 keV)

(d) Ratio of peak gains G_C(1.49 keV)/ G_C(0.28 keV)

L:D ratio, age or resistance. The time available for investigation did not, however, permit a comprehensive exploration of the "parameter space" of the 80:1 MCP and hence it is not possible to compare it in detail with the 120:1 MCP.

No further data was obtained using the 80:1 MCP and the remainder of the results described here are from the 120:1 MCP.

7.2.3. G_c (V_R) : CsI coated MCP

Figs.7.9 (a,b,c,d) illustrate the variation of G_c and $\Delta G_c/G_c$ with rear plate voltage V_R on the CsI coated half of the detector. Well developed rear plate saturation is obtained for $V_R \gtrsim 1600$ volts, somewhat higher than predicted by Eqn.(7.3). The transition from linear to saturated rear plate operation reduces the ratio of the C-K and Si-K peak gains (from a maximum value 2.44) and engenders a decrease in S , just as in the front plate. The difference in peak gains is equal to 2.2. pC and S has its minimum value (0.40) for rear plate bias voltages in the range $1550 \lesssim V_R \lesssim 1750$ volts. Optimum energy resolution is thus obtained for rear plate voltages characteristic of hard saturation, in keeping with the prediction of Section 7.1.3, but S increases again at the very highest value of V_R for which measurements were made.

7.2.4. G_c (V_G) CsI coated MCP

The effect of an accelerating interplate gap voltage on chevron FWHM, $\Delta G_c/G_c$, was discussed in Section 4.1. The measurements of the previous two sections were obtained with a high value of the interplate gap voltage, 600 volts, to minimise $\Delta G_c/G_c$. Figs.7.10 (a,b,c,d) show the effects of reducing V_G on the MCP energy resolution. The curves G_c (V_G) and $\Delta G_c/G_c$ (V_G), Figs.7.10 (a,b), have familiar shapes (Section 4.1). Reducing V_G below 50 volts degrades the energy resolution (increases S) by allowing the charge cloud emanating from the front plate to spread into

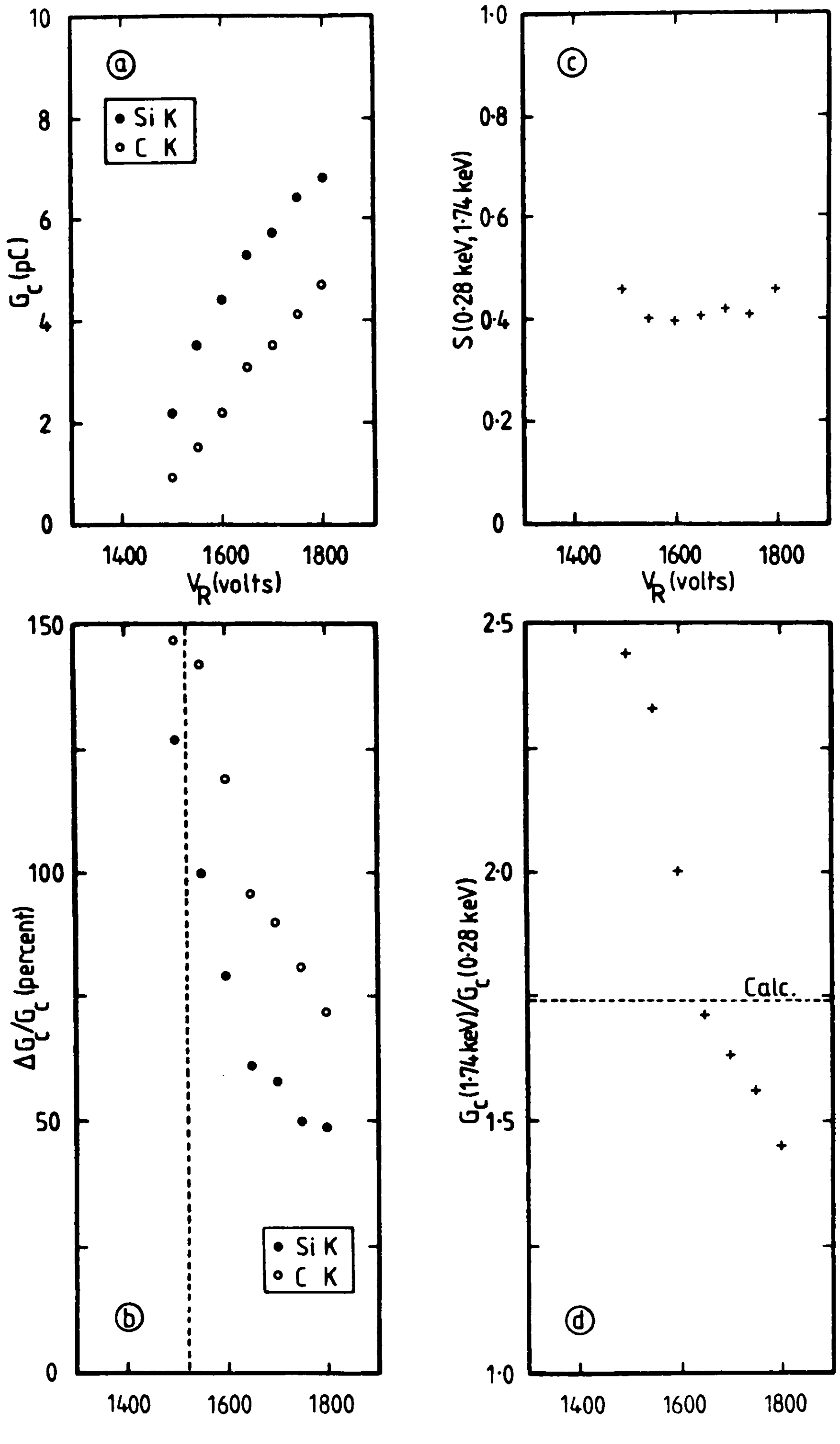

7.9. Chevron energy resolution as a function of rear plate voltage V_R. Si-K (1.74 keV) and C-K (0.28 keV) X-rays. V_F=1400 volts, V_G=600 volts, θ=5°, N_m=510 s^{-1}. x=32 mm. (CsI coated detector half.)

(a) Peak gains G_c

(b) FWHM's $\Delta G_c/G_c$. Transition voltage $(V_o)_S$ indicated by broken vertical line.

(c) Separation S (0.28 keV, 1.74 keV)

(d) Ratio of peak gains G_c(1.74 keV) / G_c(0.28 keV). Theoretical estimate as in Fig.7.7.

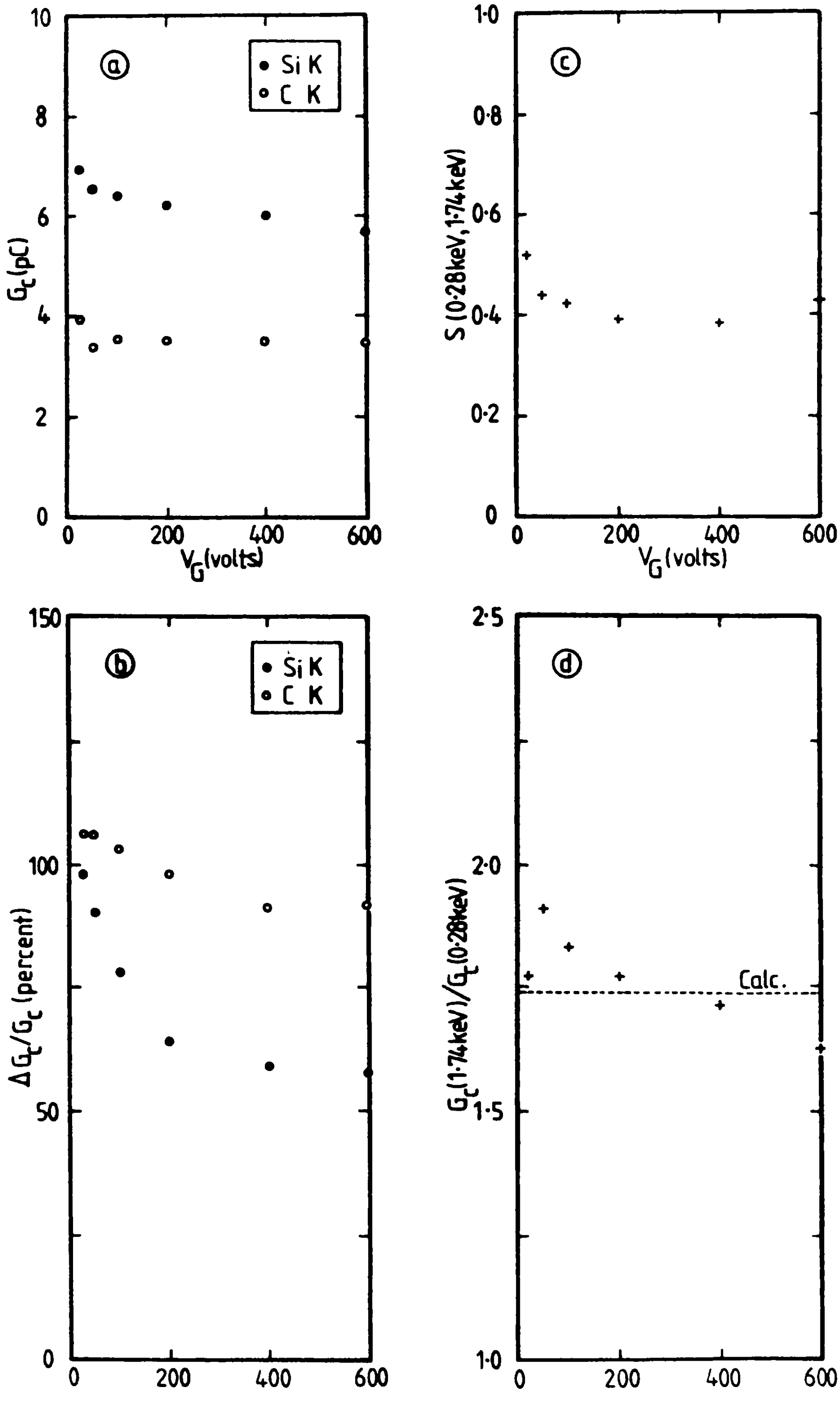

7.10. Chevron energy resolution as a function of accelerating inter-plate gap voltage V_G. Si-K (1.74 keV) and C-K (0.28 keV) X-rays. V_F=1400 volts, V_R=1700 volts, θ=5°, N_m=510 s^{-1}. x=32 mm. (CsI coated detector half.)

(a) Peak gains G_c

(b) FWHM's $\Delta G_c/G_c$

(c) Separation S (0.28 keV, 1.74 keV)

(d) Ratio of peak gains G_c(1.74 keV) / G_c(0.28 keV). Theoretical estimate indicated by horizontal line.

many more channels of the rear plate, so reducing the degree of saturation in each. Interestingly, our initial choice of V_G , 600 volts, appears to be somewhat higher than is optimum for energy resolution.

7.2.5. G_c (N_m) : CsI coated MCP

The depression of MCP gain at high output count rates has been reported by several authors [43]. It is obviously of interest to see how the energy resolution so far observed at relatively low count rates, N_m=500 s^{-1} , is preserved at higher count rates. Figs.7.11 (a,b,c,d) show that in fact a slow increase in S results from the count rate induced fall in peak gains and broadening of FWHM's. The maximum pulse current observed (output count rate times peak gain) is limited to 13% of the conduction current flowing in the rear MCP (rear plate bias voltage divided by the resistance of the active area), in agreement with previous data [43]. Gain depression at high count rates is, of course, determined by the rear plate resistance in chevron detectors and may be overcome by the use of MCP's manufactured from low resistivity glass [37].

7.2.6. G_c (θ) : both MCP halves

Figs.7.12 (a,b,c,d) illustrate the variation of G_c and $\Delta G_c/G_c$ with the angle of X-ray incidence, θ , on the CsI coated half of the front plate. The peak gain at all four X-ray energies is rather insensitive to θ , until at small angle ($\theta \lesssim 2°$) X-ray reflection from the channel walls at last becomes important. X-ray reflection, by creating a larger dispersion of avalanche initiation positions along the channel length, also accounts for the broadening of the output PHD's at small θ values (Section 2.3.2). In accordance with the prediction of Section 7.1.2, $\Delta G_c/G_c$ also increases towards large θ values because of the broadening in the photoemitted CsI electron number distributions. A shallow minimum in S results from the opposing angular influences of X-ray reflection

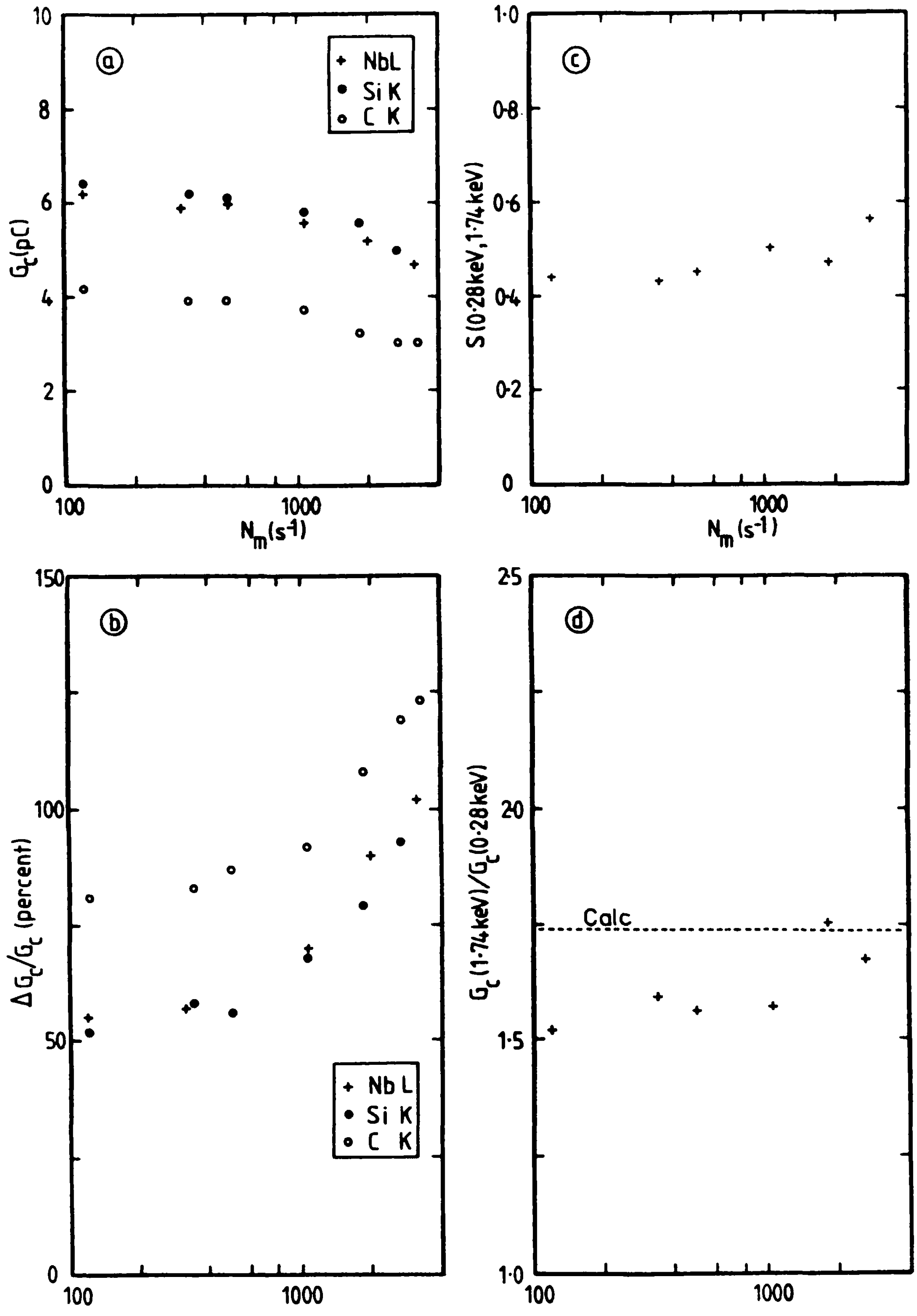

7.11. Chevron energy resolution as a function of MCP output count rate, N_m. Note that 1000 counts. s^{-1}=26 counts. mm^{-2} s^{-1}. X-ray energies Si-K (1.74 keV), C-K (0.28 keV) and Nb-L (2.28 keV). V_F=1400 volts, V_G=600 volts, V_R=1700 volts, θ=5°, x=32 mm. (CsI coated half)

(a) Peak gains G_c

(b) FWHM's $\Delta G_c/G_c$

(c) Separation S (0.28 keV , 1.74 keV).

(d) Ratio of peak gains G_c(1.74 keV) / G_c(0.28 keV). Theoretical estimate indicated by horizontal line.

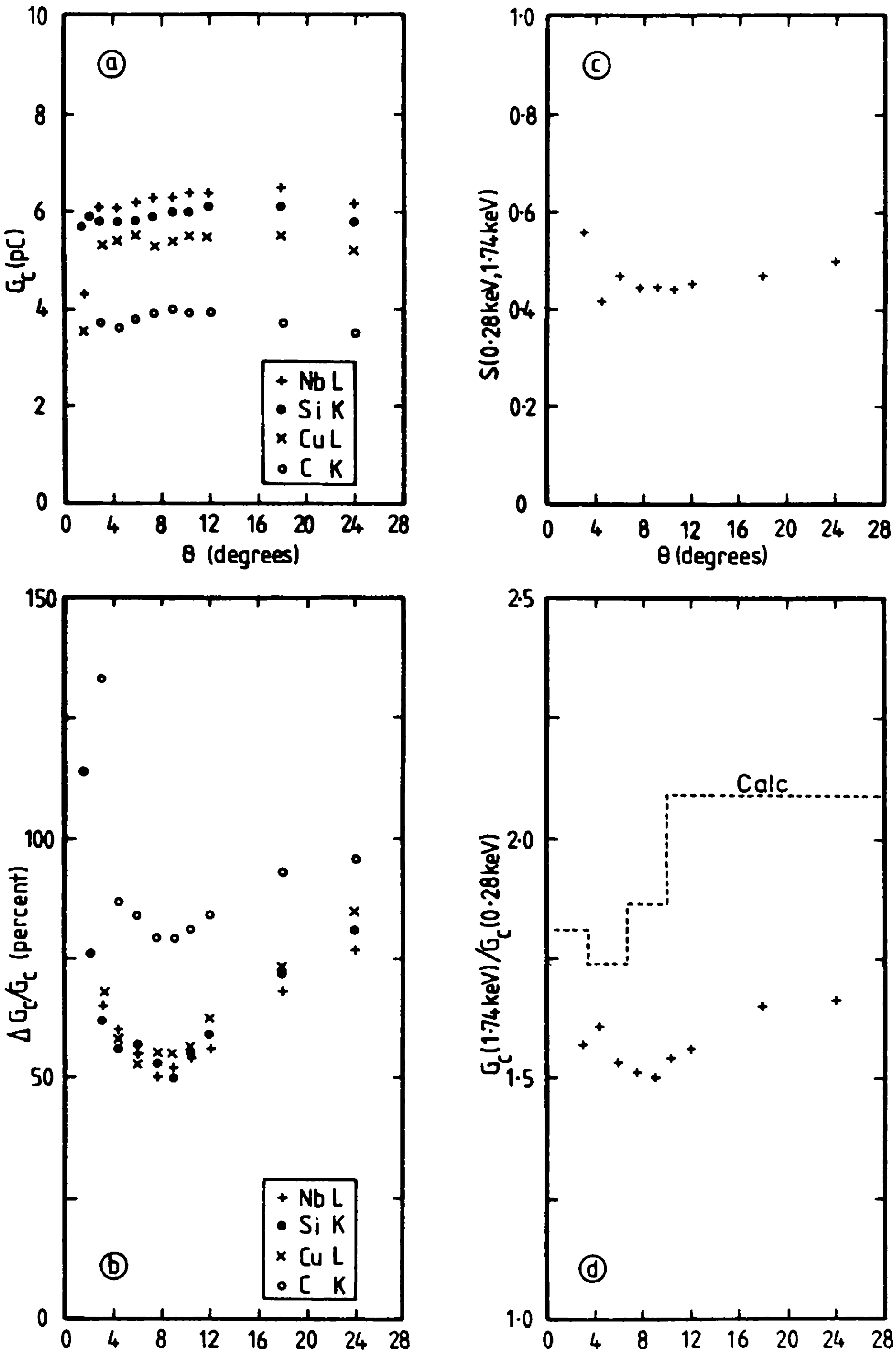

7.12. Chevron energy resolution as a function of angle of X-ray incidence, θ. X-ray energies Si-K (1.74 keV). C-K (0.28 keV), Cu-L (0.93 keV) and Nb-L (2.28 keV). V_F=1400 volts, V_G=600 volts, V_R=1700 volts, N_m=500 s^{-1}, x=32 mm (CsI coated detector half)

(a) Peak gains G_c

(b) FWHM's $\Delta G_c/G_c$

(c) Separation S (0.28 keV, 1.74 keV).

(d) Ratio of peak gains G_c(1.74 keV) / G_c(0.28 keV). Calculated ratio for 300 Å thick planar CsI layer (n_p (1.74 keV),α=θ)/n_p (0.28 keV,α=θ))$^{0.4}$

and secondary electron emission from the CsI.

It is interesting to compare this behaviour with the angular variation exhibited by the uncoated half (Figs.7.13 (a,b,c,d)). At $\theta=5°$, bare plate PHD's for Si-K and C-K X-rays are, contrary to the prediction of Section 7.1.2, well separated, with a ratio of peak gains equal to 1.45. This ratio, however, falls rapidly towards unity as θ is increased, in complete contrast to the behaviour of the corresponding ratio on the coated half of the detector. The energy resolution observed for the uncoated half would thus appear to be controlled by X-ray reflection, predominantly of the C-K radiation. All the experimental evidence for the coated plate, in contrast, supports the view that a genuine variation of the most probable number of photoemitted electrons with energy is at work.

Since the X-ray grazing angle, α, within a cylindrical microchannel varies, as noted in Section 7.1.2, between zero and θ degrees, reflection can play an important part in the gain process for θ values several times the critical angle for X-ray reflection, θ_c.

7.2.7. G_c (x) : both MCP halves

Figs.7.14 (a,b,c,d) show the measured variation of G_c and $\Delta G_c/G_c$ with X-ray beam position, x, across both CsI coated and bare halves of the front MCP. This data was obtained at an angle of incidence, $\theta=5°$, at which the reflection induced bare plate energy resolution is maximised, yet still inferior to that of the coated surface. We note a tendency for G_c and S to increase away from the plate centre on the CsI coated half. This must be related to the radial non-uniformity of the deposition photocathode and in particular to the variation in coating thickness on the channel walls [139]. The gain variation intrinsic to the microchannel plate itself is less marked.

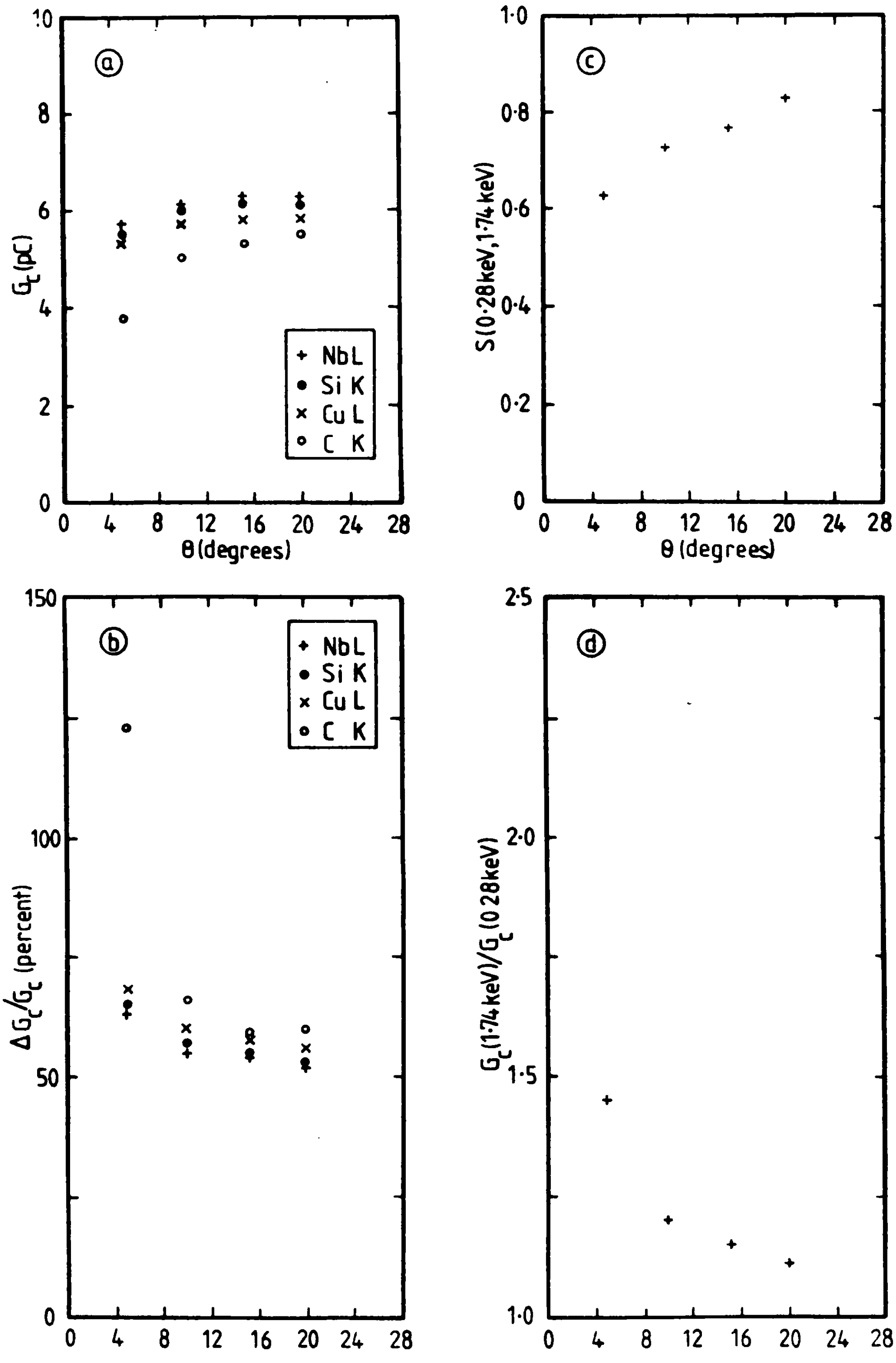

7.13. Chevron energy resolution as a function of angle of X-ray incidence, θ . All parameters as in Fig.7.12 except: V_F=1500 volts, x=19 mm. (Uncoated detector half)

(a) Peak gains G_c

(b) FWHM's $\Delta G_c/G_c$

(c) Separation S (0.28 keV, 1.74 keV)

(d) Ratio of peak gains G_c(1.74 keV) / G_c(0.28 keV).

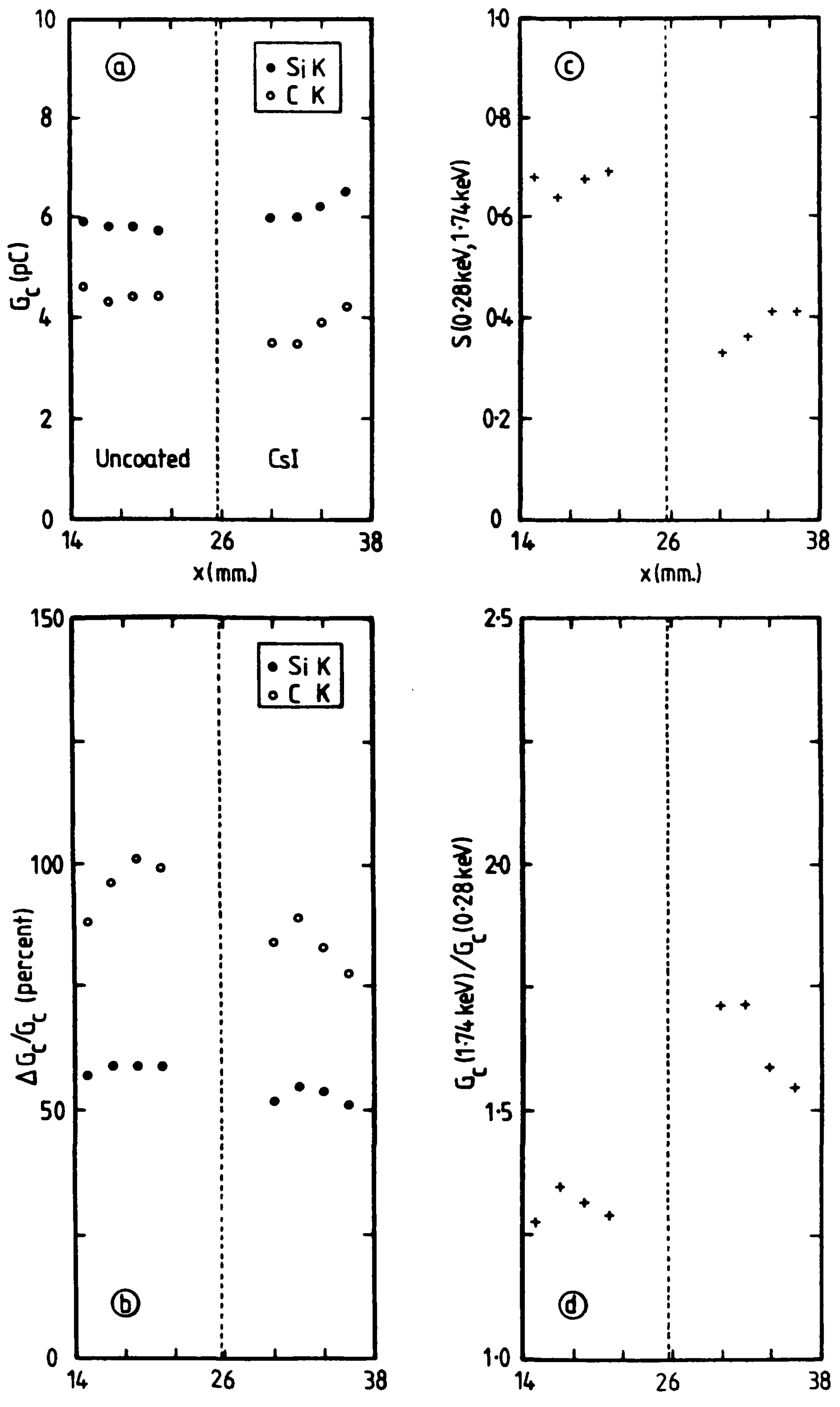

7.14. Chevron energy resolution as a function of X-ray beam position, x . X-ray energies Si-K (1.74 keV) and C-K (0.28 keV). V_F=1400 volts, V_G=600 volts, V_R=1700 volts, N_m=500 s^{-1}. θ=5°. Broken vertical line indicates division between CsI coated and uncoated front plate halves.

(a) Peak gains G_c

(b) FWHM's $\Delta G_c/G_c$

(c) Separation S (0.28 keV, 1.74 keV).

(d) Ratio of peak gains G_c(1.74 keV) / G_c(0.28 keV).

7.2.8. G_c (E_x) : both MCP halves

Figs.7.15 (a,b) display the values of G_c and $\Delta G_c/G_c$ measured on both halves of the front plate for eight X-ray energies in the 0.18-2.7 keV band. Remarkably, although the ratio of Si-K and C-K peak gains on the CsI coated plate has varied considerably with the various parameters investigated in previous sections, the relative magnitudes of the gains at all eight energies are in excellent agreement with theory for the specific configuration represented in Fig.7.15(a). The full curve of that figure connects the calculated gains.

$$6.1\ (n_p(E_x)/n_p(2.68\ \text{keV}))^{0.4}\ \text{pC}$$

That is, having calculated the most probable number of photoemitted secondary electrons n_p for each energy, we have calculated, via Eqn.(7.2), a sequence of relative gains for a chevron with 12.5 μm channels and then normalised them by the measured gain at the highest energy of the data set. The calculation of n_p assumed a planar CsI layer, T=300 Å, α=5°.

Even more remarkable is the correspondence of the measured CsI FWHM's with those values already tabulated for this configuration in Fig.7.4.

Examination of Fig.7.15 (b) confirms that the resolution of Si-K and C-K on the uncoated half of the plate was due to the effects of X-ray reflection at the lower energy. No significant trend in gain was observed with the five highest energies on the bare plate.

7.2.9. Discussion

The results presented in the previous sections clearly show that soft X-ray energy resolution can be obtained using MCP detectors The energy resolution reported here is not in any way competitive with that of the generally recognised classes of spectrally sensitive X-ray detector [150 151,152]. Nevertheless it represents a significant advance in the field of high spatial resolution instrumentation for X-ray astronomy

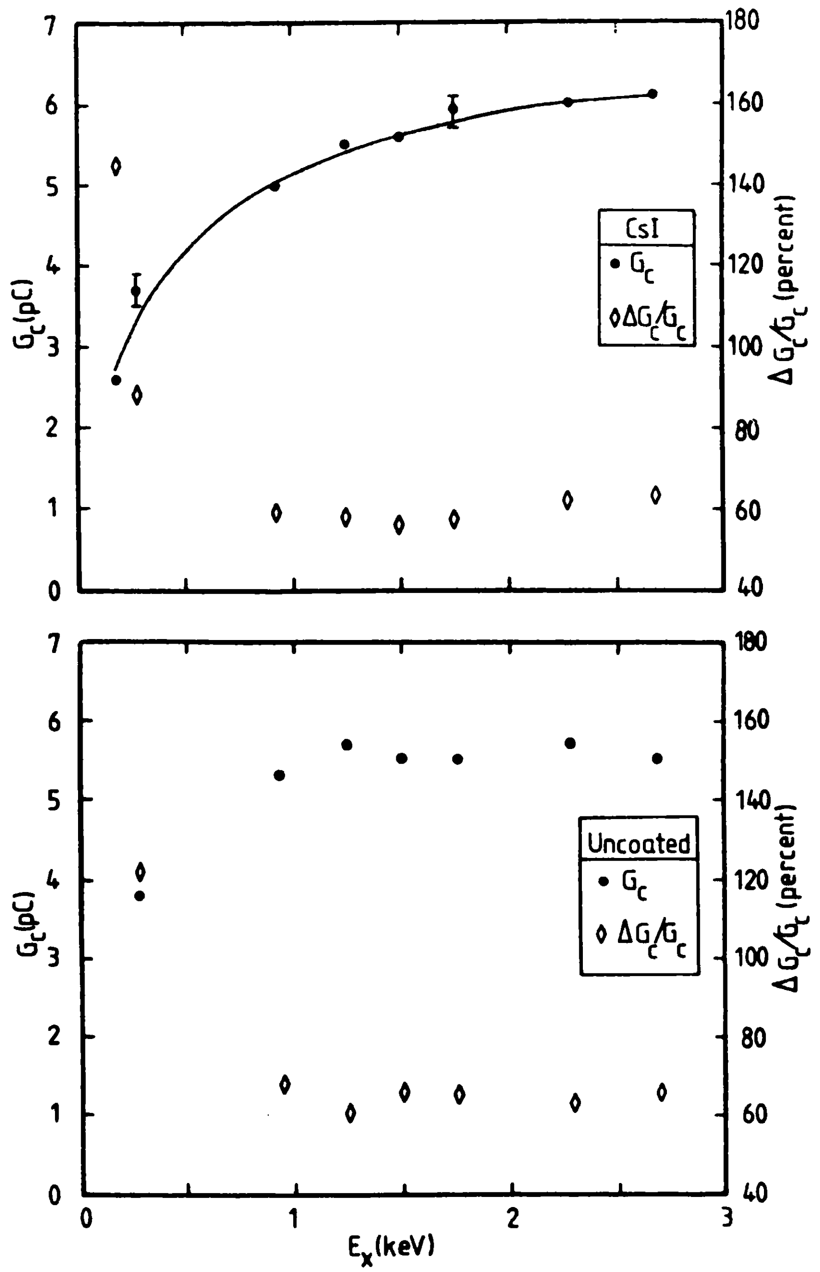

7.15. (a) Chevron peak gain G_c (circles) and FWHM G_c/G_c as functions of X-ray energy, E_x. V_F=1400 volts, V_G=600 volts, V_R=1700 volts, θ=5°, $N_m \lesssim 500\ s^{-1}$, x=32 mm. (CsI coated detector half.) Full theoretical curve - see text. The error bars indicate the range covered by several independent measurements.

(b) As Fig.7.15 (a) except that: V_F=1500 volts and x=19 mm. (Uncoated half.)

Fig.7.16 shows superimposed output charge distributions for C-K and Si-K X-rays measured on the CsI coated half of the detector with an optimum front plate voltage V_F=1400 volts. We see from Fig.7.15 (a) that an electronic discriminator set at an output charge q_o=5 pC, the intersection of the two PHD's in Fig.7.16, would roughly separate X-ray energies above and below 1.0 keV.

The achieved energy resolution is less than that which was available on the Einstein HRI by using filters (Section 7.1.1), since three energy bands were defined by the filters and the present technique only allows two colour photometry. Little use was made of the capability to do three colour photometry with the HRI, however, because the filters significantly reduced the incoming flux and hence were useful only on objects of high surface brightness. The intrinsic energy resolution of a CsI coated MCP, therefore, has a significant sensitivity advantage over any filter based system, as well as removing the necessity for a, mechanically complex, filter wheel. This could signficantly improve the reliability of an experiment because it is very difficult to produce a mechanism which moves repeatedly in a space environment without jamming.

7.3 Further Development

7.3.1. Techniques to improve energy resolution

A significant increase in the usefulness of a CsI coated MCP chevron would be achieved if three (or more) colour photometry was possible. By considering Equation (7.2) we find that the chevron gain depends on the four quantities; G_R, n_p, β , N_c . Relative gains at energies E_{x_1},E_{x_2} , however, are given by:

$$G_{c_1}/G_{c_2} = (n_p(E_{x_1})/n_p(E_{x_2}))^{1-\beta}$$

Any improvement in the energy resolution must therefore be achieved by increasing the variation in n_p or reducing the value of β .

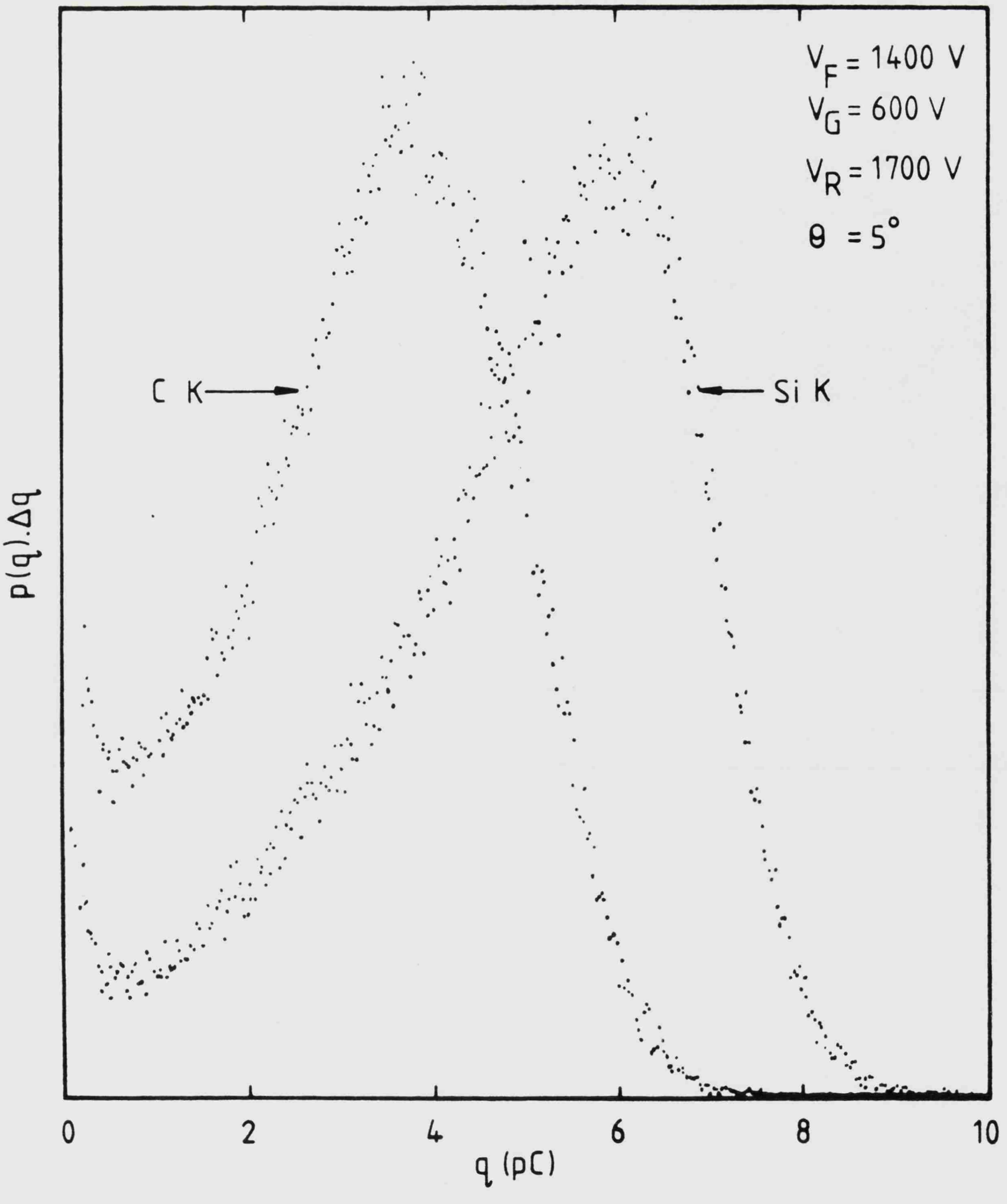

7.16. Superimposed chevron pulse height distributions for Si-K and C-K X-rays. N_m=500 s^{-1}, x=32 mm. (CsI coated detector half.)

The most probable number of electrons emitted per photon, $n_p(E_x)$, is a property of the photocathode material used. If it were possible to replace the CsI coating with a Negative Electron Affinity (NEA) material such as GaAsP [125] we would expect the ratio of peak gains G_c (3 keV)/G_c (0.85 keV) on a chevron with 12.5 μm channels to increase from 1.2 to 1.65 based on the electron number distributions of Section 7.1.2 and Ref. [125]. NEA materials are, however, stable only in high vacuum ($\sim 10^{-10}$ torr) and hence, like multialkali photocathodes [124], are probably incompatible with MCP operation as windowless X-ray detectors. It is therefore unlikely in practice that the energy resolution can be improved by increasing the variation of n_p with energy.

The best chance of improving the energy resolution is to attempt to reduce the gain parameter, β. For the present detector $\beta=0.6$, and hence the linear increase of n_p with energy (Fig.7.3) produces a non-linear increase of G_c with energy (Fig.7.15). The smaller β can be made the better will be the energy resolution (Table 7.1), and the more nearly the output of the detector will correspond to Fig.7.3. Since β appears to decrease with D (Section 7.1.3) it is anticipated that better energy resolution would be obtained with MCP's of smaller channel diameter than the 12.5 μm employed here.

Table 7.1

Calculated values for S (0.28 keV, 1.74 keV) for different values of β using the calculated electron number distributions for CsI. Compare with best achieved S ($\beta=0.6$) of 0.33.

β	S (0.29 keV, 1.74 keV)
0.6	0.34
0.4	0.22
0.2	0.16

It is difficult to assign a physical meaning to the gain parameter β. A possible interpretation is that β expresses the sensitivity of the rear MCP to the magnitude of a brief input pulse of electrons. It may therefore be possible to vary β by applying a material of high secondary electron yield to the input face of the rear MCP. To test this hypothesis a layer of CsI was applied to one half of the rear MCP (Section 7.3.2).

7.3.2. Operation with CsI coated rear MCP

Using the same technique as for coating the front MCP (Section 5.1), 12500 Å of CsI was evaporated at normal incidence onto one half (Fig 3.1) of the input surface of the rear MCP. This MCP was removed from the detector and coated without being subjected to another high temperature vacuum bake. Upon reassembly of the detector the CsI coated surfaces of both front and rear MCP's were aligned. A restricted subset of the previous measurements (Section 7.2) were then repeated on the CsI coated side of the detector.

Figs 7.17 (a,b,c,d) illustrate the variation of G_c and $\Delta G_c/G_c$ with rear plate voltage V_R. The general behaviour is very similar to that observed previously (Figs.7.9 (a,b,c,d)). The gain for a given voltage has increased but the measured values of S and the behaviour of $\Delta G_c/G_c$ and G_c (Si-K) / G_c (C-K) are essentially unchanged. The minimum value of S has shifted to a slightly higher V_R value.

The variation of G_c and $\Delta G_c/G_c$ with front plate voltage V_F is shown in Figs.7.18 (a,b,c,d). Comparison with previous data (Figs.7.7 (a,b,c,d), 7.8 (a,b,c,d)) shows the behaviour to be substantially unchanged. An increase in gain is again noted, together with an increase in the separation of the peaks. No significant change is produced in energy resolution however, with values of $S \simeq 0.4$ being obtained.

Figs.7.19 (a,b,c,d) show the variation of G_c and $\Delta G_c/G_c$ with V_G which can be compared with Figs.7.10 (a,b,c,d). The observed variation of Figs.7.19 (b,c,d) is practically identical to previous results with limiting S values of $\simeq 0.4$ being achieved. The variation of G_c

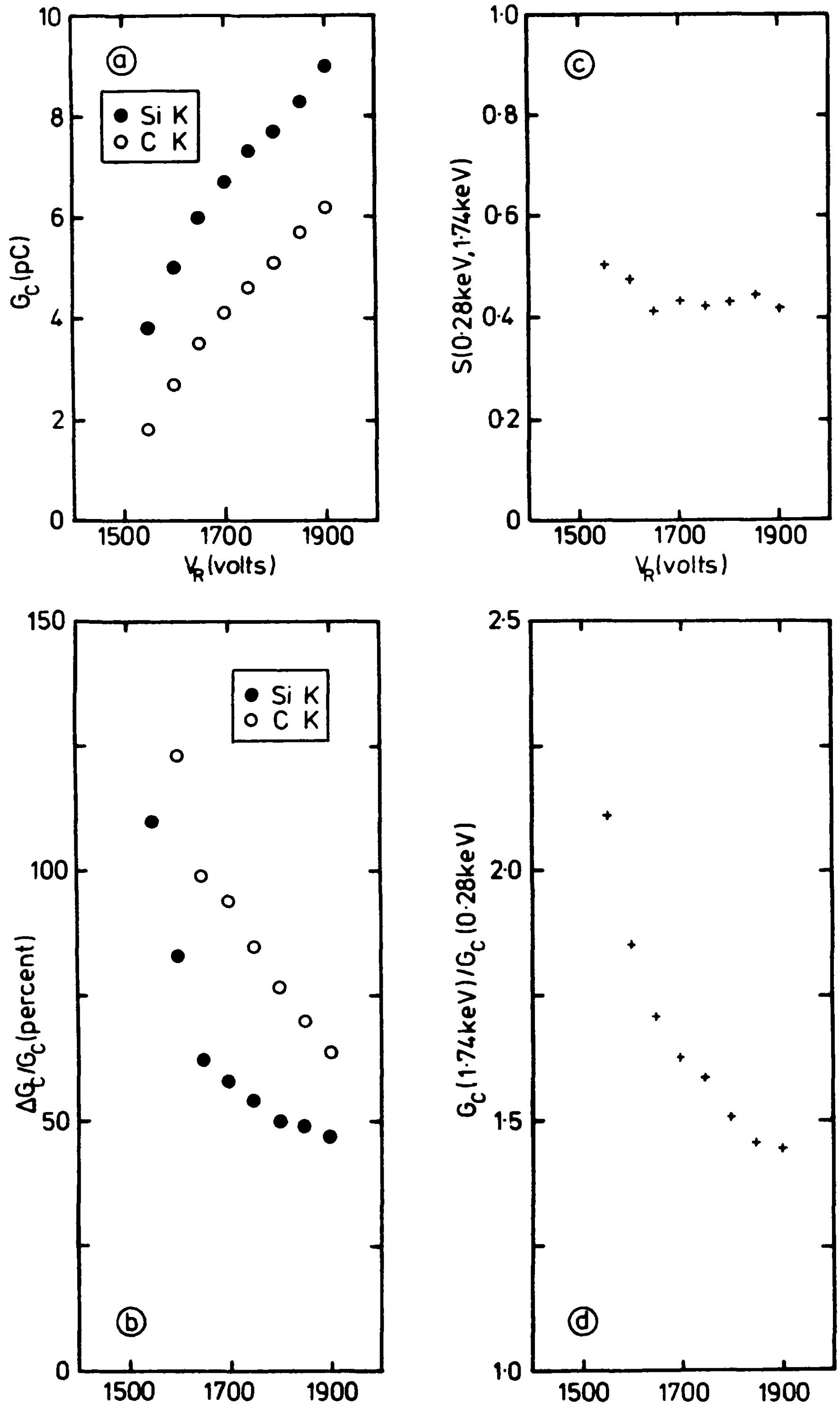

7.17. Chevron energy resolution as a function of rear plate voltage V_R. Si-K (1.74 keV) and C-K (0.28 keV) X-rays. V_F=1400 volts, V_G=600 volts, θ=5°, N_m=500 s^{-1}, x=32 mm. (Detector half with CsI coated front and rear MCP's.)

(a) Peak gains G_c

(b) FWHM's $\Delta G_c/C_c$

(c) Separation S (0.28 keV , 1.74 keV)

(d) Ratio of peak gains G_c(1.74 keV) / G_c(0.28 keV)

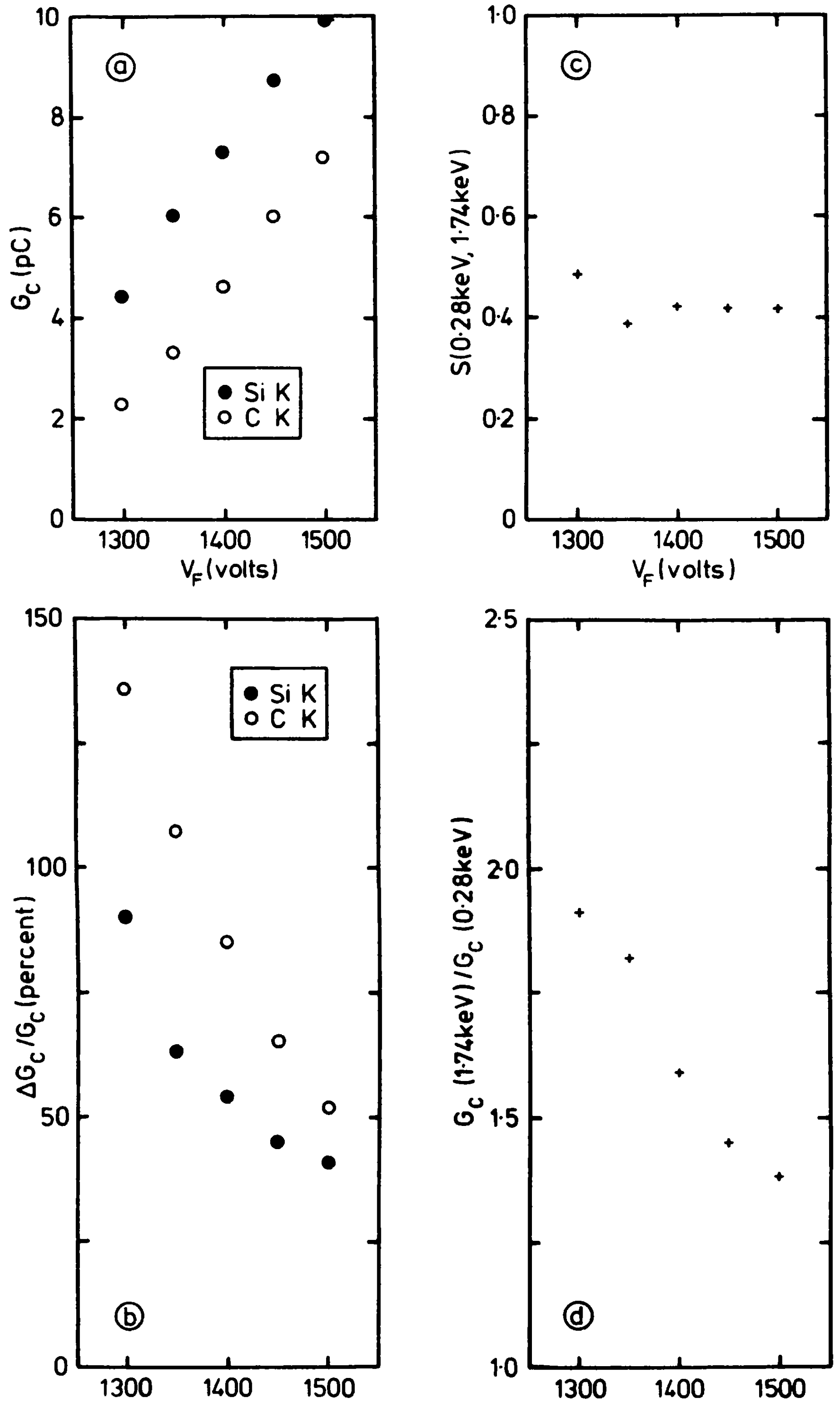

7.18. Chevron energy resolution as a function of front plate voltage V_F. Si-K (1.74 keV) and C-K (0.28 keV) X-rays. V_R=1750 volts, V_G=600 volts, θ=5°, N_m=500 s^{-1}, x=32 mm. (Detector half with CsI coated front and rear MCP's.)

(a) Peak gains G_c

(b) FWHM's $\Delta G_c/G_c$

(c) Separation S (0.28 keV, 1.74 keV).

(d) Ratio of peak gains G_c(1.74 keV) / G_c(0.28 keV).

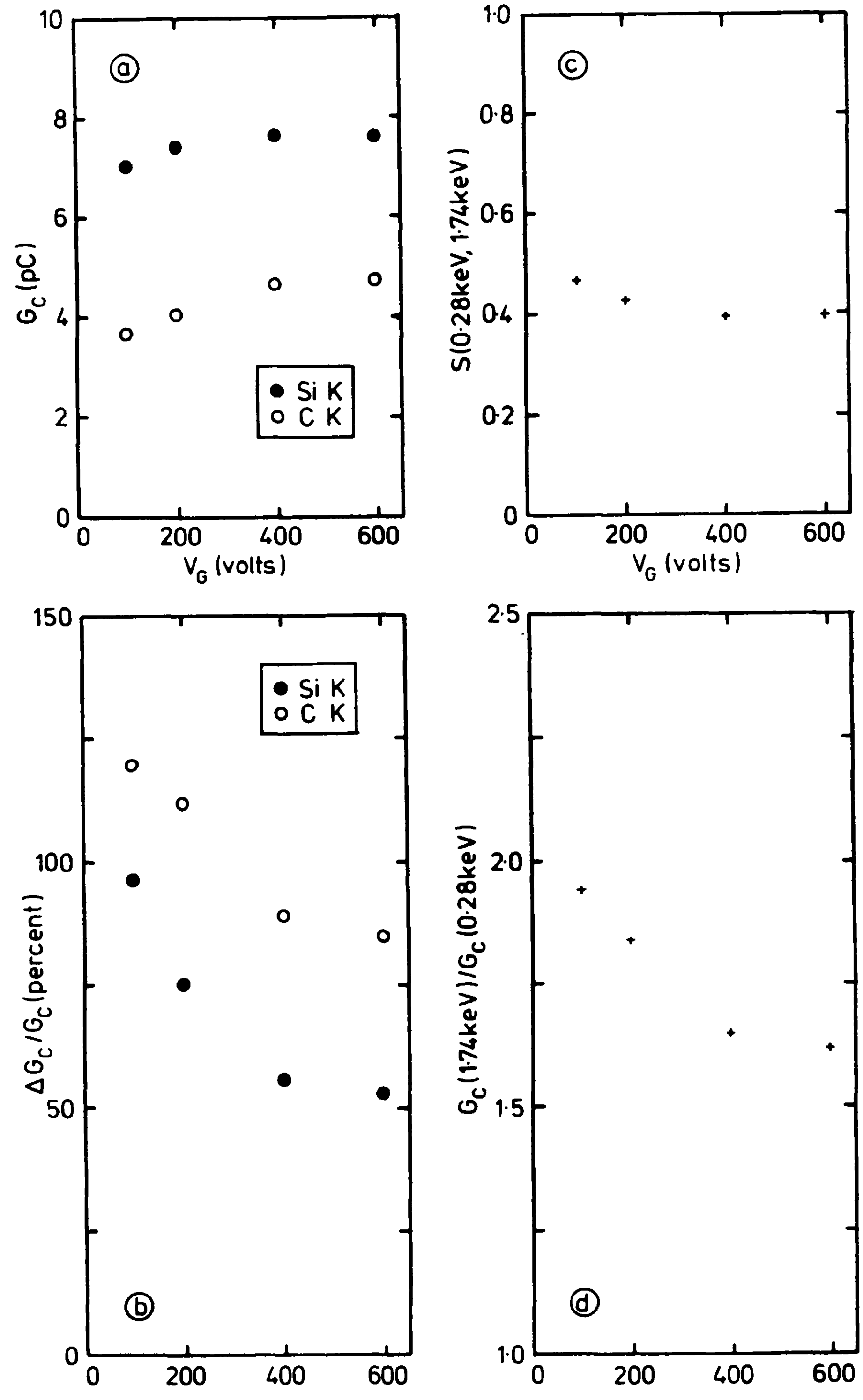

7.19. Chevron energy resolution as a function of accelerating interplate gap voltage V_G. Si-K (1.74 keV) and C-K (0.28 keV) X-rays. V_F=1400 volts, V_R=1750 volts, θ=5°, N_m=500 s^{-1}. x=32 mm. (Detector half with CsI coated front and rear MCP's.)

(a) Peak gains G_c

(b) FWHM's $\Delta G_c/G_c$

(c) Separation S (0.28 keV, 1.74 keV)

(d) Ratio of peak gain G_c(1.74 keV) / G_c(0.28 keV)

(Fig.7.19 (a)) is however significantly different from any that has been previously observed (e.g. Fig.7.10 (a)). This behaviour can be explained by the very rapidly changing secondary electron yield of CsI for electrons in the 100 eV-600 eV range [129].

As V_G increases there are three competing effects. The secondary electron yield of the CsI increases with bombarding electron energy, while the number of channels illuminated and the range of the secondary electrons emitted from the interchannel area both decrease. For $V_G \lesssim 300$ V the rapidly increasing secondary electron yield of the CsI completely dominates the decreasing number of channels illuminated and hence G_c increases with V_G. At the same time, however, the maximum electron range decreases with the reciprocal of the applied voltage and is only ~ 0.4 μm at V_G=400 volts for an electron of energy 0.5 eV (typical energy of secondary electron from CsI [107]). A range of 0.4 μm is substantially smaller than the width of the interchannel area which is typically 2.5-5 μm. The increase in secondary electron yield with increasing incident electron energy is therefore largely cancelled out for $V_G \gtrsim 400$ V because the majority of secondaries do not enter a channel and hence the gain stabilizes. Comparison between the C-K and Si-K behaviour clearly shows that the MCP itself does not limit the gain since the larger number of input electrons from a Si-K X-ray produces a higher gain.

The behaviour of G_c and $\Delta G_c/G_c$ with count rate N_m is shown in Figs.7.20 (a,b,c,d). These show the same variations previously observed (Figs.7.11 (a,b,c,d)), with a slow decrease in energy resolution as N_m increases.

For comparison with previous results a gain measurement was made at Ru-L (2.68 keV). Fig.7.21 shows the variation of G_c as a function of X-ray energy for comparison with Fig.7.15 (a). The theoretical curve shown is the same as that of Fig.7.15 (a) scaled to fit the higher gains. This, together with the practically unchanged S values shows that no

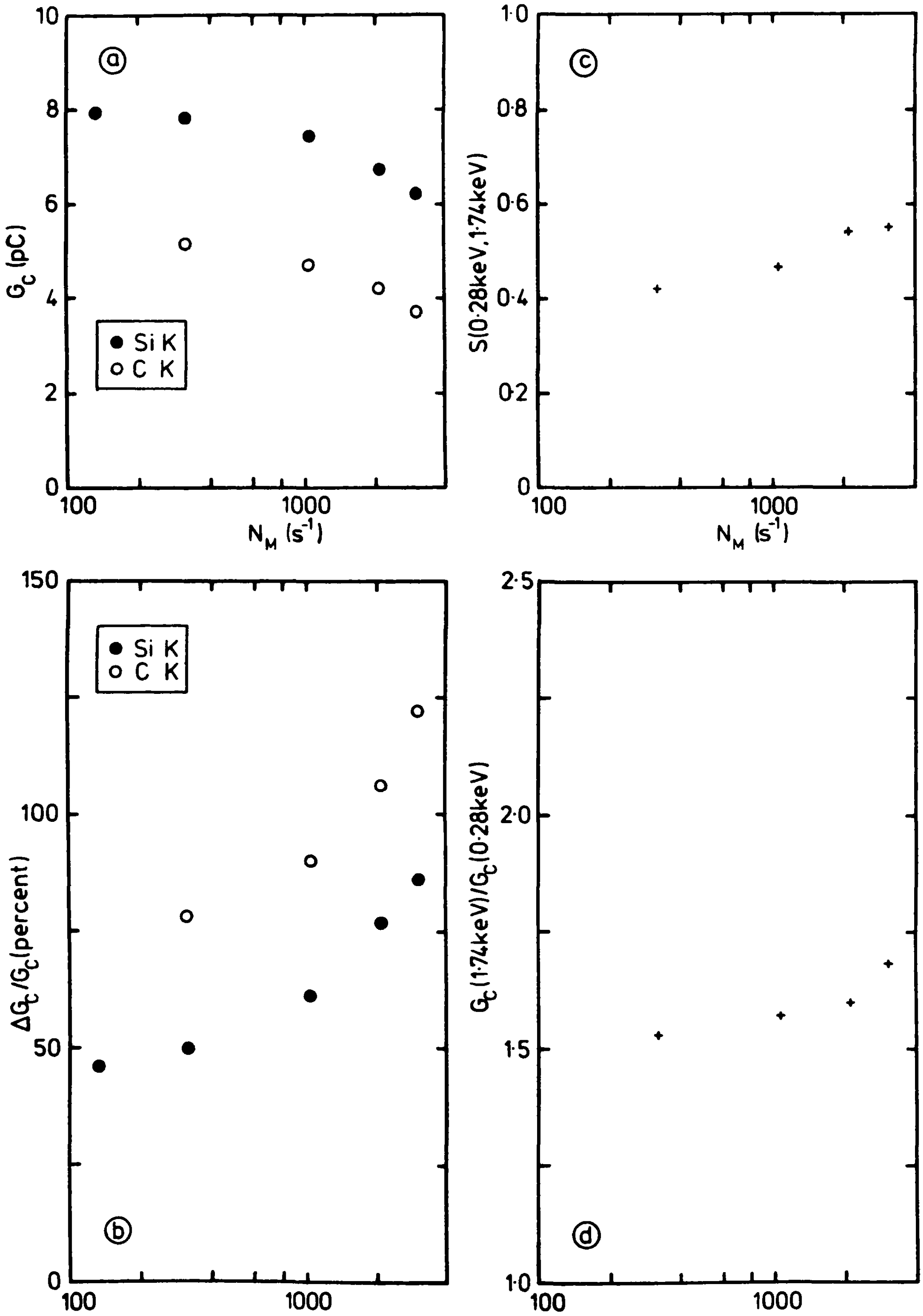

7.20. Chevron energy resolution as a function of MCP output count rate, N_m. Note that 1000 counts s^{-1}=26 counts mm^2 s^{-1}. X-ray energies Si-K (1.74 keV), C-K (0.28 keV). V_F=1400 volts, V_G=600 volts, V_R=1750 volts, θ=5°, x=32 mm. (Detector half with CsI coated front and rear MCP's).

(a) Peak gains G_c

(b) FWHM's $\Delta G_c/G_c$

(c) Separation S (0.28 keV, 1.74 keV)

(d) Ratio of peak gain G_c(1.74 keV) / G_c(0.28 keV)

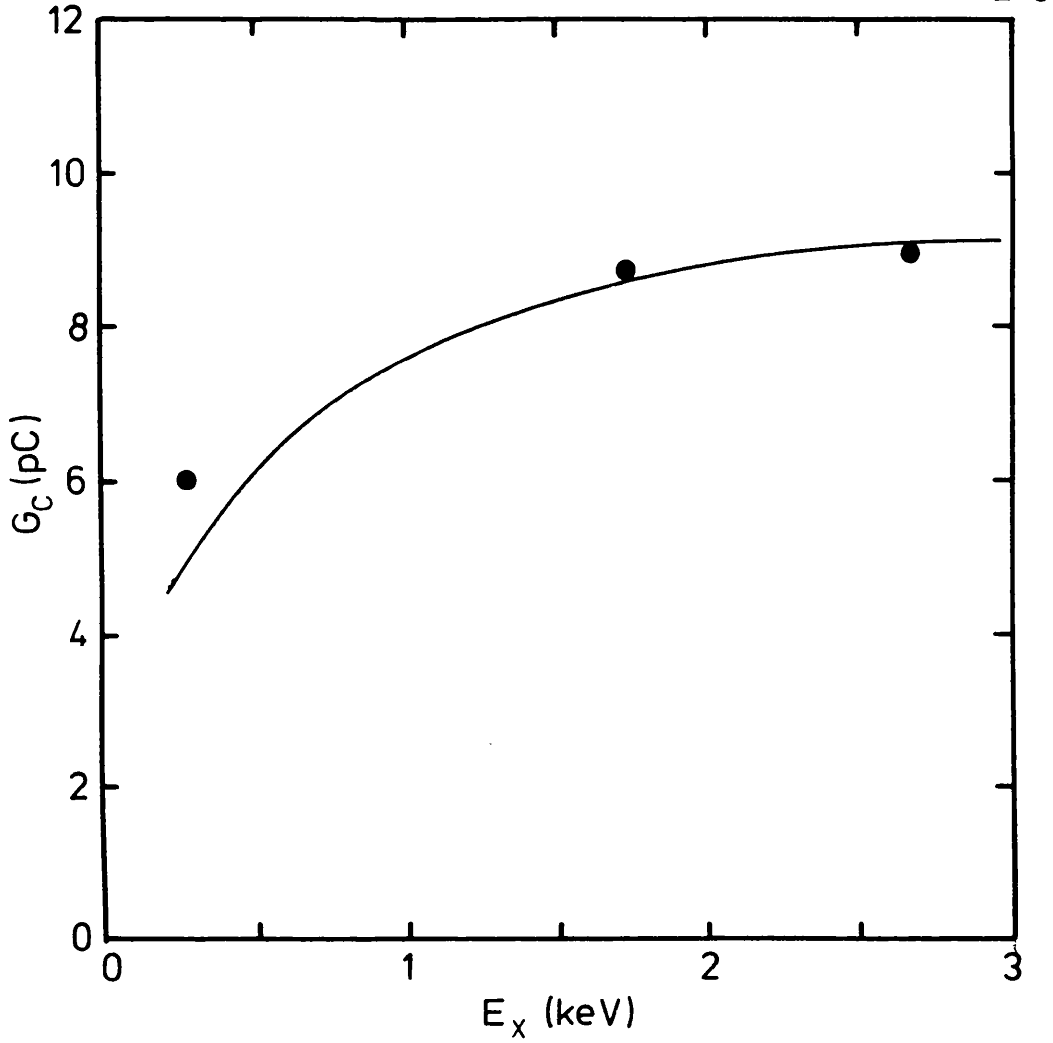

7.21. Chevron peak gain G_C as a function of X-ray energy, E_X. V_F=1400 volts, V_G=600 volts, V_R=1750 volts, θ=5°, N_m=500 s^{-1}, x=32 mm. (Detector half with CsI coated front and rear MCP's.) Theoretical curve as in Fig.7.15 scaled to fit higher gains.

significant improvement in energy resolution has been produced by coating the rear MCP with CsI. The higher ΔG_c values obtained have been cancelled out by poorer FWHM's leaving S unchanged.

The conclusion to be drawn from this is that it is not possible to change β by coating the rear MCP with a material of high secondary electron yield. This technique has, however, produced increased chevron gains and use could perhaps be made of this. A potential danger of this is the degradation of the CsI under prolonged electron bombardment [129] but the current densities involved in MCP operation may be too low for this to be a problem.

CHAPTER 8

CONCLUSIONS AND FUTURE DEVELOPMENT

8.1 Conclusions

The purpose of the work described in this thesis was the improvement of the chevron MCP detector for X-ray astronomy. This has been achieved in three areas; (1) detector design, (2) detector efficiency, (3) energy resolution. The properties of a laboratory test facility have also been described.

The results presented in Chapter 4 confirm the suitability of a chevron MCP as a focal plane instrument for X-ray astronomy. Optimum results were achieved using an accelerating potential between the front and rear MCP's, the FWHM of the output PHD being equal to the best reported for curved channel MCP's [37]. Preliminary investigation into the use of MCP's with surfaces curved to match the focal plane of an X-ray telescope established the feasibility of production methods and showed that in practice MCP's would have to be curved on both sides to give uniform gain over the whole plate.

Initial work [106] on the use of CsI as a high efficiency X-ray photocathode has been extended (Chapter 5). An investigation into photocathode stability showed the feasibility of producing much thicker (14,000 Å) photocathode layers. This was exploited in the use of a smaller coating angle than previously employed (4° instead of 15°), to maximise low angle efficiencies.

The increased efficiency obtained by using a CsI photocathode could be applied to a number of current X-ray astronomy projects. The ROSAT WFC, being developed by a consortium of British universities, will be able to take advantage of the predicted high efficiency of CsI as a photocathode in the XUV [139]. The ROSAT main telescope being developed by West Germany includes an American contribution in the form of a duplicate Einstein HRI detector. The sensitivity of this instrument could be greatly increased if the present, baseline proposal, MgF_2 photocathode was replaced with a CsI photocathode. A proposal that this should be done has been put forward by the Harvard Smithsonian Centre for Astrophysics in collaboration with Leicester University.

In the longer term, CsI would be a very strong candidate for the photocathode of any MCP detector used in the AXAF focal plane. A proposal for such a detector has been submitted, in response to the AXAF announcement of opportunity released in September 1983, as a Harvard Smithsonian Centre for Astrophysics-Leicester University joint proposal. The present results would have to be extended to high energies (6-8 keV) and competition could be expected from alternative photocathodes, e.g. field enhanced secondary electron emission photocathode [127].

The techniques developed here could also be used in other areas of physics where the detection of soft X-rays is important e.g. laser fusion, diffraction studies, medicine.

The advantages of using a field defining plane to collect electrons liberated from a CsI coated MCP front surface have also been demonstrated (Chapter 6). For practical applications it is important to consider whether the gain in efficiency is sufficient to offset the increased complexity of the system. For small angles of X-ray incidence (Table 6.1) the true increase in efficiency is very small because of X-ray absorption by the repeller grid. In this case the possible gains do not justify introducing an extra component, but they might justify biasing a suitable component that is required for other reasons, e.g. a metalised ultra-violet shield.

The case at larger angles is much more clear cut since large increases in efficiency (factors of 1.5) are possible. In practically all cases extra components would be justified, although as for low angles, larger improvements are possible if an existing detector component can be used.

The most important breakthrough, however, is the demonstration, for the first time, of energy resolution from a MCP detector (Chapter 7). An application of this energy resolution was envisaged for the low energy telescope on the High Throughput Spectrometer (HTS) mission proposed to the Science and Engineering Research Council by a consortium of U.K. institutions (including Leicester University) in November 1982. It was proposed to detect dispersed X-ray spectra, 5-30 Å ; 50-200 Å , using a CsI coated MCP. The intention was to use the energy resolution to eliminate the order confusion caused by overlapping spectra. Although the resolution demonstrated here is insufficient to achieve this aim, the orders could be resolved if the energy resolution was developed to the full extent predicted by theory.

A CsI coated HRI detector used on the ROSAT main telescope would be able to make full use of the available energy resolution since it will be operating in the 0.1-3 keV energy range. No significant amount of energy resolution is possible for the ROSAT WFC, however, since in the XUV the most probable number of electrons emitted is one regardless of incident X-ray energy.

8.2. Future Work

The continuation of this work is considered very important for the future development of MCP's in X-ray astronomy. The most pressing need at present is to extend the range of X-ray energies to cover the entire AXAF energy range. The acquisition and installation of an Fe^{55} (5.9 keV) radioactive source, as an alternative X-ray source, is at present under way in partial fulfilment of this requirement.

Another very important line of work is the further investigation and improvement of MCP energy resolution. The immediate work will concentrate on varying the basic MCP parameters. As noted in Section 7.3.1 a smaller channel diameter should reduce β and hence improve the energy resolution.

A pair of 25 mm diameter Mullard MCP's with D=8 μm and L:D=120:1 are now on order to test this hypothesis. Also of interest is the result of the variation of S with different L:D values (Section 7.2.2). This could conceivably be done over a range of L:D values using the plano -concave MCP described in Section 4.2.

It would also be of interest to investigate the performance of CsI coated curved channel MCP's [37]. The gain characteristics of these plates have been successfully modelled [38] but the degree of energy resolution expected is uncertain since there is no published X-ray data on CsI coated curved MCP's. It may be that, since there is no possibility of separating the linear and saturated gains in a single channel, very little energy resolution will be available. A difference of this kind has been observed in the detection of low energy multiple charged ions [153]. In this experiment the gain of a chevron was found to be proportional to ionic charge while the gain of a single channel electron multiplier was independent of ionic charge.

A less promising approach is the detailed study of photoemission statistics for materials other than CsI. Such a study has already been carried out on CsCl by Dr. G.W. Fraser with the conclusion that CsI is the more useful photocathode. There is unlikely to be any significantly superior stable photocathode than CsI, since materials with superior secondary electron characteristics are not normally stable when exposed to oxygen (Section 4.3.2). It is possible, however, that a significant improvement in energy resolution could be produced without requiring the prohibitive degree of cleanliness that NEA materials demand.

Future work on energy resolution could also attempt to quantify the trade off between energy resolution and efficiency which is predicted by theory (Section 7.1.2). A comparison between the output from the detection of X-rays and electrons would be of interest. Any significant differences between the two could be utilised to discriminate against background electrons, which would be a very valuable technique for satellite experiments where, depending on the orbit, electron background can be significant.

For satellite experiments with expected lifetimes of 2-5 years it is necessary to investigate the changes in efficiency, gain and energy resolution with both storage time and accumulated counts. The gain degradation of MCP's with accumulated counts is well established [46] and the changes induced in this behaviour by coating with CsI must be determined. Work is at present underway at Leicester to study the gain and efficiency changes of CsI coated MCP's. The effects of bombarding the CsI with high energy radiation, cosmic rays and high energy electrons must also be quantified before CsI can be used in a space environment.

Experimental investigation of a different photocathode material, e.g. CsCl, would also be of value. The results while important in their own right can also be used as a further check on the accuracy of the theoretical model [121,124,139]. An MCP model has been used in the past, and will be used in the future, to select promising areas of investigation and therefore it is important to test it as fully as possible.

The development of CsI technology to include field enhanced secondary emission techniques [127] is also of great interest. This approach may turn out to be the most effective for the higher energy range of AXAF, especially if some degree of energy resolution could be obtained from the low density CsI photocathodes.

Reference Abbreviations

Acta Elec.	Acta Electronica
Adv.Electron.Electron Phys.	Advances in Electronics and Electron Physics
Ann.Rev.Astr.Ap.	Annual Review of Astronomy and Astrophysics
Appl.Opt.	Applied Optics
Ap.J.	Astrophysical Journal
Bull.Acad.Sci.USSR.	Bulletin of the Academy of Science USSR: Physics Series.
IEEE Trans.Nucl.Sci.	Institute of Electrical and Electronic Engineers: Transactions on Nuclear Science
J.Appl.Phys.	Journal of Applied Physics
J.Phys.E.	Journal of Physics E : Scientific Instruments
J.Vac.Sci.Technol.	Journal of Vacuum Science and Technology
M.N.R.A.S.	Monthly Notices of the Royal Astronomical Society
Nucl.Instr.Meth.	Nuclear Instruments and Methods (in Physics Research)
Rad.Eng.Elec.Phys.	Radio Engineering and Electronic Physics
Rev.Sci.Instr.	Review of Scientific Instruments
Space Sci.Rev.	Space Science Reviews
SPIE	Society of Photo-optical Instrumentation Engineers (Proceedings)

References

(1) Wiza, J.L. : Nucl.Instr.Meth. 162 (1979) 587-601

(2) Lecomte, P. and Perez-Mendez, V. : IEEE Trans.Nucl.Sci. NS-25 (1978) 964-973

(3) Dmitriev, V.D., Luk'yanov, S.M., Penionzhkevich, Yu.E. and Sattarov, D.K. : Instruments and Experimental Techniques 25 (1982) 283-294

(4) Woodhead, A.W. and Ward, R. : The Radio and Electronic Engineer 47 (1977) 545-553

(5) Ruggieri, D.J. : IEEE Trans.Nucl.Sci. NS-19 (1972) 74-84

(6) Lo, C.C., Lecomte, P. and Leskovar, B. : IEEE Trans.Nucl.Sci. NS-24 (1977) 302-311

(7) Hocker, L.P., Zagarino, P.A., Madrid, J., Simmons, D., Davis, B. and Lyons, P.B. : IEEE Trans.Nucl.Sci. NS-26 (1979) 356-363

(8) Green, M.I., Kenealy, P.F. and Beard, G.B. : Nucl.Instr.Meth. 126 (1975) 175-179

(9) Pietri, G. : IEEE Trans.Nucl.Sci. NS-24 (1977) 228-232

(10) Woodhead, A.W. and Eschard, G. : Acta Elec. 14 (1971) 181-200

(11) Wijnaendts van Resandt, R.W., den Harink, H.C. and Los, J. : J.Phys.E. 9 (1976) 503-509

(12) Thomas, E.L. and Danyluk, S. : J.Phys.E. 4 (1971) 843-844

(13) Broadfoot, A.L. and 10 co-authors : Space Sci.Rev. 21 (1977) 183-205

(14) McClintock, W.E., Barth, C.A., Steele, R.E., Lawrence, G.M. and Timothy, J.G. : Appl.Opt. 21 (1982) 3071-3079

(15) Weiser, H., Vitz, R.C., Moos, H.W. and Weinstein, A. : Appl.Opt. 15 (1976) 3123-3130

(16) Bowyer, S., Kimble, R., Paresce, F., Lampton, M. and Penegor, G. : Appl.Opt. 20 (1981) 477

(17) Barstow, M.A. : Ph.D. Thesis, Leicester University, 1983

(18) Taylor, B.G., Andresen, R.D., Peacock, A. and Zobl, R. : Space Sci. Rev. 30 (1981) 479-494

(19) Giacconi, R. and 30 co-authors : Ap.J. 230 (1979) 540-550

(20) Lampton, M., Margon, B., Paresce, F., Stern, R. and Bowyer , S. : Ap.J. 203 (1976) L71-L74

(21) Giacconi, R., Reidy, W.P., Vaiana, G.S., Van Speybroeck, L.P. and Zehnpfennig, T.F. : Space.Sci.Rev. 9 (1969) 3-57

(22) Giacconi, R., Gursky, H. and Van Speybroeck, L.P. : Ann.Rev.Astr.Ap. 6 (1968) 373-416

(23) Giacconi, R., Kellogg, E., Gorenstein, P., Gursky, H. and Tananbaum, H. : Ap.J. 165 (1971) L27-L35

(24) Villa, G., Page, C.G., Turner, M.J.L., Cooke, B.A., Ricketts, M.J., Pounds, K.A. and Adams, D.J. : M.N.R.A.S. 176 (1976) 609-620

(25) See for instance papers in Ap.J. 234 (1979) No.1 part 2.

(26) Gorenstein, P., Gursky, H., Harnden, F.R. Jr., De Caprio, A. and Bjorkholm, P. : IEEE Trans.Nucl.Sci. NS-22 (1975) 616-619

(27) Sims, M.R., Peacock, A. and Taylor, B.G. : To be published in Nucl.Inst.Meth.

(28) Lumb, D.H. : Ph.D. thesis, Leicester University, 1983.

(29) Trumper, J. : Advances in Space Research 2 (1983) 241-249

(30) Zombeck, M.V. : SPIE 184 (1979) 50-62

(31) XMM X-ray Multi-Mirror Assessment Study. European Space Agency report SCI(83)2. September 1983

(32) The High Throughput Spectrometer - a proposal to the SERC for a UK-led space mission in X-ray spectroscopy. November 1982

(33) Barstow, M.A., Physics Department, Leicester University. Private communication

(34) Washington, D., Duchenois, V., Polaert, R. and Beasley, R.M. : Acta Elec. 14 (1971) 201-224

(35) Asam, A.R. : Optical Engineering 17 (1978) 640-644

(36) Boutot, J.P., Eschard, G., Polaert, R. and Duchenois, V. : Adv. Electron.Electron Phys. 40A (1976) 103-111

(37) Timothy, J.G. : Rev.Sci.Instr. 52 (1981) 1131-1142

(38) Fraser, G.W., Pearson, J.F., Smith, G.C., Lewis, M. and Barstow, M.A. : IEEE Trans.Nucl.Sci. NS-30 (1983) 455-460

(39) Schmidt, K.C. and Hendee, C.F. : IEEE Trans.Nucl.Sci. NS-13 (1966) 100-111

(40) Chalmeton, V. and Eschard, G. : Adv.Electron.Electron Phys. 33A (1972) 167

(41) Bouchard, C. and Carette, J.D. : J.Appl.Phys. 50 (1979) 7168-7176

(42) Field, R., Mullard Ltd. : Private Communication

(43) Parkes, W. and Gott, R. : Nucl.Instr.Meth. 95 (1971) 487-491

(44) Colson, W.B., McPherson, J. and King, F.T. : Rev.Sci.Instr. 44 (1973) 1694-1696

(45) Gatti, F., Oba, K. and Rehak, P. : IEEE Trans.Nucl.Sci. NS-30 (1983) 461-468

(46) Fraser, G.W. : To be published in Nucl.Instr.Meth.

(47) Fraser, G.W. and Mathieson, E. : Nucl.Instr.Meth. 179 (1981) 591-604

(48) Fraser, G.W. and Mathieson, E. : Nucl.Instr.Meth. 184 (1981) 537-542

(49) Wiza, J.L., Henkel, P.R. and Roy, R.L. : Rev.Sci.Instr. 48 (1977) 1217-1218

(50) Morton, J.M. and Parkes, W. : Acta Elec. 16 (1973) 85-100

(51) Kubierschky, K., Austin, G.K., Harrison, D.C. and Roy, A.G. : IEEE Trans.Nucl.Sci. NS-25 (1978) 430-436

(52) Smith, G.C., Pearson, J.F. and Mathieson, E. : Nucl.Instr.Meth. 192 (1982) 383-386

(53) Lampton, M. and Malina, R.F. : Rev.Sci.Instr. 47 (1976) 1360-1362

(54) Martin, C., Jelinsky, P., Lampton, M., Malina, R.F. and Anger, H.O. : Rev.Sci.Instr. 52 (1981) 1067-1074

(55) Timothy, J.G., Mount, G.H. and Bybee, R.L. : IEEE Trans.Nucl.Sci. NS-28 (1981) 689-697

(56) Mathieson, E., Smith, G.C. and Gilvin, P.J. : J.Phys.E. 13 (1980) 792-793

(57) Mathieson, E., Smith, G.C. and Gilvin, P.J. : Nucl.Instr.Meth. 174 (1980) 221-225

(58) Mathieson, E., Physics Department, Leicester University : Private communication

(59) American Institute of Physics Handbook (3rd Edition) : McGraw Hill, New York (1972)

(60) Bronshteyn, I.M., Yevdokimov, A.V., Stozharov, V.M. and Tyutikov, A.M. : Rad.Eng.Elec.Phys. 24 (1979) 150-152

(61) Gilvin, P.J. : Ph.D. thesis, Leicester University, 1981

(62) Gordon, J.S., Mathieson, E. and Smith, G.C. : IEEE Trans.Nucl.Sci. NS-30 (1983) 342-346

(63) Mason, I.M., Branduardi-Raymont, G., Culhane, J.L., Corbet, R.H.D., Ives, J.C. and Sanford, P.W. : IEEE Trans.Nucl.Sci. NS-31 (1984) 795-800

(64) Henry, J.P., Kellogg, E.M., Briel, U.G., Murray, S.S., Van Speybroeck, L.P. and Bjorkholm, P.J. : SPIE 106 (1977) 196

(65) Eberhardt, E.H. : IEEE Trans.Nucl.Sci. NS-28 (1981) 712-717

(66) Fraser, G.W. : Nucl.Instr.Meth. 195 (1982) 523

(67) Hill, G.E. : Adv.Electron.Electron Phys. 40A (1976) 153-165

(68) Siddiqui, S.H. : J.Appl.Phys. 48 (1977) 3053-3059

(69) Klettke, B.D., Krym, N.D. and Wolber, W.G. : IEEE Trans.Nucl.Sci. NS-17 (1970) 72-80

(70) Frank, L.A., Henderson, N.K. and Swisher, R.L. : Rev.Sci.Instr. 40 (1969) 685-689

(71) Mullard Ltd., New Road, Mitcham. Surrey, CR4 4XY

(72) Fraser, G.W. and Pearson, J.F. : Nucl.Instr.Meth. 219 (1984) 199-212

(73) Dhawan, S. and Majka, R. : IEEE Trans.Nucl.Sci. NS-24 (1977) 270-275

(74) Weston, G.F. : Vacuum 28 (1978) 209-233

(75) Roth, A. : Vacuum Technology, North Holland Publishing Co. (1976)

(76) Power, B.D., Dennis, N.T.M., Oswald, R.D. and Colwell, B.H. : Vacuum 24 (1974) 117-122

(77) Bentley, P.D. : Vacuum 30 (1980) 145-158

(78) Chou, T.S. and McCafferty, D. : J.Vac.Sci.Technol. 18 (1981) 1148-1151

(79) Becker, W. : Vakuum Technik 7 (1958) 149

(80) Mirgel, K.H. : J.Vac.Sci.Technol. 9 (1972) 408-411

(81) Chu, J.G. and Hua, Z.Y. : J.Vac.Sci.Technol. 20 (1982) 1101-1104

(82) Dennis, N.T.M., Laurenson, L., Devaney, A. and Colwell, B.H. : J.Vac.Sci.Technol. 20 (1982) 996-999

(83) Harris, N.S. : Vacuum 30 (1980) 175-181

(84) Maurice, L., Duval, P. and Gorinas, G. : J.Vac.Sci.Technol. 16 (1979) 741-745

(85) Harris, N.S. : Vacuum 31 (1981) 173-182

(86) Hoffman, D.M. : J.Vac.Sci.Technol. 16 (1979) 71-74

(87) Baker, M. and Laurenson, L. : Vacuum 16 (1966) 633-637

(88) Harris, N.S. : Vacuum 28 (1978) 261-268

(89) Registered trade mark of Varian Associates

(90) Love, G., Scott, V.D., Dennis, N.M.T. and Laurenson, L. : Scanning 4 (1981) 32-39

(91) Registered trade mark of Du Pont (UK) Ltd.

(92) Srdoc, D. and Clark, B.C. : Nucl.Instr.Meth. 78 (1970) 305-313

(93) Clark, G.C. : Applied X-rays, McGraw Hill, New York (1955) 22-23

(94) Finley, D.S., Bowyer, S., Paresce, F. and Malina, R.F. : Appl.Opt. 18 (1979) 649-654

(95) Brown, G. and Kanaris-Sotiriou, R. : J.Phys.E. 2 (1969) 551-552

(96) McTurk, G., Electron Microscope Suite, Leicester University : Private communication

(97) Clark, B.C. and Gross, W. : Rev.Sci.Instr. 40 (1969) 1178-1182

(98) Cash, W.:IEEE Trans.Nucl.Sci. NS-30 (1983) 1535-1538

(99) Lipson, H., Nelson, J.B. and Riley, D.P. : Journal of Scientific Instruments 22 (1945) 184-187

(100) Parrish, W. and Roberts, B.W. : X-ray Analysis Papers, Centrex Pub. Co. Eindhaven (1965) 31-46

(101) Lukirskii, A.P., Savinov, E.P., Ershov, O.A. and Shepelev, Yu.F. : Optics and Spectroscopy 16 (1964) 168-172

(102) Smith, D.G. and Pounds, K.A. : IEEE Trans.Nucl.Sci. NS-15 (1968) 541-550

(103) Cranfield, L.R., Johnston, R.G. and Madden, R.P. : Appl.Opt. 12 (1973) 1611-1617

(104) Saloman, E.B. : Appl.Opt. 17 (1978) 1489-1490

(105) Lukirskii, A.P., Ershov, O.A. and Brytov, I.A. : Bull.Acad.Sci.USSR 27 (1963) 798-807

(106) Fraser, G.W., Barstow, M.A., Whiteley, M.J. and Wells, A. : Nature 300 (1982) 509

(107) Henke, B.L., Knauer, J.P. and Premaratne, K. : J.Appl.Phys. 52 (1981) 1509-1520

(108) Bjorkholm, P.J., Van Speybroeck, L.P. and Hecht, M. : SPIE 106 (1977) 189-195

(109) Huizenga, H., Bleeker, J.A.M., Diemer, W.H. and Huben, A.P. : Rev.Sci.Instr. 52 (1981) 673-677

(110) Franzen, W. and Cochran, L.W. : Nuclear instruments and their uses, ed. A.H. Snell, Wiley, New York (1962) 3-81

(111) Bateman, J.E., Waters, M.W. and Jones, R.E. : Nucl.Instr.Meth. 135 (1976) 235-249

(112) Henke, B.L. and Tester, M.A. : Advances in X-ray Analysis 18 (1975) 76-106

(113) Smith, D.G. : Ph.D. thesis, University of Leicester (1968)

(114) Ott, H.W. : Noise reduction techniques in electronic systems, Wiley, New York 1976

(115) Macor : Machinable glass ceramic, Corning code 9658

(116) Rogers, D. and Malina, R.F. : Rev.Sci.Instr. 53 (1982) 1438

(117) Fraser, G.W. : Nucl.Instr.Meth. 206 (1983) 445

(118) Willingale, R., Physics Department, Leicester University : Private communication

(119) Optical Surfaces Ltd., Godstone Road, Kenley, Surrey, CR2 5AA

(120) Adams, J., and Manley, B.W. : IEEE Trans.Nucl.Sci. NS-13 (1966) 88-98

(121) Fraser, G.W. : Nucl.Instr.Meth. 206 (1983) 251

(122) Eng, W. Jnr. and Landecker, P.B. : Nucl.Instr.Meth. 190 (1981) 149-157

(123) Lapson, L.B. and Timothy, J.G. : Appl.Opt. 12 (1973) 388-393

(124) Fraser, G.W. : Nucl.Instr.Meth. 206 (1983) 265

(125) Bardas, D., Kellogg, E., Murray, S. and Enck, R.Jr. : Rev.Sci.Instr. 49 (1978) 1273-1278

(126) Fraser, G.W., Physics Department, Leicester University : Private communication

(127) Bateman, J.E. and Apsimon, R.J. : Adv.Electron.Electron Phys. 52 (1979) 189

(128) Bateman, J.E., Apsimon, R.J. and Arndt, U.W. : Rutherford Appleton Laboratory report RL-81-008 February 1981

(129) Verma, R.L. : Journal of Physics D : Applied Physics 11 (1978) 63-71

(130) Heroux, L., McMahon, W.J. and Hinteregger, H.E. : Appl.Opt. 5 (1966) 1338-1339

(131) Premaratne, K., Dietz, E.R. and Henke, B.L. : Nucl.Instr.Meth. 207 (1983) 465-467

(132) Scott, J.P. : J.Appl.Phys. 46 (1975) 661-664

(133) Saloman, E.B., Pearlman, J.S. and Henke, B.L. : Appl.Op. 19 (1980) 749-753

(134) Boutot, J.P. : Acta Elec. 14 (1971) 245-262

(135) Rager, J.P., Renaud, J.F. and Tezenas du Montcel, V. : Rev.Sci.Instr. 45 (1974) 927-928

(136) Siddiqui, S.H. : IEEE Transactions on Electron Devices ED-26 (1979) 1059-1064

(137) Whiteley, M.J., Physics Department, Leicester University : Private communication

(138) Kellogg, E., Henry, P., Murray, S., Van Speybroeck, L. and Bjorkholm, L. : Rev.Sci.Instr. 47 (1976) 282-290

(139) Fraser, G.W., Barstow, M.A., Pearson, J.F., Whiteley, M.J. and Lewis, M. : Nucl.Instr.Meth. (in press)

(140) Whiteley, M.J., Pearson, J.F., Fraser, G.W. and Barstow, M.A. : Nucl.Instr.Meth. (in press)

(141) Van der Ven, H.W. : Nucl.Instr.Meth. 75 (1969) 347-348

(142) Bates, C.W.Jr. : Adv.Electron.Electron Phys. 28A (1969) 451-459

(143) Antoniv, I.P.,Vashchenyuk, N.N., Levitskaya, Ya.A., Matyukhin, V.A. and Tsal, N.A. : Rad.Eng.Elec. Phys. 21 (1976) 82-87

(144) All scanning electron microscope data was provided by Mr. G.McTurk

(145) Taylor, R.C., Hettrick, M.C. and Malina, R.F. : Rev.Sci.Instr. 54 (1983) 171-176

(146) Panitz, J.A. and Foesch, J.A. : Rev.Sci.Instr. 47 (1976) 44-49

(147) Polaert, R. and Rodiere, J. : Phillips Technical Review 34 (1974) 270-273

(148) Smythe, W.R. : Static and Dynamic Electricity, McGraw Hill, New York (1968) 91

(149) Afanasyev, A.G. and Bronshteyn, I.M. : Rad.Eng.Elec.Phys. 21 (1976) 144-146

(150) Harvey, P., Sanders, J., Cabral, R., Morris, J., Bjorkholm, P., Ballas, J., Jagoda, N. and Harnden, F.R. : IEEE Trans.Nucl.Sci. NS-23 (1978) 487

(151) Davelaar, J., Manzo, G., Peacock, A., Taylor, B.G., and Bleeker, J.A.M. : IEEE Trans.Nucl.Sci. NS-27 (1980) 196

(152) Griffiths, R.E., Polluci, G., Mak, A., Murray, S.S. and Schwartz, D.A. : SPIE 290 (1981) 62

(153) Takagi, S., and nine co-authors : Nucl.Instr.Meth. 215 (1983) 207-211

James Findlay Pearson

Advances in Soft X-ray Performance of Microchannel Plate Detectors

Abstract

This thesis discusses the design and improvement of microchannel plate (MCP) chevron detectors for imaging soft X-ray astronomy. Particular attention is focused on the MCP quantum detection efficiency and output pulse height distribution.

Graded density electrodes are shown to be a suitable two dimensional image encoding system for MCP's. Details are given of a specially constructed vacuum system for testing chevron MCP detectors.

Significant reductions in output pulse height distribution FWHM are demonstrated by applying an accelerating potential between the two MCP's of a chevron. Preliminary work on the development of a curved surface MCP detector, for use with grazing incidence optics, is reported and recommendations given for future development.

The rational behind using CsI reflection photocathodes to improve ~~the MCP's quantum detection efficiency is examined.~~ Existing CsI photocathode techniques are reviewed and extended to allow the deposition of 14,000 Å thick layers. A detailed set of efficiency measurements is presented.

Increased high angle efficiencies are obtained by using a repeller grid with a CsI coated MCP. The results of attempting to produce an MCP with an input electrode that does not penetrate into the channels are also described. The overall usefulness of a repeller grid is discussed.

Significant intrinsic energy resolution is achieved, for the first time, from a CsI coated MCP chevron. The resolution is sufficient to allow two colour photometry, separating energies above and below 1 keV. One attempt to improve the energy resolution is documented together with suggestions for further ways in which this might be achieved.